# Fibre-Loop Ring-Down Spectroscopy Using Liquid Core Waveguides

by

Klaus J. Bescherer-Nachtmann

A thesis submitted to the Department of Chemistry

in conformity with the requirements for the

Degree of Doctor of Philosophy

Queen's University

Kingston, Ontario, Canada

(April, 2013)

To my parents

Helmut and Rosemarie Bescherer

# Abstract

Cavity ring-down spectroscopy has been used over the last twenty years as a highly sensitive absorption spectroscopic technique to measure light attenuation in gases, liquids, and solid samples. An optical cavity is used as a multi-pass cell, and the decay time of the light intensity in the cavity is measured, thereby rendering the techniques insensitive to light intensity fluctuations. Optical waveguides are used to build the optical cavities presented in this work. The geometries of such waveguides permit the use of very small liquid sample volumes while retaining the advantages of cavity ring-down spectroscopy.

In this thesis cavity ring-down measurements are conducted, both, in the time domain and by measuring phase-shifts of sinusoidally modulated light, and the two methods are theoretically connected using a simple mathematical model, which is then experimentally confirmed. A new laser driver, that is compatible with high powered diode lasers, has to be designed to be able to switch from time domain to frequency domain measurements.

A sample path length enhancement within the optical cavity is explored with the use of liquid core waveguides. The setup was optimised with respect to the matrix liquid, the geometrical matching of waveguide geometries, and the shape of liquid core waveguide ends. Additionally, a new technique of producing concave lenses at fibre ends has been developed and the output of a general fibre lens is simulated.

Finally, liquid core waveguides are incorporated into a fibre-loop ring-down spectroscopy setup to measure the attenuation of two model dyes in a sample volume

of <1 μL. The setup is characterized by measuring concentrations of *Allura Red AC* and *Congo Red* from 1 μM to a limit of detection of 5 nM. The performance of the setup is compared to other absorption techniques measuring liquid samples.

# Acknowledgements

First and foremost I want to thank my supervisor, Dr. Hans-Peter Loock, for giving me the opportunity to do this research and for his support during my studies at Queen's University. He made my publications possible, and gave me the chance to participate in conferences and to give presentations. I am grateful to always being able to discuss ideas with him and his balanced approach to fulfilling the need for laboratory supplies. Dr. Loock has constantly encouraged me during my studies but also kept my projects on track.

I also want to thank Dr. Richard D. Oleschuk and Dr. J. Hugh Horton, for their ideas and for the discussions during my Supervisory Committee meetings and for all their input into my projects and my thesis.

Furthermore, I want to express my deep gratitude to Dr. Jack A. Barnes who has inspired me with many insightful discussions, has helped with building experimental setup, and has been easily approachable with questions, concerns, and challenges within the laboratory setting. Dr. Barnes' outstanding electronic knowledge has been an invaluable resource and made the improvements of the laser diode driver possible. A special thank also goes to Dr. Helen Wächter, who has been very supportive with countless conversations and thoughts regarding cavity ring-down spectroscopy. Nicolas R. Trefiak introduced me to the exciting world of cavity ring-down spectroscopy and helped sparking my interest in this research field, for which I am very grateful to him.

Moreover, I want to express my appreciation to Dr. Igor Kozin for all his support with teaching students in a laboratory setting. Not only I, but also the students that I taught, benefitted very much from the implementation of his skills.

Additionally, I want to thank all my past and present colleagues and friends in the research groups of Dr. Hans-Peter Loock, Dr. Richard D. Oleschuk and Dr. R. Stephen Brown, who produced a friendly and stress-free working environment. My appreciation goes to Dr. Graham Gibson, especially, for sharing some of his extraordinary insight into microfluidics. Particularly, I want to express my gratitude to Dr. Michelle Douma, Fred Zeltser, John Saunders, Gillian Mackey, Lili Mats, and Jason Bornstein for their insights to the production of this thesis and helping me taking the necessary breaks during the time of its production.

Definitely, I owe a big thank you to Gary Contant and Charles Hearns for giving me the opportunity to use the machine shop equipment and for all their help with machining parts for my experimental setups. Thank you also to the people in science stores, for their help with ordering research equipment, to the Undergraduate Laboratory Technicians, Tom Hunter, Len Rose, and Lyndsay Hull, to the Electronics and IT Technicians, Robin Roberts and Ed Maracle, for their generous help when I had a question or problem, and to the people in the general office, especially Annette Keyes, Barb Armstrong, and Michelle Boutilier, for all their help with organizing my studies.

In addition, I want to express my gratitude to Dr. John A. Gladysz and Dr. Kendall N. Houk for helping me acquire fundamental knowledge in Chemistry, gain confidence in the essential skills needed for pursuing my research and academic degrees, and for all the encouragement they provided about the decision to go abroad.

Especially, I want to thank my parents, Helmut and Rosemarie Bescherer, very much for all their unconditional love and constant support in every way imaginable, as well as their families, particularly my grandparents and my godfather, for laying the foundations for my skills and inquisitive personality, and therefore also for my professional success.

My deepest gratitude goes to my wife, Marina Nachtmann, for the love and laughter, and also for backing and assistance in good and in bad times. Her support on a personal, but also on a scientific level, helped me excel in my career.

Furthermore, many thanks go to my sister, Monika Groh, and her family, Andreas Groh, our godson Tobias, and our niece Jennifer, for their affection and the various stimulations.

Moreover, I want to express special thanks to my parents-in-law, Christa and Ludwig Nachtmann and their family, for integrating me fully, for being always there for me, and for their encouraging support. I am also grateful to my brother-in-law, Niklas Nachtmann, and his family, Nina Nachtmann, our godson Nikolai, and our niece Natalia, for the entertaining and inspiring private and professional discussions.

Finally, I very much appreciate the friendship of my friends in Kingston, Ontario, and in Nuremberg, Germany, that I greatly value. Despite the distance, the latter have never made me feel lacking closeness, while my friends in Canada have made it my home.

## Statement of Originality

I hereby certify that all of the work described within this thesis is the original work of the author unless otherwise stated. The theoretical model of ring-down measurements in the frequency domain was proposed by Nicolas R. Trefiak, and Dr. Helen Waechter assisted in the experimental proof of this model. Dr. Jack A. Barnes supported my research with contributions to the manufacture of experimental setups. Dorit Munzke performed the experimental visualization of the concave fibre lens output.

Any published (or unpublished) ideas and/or techniques from the work of others are fully acknowledged in accordance with the standard referencing practices.

Klaus J. Bescherer-Nachtmann

(April, 2013)

# Table of Contents

# List of Figures

# List of Tables

# List of Abbreviations

AC ..... alternating current

AFG ..... arbitrary function generator

AOM ..... acousto-optic modulator

ARROW ..... anti-reflecting resonant optical waveguides

ASE ..... amplified spontaneous emission

BBE ..... broadband emission

BNC ..... Bayonet-Neill-Concelman

CCD ..... charge coupled device

CEAS ..... cavity enhances absorption spectroscopy

CRDS ..... cavity ring-down spectroscopy

*cw* ..... continuous wave

DMSO ..... dimethylsulfoxide

DNA ..... deoxyribonucleic acid

EDFA ..... erbium-doped fibre amplifier

EOM ..... electro-optic modulator

FBG ..... fibre Bragg grating

FC/PC ..... ferrule connector / physical contact

FLRDS ..... fibre-loop ring-down spectroscopy

FSR ..... free spectral range

GRIN ..... gradient index

HPLC ..... high performance liquid chromatography

IC ..... integrated circuit

ICOS ..... integrated cavity optical spectroscopy

$Ø_{ID}$ ..... inner diameter

LCETS ..... locked cavity enhanced transmission spectroscopy

LCW ..... liquid core waveguide

LED ..... light emitting diode

LOD ..... limit of detection

LPG ..... long period grating

M.Sc. ..... Master of Science

NA ..... numerical aperture

Nd:YAG ..... neodymium-doped yttrium aluminum garnet

NICE-OHMS ..... noise-immune cavity-enhanced optical heterodyne molecular spectroscopy

$Ø_{OD}$ ..... outer diameter

OpAmp ..... operational amplifier

PCB ..... printed circuit board

PCF ..... photonic crystal fibre

PEEK ..... polyether ether ketone

PMT ..... photomultiplier tube

PS-CRDS ..... phase-shift-cavity ring-down spectroscopy

RC ..... resistor-capacitor

RI ..... refractive index

SEM ..... scanning electron microscopy

SMA ..... sub miniature A

SMD ..... surface mounted

SMF ..... single-mode fibre

TEC ..... thermoelectric cooler

USB ..... universal serial bus

UV ..... ultraviolet

VB ..... visual basic

Vis ..... visible

# Chapter 1.

# Introduction

## 1.1. Cavity Enhanced Methods

Optical spectroscopy is one of the longest-used techniques of identifying and quantifying chemical substances. In the eighteenth and nineteenth century, the Beer-Lambert law was derived, which describes the intensity decay of light when it travels through a medium.[1-3] This intensity decay is commonly expressed as the absorbance

$$A = -\log\frac{I}{I_0} = \varepsilon C d \qquad (1.1)$$

In this equation, $d$ is the length of the path that the light travels through the absorbing medium, ε is the molar extinction coefficient and C is the concentration of the analyte. $I_0$ and $I$ are the light intensities before and after the sample, respectively. In most commercial instruments, the absorbance is measured using a 1 cm path length cuvette, which requires a sample volume of a few millilitres. Since the absorbance is related to the ratio of light intensity before and after the sample, at small concentrations a very small change of a large (background) signal has to be detected. To overcome this limitation, the path length, $d$, can be extended, but this requires more sample to be present.

In the following, a comparison of different absorption spectroscopy configurations and their sensitivity is made. The sensitivity, the change in signal as a function of

concentration, is used as the distinguishing quantity. To increase the path length without increasing the volume, the light may be sent through the sample multiple times with the use of multi-pass cells, like Herriot cells[4], White cells[5, 6], or astigmatic mirror cells[7] (cf. Figure 1.1). The disadvantage these cell types have in common is that, although the optical path length is greatly enhanced, the sample volume inside the optical cell is not completely interrogated, which requires a homogeneous sample distribution in the cell. Additionally, these cells are sensitive to the alignment of the light beam.

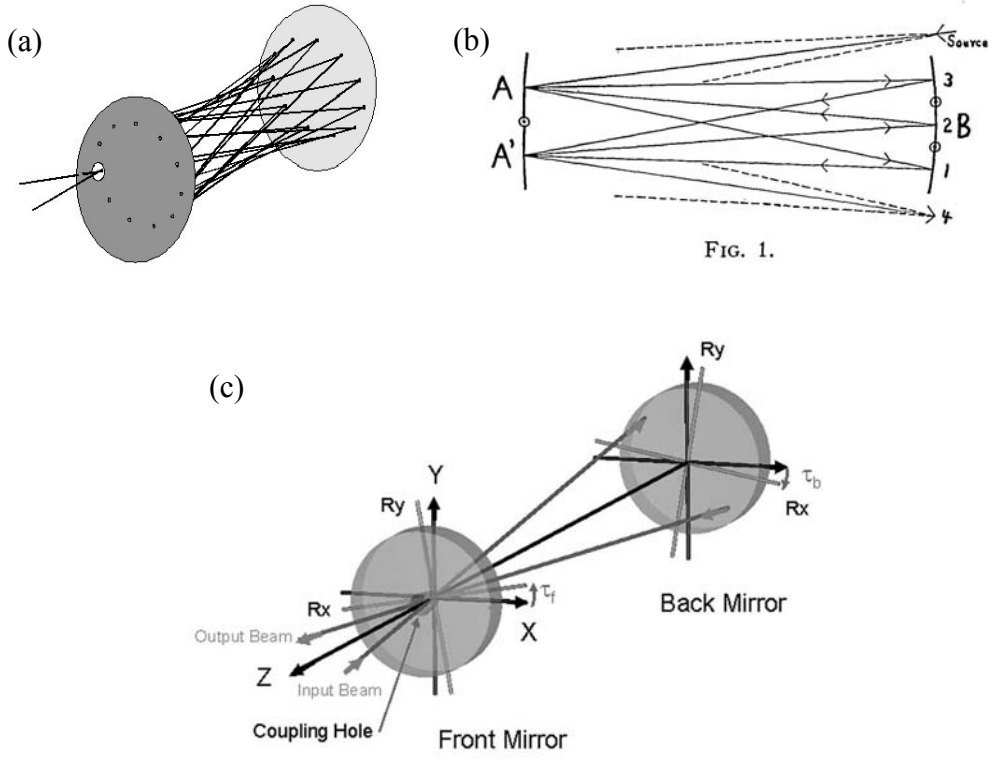


Figure 1.1. Multi-pass cells used in absorption spectroscopy: (a) Herriot cell[8], (b) White cell[6], and (c) astigmatic mirror cell[9].

Enhancing the sample path, by either using a longer cuvette, or by sending the light through the sample multiple times, being reflected back and forth by mirrors, results

in a greater sensitivity, but undoubtedly, there are other analytical methods which are more sensitive, like fluorescence spectroscopy (fluorometry). However, the disadvantage of fluorometry is that all analytes that do not exhibit natural fluorescence need to be labelled with a fluorescing tag, which alters the analyte and may therefore not be suitable for many applications. Non-spectroscopic techniques, for example, mass spectrometry, laser induced breakdown spectroscopy, atomic absorption or emission spectroscopy, and others, are also very sensitive but all destroy the analyte.

Extending the sample path eliminates to some extent one of the disadvantages of absorption spectroscopy, but it does not solve the problem of having to distinguish light source fluctuations from intensity changes that are due to absorption of an analyte. Spectrometers with two beam paths, one for the sample and one for a reference solution, overcome this problem, but the requirements for two balanced detectors and matching the matrix liquid of the sample can be very demanding.

In the last quarter of the twentieth century, optical cavities were discovered for absorption spectroscopy. In 1988, Deacon and O'Keefe invented *cavity ring-down spectroscopy (CRDS)* using an optical cavity made from two highly reflective mirrors to probe a strongly forbidden transition of gaseous molecular oxygen[10]. Although the utilization of this technique for absorbance spectroscopy was a novelty, the technique had already existed in a rudimentary form since the 1960s. In 1961, Jackson used a Fabry-Perot cavity with an absorbing medium inside[11] and in 1962, Kastler measured atomic absorption and emission in a passive optical cavity[12]. In the year 1974, Kastler also determined that the light in an optical cavity decayed exponentially with time[13]. He expressed this with an

exponential decay law, which became the core of cavity ring-down spectroscopy. A typical CRDS setup is shown in Figure 1.2. Commonly, a pulsed laser is coupled into an optical cavity made from two high reflective mirrors and the cavity output is observed. From the rate of the intensity decay of the light in the cavity, losses in the cavity are extracted and with that, the absorbance of the sample in the cavity is determined. CRDS is explained in more detail later in this chapter.

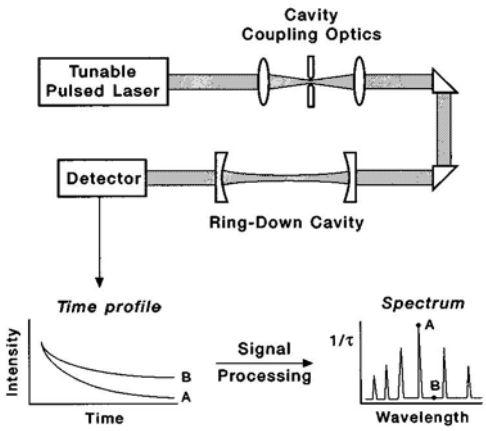


Figure 1.2. Conventional cavity ring-down spectroscopy setup and data acquisition. A laser pulse from a tunable pulsed laser source is coupled into an optical cavity, The intensity of the pulse trapped inside the cavity decays with time because of absorption, scatter, and other loss processes. This intensity decay is monitored by a detector placed behind the optical cavity and intensity-time profiles, or ring-down traces, are recorded (A or B). If a laser source with a short pulse is used, a pulse train is to be seen on the detector and the envelope of this pulse train is represented by the decay trace (A or B). If the laser pulse is sufficiently long, the decay trace is measured directly on the detector. Higher losses within the cavity produce a fast decaying intensity (A), while low losses give rise to longer decay traces (B). This applies to either one cavity mode, or to an ensemble of modes. For each wavelength of the final spectrum a ring-down trace (A or B) has to be measured. In the 'Signal processing' step, the decay time $\tau$ is extracted from a fit to the decay trace. Adapted from Reference 14.[14] To efficiently couple the light pulse into the optical cavity, the mode spectrum of the cavity and the frequency of the laser light have to be matched. Additionally, the temporal pulse width has to be considered, since the frequency range is larger for shorter laser pulses. This will be discussed in detail in Chapter 3.

Shortly after the invention of CRDS by Deacon and O'Keefe, cavity enhanced methods were developed, such as cavity enhanced absorption spectroscopy (CEAS), integrated cavity output spectroscopy (ICOS), locked cavity enhanced transmission spectroscopy (LCETS), noise-immune cavity-enhanced optical heterodyne molecular spectroscopy (NICE-OHMS) and others.

In short, in ICOS measurements, a high finesse optical cavity, similar to cavities used in CRDS, is excited with a narrow bandwidth *cw*-laser and the absolute output of the cavity is recorded.[15, 16] The intensity output, $I$, of the cavity depends on the incident light, $I_0$, on the mirror transmission, $T$, on the average effective mirror reflectivity, $R'$, on the intra-cavity absorption per unit length, $\alpha$, and on the length of the cavity $l$ (cf. Equation 1.2).

$$\text{ICOS: } I = I_0 T^2 e^{-\alpha l} \times \left[ 2 \log\left( R' \right) \right]^{-1} \tag{1.2}$$

The difference to cavity ring-down spectroscopy is that one of the cavity mirrors was dithered with an actuator at a frequency much lower than the reciprocal decay time in the cavity, usually in the low kHz range. This dithering motion randomized the mode spectrum of the cavity and produced a pseudo-continuous cavity spectrum. A laser, which is scanned over multiple free-spectral-ranges (*FSR*, cf. Chapter 3) of the cavity, is then on resonance with an individual cavity mode only for a short period of time. Consequently, some intensity accumulates in the cavity but no intensity build-up as in CRDS is observed. One has to consider that sine-modulation of the mirror position, as would be typical for

dithering, results in the mirror spending more time at the turning points. This would preferentially populate cavity modes corresponding to these lengths. To account for this effect, additional frequency modulation of the laser reduces the longer mode overlaps at the turning points of the mirror dithering motion and is therefore beneficial to the intensity detection. This randomizing of the cavity mode spectrum, together with the frequency modulation of the laser, results in an extension of the effective sample path and, with it, in an increase of the sensitivity of the system. A typical setup is displayed in Figure 1.3.

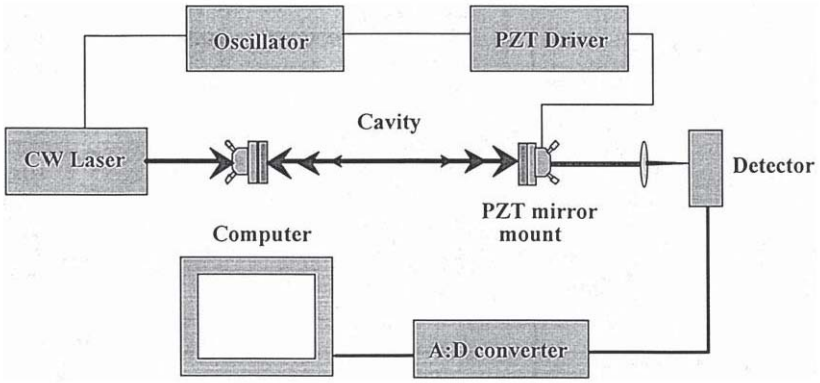


Figure 1.3. Typical *cw*-ICOS setup. A laser is coupled into a linear mirror cavity. One cavity mirror is moved at a frequency of 1 kHz with low amplitude, effectively randomizing the cavity mode structure. Additionally, the laser is frequency modulated, to reduce any residual light build-up when the laser and the cavity are on resonance. The 'oscillator' denotes an oscilloscope, which is used for diagnostic purposes only.[16]

CEAS is a very similar technique to ICOS, with the small difference that the cavity is not actively destabilized by jittering or dithering one of the cavity mirrors.[17] The laser is scanned over the spectral region of interest, and the integrated cavity output at each wavelength is recorded with a photodiode or photomultiplier tube (PMT). Several scans are summed to increase the signal-to-noise ratio. In CEAS, the cavity is stabilized but not locked to the laser and only the random jitters in the cavity mode structure provide the

randomness of the resonant frequencies. For CEAS, the frequency scan time of the laser has to be short enough to resonantly populate all cavity modes equally. The experimental setup is very similar to the *cw*-ICOS setup in Figure 1.3, but the piezo mirror mounts, scrambling the mode structure, are not used.

In 1999, Gianfrani et al. locked their laser output to a cavity mode. They scanned over the absorption feature of molecular oxygen around 762 nm in a mirror-based optical cavity and with that, they employed locked cavity enhanced transmission spectroscopy.[18, 19] The laser was locked with the Pound-Drever-Hall scheme to the cavity. A detailed description of the locking scheme can be found in the publications of Drever and Black.[20, 21] Gianfrani et al. did not record the ring-down signal of their optical cavity but rather measured the absolute output intensity while the laser was locked to a cavity mode, and the cavity mode was scanned over an absorption feature. Furthermore, they employed an acousto-optical modulator (AOM) to stabilize the intensity output of their light source. The empty cavity output and the filled cavity output signals allowed them to calculate the actual absorption. They greatly increased the sensitivity versus traditional transmission spectroscopy, although the detection scheme requires much more technical equipment and cannot be scanned over hundreds of nanometers, to produce broad spectra.

The last cavity enhanced method to be described here, is noise-immune cavity-enhanced optical heterodyne molecular spectroscopy (NICE-OHMS) and was invented by Ye et al. in 1998.[22] So far, NICE-OHMS is, according to the author's knowledge, the most sensitive cavity enhanced absorption technique. In NICE-OHMS, the laser is frequency

modulated with a radio frequency that corresponds to exactly the free spectral range frequency of the cavity. The frequency modulation generates sidebands of the carrier frequency at an FSR distance. In addition, the laser is locked to one cavity mode by the Pound-Drever-Hall approach[20, 21], which causes the sidebands from the initial frequency modulation to also align with two adjacent cavity modes. With that, the carrier light and the two sidebands are transmitted through the cavity. If there is no absorber in the cavity at this point, the contributions of the sidebands to the output signal are cancelling each other out and the frequency modulated signal is zero. This scheme results in the noise-immunity of the system. When scanning the cavity over an absorption feature of the sample now, the mode that the carrier is locked to shifts due to a refractive index change and the contributions of the sidebands are no longer balanced, which gives rise to a signal. This is depicted in Figure 1.4.a. Figure 1.4.b shows a general setup of a NICE-OHMS experiment. The laser is frequency modulated by the first electro-optical modulator (EOM) to match the FSR of the cavity, and a second EOM is used to produce the Pound-Drever-Hall locking signal.

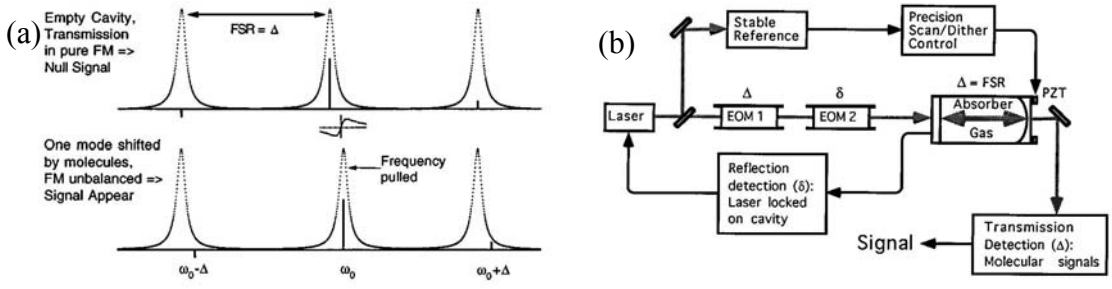


Figure 1.4. NICE-OHMS working principle and setup. (a) NICE-OHMS detection principle without and with absorber present. The cavity mode of the carrier shifts, due to the absorber, and the sidebands are not properly aligned with their respective cavity modes anymore, which gives rise to a signal. (b) A typical NICE-OHMS setup with two electro-optic modulators, producing the NICE-OHMS sidebands at a distance of +/- FSR, and the Pound-Drever-Hall locking signal.[22]

All the earlier described cavity enhanced methods measure the steady-state light output of the optical cavity and relate this to the sample absorption. Unfortunately, measuring intensities eliminates the immunity towards light intensity fluctuations that is inherent to CRDS. However, the major advantage of these methods over time-resolved CRDS is, that they do not require fast data acquisition, fitting procedures, or expensive A/D equipment and therefore, data can be acquired much faster than in CRDS. In this thesis, the focus is nonetheless on cavity ring-down spectroscopy because of its noise immunity and sensitivity advantages over ICOS, CEAS, and LCETS and the reduced complexity with respect to NICE-OHMS.

## 1.2. Overview of Cavity Ring-Down Spectroscopy

### 1.2.1. Mirror Cavities

Early CRDS measurements were solely performed on molecules in the gas phase and on gas phase processes, such as molecular beams[23, 24], photo dissociation processes[25], reactions in the gas phase at hot filaments[26], quantitative kinetic measurements[27], amongst others. More recently, CRDS has also been applied to liquid samples. Two simple approaches are filling the entire gas phase cavity with liquid[28] and inserting a liquid flow cell into the cavity. In order to minimize loss in the cavity, the liquid flow cells have been placed at Brewster's angle[29, 30] or sample containers are omitted at all and a free flowing liquid sheet is directed through the cavity[31, 32]. Short cavities, with a distance between the

mirrors of only a few centimeters or even millimeters, are used to reduce the amount of solution needed to fill the whole cavity.[28, 33, 34] Attempts to combine CRDS measurements with separation techniques such as, for example, high performance liquid chromatography (HPLC), and capillary electrophoresis, are made.[35] Also, liquid and even solid phases are probed by the evanescent field of the circulating light[36-38] (cf. Figure 1.5).

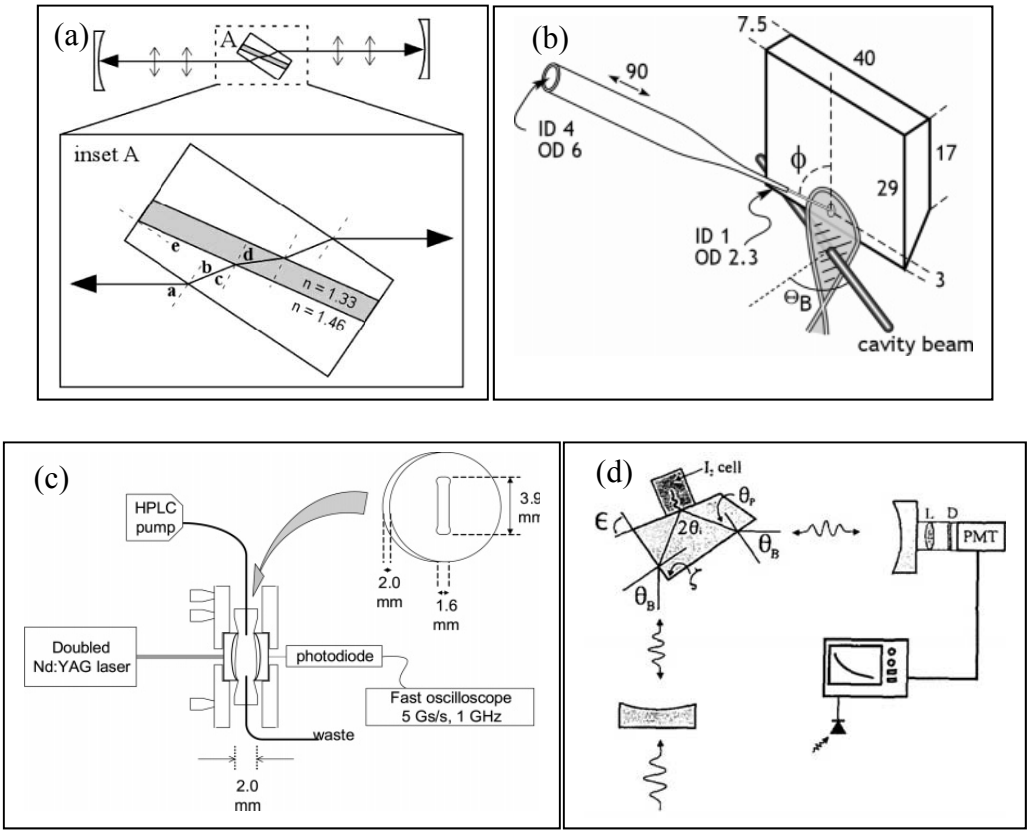


Figure 1.5. Various schemes to introduce liquid and solid samples into the optical cavity in CRDS: (a) detection cell at Brewster's angle[29], (b) free flowing liquid sheet[31], (c) short mirror cavity completely filled with liquid[33], (d) evanescent wave detection in an optical prism[36].

The first measurement of O'Keefe and Deacon was performed in the visible region at around 680 nm. Due to the availability of highly reflective mirrors from the UV to the infrared, experiments from about 200 nm[26, 39], through the visible[24], to the near-

infrared at about 3500 nm[40, 41], and even to the mid infrared spectral region at 11 μm[42] have been conducted in order to investigate either fundamental or overtone vibrational transitions.

Conventional CRDS relies on a laser light source, which is ideally tuneable over a wide spectral range for measuring absorption spectra, on the one hand. On the other hand, to resolve detailed absorption features, a narrowband light source is needed, as mentioned previously, which should be capable of providing pulses that are considerably shorter than the cavity ring-down time. Such light sources can be quite expensive. Hence, they have been replaced by cheaper diode lasers, as soon as these have been developed in the appropriate wavelength range, keeping a cost effective setup in mind. Most recently, high power light emitting diodes (LEDs) have been also used at different wavelengths, lowering the costs even more.[43] Since LEDs emit light over a broad not tunable region, their lack of wavelength resolution prohibits their use in rotational or vibrational spectroscopy but they can be utilized in spectroscopy on liquids. With these light sources commercial field spectrometers can be developed.

The first optical ring-down cavities were made of two highly reflective mirrors (reflectivities from 99% to 99.99984%[26]) where the light is coupled into the cavity by transmission through the back of one of the cavity mirrors and the transmitted light through the second mirror is detected. This cavity model has been used for more than twenty years, but has evolved, due to better mirrors and other developments. Nowadays, cavities may

have three or four mirrors, while other optical cavities, like prisms[36, 37], micro-resonators[44], and optical fibres[45, 46] have also been explored.

### 1.2.2. Waveguide Cavity Ring-Down

The research described in this thesis is mainly concerned with the application of wave guiding optics to CRDS, where the optical cavity is made from optical fibres or other waveguides, and it is useful to review waveguide supported CRDS. Waveguide supported CRDS has its advantages in, for example, being able to interrogate small sample volumes and being able to be bent to minimize the footprint of such a setup, but it has disadvantages in higher intra-cavity losses, which reduce the ring-down times that are measured. For example, by using two identical *Fibre Bragg Gratings* (*FBG*s) at the ends of a strand of *single-mode fibre* (*SMF*), a simple analog to conventional CRDS can be made.[47] FBGs behave like fibre optic mirrors with a reflectivity comparable to that of high reflective mirrors in traditional CRDS. An FBG is a periodic change of the refractive index within the core of a fibre[48, 49]. Light is reflected by the FBG if its wavelength satisfies the Bragg condition $\lambda = 2n\Lambda$, where $\Lambda$ is the period of the grating and $n$ is an integer number. This setup can be easily combined with flow systems, to gather absorbance data in small liquid samples by intersecting the strand of fibre with the sample flow, while no complicated alignment of the mirrors is necessary. The FBG reflection spectrum is sensitive to mechanical deformation and to temperature, which led to the usage of FBG CRD measurements for pressure or temperature sensing applications.[50] Moreover, instead of

using FBGs, the end facets of fibres can be coated with dielectric coatings, in order to produce a reflective surface.[51]

On account of the flexibility of optical waveguides, another type of setup can be built quite easily, by directing the ends of a strand of multimode fibre towards each other and forming a loop as optical cavity.[45, 46, 52] The advantage of fibre-loops over cavities made from FBGs lies in the inherently broad cavity spectrum which is limited only by the transmission range of the fibre material (about 350 nm to 1700 nm for a silica fibre). By comparison mirror or FBG cavities only reflect efficiently in a narrow region of typically a few nanometers of the spectrum.

As in conventional CRDS, in *Fibre-Loop Ring-Down Spectroscopy* (*FLRDS*), the ring-down time is calculated as the ratio of the round trip time and all cavity losses. However, in FLRDS the different losses, and also the round trip time, are expressed differently with respect to the cavity length. In CRDS, a round trip is twice the length of the cavity. In FLRDS the length of the cavity equals one round trip. Furthermore, the round trip time is now dependent on the refractive index of the waveguide material, as the speed of light changes with the refractive index of the medium. In conventional CRDS, the refractive index change, due to the cavity medium, can usually be neglected. Therefore, the round trip time in CRDS and FLRDS is:

$$\text{CRDS: } t_{RT} = \frac{2l}{c_0} \tag{1.3}$$

$$\text{FLRDS: } t_{RT} = \frac{nL}{c_0} \tag{1.4}$$

with the round trip time being $t_{RT}$, the length of the CRDS cavity being $l$, the speed of light in vacuum being $c_0$, the refractive index of the fibre material being $n$, and $L$ being the loop length in FLRDS.[53] In addition, there are different losses associated with the use of fibres than with traditional CRDS. In the latter, the non-sample losses only result from the reflectivity, $R$, of the mirrors. Note that for high reflective mirrors, the simplification $-\ln R = 1 - R$ is usually made. In analogy to Equation 1.5 for CRDS, the ring-down time for FLRDS is calculated as

$$\text{CRDS: } \tau = \frac{t_{RT}}{2\left(1 - R + \sum \varepsilon C l\right)} \tag{1.5}$$

$$\text{FLRDS: } \tau = \frac{t_{RT}}{\left(-\ln T_{splice} - \ln T_{gap} + \alpha L + \sum \varepsilon C d\right)} \tag{1.6}$$

with the overall transmission, $T_{splice}$, of the fibre splices (typically 0.02 dB loss for fused spliced and 0.23 dB for mechanical splices)[54] and couplers (estimated to have a 0.46 dB insertion loss in addition to the coupling losses depending on the coupling ratio), the transmission, $T_{gap}$, due to the sample gap (typically minimum 0.2 dB, depending on the sample gap width), $\alpha$ being the attenuation coefficient of the fibre material (3.1 dB/km loss for a optimized fibre at its designated wavelength; about 1 dB/m for UV enhanced fibres is also very common), $L$ being the length of the fibre-loop, and $\Sigma\varepsilon Cd$ being the sum of all the sample losses in the sample gap with the length $d$.[45, 46] A general schematic of a FLRDS setup is shown in Figure 1.6.

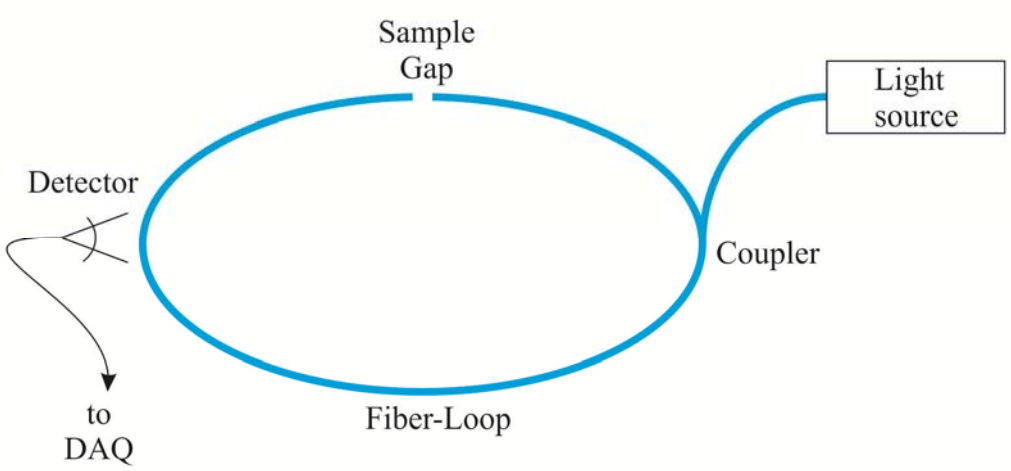


Figure 1.6. General setup of fibre-loop ring-down spectroscopy. Light from a pulsed or cw-light source is launched into one end of a fibre optic coupler, which transfers a small amount (< 10%) into the loop cavity. The light then circulates within the cavity. Intensity gets lost by sample absorption in the sample gap ($\sum \varepsilon C d$), but also by reduced transmission across the sample gap ($-\ln T_{gap}$), by absorption by the fibre material ($-\alpha L$), by insertion losses of the coupler, by coupling losses within the coupler, and by bending losses (the latter are combined in the term $-\ln T_{splice}$). The light in the cavity is monitored, for example, by a PMT, which is placed next to a slight bend of the loop fibre. Scattered light, which is proportional to the light intensity in the fibre-loop, leaks out at this bend.

### 1.2.2.1. Coupling Light into Waveguide Cavities

Owing to the lack of mirrors (and of FBGs) in FLRDS, a different approach for coupling light into the fibre-loop than in traditional CRDS (which relies on the very small transmission of one of the mirrors) is needed. The first technique described here for coupling light into a fibre-loop is based on the use of commercially available fibre couplers. For the telecom wavelength region, these fused silica fibre couplers can be bought off-the-shelf with different coupling ratios. Couplers at other wavelengths are also developed and by now, they are available for some visible wavelengths. By reason of the

much higher attenuations of optical fibres in the UV region, no couplers are available for this region yet, but recent improvements of UV-enhanced fibres with a transmission of 93% per meter at wavelengths as short as 250 nm indicate that couplers for UV wavelengths may be much more available in the near future.

Unfortunately, couplers, like most other optical devices that are spliced into a fibre cavity, introduce an insertion loss. For example, a coupling ratio of 99% : 1% does not mean that the total transmitted light at both outputs of the coupler adds up to 100% of the incident light, as couplers have an insertion loss of about 2% to 4%, and the rest of the intensity is split according to the coupling ratio.[55] Therefore, when using fibre couplers, the insertion loss has to be taken into account and included in the denominator of Equation 1.6.

A second approach, of getting light into the cavity is side-pumping of the fibre-loop. This means that the laser light is directed onto a slightly bent section of the fibre-loop in an almost tangential way with a maximum angle of 30˚ between the loop fibre and the light beam. A coupling ratio for this setup is hard to predict and is relatively low but, unlike couplers, this approach does not introduce any major loss into the loop, besides the bending loss, which may be reduced to be insignificantly small. Directing the light onto the loop cavity can either be done by focussing the beam onto the waveguide or by using a delivery fibre where the light is coupled into beforehand. More details about coupling methods can be extracted from the M.Sc. thesis of Mr. Trefiak.[55] These results might have to be revised for the UV region, when couplers are developed in this region.

Instead of commercial couplers, or side pumping, a third option for light coupling is the usage of field access blocks, which couple light evanescently from one to another

fibre. The fibres are affixed in a glass block at a slight bend and the cladding of the fibre is reduced or completely removed. Due to the thinned cladding region the evanescent tail of the core modes extends to the outside of the fibre and energy can be transferred if the evanescent wave is coupled into a second waveguide. The resulting cladding material thickness determines the intensity of the evanescent wave and the coupling ratio between two field access blocks can be adjusted.[56]

A fourth option to introduce light into a fibre-loop cavity was developed in our group by Waechter et al.[57] Light is introduced into the cavity at the same point where the sample is introduced, which is at the gap in the loop, thereby reducing additional losses in the cavity (cf. Figure 1.7.c). Light from a delivery fibre was shone onto the receiving fibre end of the sample gap at a shallow angle. For this purpose, a new sample interface-coupler combination was developed: The two loop fibres and the light delivery fibre were placed into V-grooves in a plastic plate for alignment purposes and were then sealed in place with a second plastic plate as a cover and using UV-curable epoxy adhesive. Into both plates, small holes were drilled for the injection of liquid.

A fifth technique was presented in a recent study by Rushworth et al. who coupled light into and out of a fibre-loop cavity by introducing a small reflective facet into a fibre (cf. Figure 1.7.a). The reflectively coated facet directed light from a perpendicular light source into the core of the waveguide.[58] The "top notch" was fabricated by polishing a 45° facet onto a multimode fibre end in such a way, that the facet protrudes very slightly into the core of the waveguide. After coating the entire end of the facetted fibre with a mirror coating, the front end was polished again, in order to remove the coating and make it transparent again. Then, this fibre end was carefully aligned with the opposite end of the

fibre strand, forming a loop cavity. Shining light perpendicular to the major fibre dimension onto the fibre facet reflects the beam inside the core of the second end of the fibre strand, so that, light is being coupled into the cavity. This coupling scheme has the added benefit, that the facet can also be used as an output coupler for detection. Figure 1.7 illustrates the working principle of the different coupling methods.

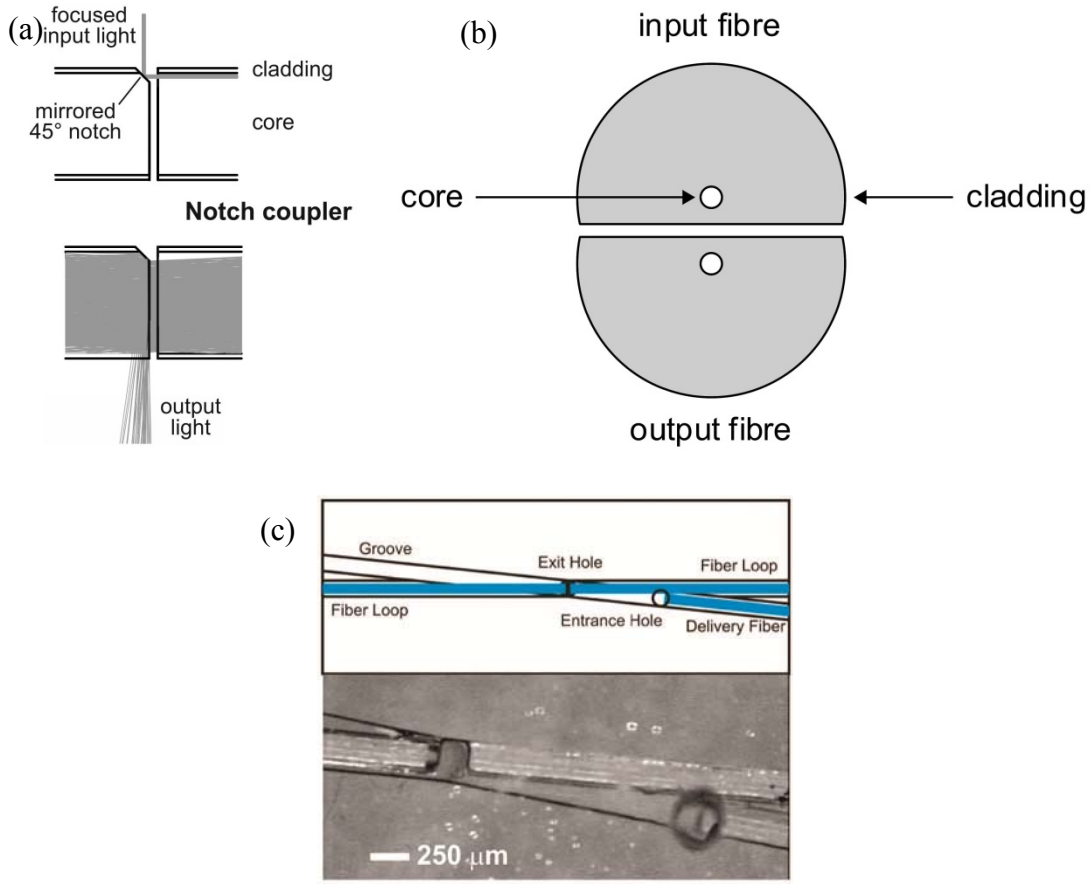


Figure 1.7. Different fibre couplers for introducing light into a ring cavity: (a) notch coupler[58], (b) field access blocks cross section[55]. The distance between the cores of the field access blocks determines the coupling ratio. (c) Coincided sample interface and light coupling region[57].

#### 1.2.2.2. Lenses Used in Fibre-Loop Ring-Down Spectroscopy

As indicated in Equation 1.5 and 1.6, the ring-down time is dependent on the overall loss of the cavity. To make a ring-down setup very sensitive to analyte absorption, the loss introduced by the sample should be larger than the cavity's inherent losses. This can be achieved by, for example, improving the mirror reflectivity in CRDS or increasing the overall fibre transmission in FLRDS. The most prominent and highly undesired loss mechanism in FLRDS is the reduced transmission across the sample gap. Set out to overcome this effect, Trefiak investigated the efficiency of lensed fibre ends versus straight cut fibre ends[55]. The transmission between two fibre ends was measured as a function of axial displacement for single-mode fibres and multi-mode fibres in a fibre patch cord.[55] Lensed fibres were produced by melting the fibre ends in an electric arc, causing surface tension to pull the molten glass into a hemispherical lens. It was found that lenses have a superior transmission across gaps filled with air or water, compared to straight-cut fibre ends, except at very small displacements. Another detailed example for lensed fibres in FLRDS is given in Chapter 4.2.5, where lenses with a negative curvature in combination with higher refractive index liquids are discussed. Gradient index (GRIN) lenses are commercially used to collimate light and focus it over longer distances. They are usually coupled to single-mode fibre optic cables and have been incorporated in experimental setups.[59] Although all lenses can increase the transmission of light over a small gap, they require precise alignment, including angular alignment.

#### 1.2.2.3. Amplified Fibre-Loop Ring-Down Spectroscopy

To increase ring-down times, and thereby the sensitivity of the measurements, one may also amplify the light within the cavity to compensate for all losses ($-\ln T_{splice}$, $-\ln T_{gap}$, $-\alpha L$, cf. Equation 1.6), except the desired losses due to the sample absorption ($\sum \varepsilon C d$). Ideally, an amplifier compensates for all optical losses that are not due to the sample and hence, are undesired. This idea was investigated by Stewart and Culshaw with a modified FLRDS setup.[59, 60] In their experiment, an erbium-doped fibre amplifier (EDFA) was used to amplify the light intensity at a wavelength of around 1550 nm (cf. Figure 1.8). If the losses without any sample can be exactly compensated by amplification, theoretically, an infinitely long ring-down time can be achieved when no sample is present. In this ideal case, the only loss that is measured is the attenuation loss on account of the sample, which results in a very high sensitivity. The main problem with such a scheme is the exact adjustment of the amount of amplification, so that only the undesired losses are compensated for. Additionally, this exact amplification needs to be maintained over the course of the experiment. Unfortunately, EDFAs are designed to amplify by a factor of 100 - 1000, whereas the required amplification for FLRD systems is much lower. For example, when 15% background loss in a loop has to be compensated for the amplification factor, or gain, has to be only 1.15. EDFAs are developed for telecom purposes to boost the signal intensity in long optical telephone lines. Efforts have been made to overcome this deficiency and are briefly described below. The output spectrum of an EDFA lies in the near-infrared region, which limits the use of this technique to this wavelength range.

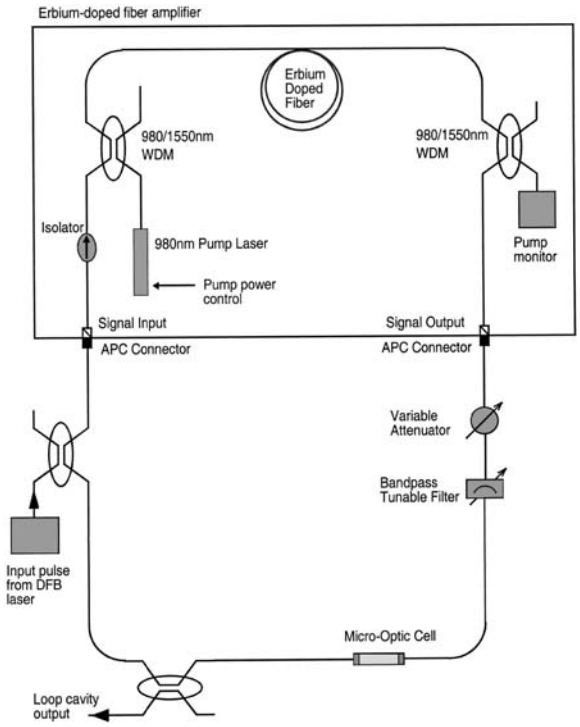


Figure 1.8. Amplified cavity ring-down setup, used by Stewart and Culshaw at a wavelength of around 1550 nm.

To improve on this detection scheme and circumvent the gain issue, the pump power of the EDFA can be set sufficiently high to exceed the lasing threshold. This transforms the EDFA in a fibre laser (if the EDFA is part of a feedback system such as a loop cavity), and ring-down measurements can be performed at wavelengths other than the lasing wavelength. Stewart and Culshaw implemented this idea and achieved ring-down times up to 100 μs.[60] Since the gain profile of the EDFA is not flat, the gain of the probe wavelength depends on the proximity to the lasing wavelength of the EFDA. With wavelengths very close to each other, new difficulties arise with the increase of relaxation oscillations stemming from perturbations of the population of individual vibrational levels of the excited state. These relaxation oscillations can be on the order of milliseconds in case of Erbium, due to the long lifetime of the excited state of Erbium. Although ring-

down times can still be extracted, these oscillations cause an unstable environment in the experiment and the accuracy and reproducibility is limited. Further improvements were made by Stewart et al. by using a digital narrow band-pass filter which made observations of ring-down times in the millisecond region possible.[61] In consequence of the requirement of having the probe wavelength and the lasing wavelength very close together, recording a spectrum is problematic. A solution to this may be having two nested loops that both share one amplifier. A setup like this has been described by Stewart et al. but not yet implemented.

Loock et al. have revisited this experiment and designed a setup, in which the inner loop was made into the fibre laser, while the outer loop was used as a sample cavity.[62, 63] The gain between both loops was adjusted with an optical attenuator in such a way that the outer loop performed just below the lasing threshold, while the inner loop was lasing. A band-pass filter prevented crosstalk between the loops. In a preliminary experiment, a 6 cm gas cell had been used and the P(13) line of the $\nu_1+\nu_3$ combination band of acetylene had been probed.[63] Two GRIN lenses collimated the beam through the sample cell and ring-down times of hundreds of microseconds were achieved. A schematic drawing of the setup can be seen in Figure 1.9.

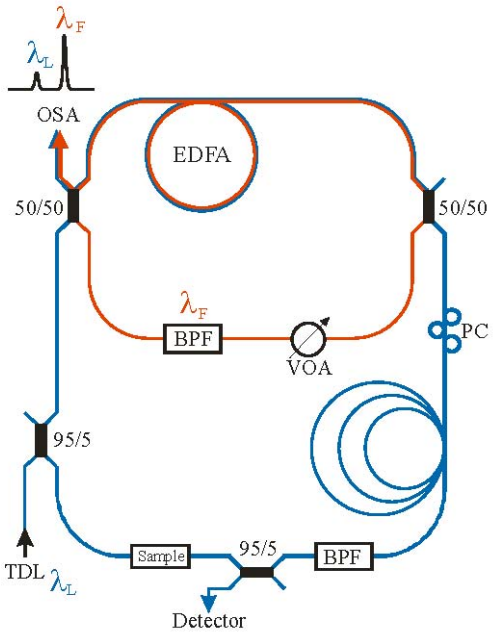


Figure 1.9. Amplified FLRDS system with two nested loops.[63]

### 1.2.2.4. Sensors Used in CRDS

The CRDS techniques presented here all interrogated the sample by shining the light beam through a liquid or gaseous sample or by examining solids with the evanescent wave of the light in the cavity. Obviously, there are numerous ways to incorporate different sensors into ring-down spectroscopy. The most common sensors for probing chemical analytes are transmission sensors. When using these, the sample is introduced into the optical cavity and absorption, scattering and dispersion can be studied. Gas diffusion through an optical waveguide also attenuates the light intensity and can also be seen as an absorption detector.[64, 65]

Evanescent wave absorption sensors use the attenuation of the evanescent tail of a propagating mode to probe the sample. For this to be used, the evanescent wave has to be made accessible, since it is usually contained within the cladding of waveguide to facilitate low loss guiding of light. To expose the evanescent wave to the environment of the waveguide the waveguide can be tapered or the cladding of the waveguide can be (partly) removed. The latter can be accomplished by etching away some of the cladding material or by building a field access block as described above (cf. Chapter 1.2.2.1).

Furthermore, a different type of evanescent wave sensors can be made by transferring some intensity from core modes to cladding modes, since the evanescent tail of the cladding modes stick out into the immediate surroundings of the waveguide. As Pu and Gu showed, long period gratings (LPGs) can couple light from the core mode of the used single mode fibre to cladding modes and back.[66] LPGs are similar to FBGs but their periodicity of the changing refractive index is much longer. Such LPGs efficiently transfer energy from high order core modes to low order cladding modes and back. Consequently, a consecutive pair of identical LPGs can be used to frame the evanescent wave sensing region of an optical fibre as shown in Figure 1.10.c.

Furthermore, total internal reflection on the inside of an optical prism also exposes the evanescent wave of the into the cavity coupled light beam as has been exploited by Pipino et al[36, 37] and by MacKenzie et al[67, 68].

More details about sensors that are used in CRDS can be found in two recent reviews by Waechter et al.[63] and Wang[69]. Besides chemical detection, CRDS can also be used for the sensing of temperature[50], pressure[70, 71], strain[55, 72], and bending losses[46, 73].

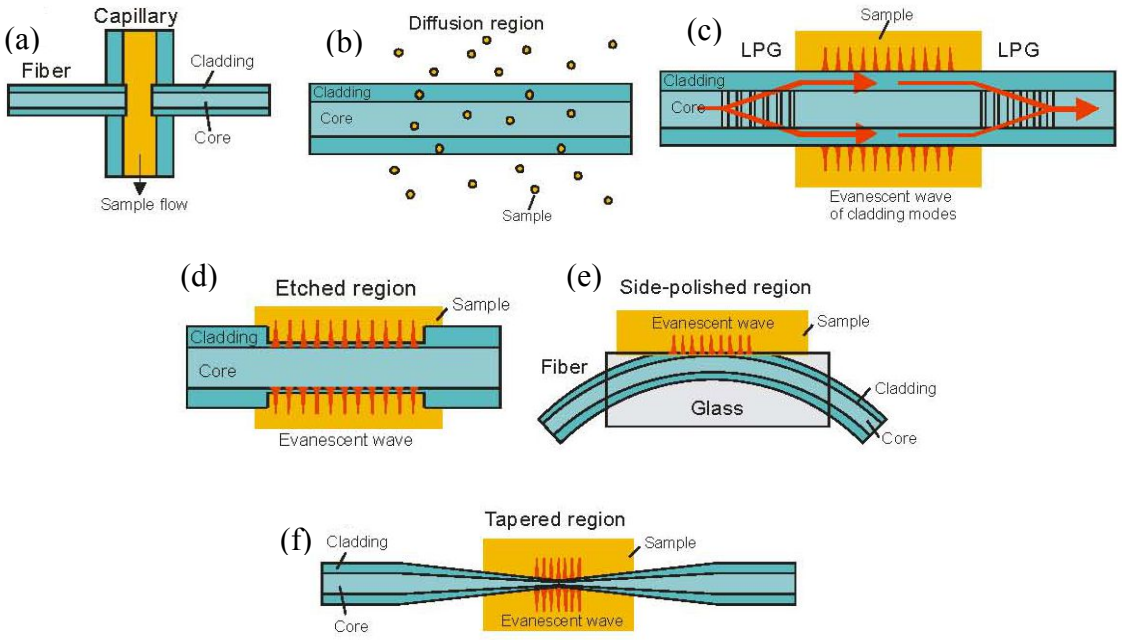


Figure 1.10. Different sensor schemes used in CRDS: (a) transmission sensor, (b) sensor based on gas diffusion through optical fibres, (c) energy transfer from core modes to cladding modes, utilizing LPGs and the attenuation of the evanescent wave of cladding modes, (d) cladding thickness reduced for exposing evanescent fields of core modes, (e) field access block with reduced cladding and evanescent sensing, (f) tapered region in an optical fibre, making evanescent waves of core modes accessible. Adapted from Reference 62.

## 1.3. Liquid Core Waveguides

To decrease the detection limit of a spectroscopic technique, the most obvious method is to increase the light's path through the sample (cf. Equation 1.1). Enhancing the sample path in traditional CRDS, achieved by increasing the distance between the two mirrors, is restricted by the pointing stability and the alignment capabilities of the mirrors, while in FLRDS, lengthening the path is limited by the transmission across the sample gap. The light guiding mechanism of a typical optical fibre is total internal reflection, which

requires that the core refractive index is greater than the cladding refractive index (cf. Chapter 4.1). The light, leaving a straight-cut fibre end, will always form a diverging cone, of which only a fraction is sampled by the receiving fibre end. The fraction decreases rapidly with the distance between the emitting and the receiving fibre ends. Lenses, such as hemispherical lenses made through melting the fibre in an electric arc[55] or GRIN lenses, somewhat reduce these losses but are not able to increase the transmission to over 90%.

Consequently, in a FLRDS setup the sample path is restricted to a small gap between the fibre ends. An alternative to increasing the sample path between the fibre ends would be, to contain the sample within the core of the waveguide. In such a setup, the analyte solution replaces the core material of the waveguide. Still, light guiding is achieved whenever the cladding material around the now liquid core, for example, a glass capillary, has a lower refractive index than the liquid core. Such waveguides are direct analogs to optical fibres including the light guiding principle, and are called liquid core waveguides (LCW). LCWs are made from capillaries, low refractive index tubing, or channels in lab-on-a-chip devices. Exchanging the optical fibre cavity completely for an LCW increases the sample gap from a few tens of micrometers in FLRDS to the entire length of the waveguide loop, which may be centimeters or even meters long. If a capillary is used as waveguide, a sample volume of only 40 μL is needed to fill the capillary, assuming a typical inner diameter of 100 μm and a length of 5 m. This volume is still compatible with many analytical separation techniques, yet, the path length is increased by over four orders of magnitude, compared to a 100 μm sample gap. It is in turn expected that the limit of detection is lowered by the same factor, in cases when all other factors stay constant. A similar approach to increase the sample path length, while keeping the light coupling

mechanisms and detection methods from FLRDS, is to incorporate an LCW as a sample gap into a FLRDS system. Challenges and opportunities associated with this combination are extensively explored in Chapter 4 and results are given in Chapter 5.

Liquid core waveguides have been applied to a multitude of analytical techniques over the last few decades. Before the end of the 1980s, no tubing material that had a refractive index (RI) lower than water (RI = 1.33) existed, and liquid core waveguides were either restricted to high refractive index solvents[74], required a reflective coating on the inside or outside surfaces of the waveguides[75, 76], or were relying on total internal reflection at the glass-air boundary. The latter decreased the interaction with the core and led to lower sensitivities. In 1989, DuPont invented a low refractive index fluorous polymer family, called Teflon AF[77], which has a refractive index (RI = 1.29 – 1.31) lower than that of water. This invention gave rise to a variety of liquid core waveguide applications, like fluorescence[78-86] and Raman spectroscopy[87-93], as well as absorption spectroscopy from the ultra violet to the infra-red wavelength range[85, 94-103].

There are two distinct major ways to implement the Teflon AF materials in liquid core waveguides. First, a tube or channel can be coated with the material to produce the low RI surface or, second, the tubing can be made from the Teflon AF material itself. The first experiments were performed on coated waveguides, for which capillaries were dip-coated with a solution of Teflon AF.[104] Teflon AF has many more advantages other than a low refractive index. The material is flexible, which means it can be bent or coiled, decreasing the footprint of experimental setup. Also, Teflon AF is to some extent porous, which can be utilized for diffusing gas through the walls into the waveguide.[96, 105] Thus,

the porosity can have desired effects in some experiments, while for other applications, in which these effects are not desired, either a Teflon AF coated waveguide or a coated, pure Teflon AF waveguide must be used to decrease the gas permeability. All these properties of the Teflon AF material inspired its extensive use as waveguides in spectroscopic experiments.

The elongated sample path provided by a Teflon AF-based LCW has led to a variety of analytical experiments in chemistry. Measurements of, for example, hydrogen sulfide[94], mercury atoms[106], iron[95], hexachromium[107], bromthymol blue[108], aluminium(III)[85], nitrate and nitrite[98, 109-111], colored dissolved organic matter[112], acetylsalicylic acid, acetone, and toluene in water[97], and many more have been performed with different techniques. In 2010, Pan et al. published an article on a hand-held photometer that measures "the quality and quantity of DNA samples"[113]. They used two UV-LEDs at 260 nm and 280 nm and a Teflon AF waveguide. Furthermore, they developed a bent input and output coupler, to introduce light into the LCW. With a sample of only about 350 nL, a detection limit of 0.1 µg/mL was achieved, which is comparable to a conventional photometer.

Due to the permeability of the Teflon AF material it has also been used as a gas sensor for chlorine, nitrogen dioxide, carbon dioxide, and others.[96, 106] Due to differences in diffusion rates through the material, different gases can be distinguished with the use of multiple liquid core waveguides with different wall thicknesses, although the absorption of the gases is comparable.

Besides the use of Teflon AF-based LCWs as long path length cells or gas diffusion sensors, waveguides made from Teflon AF have been also used for fluorescence measurements. The fluorescence emission of a molecule has an isotropic distribution and is usually detected at an angle of 90˚ to the excitation beam. If a fluorophore is excited in a liquid core waveguide, some of the isotropic emission will be emitted in such an angle that the fluorescence emission is guided in the waveguide. Although only a small fraction of the emitted light is guided by the waveguide, depending on the core and cladding materials, it can still be easily detected at the end of the LCW. This technique has been utilized in various ways and for multiple analytes.[85, 94, 114] Often, experimental setups that utilize both absorption spectroscopy and fluorescence spectroscopy have been devised. In 2002, Olivares et al. have developed a setup, in which they scanned an excitation laser along a Teflon AF waveguide, which also acted as an electrophoresis column, for separating and detecting different DNA samples.[115] Scanning of the laser allowed them to illuminate single bands of the electrophoretically separated DNA mixture. Many other research groups also recognized the use of such a liquid core waveguide for electrophoretic separations coupled with fluorescence detection.[80, 116-118]

Axial excitation of the liquid in the waveguide has been used for Raman spectroscopy as well. Owing to the ability of the waveguide to guide both the excitation light and Raman emission, a considerable enhancement in the signal can be observed without the need for surface enhancement or resonant Raman techniques. In 1999, Marquardt et al. demonstrated the combination of high performance liquid chromatography with a Teflon AF-based liquid core waveguide detection system. They measured alcohols

in aqueous solutions and reported an enhancement factor of three orders of magnitude over conventional Raman spectroscopy.[90] Other groups have utilized LCW techniques in combination with Raman spectroscopy to measure biomolecules[91, 92] or organic molecules, such as benzene, toluene, and p-xylene[87]. The small volume required to fill liquid core waveguides "is an added benefit when limited quantities of sample are available".[92]

Besides the mentioned optical techniques, chemiluminescence experiments can also be performed with the aid of Teflon AF liquid core waveguides.[119] More details on this can be found in a review by Dallas et al.[120] In a more recent review by Pena-Pereira et al., multiple micro-cells for analytical chemistry are presented, including but not limited to liquid core waveguides.[121]

## 1.4. Conclusion

For the research presented in this thesis, a glass capillary has been used as a waveguide and has been incorporated into a FLRDS detection system in order to lengthen the sample path. Although Teflon AF has advantageous characteristics over glass, a glass capillary has been used, as it is more transparent at all wavelengths used in this thesis and scatters considerably less than Teflon AF. The goal of this research project was to detect concentrations of sub micromolar quantities of two model dyes, *Congo Red* and *Allura Red AC*, with a maximal sample volume of 1 μL. The volume restriction stems from a potential combination of the technique with separation techniques used in pharmaceutical industry

such as HPLC or from the need of modern analytical techniques to analyze small quantities. In modern HPLC analysis systems, a UV-Vis detector is used to track the different compounds eluting from the HPLC column. The detection volume of such a UV-Vis detector is on the order of 10 μL. For a well-constructed single-pass liquid core waveguide experiment, the limit of detection is on the order of tens of nanomoles for a strong absorbing dye (cf. Table 5.1), such as the sample dyes used in this thesis.

To the best of the author's knowledge, successfully combining a liquid core waveguide with fibre-loop ring-down spectroscopy had not been done before.

This thesis describes two separate projects. The first is presented in Chapters 2 and 3, whereas the second project is presented in Chapters 4 and 5. Chapter 2 discusses the improvement of a high power laser driver that is needed for the experiments described in Chapter 3. The laser driver had been custom built by a company which has gone out of business soon afterwards. Since documentation did not exist for this laser driver, the circuit was inspected very closely and circuit diagrams were constructed.

After improving the laser driver with respect to the shut-off times of our laser diode, it could be used for the experiments described in Chapter 3. In Chapter 3, a theoretical model is described to determine ring-down times in the frequency domain. Experimental verification of the models with an electrical circuit and a fibre-loop cavity are shown and discussed.

Chapter 4 and 5 describe the second project of this Ph.D. thesis. Chapter 4 provides preliminary experiments for the combination of liquid core waveguides with fibre-loop ring-down cavities. As a start, a suitable matrix liquid for the LCW is

determined, then, geometrical matching of the dimensions of the fibre and the LCW is explored. After examining the shape of the liquid core waveguide end faces, the use of collimating lenses is investigated. A theoretical model for simulating lenses at fibre ends is developed and described in detail.

In Chapter 5, a liquid core waveguide fibre-loop ring-down spectroscopy setup is constructed and two model dyes, *Allura Red AC* and *Congo Red*, are injected into the LCW. A limit of detection of 5 nM for both dyes is found and experiments to characterize the setup are performed.

After a general conclusion in Chapter 6, further improvements and projects opened by the found results are discussed in detail. The appendix shows small devices which were built to successfully facilitate the experiments described in this thesis.

## 1.5. References


1. Bouguer, P., *Essai d'optique sur la gradation de la lumière*. Paris, 1729; p 164.

2. Lambert, J. H., *Photometria sive de mensura et gradibus luminis, colorum et umbrae [Photometry, or, On the measure and gradations of light, colors, and shade]*. Eberhardt Klett: Augsburg ("Augusta Vindelicorum"), Germany, 1760.

3. Beer, A., Bestimmung der Absorption des rothen Lichts in farbigen Flüssigkeiten (Determination of the absorption of red light in colored liquids). *Annalen der Physik und Chemie* 1852, 86, 78-88.

4. Herriott, D.; Kompfner, R.; Kogelnik, H., Off-Axis Paths in Spherical Mirror Interferometers. *Applied Optics* 1964, 3, 523-&.

5. White, J. U., Very Long optical Paths in Air. *Journal of the Optical Society of America* 1976, 66, 411-416.

6. White, J. U., Long optical paths of large aperture. *Journal of the Optical Society of America* 1942, 32, 285-288.

7. McManus, J. B.; Kebabian, P. L.; Zahniser, W. S., Astigmatic Mirror Multipass Absorption Cells for Long-Path-Length Spectroscopy. *Applied Optics* 1995, 34, 3336-3348.

8. Ivanenko, M.; Hering, P. Laser-Induced Carbon Isotopes Separation. http://www.uni-duesseldorf.de/WWW/MedFak/LaserMedizin/hering/isotop/isotop.html (accessed 12.10.2012).

9. McManus, J. B., Paraxial matrix description of astigmatic and cylindrical mirror resonators with twisted axes for laser spectroscopy. *Applied Optics* 2007, 46, 472-482.

10. O'Keefe, A.; Deacon, D., Cavity ring-down optical spectrometer for absorption measurements using pulsed laser sources. *Review of Scientific Instruments* 1988, 59, 2544.

11. Jackson, D. A., Spherical Fabry-Perot Interferometer as an Insrument of High Resolving Power for Use with External or with Internal Atomic Beams. *Proceedings of the Royal Society of London Series a-Mathematical and Physical Sciences* 1961, 263, 289-&.

12. Kastler, A., Atomes a Iinterieur Dun Interferometre Perot-Fabry. *Applied Optics* 1962, 1, 17-24.

13. Kastler, A., Transmission of Light Pulse Through a Fabry-Perot-Interferometer. *Nouvelle Revue D Optique* 1974, 5, 133-139.

14. Zalicki, P.; Zare, R. N., Cavity Ring-Down Spectroscopy for Quantitative Absorption-Measurements. *Journal of Chemical Physics* 1995, 102, 2708-2717.

15. O'Keefe, A., Integrated cavity output analysis of ultra-weak absorption. *Chemical Physics Letters* 1998, 293, 331-336.

16. O'Keefe, A.; Scherer, J. J.; Paul, J. B., cw Integrated cavity output spectroscopy. *Chemical Physics Letters* 1999, 307, 343-349.

17. Engeln, R.; Berden, G.; Peeters, R.; Meijer, G., Cavity enhanced absorption and cavity enhanced magnetic rotation spectroscopy. *Review of Scientific Instruments* 1998, 69, 3763-3769.

18. Nakagawa, K.; Katsuda, T.; Shelkovnikov, A. S.; de Labachelerie, M.; Ohtsu, M., Highly Sensitive Detection of Molecular Absorption Using a High Finesse Optical Cavity. *Optics Communications* 1994, 107, 369-372.

19. Gianfrani, L.; Fox, R. W.; Hollberg, L., Cavity-enhanced absorption spectroscopy of molecular oxygen. *Journal of the Optical Society of America B-Optical Physics* 1999, 16, 2247-2254.

20. Drever, R. W. P.; Hall, J. L.; Kowalski, F. V.; Hough, J.; Ford, G. M.; Munley, A. J.; Ward, H., Laser Phase and Frequency Stabilization Using an Optical-Resonator. *Applied Physics B-Photophysics and Laser Chemistry* 1983, 31, 97-105.

21. Black, E. D., An introduction to Pound-Drever-Hall laser frequency stabilization. *American Journal of Physics* 2001, 69, 79-87.

22. Ye, J.; Ma, L. S.; Hall, J. L., Ultrasensitive detections in atomic and molecular physics: demonstration in molecular overtone spectroscopy. *Journal of the Optical Society of America B-Optical Physics* 1998, 15, 6-15.

23. Paul, J. B.; Collier, C. P.; Saykally, R. J.; Scherer, J. J.; Okeefe, A., Direct measurement of water cluster concentrations by infrared cavity ringdown laser absorption spectroscopy. *Journal of Physical Chemistry A* 1997, 101, 5211-5214.

24. Romanini, D.; Lehmann, K. K., Ring-Down Cavity Absorption-Spectroscopy of the very Weak HCN Overtone Bands with 6, 7, and 8 Stretching Quanta. *Journal of Chemical Physics* 1993, 99, 6287-6301.

25. Enami, S.; Hoshino, Y.; Kawasaki, M., A kinetic study of the gas-phase reactions of OIO with NO, NO2, and Cl-2. *International Journal of Chemical Kinetics* 2007, 39, 688-693.

26. Zalicki, P.; Ma, Y.; Zare, R. N.; Wahl, E. H.; Dadamio, J. R.; Owano, T. G.; Kruger, C. H., Methyl Radical Measurement by Cavity Ring-Down Spectroscopy. *Chemical Physics Letters* 1995, 234, 269-274.

27. Yu, T.; Lin, M. C., Kinetics of Phenyl Radical Reactions Studied by the Cavity-Ring-Down Method. *Journal of the American Chemical Society* 1993, 115, 4371-4372.

28. Hallock, A. J.; Berman, E. S. F.; Zare, R. N., Direct monitoring of absorption in solution by cavity ring-down spectroscopy. *Analytical Chemistry* 2002, 74, 1741-1743.

29. Snyder, K. L.; Zare, R. N., Cavity ring-down spectroscopy as a detector for liquid chromatography. *Analytical Chemistry* 2003, 75, 3086-3091.

30. Bechtel, K. L.; Zare, R. N.; Kachanov, A. A.; Sanders, S. S.; Paldus, B. A., Moving beyond traditional UV-visible absorption detection: Cavity ring-down spectroscopy for HPLC. *Analytical Chemistry* 2005, 77, 1177-1182.

31. Alexander, A. J., Flowing liquid-sheet jet for cavity ring-down absorption measurements. *Analytical Chemistry* 2006, 78, 5597-5600.

32. Vogelsang, M.; Welsch, T.; Jones, H., A free-flowing soap film combined with cavity ring-down spectroscopy as a detection system for liquid chromatography. *Journal of Chromatography A* 2009, doi:10.1016/j.chroma.2009.10.053.

33. Bahnev, B.; van der Sneppen, L.; Wiskerke, A. E.; Ariese, F.; Gooijer, C.; Ubachs, W., Miniaturized cavity ring-down detection in a liquid flow cell. *Analytical Chemistry* 2005, 77, 1188-1191.

34. van der Sneppen, L.; Wiskerke, A.; Ariese, F.; Gooijer, C.; Ubachs, W., Improving the sensitivity of HPLC absorption detection by cavity ring-down spectroscopy in a liquid-only cavity. *Analytica Chimica Acta* 2006, 558, 2-6.

35. Loock, H.-P., Ring-down absorption spectroscopy for analytical microdevices. *Trac-Trends in Analytical Chemistry* 2006, 25, 655-664.

36. Pipino, A. C. R.; Hudgens, J. W.; Huie, R. E., Evanescent wave cavity ring-down spectroscopy for probing surface processes. *Chemical Physics Letters* 1997, 280, 104-112.

37. Pipino, A. C. R.; Hudgens, J. W.; Huie, R. E., Evanescent wave cavity ring-down spectroscopy with a total-internal-reflection minicavity. *Review of Scientific Instruments* 1997, 68, 2978-2989.

38. Pipino, A. C. R., Ultrasensitive surface spectroscopy with a miniature optical resonator. *Physical Review Letters* 1999, 83, 3093-3096.

39. Meijer, G.; Boogaarts, M. G. H.; Jongma, R. T.; Parker, D. H.; Wodtke, A. M., Coherent Cavity Ring Down Spectroscopy. *Chemical Physics Letters* 1994, 217, 112-116.

40. He, Y. B.; Hippler, M.; Quack, M., High-resolution cavity ring-down absorption spectroscopy of nitrous oxide and chloroform using a near-infrared cw diode laser. *Chemical Physics Letters* 1998, 289, 527-534.

41. Scherer, J. J.; Voelkel, D.; Rakestraw, D. J.; Paul, J. B.; Collier, C. P.; Saykally, R. J.; Okeefe, A., Infrared Cavity Ringdown Laser-Absorption Spectroscopy (IR-CRLAS). *Chemical Physics Letters* 1995, 245, 273-280.

42. Engeln, R.; vandenBerg, E.; Meijer, G.; Lin, L.; Knippels, G. M. H.; vanderMeer, A. F. G., Cavity ring down spectroscopy with a free-electron laser. *Chemical Physics Letters* 1997, 269, 293-297.

43. Thompson, J. E.; Myers, K., Cavity ring-down lossmeter using a pulsed light emitting diode source and photon counting. *Measurement Science & Technology* 2007, 18, 147-154.

44. Armani, D. K.; Kippenberg, T. J.; Spillane, S. M.; Vahala, K. J., Ultra-high-Q toroid microcavity on a chip. *Nature* 2003, 421, 925-928.

45. Brown, R. S.; Kozin, I.; Tong, Z.; Oleschuk, R. D.; Loock, H.-P., Fiber-loop ring-down spectroscopy. *Journal of Chemical Physics* 2002, 117, 10444-10447.

46. Tong, Z. G.; Jakubinek, M.; Wright, A.; Gillies, A.; Loock, H.-P., Fiber-loop ring-down spectroscopy: A sensitive absorption technique for small liquid samples. *Review of Scientific Instruments* 2003, 74, 4818-4826.

47. Gupta, M.; Jiao, H.; O'Keefe, A., Cavity-enhanced spectroscopy in optical fibers. *Optics Letters* 2002, 27, 1878-1880.

48. Hill, K. O.; Malo, B.; Bilodeau, F.; Johnson, D. C.; Albert, J., Bragg Gratings Fabricated in Monomode Photosensitive optical Fiber by UV Exposure Through a Phase Mask. *Applied Physics Letters* 1993, 62, 1035-1037.

49. Kashyap, R., *Fiber Bragg Gratings*. Academic Press, Elsevier: San Diego, 1999.

50. Wang, C. J.; Mbi, A., An alternative method to develop fibre grating temperature sensors using the fibre loop ringdown scheme. *Measurement Science & Technology* 2006, 17, 1741-1751.

51. von Lerber, T.; Sigrist, M. W., Cavity-ring-down principle for fiber-optic resonators: experimental realization of bending loss and evanescent-field sensing. *Applied Optics* 2002, 41, 3567-3575.

52. Loock, H.-P., Cavity Ring-Down Spectroscopy Using Waveguides. In *Cavity Ring-Down Spectroscopy: Techniques and Applications*, 1st Edition ed.; Berden, G.; Engeln, R., Eds. Wiley-Blackwell: Hoboken, NJ, USA, 2009.

53. Jakubinek, M.; Tong, Z. G.; Manzhos, S.; Loock, H.-P., Configuration of ring-down spectrometers for maximum sensitivity. *Canadian Journal of Chemistry-Revue Canadienne De Chimie* 2004, 82, 873-879.

54. Tong, Z. Fiber-Loop Ring-Down Spectroscopy. Dissertation, Queen's University, 2004.

55. Trefiak; Ronald, N. Ringdown spectroscopy in optical waveguides. Master of Science, Queen's University, Kingston, 2007.

56. Sharma, A.; Kompella, J.; Mishra, P. K., Analysis of Fiber Directional-Coulers and Coupler Half-Blocks Using a New Simple-Model for Single-Mode Fibers. *Journal of Lightwave Technology* 1990, 8, 143-151.

57. Waechter, H.; Bescherer, K.; Dürr, C.; Oleschuk, R. D.; Loock, H.-P., 405 nm Absorption Detection in Nanoliter Volumes. *Analytical Chemistry* 2009, 81, 9048.

58. Rushworth, C. M.; James, D.; Lee, J. W. L.; Vallance, C., Top Notch Design for Fiber-Loop Cavity Ring-Down Spectroscopy. *Analytical Chemistry* 2011, 83, 8492-8500.

59. Stewart, G.; Atherton, K.; Yu, H. B.; Culshaw, B., An investigation of an optical fibre amplifier loop for intra-cavity and ring-down cavity loss measurements. *Measurement Science & Technology* 2001, 12, 843-849.

60. Stewart, G.; Atherton, K.; Culshaw, B., Cavity-enhanced spectroscopy in fiber cavities. *Optics Letters* 2004, 29, 442-444.

61. Stewart, G.; Shields, P.; Culshaw, B., Development of fibre laser systems for ring-down and intracavity gas spectroscopy in the near-IR. *Measurement Science & Technology* 2004, 15, 1621-1628.

62. Litman, J. Detection of Chemical Compounds Using Amplified Fiber Loop Ring-Down Spectroscopy. Master of Science, Queen's University, Kingston, 2011.

63. Waechter, H.; Litman, J.; Cheung, A. H.; Barnes, J. A.; Loock, H.-P., Chemical Sensing Using Fiber Cavity Ring-Down Spectroscopy. *Sensors* 2010, 10, 1716-1742.

64. Tanifuji, T.; Matsumoto, M.; Tokuda, M.; Miyauchi, M., Wavelength-Dependent Optical Loss Increase in Graded-Index Optical Fiber Transmission-Lines. *Electronics Letters* 1984, 20, 13-14.

65. Vogler, D. E.; Muller, M. G.; Sigrist, M. W., Fiber-optic cavity sensing of hydrogen diffusion. *Applied Optics* 2003, 42, 5413-5417.

66. Pu, S. A.; Gu, X. J., Fiber loop ring-down spectroscopy with a long-period grating cavity. *Optics Letters* 2009, 34, 1774-1776.

67. Mazurenka, M.; Wilkins, L.; Macpherson, J. V.; Unwin, P. R.; Mackenzie, S. R., Evanescent wave cavity ring-down spectroscopy in a thin-layer electrochemical cell. *Analytical Chemistry* 2006, 78, 6833-6839.

68. Schnippering, M.; Neil, S. R. T.; Mackenzie, S. R.; Unwin, P. R., Evanescent wave cavity-based spectroscopic techniques as probes of interfacial processes. *Chemical Society Reviews* 2011, 40, 207-220.

69. Wang, C. J., Fiber Loop Ringdown - a Time-Domain Sensing Technique for Multi-Function Fiber Optic Sensor Platforms: Current Status and Design Perspectives. *Sensors* 2009, 9, 7595-7621.

70. Wang, C. J.; Scherrer, S. T., Fiber loop ringdown for physical sensor development: pressure sensor. *Applied Optics* 2004, 43, 6458-6464.

71. Wang, C. J.; Scherrer, S. T., Fiber ringdown pressure sensors. *Optics Letters* 2004, 29, 352-354.

72. Gagliardi, G.; De Nicola, S.; Ferraro, P.; De Natale, P., Interrogation of fiber Bragg-grating resonators by polarization-spectroscopy laser-frequency locking. *Optics Express* 2007, 15, 3715-3728.

73. Vogler, D. E.; Lorencak, A.; Rey, J. M.; Sigrist, M. W., Bending loss measurement using a fiber cavity ringdown scheme. *Optics and Lasers in Engineering* 2005, 43, 527-535.

74. Fujiwara, K.; Fuwa, K., Liquid Core Optical Fiber Total Reflection Cell as a Colorimetric Detector for Flow-Injection Analysis. *Analytical Chemistry* 1985, 57, 1012-1016.

75. Dasgupta, P. K., Multipath Cells for Extending Dynamic-Range of Optical Absorbance Measurements. *Analytical Chemistry* 1984, 56, 1401-1403.

76. Charlton, C.; Inberg, A.; Croitoru, N.; Mizaikoff, B., Hollow waveguide infrared gas sensing for biomedical applications. In *Optical Fibers and Sensors for Medical Applications Iii*, Gannot, I., Ed. 2003; Vol. 4957, pp 116-123.

77. DuPont Fluoroproducts , Teflon AF Amorohous Fluoropolymers H-16577-1. DuPont: Wilmington, DE 19880-0711, USA.

78. Langer, P.; Muller, R.; Drost, S.; Werner, T., A new method for filter-free fluorescence measurements. *Sensors and Actuators B-Chemical* 2002, 82, 1-6.

79. Hanning, A.; Westberg, J.; Roeraade, J., A liquid core waveguide fluorescence detector for multicapillary electrophoresis applied to DNA sequencing in a 91-capillary array. *Electrophoresis* 2000, 21, 3290-3304.

80. Hanning, A.; Lindberg, P.; Westberg, J.; Roeraade, J., Laser induced fluorescence detection by liquid core waveguiding applied to DNA sequencing by capillary electrophoresis. *Analytical Chemistry* 2000, 72, 3423-3430.

81. Li, J. Z.; Dasgupta, P. K., Measurement of atmospheric hydrogen peroxide and hydroxymethyl hydroperoxide with a diffusion scrubber and light emitting diode-liquid core waveguide-based fluorometry. *Analytical Chemistry* 2000, 72, 5338-5347.

82. Toda, K.; Dasgupta, P. K.; Li, J. Z.; Tarver, G. A.; Zarus, G. M., Fluorometric field instrument for continuous measurement of atmospheric hydrogen sulfide. *Analytical Chemistry* 2001, 73, 5716-5724.

83. Li, J. Z.; Dasgupta, P. K.; Tarver, G. A., Pulsed excitation source multiplexed fluorometry for the simultaneous measurement of multiple analytes. Continuous measurement of atmospheric hydrogen peroxide and methyl hydroperoxide. *Analytical Chemistry* 2003, 75, 1203-1210.

84. Li, J. Z.; Dasgupta, P. K.; Genfa, Z., Transversely illuminated liquid core waveguide based fluorescence detection - Fluorometric flow injection determination of aqueous ammonium/ammonia. *Talanta* 1999, 50, 617-623.

85. Li, Q. Y.; Morris, K. J.; Dasgupta, P. K.; Raimundo, I. M.; Temkin, H., Portable flow-injection analyzer with liquid-core waveguide based fluorescence, luminescence, and long path length absorbance detector. *Analytica Chimica Acta* 2003, 479, 151-165.

86. Lacki, P.; Nowakowski, A.; Dress, P.; Franke, H., Fluorescence measurements with Liquid Core Waveguide. In *Optoelectronic and Electronic Sensors Iii*, Nowakowski, A.; Chachulski, B., Eds. 1999; Vol. 3730, pp 112-117.

87. Tanikkul, S.; Jakmunee, J.; Rayanakorn, M.; Grudpan, K.; Marquardt, B. J.; Gross, G. M.; Prazen, B. J.; Burgess, L. W.; Christian, G. D.; Synovec, R. E., Characterization and use of a Raman liquid-core waveguide sensor using preconcentration principles. *Talanta* 2003, 59, 809-816.

88. Holtz, M.; Dasgupta, P. K.; Zhang, G. F., Small-volume raman spectroscopy with a liquid core waveguide. *Analytical Chemistry* 1999, 71, 2934-2938.

89. Altkorn, R.; Koev, I.; VanDuyne, R. P.; Litorja, M., Low-loss liquid-core optical fiber for low-refractive-index liquids: fabrication, characterization, and application in Raman spectroscopy. *Applied Optics* 1997, 36, 8992-8998.

90. Marquardt, B. J.; Vahey, P. G.; Synovec, R. E.; Burgess, L. W., A Raman waveguide detector for liquid chromatography. *Analytical Chemistry* 1999, 71, 4808-4814.

91. Dijkstra, R. J.; Slooten, G. J.; Stortelder, A.; Buijs, J. B.; Ariese, F.; Brinkman, U. A. T.; Gooijer, G., Liquid-core waveguide technology for coupling column liquid

chromatography and Raman spectroscopy. *Journal of Chromatography A* 2001, 918, 25-36.

92. Pelletier, M. J.; Altkorn, R., Raman sensitivity enhancement for aqueous protein samples using a liquid-core optical-fiber cell. *Analytical Chemistry* 2001, 73, 1393-1397.

93. Dijkstra, R. J.; Bader, A. N.; Hoornweg, G. P.; Brinkman, U. A. T.; Gooijer, C., On-line coupling of column liquid chromatography and raman spectroscopy using a liquid core waveguide. *Analytical Chemistry* 1999, 71, 4575-4579.

94. Byrne, R. H.; Yao, W. S.; Kaltenbacher, E.; Waterbury, R. D., Construction of a compact spectrofluorometer/spectrophotometer system using a flexible liquid core waveguide. *Talanta* 2000, 50, 1307-1312.

95. Waterbury, R. D.; Yao, W. S.; Byrne, R. H., Long pathlength absorbance spectroscopy: trace analysis of Fe(II) using a 4.5m liquid core waveguide. *Analytica Chimica Acta* 1997, 357, 99-102.

96. Dasgupta, P. K.; Genfa, Z.; Poruthoor, S. K.; Caldwell, S.; Dong, S.; Liu, S. Y., High-sensitivity gas sensors based on gas-permeable liquid core waveguides and long-path absorbance detection. *Analytical Chemistry* 1998, 70, 4661-4669.

97. Klein, K. F.; Belz, M.; Dress, P.; Schelle, B.; Boyle, W. J. O.; Grattan, K. T. V.; Franke, H., Ultrasensitive detection system for fiber-optic-based ultraviolet spectroscopy. In *Micro- and Nanofabricated Structures and Devices for Biomedical Environmental Applications*, Gourley, P. L.; Katzir, A., Eds. 1998; Vol. 3258, pp 75-81.

98. Steimle, E. T.; Kaltenbacher, E. A.; Byrne, R. H., In situ nitrite measurements using a compact spectrophotometric analysis system. *Marine Chemistry* 2002, 77, 255-262.

99. Byrne, R. H.; Kaltenbacher, E., Use of liquid core waveguides for long pathlength absorbance spectroscopy: Principles and practice - Comment. *Limnology and Oceanography* 2001, 46, 740-742.

100. D'Sa, E. J.; Steward, R. G., Liquid capillary waveguide application in absorbance spectroscopy (Reply to the comment by Byrne and Kaltenbacher). *Limnology and Oceanography* 2001, 46, 742-745.

101. Saggese, S. J.; Harrington, J. A.; Sigel, G. H.; Altkorn, R.; Haidle, R., Novel Lightpipes for Infrared-Spectroscopy. *Applied Spectroscopy* 1992, 46, 1194-1197.

102. Meister, J.; Diemer, S.; Jung, R.; Klein, S.; Fuss, W.; Hering, P., *Liquid core fused silica capillary lightguides for applications in the UV/VIS and NIR spectral range*. 1997; Vol. 2977, p 58-66.

103. Diemer, S.; Meister, J.; Jung, R.; Klein, S.; Haisch, M.; Fuss, W.; Hering, P., Liquid-core light guides for near-infrared applications. *Applied Optics* 1997, 36, 9075-9082.

104. Dress, P.; Franke, H., Increasing the accuracy of liquid analysis and pH-value control using a liquid-core waveguide. *Review of Scientific Instruments* 1997, 68, 2167-2171.

105. Dasgupta, P. K.; Liu, S.-Y. Chemical Sensing Techniques Employing Liquid Core Optical Fibers. 6.011.882, 2000.

106. Tao, S. Q.; Gong, S. F.; Xu, L.; Fanguy, J. C., Mercury atomic absorption by mercury atoms in water observed with a liquid core waveguide as a long path absorption cell. *Analyst* 2004, 129, 342-346.

107. Tao, S. Q.; Winstead, C. B.; Xian, H.; Soni, K., A highly sensitive hexachromium monitor using water core optical fiber with UV LED. *Journal of Environmental Monitoring* 2002, 4, 815-818.

108. Mishra, S. K.; Dasgupta, P. K., Capillary scale light emitting diode based multi-reflection absorbance detector. *Analytica Chimica Acta* 2007, 605, 166-174.

109. Yao, W. S.; Byrne, R. H.; Waterbury, R. D., Determination of nanomolar concentrations of nitrite and nitrate in natural waters using long path length absorbance spectroscopy. *Environmental Science & Technology* 1998, 32, 2646-2649.

110. Zhang, J. Z., Shipboard automated determination of trace concentrations of nitrite and nitrate in oligotrophic water by gas-segmented continuous flow analysis with a liquid waveguide capillary flow cell. *Deep-Sea Research Part I-Oceanographic Research Papers* 2000, 47, 1157-1171.

111. Zhang, J. Z.; Wanninkhof, R.; Lee, K., Enhanced new production observed from the diurnal cycle of nitrate in an oligotrophic anticyclonic eddy. *Geophysical Research Letters* 2001, 28, 1579-1582.

112. D'Sa, E. J.; Steward, R. G.; Vodacek, A.; Blough, N. V.; Phinney, D., Determining optical absorption of colored dissolved organic matter in seawater with a liquid capillary waveguide. *Limnology and Oceanography* 1999, 44, 1142-1148.

113. Pan, J. Z.; Yao, B.; Fang, Q., Hand-held Photometer Based on Liquid-Core Waveguide Absorption Detection for Nanoliter-scale Samples. *Analytical Chemistry* 2010, 82, 3394-3398.

114. Fujiwara, K.; Kagoshima, T.; Uchida, T.; Miyakawa, T., Fluorometric characteristics of a wave-guide cell with low refractive index. *Spectroscopy Letters* 2003, 36, 551-560.

115. Olivares, J. A.; Stark, P. C.; Jackson, P., Liquid core waveguide for full imaging of electrophoretic separations. *Analytical Chemistry* 2002, 74, 2008-2013.

116. Wang, S. L.; Huang, X. J.; Fang, Z. L.; Dasgupta, P. K., A miniaturized liquid core waveguide-capillary electrophoresis system with flow injection sample introduction and fluorometric detection using light-emitting diodes. *Analytical Chemistry* 2001, 73, 4545-4549.

117. Miller, R. L.; Belz, M.; Del Castillo, C.; Trzaska, R., Determining CDOM absorption spectra in diverse coastal environments using a multiple pathlength, liquid core waveguide system. *Continental Shelf Research* 2002, 22, 1301-1310.

118. Liu, Z.; Pawliszyn, J., Capillary isoelectric focusing of proteins with liquid core waveguide laser-induced fluorescence whole column imaging detection. *Analytical Chemistry* 2003, 75, 4887-4894.

119. Li, J. Z.; Dasgupta, P. K., Measurement of gaseous hydrogen peroxide with a liquid core waveguide chemiluminescence detector. *Analytica Chimica Acta* 2001, 442, 63-70.

120. Dallas, T.; Dasgupta, P. K., Light at the end of the tunnel: recent analytical applications of liquid-core waveguides. *Trac-Trends in Analytical Chemistry* 2004, 23, 385-392.

121. Pena-Pereira, F.; Costas-Mora, I.; Romero, V.; Lavilla, I.; Bendicho, C., Advances in miniaturized UV-Vis spectrometric systems. *Trac-Trends in Analytical Chemistry* 2011, 30, 1637-1648.

# Chapter 2.

# Laser Driver Circuit

## 2.1. Introduction

The ring-down time of optical cavities can be measured either from the response of the cavity to an input pulse in the time domain, or from the phase-shift of an intensity modulated input (cf. Chapter 3). In the time domain, one can either excite the cavity by coupling in a short pulse with the pulse duration being much shorter than the round trip time and observe the decay of the intensity of this pulse from the exponential decay of the emitted pulse train, or one can couple in a very long 'pulse' with a duration that is much longer than the round trip time, but a switch-on/off time that is shorter than the round trip time. In the latter case, intensity is building up in the cavity during the 'on'-cycle of the square wave, and the ring-down event can be detected during the 'off'-cycle. This approach has a distinct advantage, since the ring-down trace does not need to be fitted to a few points represented by the peaks of the pulse train observed in the first method. Additionally, the duty cycle of a square wave intensity modulated light source can be much greater than that of a pulsed laser light source, with a fixed repetition rate. Hence, the requirements for time domain measurements are either short pulses or a fast switch-on/off for square-wave modulated light sources.

If the ring-down time is measured in the frequency domain, a *cw*-light source is used. The intensity of the light source, for example a *cw*-laser, is sinusoidally modulated

and the phase-shift between the light introduced into the cavity and the cavity output can be related to the ring-down time (cf. Chapter 3).

There are multiple ways to produce modulated laser light. One very common way is external modulation by the use of optical choppers. Choppers, which can be slotted disks or paddles[1, 2], are placed into the light beam path, to modulate a continuous output. Paddles, also known as tuning fork choppers, can only produce frequencies of a few kHz and give mostly quasi-sinusoidal modulations. For rotating choppers, the combination of the number of revolutions per second and the number of slots in the disk are directly proportional to the modulation frequency. Such choppers work very well for low modulation frequencies in the Hertz to mid kilohertz range. A high rotation speed and many slots would be necessary to reach hundreds of Kilohertz to Megahertz frequencies, but the rotation speed is limited by the speed of sound for the speed of the outer rim of the chopper disk[3]. Furthermore, the combination of geometries of laser beam diameters and slot widths does not produce the required steep slopes for square wave-modulated beams at high frequencies[4]. Moreover, for switching from square wave modulation to sine wave modulation or other modulation waveforms, the chopping disk has to be exchanged, which is inconvenient and might even require realignment of the setup.

Besides mechanical choppers placed into the light path, there are also other spatial light modulators available, like digital mirror devices, optical masks, wave plates, liquid crystal-based modulators, holographic polymer dispersed liquid crystal gratings, and many more[5-12]. They all have their advantages and disadvantages and for each one there appears to be an ideal application. For our application, the requirements have been the ability to modulate the light in a square wave fashion with fast rise and fall times (< 20 ns) and the

ability to produce a sinusoidal intensity modulation up to MHz frequencies without having to change the setup but only the input to the modulator. The above mentioned modulation devices do not satisfy all of our requirements and were therefore not considered applicable.

Another external modulation method, which was not applicable for our experiment, but is very common for fibre-coupled laser beams, is the use of Mach-Zehnder-Interferometers. These interferometers do commonly only exist for telecom wavelengths and are not applicable for our 810 nm experiment. The Mach-Zehnder-Interferometers work on the principle that the output intensity can be modulated by constructive and destructive interference of two light paths. In general, a light beam is split equally between two interferometer arms, where the optical path length of one arm is fixed and can be varied in the other arm (cf. Figure 2.1). The two light beams are then recombined and, due to the path length difference, the intensities interfere constructively or destructively. Varying the path length, or changing the phase of the light with respect to the other interferometer arm, in a sinusoidal or square wave fashion, produces the desired waveform. Using fibre-based Mach-Zehnder interferometers, light can be modulated up to multiple MHz by simply applying the correct modulation voltage and waveform to a non-linear object (an electro-optic modulator, usually a Pockels cell), used to delay the phase in the variable arm.

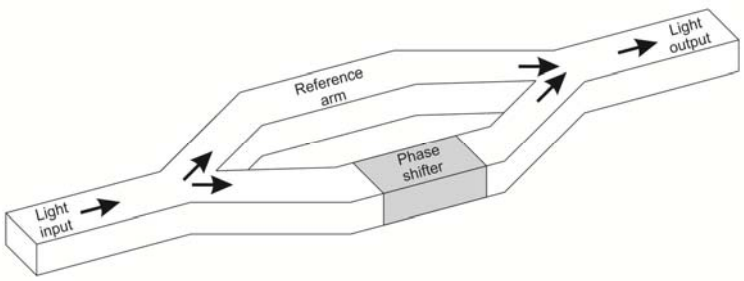


Figure 2.1. General schematic of a waveguide Mach-Zehnder interferometer. The incoming light is split evenly into two waveguide arms. Changing the phase of the light in one of the arms by a phase-shifter and recombining the light from the two arms results in a constructive or destructive interference of the light at the output.

Besides electro-optic modulators used in fibre-based Mach-Zehnder interferometers, acousto-optic modulators are also used to modulate the light intensity of free space laser beams. An acoustic wave travelling through a medium changes the refractive index of the medium along the propagation direction with the periodicity of the sound wave. This periodical change in the refractive index produces a grating. A light beam, which is travelling almost perpendicular to the sound wave, may experience the Bragg condition depending on the grating period and the light wavelength. If the Bragg condition is satisfied, the light is diffracted by a certain angle. This effect is utilized in acousto-optic modulators, refracting light beams on the acoustically induced grating. Furthermore, the intensity of the refracted light depends on the sound intensity if the sound intensity is sufficiently weak. At high sound intensities, the effect saturates and total reflection can occur, which is exploited in acousto-optic switches. Figure 3.2 shows the working principle of an acousto-optic modulator.[13]

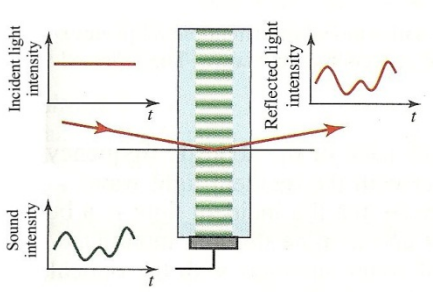


Figure 2.2. Working principle of an acousto-optic modulator.

Finally, the method of choice, since it satisfies our requirements, and the most common modulation technique for diode lasers is direct modulation of the laser current. Here, the laser output intensity is varied directly by changing the current through the laser diode. After reaching a threshold current, any further increase of current is proportional to an increase in light intensity. This means in turn that a modulation of the laser current above the threshold produces a modulated output with the same characteristics as the modulation signal. Due to the widespread usage of this technique, laser drivers or laser driver additions that utilize this technique can be purchased.

Although, changing the current going through a laser diode has the major effect of changing the intensity, there is a minor effect in changing the wavelength also associated with this, since a higher current will heat up the diode. This temperature change is reflected by a change in the dimensions of the cavity of the laser diode due to thermal expansion and with that the wavelength of the laser will change slightly. This can be utilized to fine tune the wavelength of the laser. As mentioned, this effect is very small and will change the wavelength only by a fraction of a nanometer. Such a change in wavelength is not of any concern for our experiments, since absorption features of liquids are usually several nanometers wide. Another effect is the thermo-optic effect, which changes the refractive

index of the lasing medium when the temperature changes. This also affects the lasing wavelength of the diode laser. Nevertheless, a sinusoidal modulation of the laser diode keeps the average temperature, and with this the wavelength of the laser, constant, since the current fluctuates around a static offset. Additionally, the optical cavities discussed in this thesis are broadband cavities and no special care has to be taken to mode match the laser and the cavity.

The laser diode driver that was used in the herein described experiments used the method of intensity modulation by modulating the laser current. Details on the laser diode driver, what problems were associated with it, and how it was improved, are discussed later in this chapter. Although as stated later in this chapter, a similar product is available commercially from *Thorlabs*, but the laser driver described in this chapter is capable of switching a much higher current than its commercially available analogue (3A vs. 250 mA), which was needed for our high power laser diode.

## 2.2. Custom Built Laser Driver Circuit

The laser diode used in the experimental setup (*JDSU, SDL-2372, 2W*) was initially driven by a circuit that was custom built by a company, which has gone out of business and unfortunately, no documentation for the laser driver exists. The laser driver circuit was built to be externally modulated by the use of an arbitrary function generator. The circuit had been commissioned to be used with either square wave or sinusoidally modulated inputs for time and frequency domain CRDS measurements. Examining the

square wave modulation of the laser however, revealed that the shut-off time for the laser diode was much more than 100 ns (cf. Figure 2.5).

This was unacceptably slow for our experimental requirements and the laser driver was examined in detail. As can be seen in Figure 2.3, the laser driver was built with wire wrapped components. Wire wrapped electrical components can increase intrinsic capacitances, which lead to delayed electrical responses. After carefully examination the circuit, a schematic was produced, which can be seen in Figure 2.4.

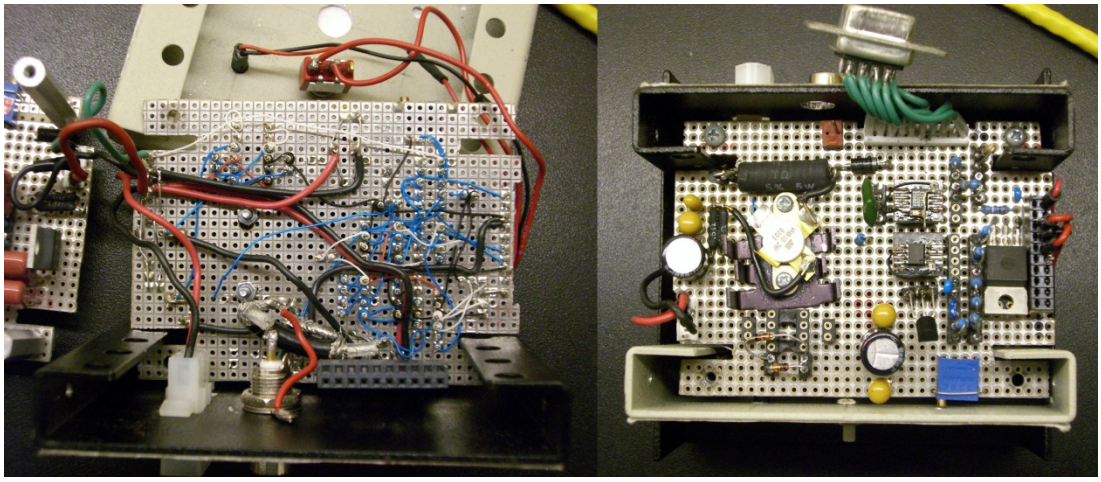

Figure 2.3. Picture of the interior of the custom built laser driver. Bottom side (left) and top side (right) of laser driver circuit board used for modulating an 810 nm laser diode (*JDSU, SDL-2372, 2W*). As can be seen on the left-hand side, the connections of the components are established by the wire wrap method. The input BNC connector can be seen on the lower black housing panel in the left picture, next to the white power connector. On the right-hand side, the D-Sub connector (green wires – top of picture) for the laser diode can be seen.

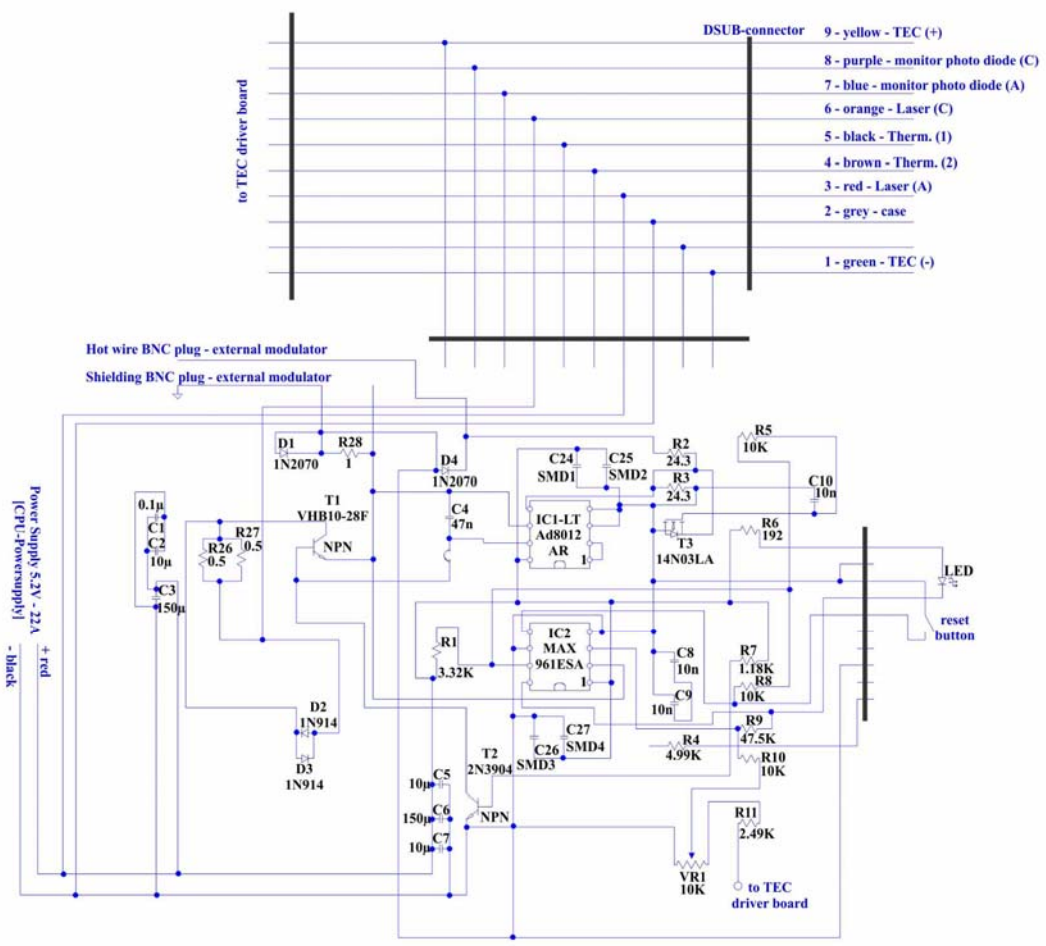


Figure 2.4. Retraced circuit diagram of the laser driver. Here, it can be seen that some components have been incorporated that do not serve any purpose (cf. C8 and C9 or D1) and that some connections are not connected to anything else and therefore lead nowhere (cf. R4).

The basic driving mechanism of the laser diode with this driver circuit is direct modulation of the laser current from the BNC input through the power transistor (T1 – VHB10-28F) and will be explained more detailed below. Additional components, like a comparator (IC2 – Maxim Integrated Products MAX961ESA), are used to protect the laser diode from high currents which can destroy it very easily. Unfortunately, such components can also introduce a lag in the response time.

### 2.2.1. Working Principle of Laser Driver Components

As mentioned above, the basic working principle of this laser diode driver is direct modulation of the laser current. In detail, this is achieved by directing the inputted waveform (for example, a sinusoidal waveform from a function generator) from the BNC input connector over a resistor for termination purposes into the positive port of a high bandwidth operational amplifier (IC1 – Analog Devices AD8012AR). The negative port of this amplifier is directly connected to the output, which causes the amplifier to have a unity gain. The output of the operational amplifier (OpAmp) circuit is connected to the base of a high power transistor (T1 – VHB10-28F). The collector of the transistor is connected to the laser diode cathode, whereas the emitter of the transistor is connected via a resistor to ground. The laser diode anode is directly connected to the positive port of the power supply. With this configuration, the transistor regulates the current through the laser diode according to the waveform inputted at the base of the transistor by changing the resistance between the laser diode cathode and ground.

In order to protect the laser diode, the circuit does more than *only* modulating the current. The integrated circuit IC2 (Maxim Integrated Products MAX961ESA) compares the voltage drop over the laser diode with a set voltage created by a resistor network and the potentiometer (VR1). If the voltage over the laser diode exceeds the set voltage, the comparator chip activates its outputs Q and \Q and switches the transistors T2 and T3 into their ‘ON’ positions. Consequently, the transistor T2 connects the circuit to ground in front of the power transistor (T1), so that no current goes through the base of the power transistor any longer and the laser diode turns off. However, this security feature is

somewhat redundant, since connecting the input signal from the BNC connector to ground through transistor T3, switched also by IC2, results in no input to the OpAmp and, with that, in no input to the power transistor. In this way, the circuit isolates the input from the OpAmp and the laser diode and creates its own fail safe. The comparator chip (IC2) stays in the fault position until it is reset, by pressing the reset button, which connects the 'Latch enable' port of the IC2 to ground. To signal the user that the set current has been exceeded, the designers also incorporated an LED, which is also controlled by the comparator chip, IC2, and resetting the circuit with the reset button switches the LED off.

Capacitors C1-C3, C5-C7, and C24-C27 stabilize the DC voltage used to power the circuit.

### 2.2.2. Shut-Off Time of Laser Diode with Our Custom Built Laser Driver

This laser driver is connected to a function generator (LeCroy 9100) and is driven by a square wave-modulated signal with 10 kHz repetition rate and a voltage from 1.35V to 3.5V. The emitted laser light of the laser diode is coupled into an optical fibre, which is fixed onto a photomultiplier tube in a small bend, and the signal is recorded on an oscilloscope triggered on the falling slope of the inputted square wave. The shut-off signal is displayed in Figure 2.5.

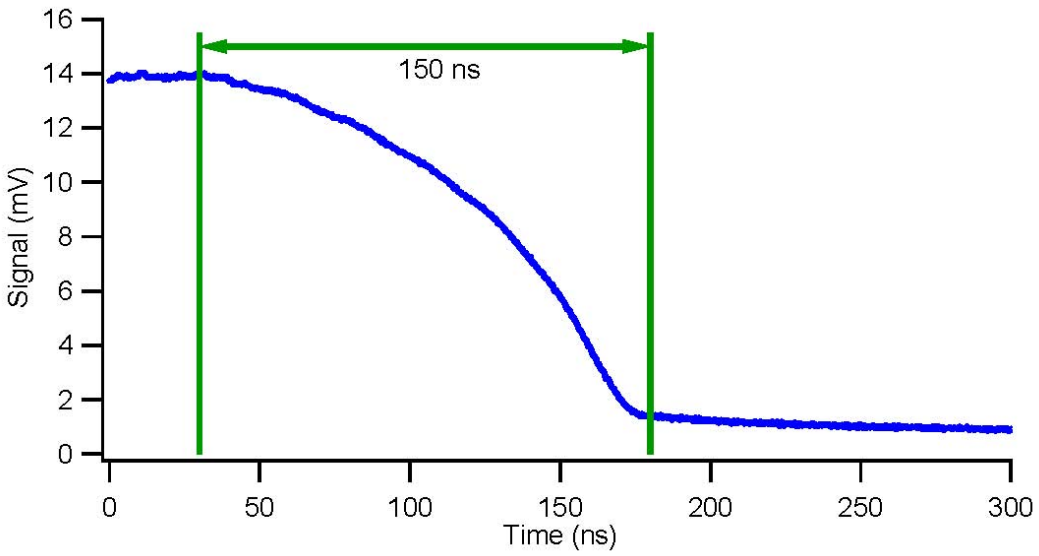


Figure 2.5. Time response of the shut-off process of the laser diode while using the custom built original laser driver. A square wave is used as input to the driver circuit and the output signal is recorded with a fast photomultiplier tube. Instead of the expected exponential shut-off curve a differently looking shut-off response is seen. The measured shut-off time is approximately 150 ns.

The function generator has a fast shut-off time of <5 ns but it can be seen that the laser is emitting over much longer time, although the drive current is zero. After the signal from the function generator has been shut off, the laser emits light at full intensity for about 30 ns until the intensity slowly decreases. This time delay in the response is undesired but does not affect the ring-down measurements. The rather long shut-off time of 150 ns is unsuitable for measuring short ring-down times in the time domain and an attempt was undertaken to improve the laser driver.

With respect to frequency domain measurements, the circuit was tested for the generation of higher harmonics when driven with a sinusoidal modulation. Not generating higher harmonics is especially important as a lock-in amplifier is used. Generally, lock-in

amplifiers determine the phase-shift between a reference and a signal, but a strong contribution of higher harmonics in the signal can skew the measurement.

The laser diode was modulated at frequencies from 40 kHz to 300 kHz and the laser output was measured with a photomultiplier tube. A Fourier transform of the recorded waveform was produced on the oscilloscope and transferred to a computer. The intensities, relative to the intensity of the fundamental frequency, of the 2nd to 5th harmonic were extracted and are shown in Figure 2.6. It can be seen that there is a large second harmonic contribution, and also the 3rd harmonic sometimes contributes considerably to the waveform.

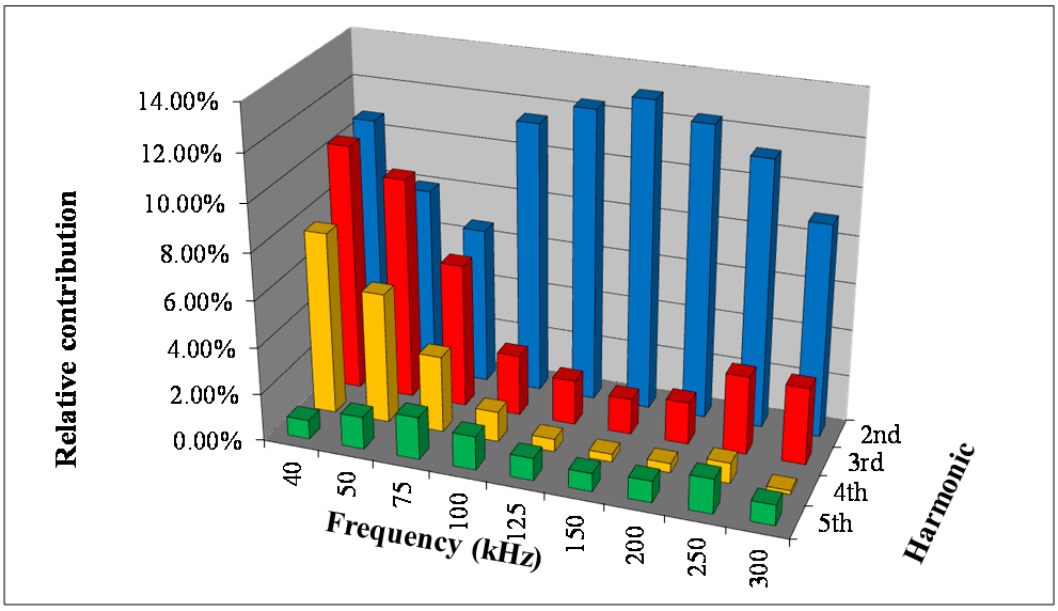


Figure 2.6. Harmonic contribution of the output signal of the laser diode, modulated by the original custom built diode driver. Measurements were taken at different frequencies (40 kHz to 300 kHz) with a modulation from 1.35V to 3.5V. All the contributions are normalized to the fundamental frequency.

## 2.3. Redesigned Laser Driver Circuit

To decrease possible capacitances caused by the wire wrapped components, a circuit board was designed and produced. In order to keep electric distances for high currents and the modulation voltage short, particular care was taken in the design. A drawing of the new electric circuit board is shown in Figure 2.7. To also avoid grounding defects, a ground plane was introduced and incorporated in the design.

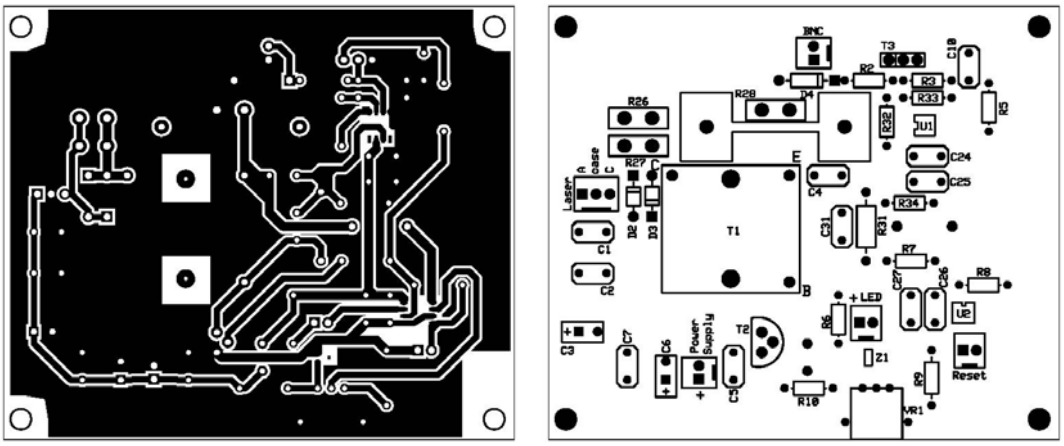


Figure 2.7. Circuit board diagram of the reengineered laser driver circuit. The bottom copper layer of the printed circuit board (PCB) is shown on the left, and the silk screen layer, with all the component descriptions, is shown on the right.

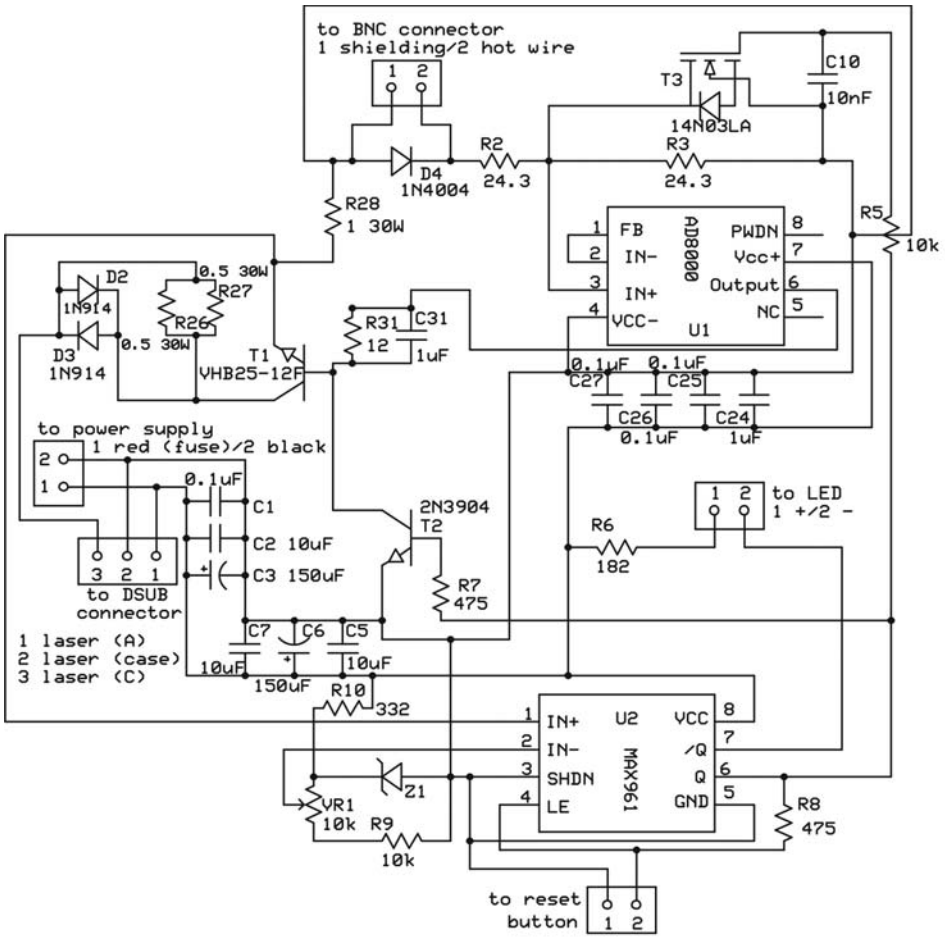


Figure 2.8. Cleaned up circuit diagram of the commercial laser driver circuit. On the center left, connectors to the power supply and to the laser diode are shown. The connector on the top center connects to the modulation input via a BNC connector. Two other connectors, on the center right and on the bottom, connect to the 'too-high-current' fault LED and to the reset button. The integrated circuit (U1, top right) is a high bandwidth operational amplifier for the modulation signal. To protect the laser diode, a comparator chip is also installed (U2, lower right). Additionally, a fast wire fuse (3.1 A) is installed between the power supply and the driver circuit.

Figure 2.8 shows the new circuit diagram, which is cleaned up regarding unnecessary components and connections that were originally present in the custom built driver. Additionally, new electronic components were used, due to the discontinuation of some previously used parts. Simultaneously, a fast wire fuse was installed between the power supply and the circuit, in order to further protect the laser diode. The resistor

network, for set a maximum laser diode current, was exchanged for a Zener diode. In Figure 2.9, a picture of the new laser driver board is displayed.

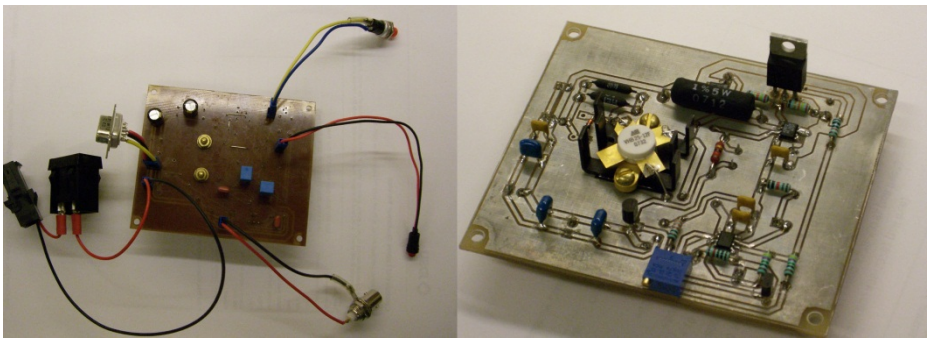

Figure 2.9. Pictures of the reengineered laser diode driver circuit board. On the left, the bottom of the PCB is shown after having been populated with all the electrical components. On the left side of this picture, the fuse housing of the fast wire fuse is shown next to the power supply connector. The right picture shows the top side of the completed PCB.

Again, the shut-off time was measured by inputting a square wave from a fast function generator. The decay trace is shown in Figure 2.10 below.

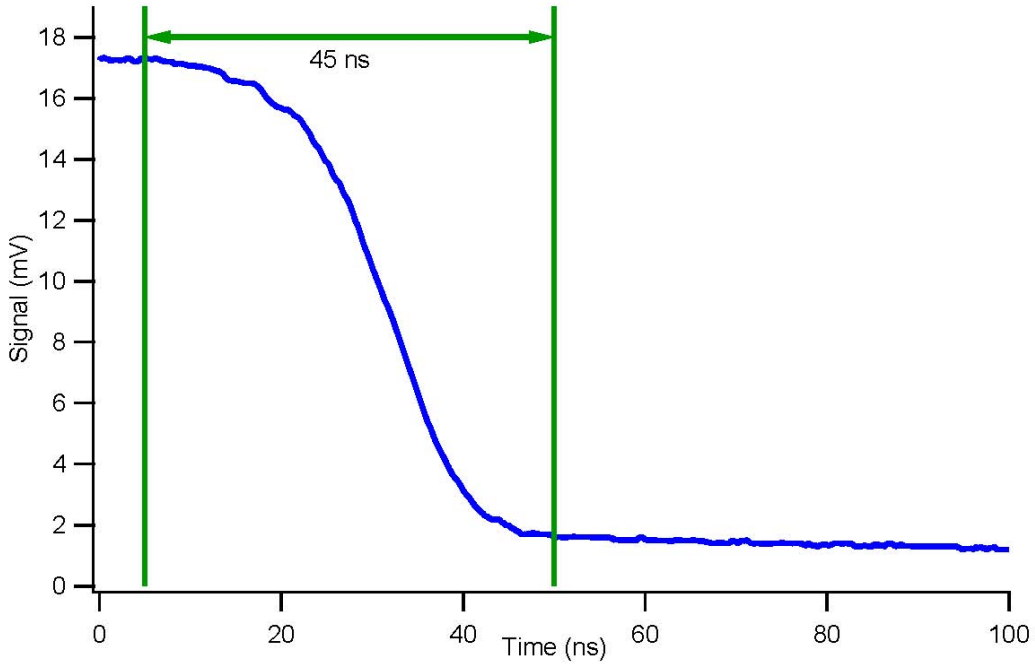


Figure 2.10. Decay trace of the new, rebuilt laser diode driver circuit. A square wave signal from a fast arbitrary function generator was used as an input. The light output of the laser diode was recorded in an optical fibre with a PMT. To couple the light into the optical fibre, the light from the laser diode was shone directly onto the end facet of the fibre. The PMT has a rise and fall time of < 2 ns. The shut-off time of the laser diode is determined to be 45 ns.

Obviously, the performance has improved considerably compared to the performance of the original circuit, and the shut-off time has been reduced to 45 ns.

Furthermore, it has been concluded that, although high bandwidth components were used, the sum of the delays of all the components resulted in a shut-off time of the laser diode, which was still longer than expected. Also, the used power resistor (R1) was a wire wrapped resistor, which might not have been able to be switched fast enough, due to inherent capacitances. Based on these observations, the design of the laser diode driver circuit has been changed again. The input signal has been connected directly to the base of

the power transistor, and the OpAmp has been decommissioned. Additionally, the termination resistor for the input signal has been changed to 49.9 Ohm, instead of 2x 24.3 Ohm. The resistor and the capacitor, which had been wired in parallel, directly in front of the high power transistor, have been removed, as well as the resistors and the diodes right after the laser diode, which had also been wired in parallel. A new ceramic power resistor (R1) has been incorporated. The resulting circuit diagram is shown in Figure 2.11.

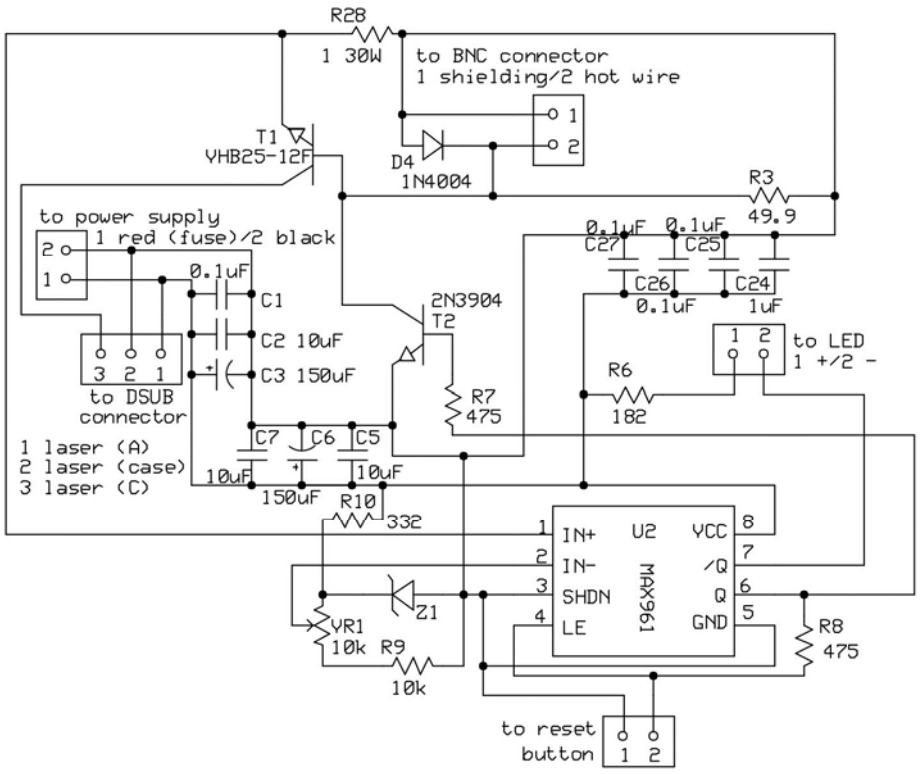


Figure 2.11. Final laser diode driver circuit diagram. The operational amplifier (U1, Figure 2.8) has been left out. A termination resistor of 49.9 Ohm has been installed, instead of the previously used two 24.3 Ohm resistors. Furthermore, the wire wrapped 1 Ohm resistor has been exchanged for a ceramic resistor.

Once more, the shut-off time was determined. As shown in Figure 2.12, the shut-off time has improved considerably from the original 150 ns to about 6 ns.

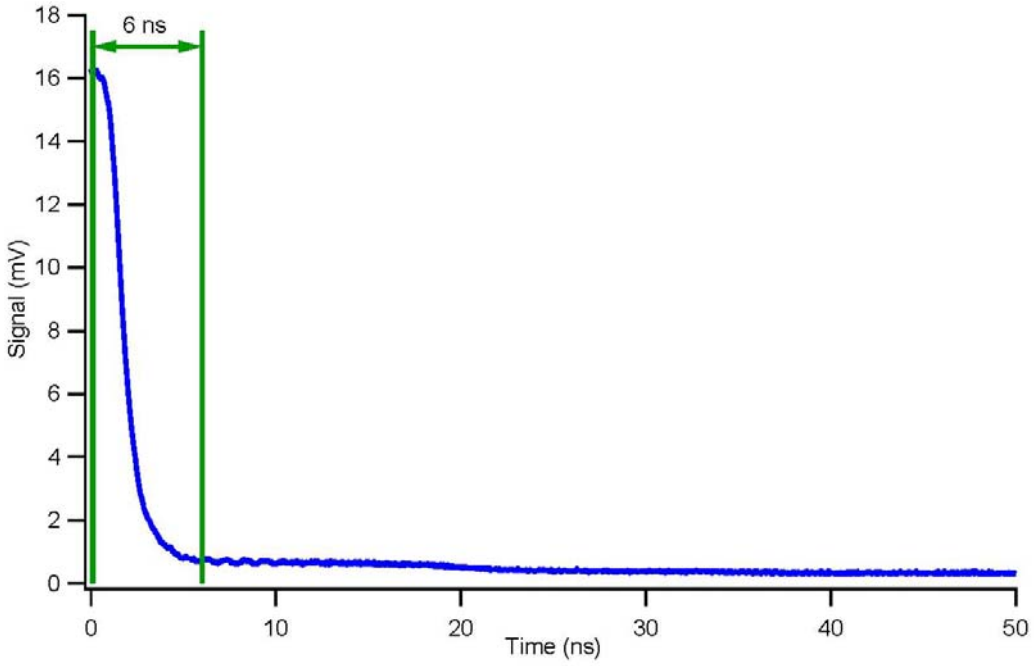


Figure 2.12. Intensity shut-off trace of final driver circuit. The input waveform is the same as in the two cases above and it can clearly be seen that the shut-off time has greatly decreased to about 6 ns. The shut-off signal of the previous version of the laser driver would have extended over the whole x-axis scale.

The only safety systems remaining in the circuit to protect the laser diode are the comparator chip and the fast fuse that is installed between the power supply and the laser diode driver.

It has been discovered, after these changes have been performed that the resulting circuit is very similar to a direct current laser diode driver commercialized and sold by *Thorlabs* under the name of *Bias-T*. Yet our homebuilt circuit sustains much higher power and has more safety features. This is important for our used 810 nm laser diode, which draws 3 amperes of current, versus the usual 250 mA of a common commercial laser diode.

After having achieved a very fast shut-off time of less than 10 ns, our redesigned laser driver was modulated with a sinusoidal waveform again, in order to see if the

performance increased with respect to harmonic generation as well. Fourier transforms of the laser output at different frequencies were measured with an oscilloscope. The intensities of higher harmonics ($2^{nd}$ to $5^{th}$) were extracted from this and normalized with respect to the intensity of the fundamental frequency. A higher harmonic contribution plot is shown in Figure 2.13.

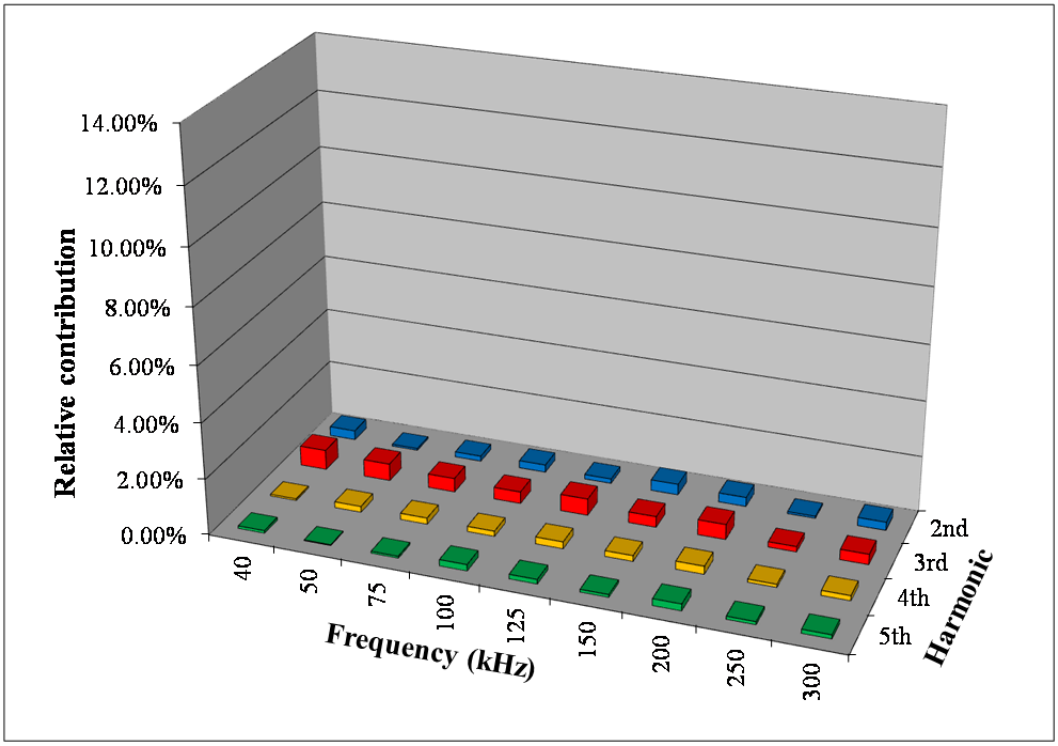


Figure 2.13. Harmonic contributions of the laser diode modulated with the final driver circuit. Intensities were measured in a frequency range from 40 kHz to 300 kHz and were normalized with respect to the intensity of the fundamental frequency. The y-scale is chosen to be the same as in Figure 2.6, to make comparisons easier. The measurement was further extended to 1MHz (data not shown) and it was found that the highest harmonic contribution in this frequency range is below 1%.

The harmonics measurement revealed that the contribution with respect to the intensity of the fundamental frequency has been improved to less than 1% in a frequency range from 40 kHz to 1MHz.

## 2.4. Conclusion

In conclusion, it can be said, that re-engineering the laser driver, using new components and eliminating unnecessary parts, was successful in improving the laser diode driver. The switch-off time for the laser has been reduced from 150 ns to less than 10 ns for time domain measurements. Additionally, the newest laser driver creates less higher harmonic frequencies (<1% up to 1MHz), which would interfere with phase-shift measurements with a lock-in amplifier. After this optimisation, the laser diode has been used for phase-shift measurements up to a modulation frequency of 2 MHz without noticeable distortion of the signal.

Further improvements to the diode driver circuit are possible by also monitoring the temperature of the laser diode. In our final design, the temperature controller built by the original driver manufacturer was not used anymore because of the poor build of the whole driver circuit. Schematics for a redesigned (but not executed) temperature controller board are given in Chapter 2.5.

## 2.5. Appendix

### 2.5.1. New Design of the Thermoelectric Cooler Controller for the Laser Diode

In addition to examining the laser driver portion of the commercial built laser driver, also the temperature controller is inspected. A circuit diagram for this controller is constructed and is shown in Figure 2.14 below.

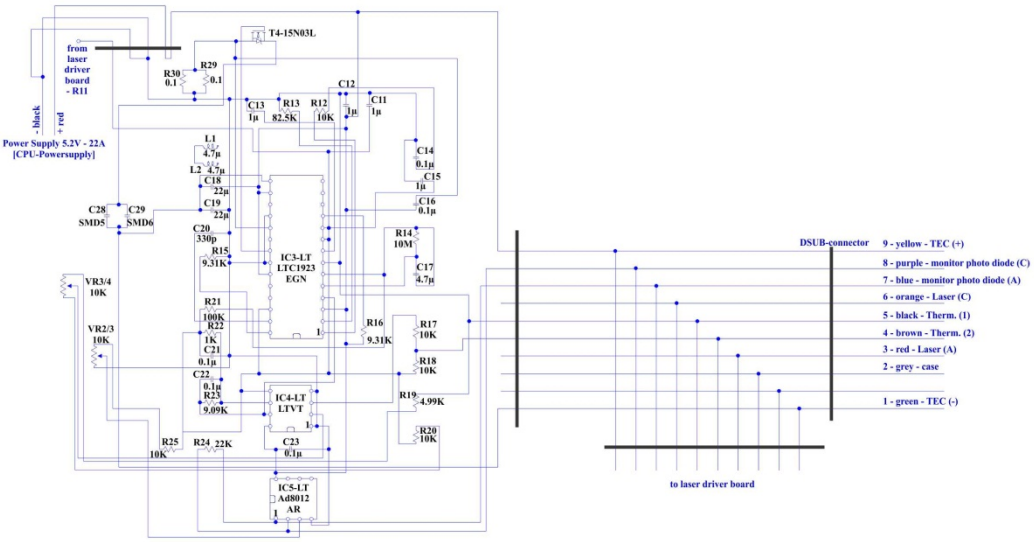


Figure 2.14. Circuit diagram of the original, commercial built diode laser temperature controller for the thermoelectric cooler, built into the laser diode.

The temperature controller adjusts the current through the thermoelectric cooler (TEC), which is built into the laser diode housing to either cool or heat the laser diode. The output wavelength of diode laser can be tuned slightly by changing its operating temperature. Consequently, controlling the temperature of a laser diode decreases wavelength fluctuations.

From the original circuit diagram, a printed circuit board is designed. This circuit board is much more complex than the circuit board for the laser driver, since many more components have to be connected. This complexity leads to a double sided circuit board which is shown, including its silk screen layer, in Figure 2.15a-c.

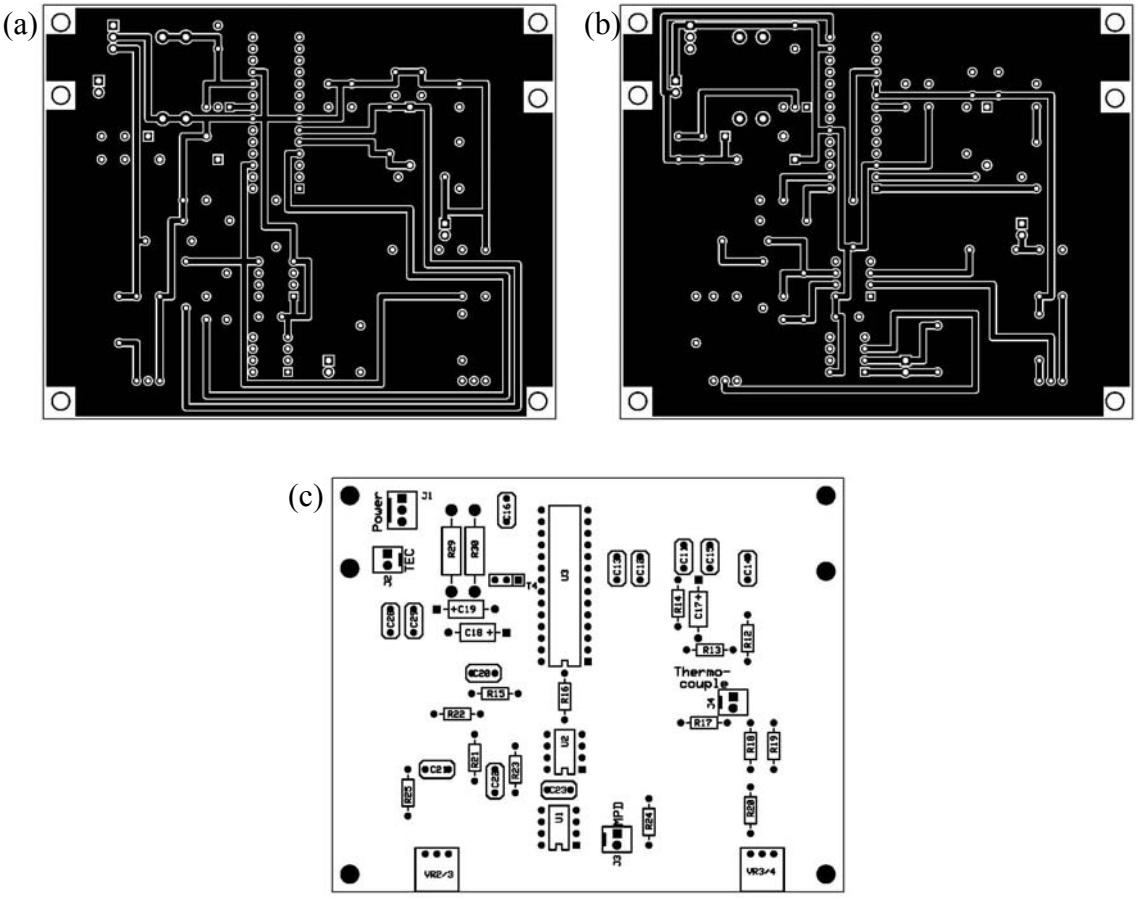


Figure 2.15. Printed circuit board for the temperature controller for the diode laser. (a) Bottom copper layer for the electronic components used in the commercial built TEC driver. (b) Top copper layer and (c) silk screen layer with the electronic part identifiers.

Due to a discrepancy in the technical specifications between the main control integrated circuit (IC) and the thermoelectric cooler built into the laser diode, the main IC was switched to an appropriate version built by Maxim Integrated Products (MAX1979).

This change also required redesigning of the TEC controller circuit board. The two copper layers and the silk screen layer with the component identifiers are shown in Figure 2.16.

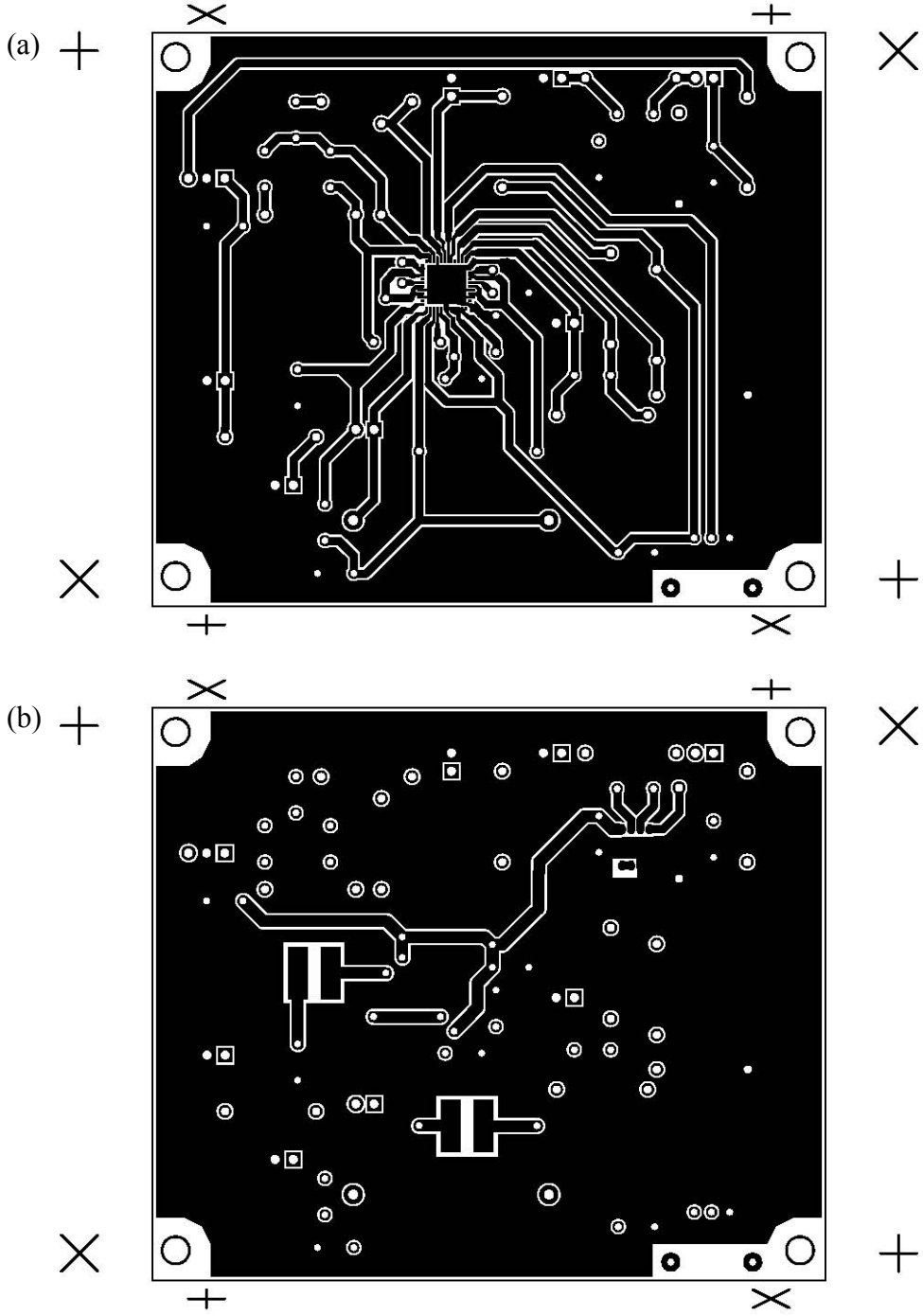

(c)

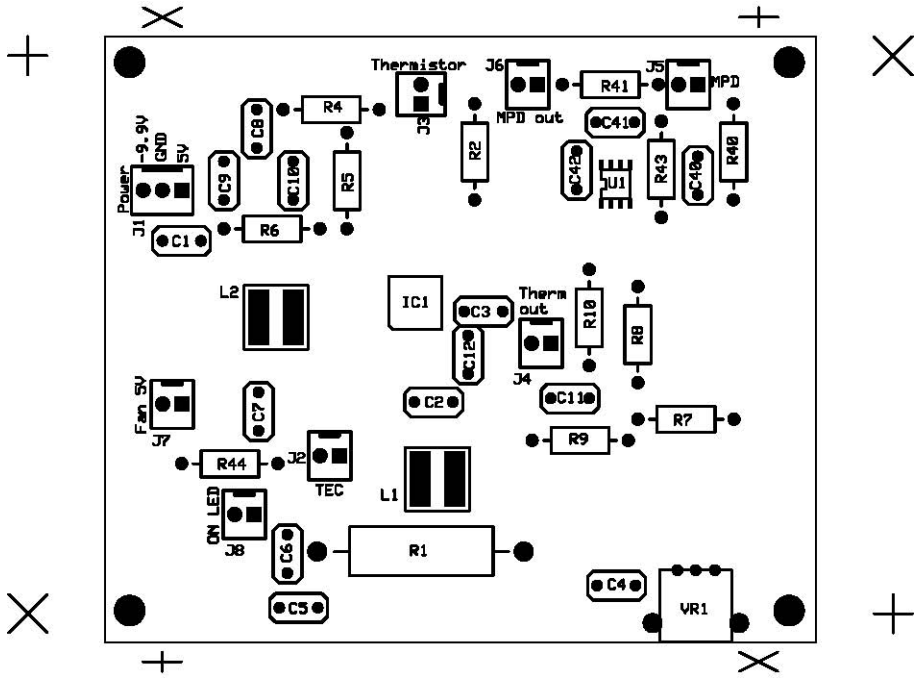


Figure 2.16. Design of the new TEC controller board for the laser diode *JDSU SDL2372*. (a) The copper bottom layer is shown with the connections to the new IC (*MAX1979*) in the middle. (b) Layout of the top copper layer of the new printed circuit board (PCB). The two contact pairs of the needed inductors can be seen in the middle and on the left of the layout. (c) The silk screen layer of the new PCB with the identifiers of all the electrical components is shown. Alignment markings can be seen outside of the PCB on each layer.

Unfortunately, the SMD package of the new TEC controller (*MAX1979*) made it impossible to solder this component to the circuit board by hand. After a few unsuccessful attempts to find a commercial service to assemble the PCB in Kingston, Ontario, Canada, it was decided that the laser was to be used without controlling the temperature and the project to build the TEC controller board was dismissed.

## 2.6. References


1. Optical Modulators, Choppers, Beam Deflectors, and Shutters. http://www.eopc.com/choppers.html (accessed 07.10.2012).

2. Tuning Fork Optical Choppers. http://www.scitec.uk.com/resonantmodulators/tuning_fork_choppers (accessed 07.10.2012).

3. Optical Chopper Frequently Asked Questions. http://www.scitec.uk.com/optical_chopper/faq (accessed 07.10.2012).

4. Duma, V. F.; Nicolov, M. F.; Kiss, M., Optical choppers: modulators and attenuators. In *Romopto 2009: Ninth Conference on Optics: Micro- to Nanophotonics Ii*, Vlad, V. I., Ed. 2010; Vol. 7469.

5. Xie, X. S.; Liu, Y. K.; Zhang, M. D.; Zhou, J. Y.; Wong, K. S., Manipulating spatial light fields for micro- and nano-photonics. *Physica E-Low-Dimensional Systems & Nanostructures* 2012, 44, 1109-1126.

6. Zheng, J. H.; Jiang, Y. M.; Wang, T. T.; Huang, A. Q.; Zhuang, S. L.; Yin, S., Experiments of Electrically Controlled Optical Choppers Based on H-PDLC Gratings. In *Photonic Fiber and Crystal Devices: Advances in Materials and Innovations in Device Applications V*, Yin, S.; Guo, R., Eds. 2011; Vol. 8120.

7. Marshall, K. L.; Jacobs, S. D.; Miller, J. E., Midinfrared Modulation Through the Use of Field-induced Scattering in Ferroelectric Liquid-Crystals. *Applied Optics* 1995, 34, 6704-6713.

8. Kim, S. M.; Kim, D. M.; Kang, S. N., Replication of micro-optical components by ultraviolet-molding process. *J. Microlithogr. Microfabr. Microsyst.* 2003, 2, 356-359.

9. Erdmann, L.; Deparnay, A.; Maschke, G.; Langle, M. L.; Brunner, R., MOEMS-based lithography for the fabrication of micro-optical components. *J. Microlithogr. Microfabr. Microsyst.* 2005, 4.

10. Beeckman, J.; Neyts, K.; Vanbrabant, P. J. M., Liquid-crystal photonic applications. *Optical Engineering* 2011, 50.

11. Mias, S.; Camon, H., A review of active optical devices: I. Amplitude modulation. *J. Micromech. Microeng.* 2008, 18.

12. Lu, Y. Q.; Du, F.; Lin, Y. H.; Wu, S. T., Variable optical attenuator based on polymer stabilized twisted nematic liquid crystal. *Optics Express* 2004, 12, 1221-1227.

13. Saleh, B. E. A.; Teich, M. C., *Fundamentals of Photonics*. John Wiley & Sons: Hoboken, New Jersey, 2007.

# Chapter 3.

# Measurement of Multi-Exponential Decays by Phase-Shift CRDS

## 3.1. Measurement Techniques in Cavity Ring-Down Spectroscopy

In cavity ring-down spectroscopy not the absolute amount of absorbed light is measured, but the decay of the light intensity in the optical cavity with time is recorded. Typically, a light pulse is introduced into a mirror cavity with highly reflective mirrors. The pulse then bounces back and forth between the mirrors, hereby enhancing the effective path length multiple times. This enhancement can be of as much as a few tens of kilometers in a regular 1 m cavity. When measuring time-dependent intensity decays, fluctuations of the initial light intensity do not affect the measurement of the optical loss. The CRD technique is therefore compatible with pulsed lasers as light sources. It makes large intra-cavity light intensities possible but is also largely immune against pulse-to-pulse intensity fluctuations that for many lasers can be greater than 10%. The decay time, or ring-down time, $\tau$, is dependent on all of the losses in the optical cavity and can be expressed by

$$\tau = \frac{t_{RT}}{2\left(1 - R + \sum \varepsilon C l\right)} \qquad (1.5)$$

where: $t_{RT}$ is the round trip time for a laser pulse in the cavity; $R$ is the average overall reflectivity of the mirrors; $\varepsilon$ is the sample absorption coefficient; $C$ is the

concentration of the sample; and $l$ is the sample length.[1] Since the reflectivity of the used mirrors, $R$, is usually close to unity, the reflectivity loss $-\ln R$ has been substituted by the approximation $1-R$.

As expressed in this equation, the ring-down time is longest when the reflectivity, $R$, is very close to unity and there is no absorber present (i.e. $\varepsilon Cl$ is zero). In this case, the ring-down time only depends on the mirror reflectivities. That means that as the sample absorption decreases, the ring-down time increases, and with it the sensitivity of the measurement increases. It is assumed that the sensitivity of the ring-down time measurement is given by the bandwidth of the data acquisition. This increase in sensitivity along with decreasing sample absorption or sample concentration is contrary to usual absorption measurements and a unique property to all CRDS schemes.

When pulsed lasers are used with CRDS, the cavity output is a trail of decaying light pulses, shown in Figure 3.1, and an exponential decay curve can be fitted to the peak amplitudes of the recorded pulses.

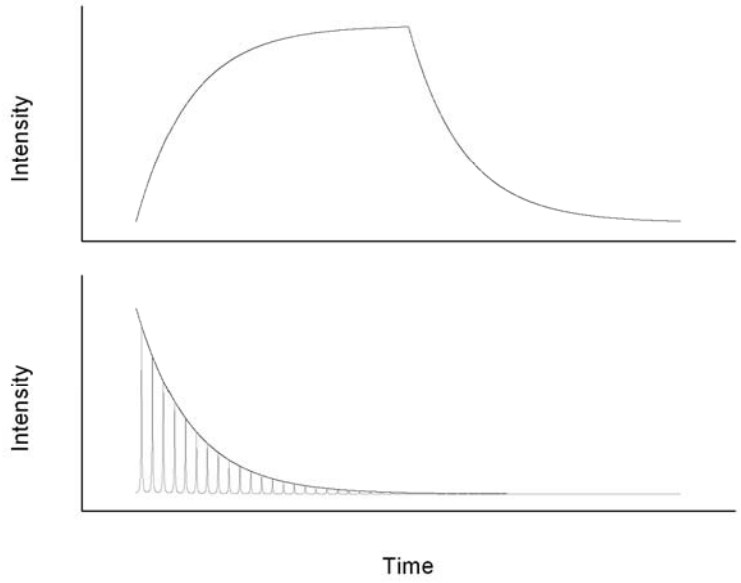


Figure 3.1. Typical intensity decay traces recorded using cavity ring-down spectroscopy.[2] The top curve shows a decay form produced by a continuously excited cavity. The cavity is filled with light from the light source at first, then the light source is switched off very quickly, which produces the intensity decay. The bottom graph shows a cavity output from a pulsed excitation of the cavity. Here, the pulse intensity decays with time also in an exponential way. The peak intensities have to be fitted to the exponential decay function.

According to Zalicki and Zare, the laser line width, the free spectral range of the optical cavity, and the width of the absorption feature need to be compared to get to a reliable spectrum.[1] The laser line width, $\Delta\lambda$, is defined as the full-width-half-max of the Lorentzian line shape of the frequency distribution of the laser light. In an optical cavity, only those wavelengths resonate that constructively interfere. These wavelengths, called cavity modes, depend on the reflectivity range of the mirrors (or the transmission range of the optical waveguide material) and the cavity length. A similar quantity to the laser line width can be defined for cavity modes as well. Here, this quantity is called *bandwidth* and denotes the full-width-half-maximum of the individual cavity modes. The frequency separation of these modes is called *mode spacing* or *free spectral range*, *FSR*, and is

dependent on the length of the cavity and on the refractive index of the cavity medium, The shorter the cavity, the wider is the mode spacing. Two more quantities can be defined for optical cavities: The finesse of an optical cavity is the ratio of the mode spacing of the cavity divided by the bandwidth of the cavity modes, and the quality factor (or Q-factor) is the ratio of the frequency on one individual mode divided by its bandwidth. Both quantities are measures for the cavity quality and for the cavity enhancement. Whenever the absorption feature is wider than both the laser line width and the FSR, two different limiting cases have to be examined.

In the first case, the laser line width is smaller than the FSR (the mode spacing in the cavity) and in the second case, the laser line is wide enough to encompass many cavity modes. This is typically the case for pulsed lasers where $\Delta\lambda \propto \frac{1}{\Delta t}$ ($\Delta t$ is the pulse duration). If, on the one hand, the laser line width is sufficiently small, with respect to the mode spacing, light enters the cavity only when the laser line and the cavity mode overlap and absorption will only be seen at these frequencies, while the decay for each of these frequencies will follow a single respective exponential decay curve. If, on the other hand, the laser line width is broader than the mode spacing, multiple cavity modes are excited simultaneously. If simultaneously excited modes are absorbed at the same rate, an overall single exponential decay is to be seen. If simultaneously excited modes experience different absorptions, a multi-exponential decay is the consequence.

A multi-exponential decay can also be observed if the line width of the light source is broader than the absorption feature and the absorption feature again is broader than the mode spacing in the cavity. Extreme cases for absorption features are, for example, a rotational line in a molecular-beam jet-cooled sample (narrow Doppler width

and lifetime broadened), which can be as low as a few kHz, whereas absorption features in liquids are multiple orders of magnitude broader (multiple THz).

If the decay waveform is a single exponential decay, the cavity output can be easily fitted with an appropriate certainty to an exponential decay function to acquire the ring-down time, whereas a multi-exponential decay is more difficult to fit with the same precision. If different decays are fairly close to each other, a high fitting accuracy for each one of them can no longer be achieved. Consequently, for highly accurate rotationally and/or vibrationally resolved spectra, a very narrow laser line width is preferred for determining all absorption features and consistently fitting only single exponential decays with high precision. Then, also a close look at cavity mode structures should be considered. For a more qualitative spectroscopic measurement, even a broadband light source can be used.[3-5] Cavity mode structures are not be discussed here in detail, since the detailed cavity spectrum is irrelevant for the this thesis. Further information about cavity modes can be found in many optical textbooks, such as "Fundamentals of Photonics" by B.E.A. Saleh and M.C. Teich.[6]

One would expect that if the absorption feature is smaller than the FSR, the absorption feature may not be detected by the measurement. However, Wheeler et al. mention that "in practice, the frequency restrictions imposed by cavity longitudinal modes are considerably relaxed by transverse mode structure and by cavity instabilities, so that the frequencies supported by a cavity are essentially continuous."[7] Consequently, the instance in which the absorption feature is not detected is encountered very rarely and applies only to very small cavities, when the mode spacing is sufficiently large.

The temporal pulse width determines the shape of the detected output of the cavity. If the pulse width is considerably larger than the ring-down time, there is a build-up of intensity in the cavity. After the light is shut off, a ring-down event can be detected, but without distinct pulses (cf. Figure 3.1 top). Introducing a 'broad pulse' into the cavity is identical with using square wave amplitude modulated light to excite the cavity. Here, the cavity output provides an exponential decay directly without having to find the individual peak intensities of the pulse trail to produce the decay. Injecting a pulse or a square wave are two methods to measure ring-down times in the time domain and require a good signal-to-noise ratio and to average the cavity output. Averaging is time consuming and therefore 'slows down' the detection technique and makes it difficult to combine CRDS with fast separation techniques or to use it with fast reactions. Also, the maximum duty cycle for the square wave-modulated technique is 0.5 and for the pulsed detection scheme, the duty cycle may be only at around 0.01 or even less. Since the previously mentioned build-up of intensity follows the same function, just with opposite sign, the ring-down time can be extracted from the build-up as well. Keeping this in mind, the maximum data acquisition time for a square wave excited system is twice the data acquisition time for a pulsed system, since besides ring-down events also build-up events can be analyzed.

Besides these two time domain methods, a third approach exists, that transfers the detection scheme into the frequency domain, in which sine wave amplitude modulated light is coupled into the cavity. The obvious improvement in comparison to time domain measurements is that the duty cycle is quasi unity here, but with high modulation frequencies it also allows to increase the detection speed. This frequency-based detection

scheme does not directly detect an exponential decay, but the ring-down time can be extracted from the phase-shift that the cavity output exhibits with respect to the cavity input (cf. Figure 3.2). This technique is called *phase-shift-cavity ring-down spectroscopy (PS-CRDS)* and was first applied by Engeln et al. in 1996.[8]

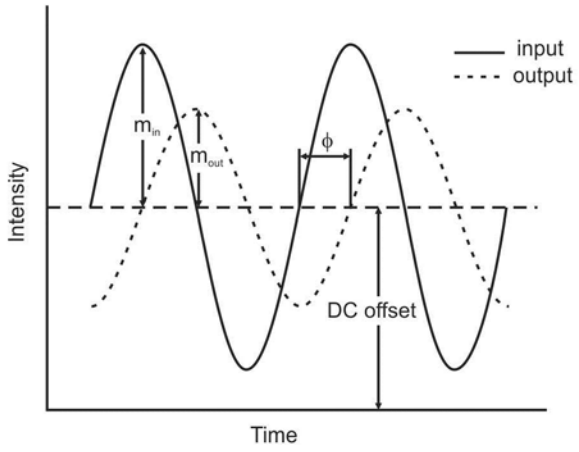


Figure 3.2. Sinusoidally modulated intensity input into and output of the optical cavity. The output is phase-shifted with respect to the input by a phase angle $\phi$, and the amplitude $m$ is decreased.[2]

In the remainder of this chapter, a general model to measure multi-exponential decays in the frequency domain will be described and verified using examples of an electronic circuit and a multimode fibre-loop cavity ring-down setup. While the practical verifications had not been performed previously, the theoretical model was already proposed by my colleague Mr. Nicolas R. Trefiak and can also be found in his M.Sc. thesis.[2]

## 3.2. Theoretical Model

In common cavity ring-down spectroscopy, the decay of light is monitored in time. The characteristic ring-down time is dependent on every single decay process, such as transmission at the mirrors, scatter of light at imperfections of the cavity, absorption of the light by the analyte and/or by the matrix in the cavity, and many more. Each one of these decay processes decreases the light intensity by a certain fraction. If the decay processes work in series, like mirror loss, scatter, and sample absorption, they give rise to a single comprehensive decay process. When there are decay processes that occur simultaneously and independently, such as light decaying in different cavity modes or in the cladding and in the core of an optical fibre, the overall intensity is given by the sum of all the *N*-decay processes, as shown in Equation 3.1.

$$I(t) = \sum_i^N \alpha_i e^{\frac{-t}{\tau_i}} \tag{3.1}$$

This is called the *impulse response function of the system with N-decay processes*. In phase-shift cavity ring-down spectroscopy, the cavity is excited with amplitude modulated light. The response to this input can be calculated from a Laplace transform of Equation 3.1, which is given below[2, 9]:

$$I(\omega) = \mathcal{L}\big(I(t)\big) = \sum_i^N \frac{\alpha_i \tau_i}{\tau_i s + 1} \tag{3.2}$$

with $s = j\omega + \sigma$, and $j = \sqrt{-1}$. The excitation light for the system considered here is modulated with an angular frequency of $\omega = 2\pi f$. The parameter σ is considered to be zero, since it is assumed that neither the modulation depth nor the amplitude will change over the time the experiment is performed, as has been assumed for all previous and present experiments in the literature. After rearranging the Laplace transform, the imaginary and real parts can be separated, which leads to the following equation:

$$\mathcal{L}\big(I(t)\big) = j\left(-\sum_i^N \frac{\omega\alpha_i\tau_i^2}{\omega^2\tau_i^2+1}\right) + \sum_i^N \frac{\alpha_i\tau_i}{\omega^2\tau_i^2+1} = jN_\omega + D_\omega \qquad (3.3)$$

The phase angle and the absolute modulation depth can be extracted from this equation and are given in Equations 3.4 and 3.5 respectively.[2, 10]

$$\tan\phi = \frac{N_\omega}{D_\omega} = \frac{-\sum_i^N \frac{\omega\alpha_i\tau_i^2}{\omega^2\tau_i^2+1}}{\sum_i^N \frac{\alpha_i\tau_i}{\omega^2\tau_i^2+1}} \qquad (3.4)$$

$$m = \sqrt{N_\omega^2 + D_\omega^2} \qquad (3.5)$$

If the latter equation is divided by the integrated intensity $\sum_i^N \alpha_i\tau_i$, one obtains the modulation depth relative to the total signal. Lakowicz et al. have reported similar expressions previously and have applied these to fluorescence decay measurements.[10] It should be noted that the integrated intensity in Lacowicz et al. has been normalized, while the Equation 3.1 is not normalized. A sinusoidal signal, commonly defined through phase angle and intensity, can be represented by a vector diagram (sometimes also called phasor

diagram) of its imaginary and real part, as shown in Figure 3.3.a. A two component case, similar to the cases presented by Kasyutich et al., is shown in Figure 3.3.b[11].

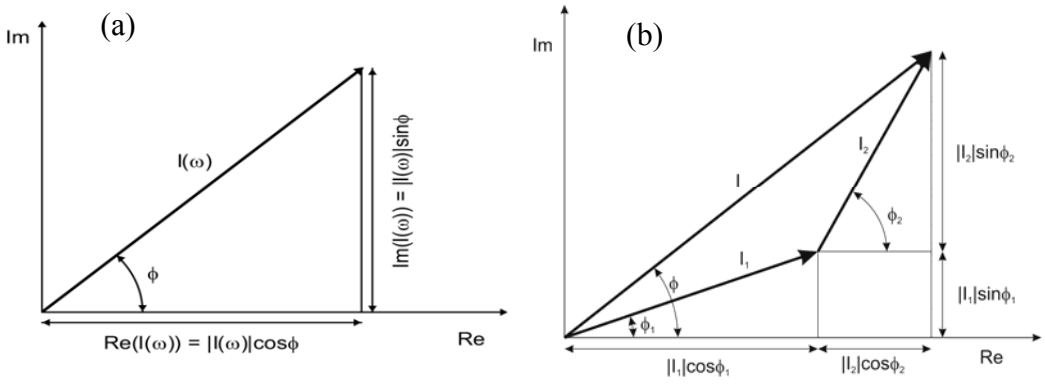


Figure 3.3. (a) Phasor representation of a sinusoidal signal.[2] (b) Overall phasor diagram for a signal consisting of two individual components, similar to Kasyutich et al.[11]

It is obvious, that for *N* decay processes, the overall phase angle and modulation depth can be described in terms of the phase angle and modulation depth of each decay component *i*. This results in the following equations:

$$\tan\phi = \frac{\sum_i^N |I_i| \sin\phi_i}{\sum_i^N |I_i| \cos\phi_i} \tag{3.6}$$

$$m = \sqrt{(\sum_i^N |I_i| \sin\phi_i)^2 + (\sum_i^N |I_i| \cos\phi_i)^2} \tag{3.7}$$

Since the cavity can only introduce a phase lag, all phase angles $\phi_i$ have to be negative, which in turn results in a negative value for $\tan\phi$ in Equation 3.6. Simultaneous, if the decay processes in cavity ring-down spectroscopy are independent from each other

(and therefore their vector representation as well), we can express the individual phase angle and the individual modulation depth as

$$\tan \phi_i = -\omega \tau_i \tag{3.8}$$

$$m_i = |I_i| = \sqrt{(|I_i| \sin \phi_i)^2 + (|I_i| \cos \phi_i)^2} = \frac{\alpha_i \tau_i}{\sqrt{1+\omega^2 \tau_i^2}} \tag{3.9}$$

Herbelin et al. have applied Equation 3.8 in 1980 to characterize a high finesse cavity. This may be considered to be the first report on phase-shift CRDS. In 2004, van Helden et al. gave Equations 3.8 and 3.9 in their discussion of a single exponential decay in CRDS.[12] Equations 3.6 and 3.7 can be transformed into Equations 3.4 and 3.5 by using Equations 3.8 and 3.9. According to Trefiak[2], "It is interesting to note that the simplest expression relating the time domain metrics to the frequency domain metrics is"

$$\alpha_i \tau_i = \frac{m_i}{\cos \phi_i} \tag{3.10}$$

The fractional steady-state intensity of each component (for $\omega = 0$) can be defined as

$$\gamma_i = \frac{\alpha_i \tau_i}{\sum_i^N \alpha_i \tau_i} \tag{3.11}$$

A fit of $\phi(\omega)$ to Equations 3.4 and 3.5 results in values for relative intensities, $\alpha_i$, and ring-down times, $\tau_i$, without having to determine light intensities or even a background light level (as for time domain CRD). Although this is undeniable, in an actual experiment,

a second phase angle needs to be determined. A phase-shift offset, $\phi_0(\omega)$, is introduced by the electronic components, such as the lock-in amplifier, the detector, cables, and other components, that is hard to predict or to eliminate. This offset phase angle is frequency-dependent and can be determined by measuring the phase-shift of the cavity at 'infinite loss', using, for example, an open fibre-loop, a misaligned mirror-cavity, or a strong absorber in a mirror-cavity.

## 3.3. Experimental Setup and Results

### 3.3.1. Electrical RC Circuit as Analog to Optical System

Electrical circuits have been used previously to simulate the response of optical systems to various inputs[13-15]. To model an exponential optical decay with decay time $\tau$, one can use an *RC* circuit as an analog, with $\tau = RC$. Consequently, a circuit containing multiple *RC* circuits, that are summed together, creates a model for multiple independent optical decay processes, such as in a ring-down cavity or in a fluorescence lifetime experiment. Here, two *RC* circuits were used and their respective outputs have been added in an inverting summing amplifier. R and C values were chosen to give decay constants that are comparable to typical CRD cavities. Figure 3.4 shows the circuit diagram for this bi-exponential electrical equivalent to an optical cavity. The circuit was stimulated with either a square wave or a sinusoidally modulated AC input, for the purpose of obtaining voltage signals in the time or frequency domain measurement, respectively.

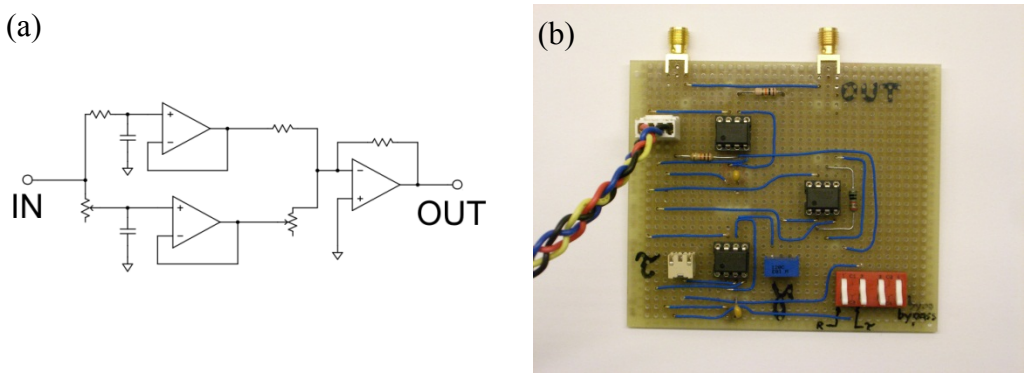


Figure 3.4. Bi-exponential electrical circuit. (a) Circuit diagram of the used bi-exponential circuit with one decay time fixed at 90 µs (top RC circuit) and the second one adjusted to 10 µs (bottom *RC* circuit). The mixing ratio can be varied and was set to a 1:1 ratio. (b) The actual circuit board is displayed, the input connector being on the top left, the output connector being on the top right, the adjustable decay time being on the lower left (τ), the adjustable mixing ratio being on the bottom center (γ), and the power cable to power the operational amplifiers (left). The dip switch is installed to be able to use the circuit also as a single *RC* device.

As can be seen in Figure 3.5, the input response to the square wave stimulation is a multi-exponential decay, and a fit to a bi-exponential function resulted in two ring-down times, namely of 90.8 µs and of 12.6 µs.

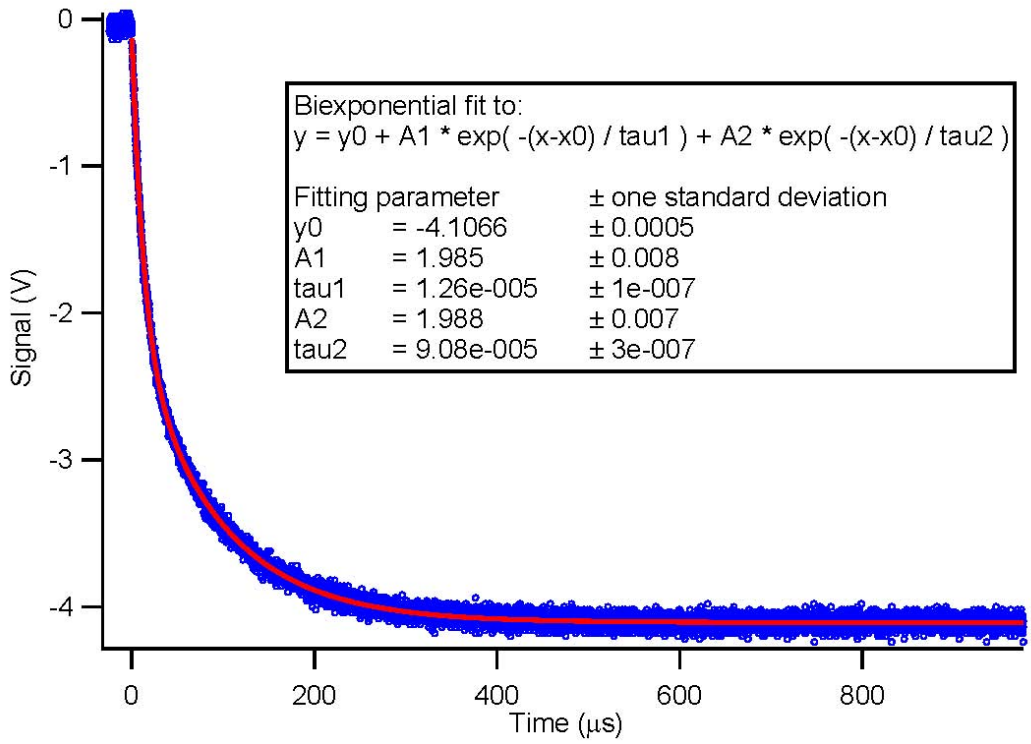


Figure 3.5. Time domain measurement of the input response of the circuit to a square wave stimulation. A bi-exponential fit resulted in the decay times of 90.8 ± 0.3 µs and 12.6 ± 0.1 µs. From the nominal values of the electrical components, the ring-down times can be calculated to be 90 µs and 10 µs, but the uncertainty of the nominal values could be as high as 10%, depending on the components used. The ratio of the amplitudes has equalled the set mixing ratio of 1:1.

In the phase domain, multiple ring-down times cannot be determined from only one measurement at one frequency. Hence, a sweep through multiple frequencies has to be performed. Changing the modulation frequency in discrete steps over two decades has resulted in output phase delays which approach $\pi/2$, while ω tended to infinity (cf. Figure 3.6). A fit of $\tau_1$, $\tau_2$, $\alpha_1$, and $\alpha_2$ to Equation 3.4 resulted in an over-determined fit, which left the amplitudes strongly correlated to each other. This resulted in very large errors ($\alpha_1 = 30 \pm 700$, and $\alpha_2 = 4 \pm 80$). A second fit has been executed, taking into account Equation 3.11. Instead of the individual amplitudes, only one parameter

$\gamma_1 = \alpha_1\tau_1 / (\alpha_1\tau_1 + \alpha_2\tau_2)$ is used. The fit results in the values predicted from the time domain measurement, thus confirming the mathematical model given above. A correction for $\phi_0$ has not been necessary here.

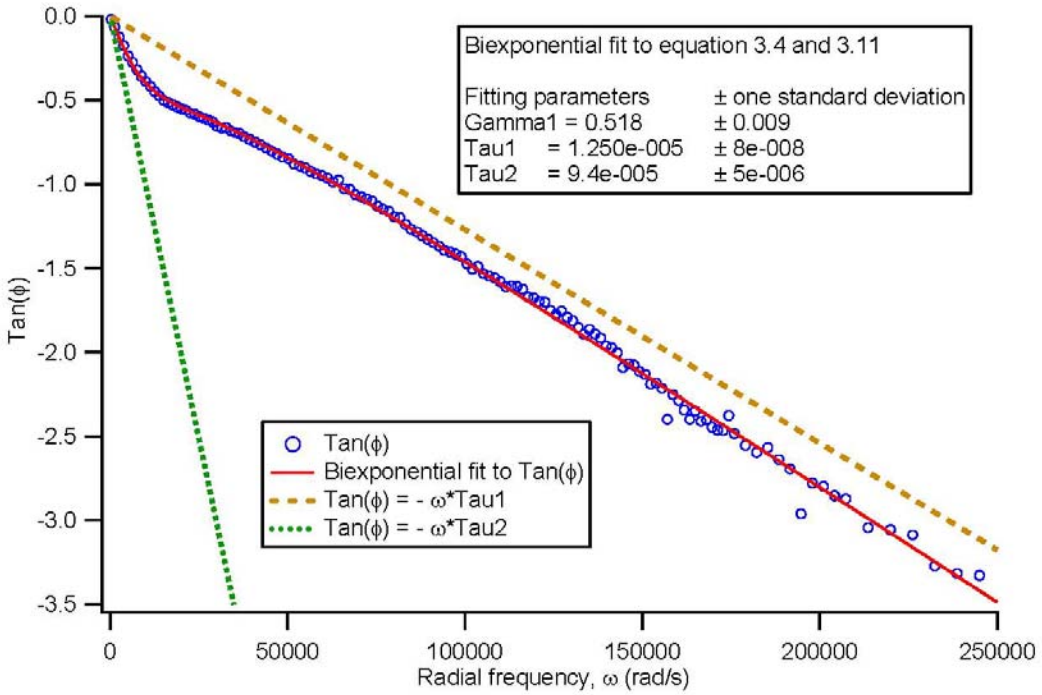


Figure 3.6. Tangent of the phase-shift output of the electrical circuit at frequencies from 50 Hz to 40 kHz. The red curve represents a fit to $\tau_1$, $\tau_2$, $\gamma_1$, in Equation 3.4, taking Equation 3.11 into account, and it gives values of $\tau_1 = 94 \pm 5\ \mu s$, $\tau_2 = 12.50 \pm 0.08\ \mu s$, $\gamma_1 = 0.518 \pm 0.009$. The relative amplitudes (cf. Equation 3.11) result in a ratio of about 1:1, as it was set in the circuit. Values for the ring-down times, calculated from the values of the electrical components, can be found in the figure caption of Figure 3.5 and have been found to agree with the here found values. The dotted and dashed lines represent the single exponential decays. The factor $\gamma_1$ denotes the fractional intensity of the steady-state intensity. A parameter $\gamma_2$ is not displayed, but the sum of all factors $\gamma$ has to add up to 1.

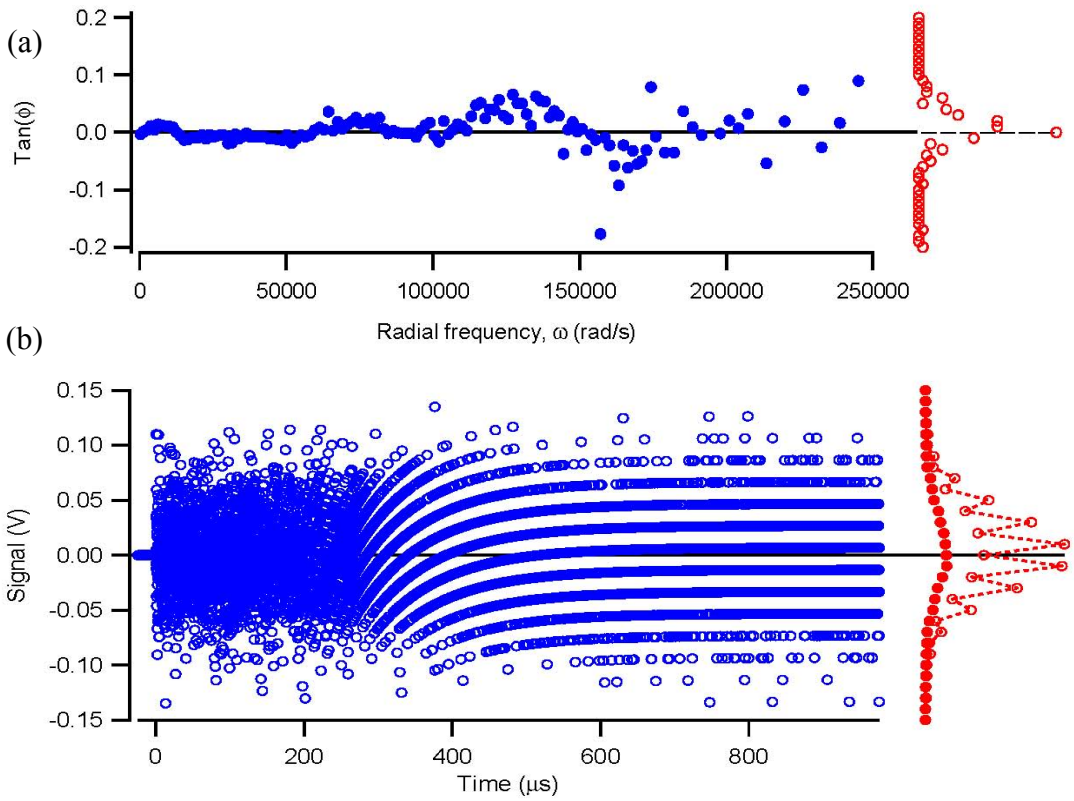


Figure 3.7. Residuals of time and frequency domain fits. (a) Residual of bi-exponential fit to frequency domain phase-shift data. (Figure 3.6). The open red circles on the right show that the residuals follow a Gaussian distribution centered around zero. (b) Residual of bi-exponential fit to time domain data (Figure 3.5). Again, the red circles on the right show the distribution of the residuals. Here, the closed circles show the distribution of only the first 200 μs and the open circles show the distribution of the whole data set. The peaks and valleys stem from the discretization of the values from about 200 μs onwards, which comes from the oscilloscope used. Overall the fitting residuals follow a Gaussian distribution around zero.

Examination of the errors of the fitting parameters to the time domain and to the frequency domain data has revealed that the errors are slightly larger in the frequency domain. The ring-down times, 10 μs and 90 μs, in the time domain have errors of 0.8% and 0.3%, while the errors in the frequency domain are 0.6% and 5.8%, respectively. The first reason why the errors differ so much lies in the number of points the fit has been applied to. The time domain data set consists of 10000 points, while the frequency domain data is

based on only 136 points. Second, in the time domain, the long ring-down time is represented by the long shallow part of the decay, while the short ring-down time is represented by the steep part of the decay trace. The fraction of the data points the individual ring-down time can be extracted from is reflected to some extent in the fitting errors. The same applies to the frequency domain, but the roles of the short and long ring-down times are switched. Here, the long ring-down time is represented by the first steeper part of the data, which obviously has fewer points than the part representing the short decay.

However, considering the residuals of the fits (cf. Figure 3.7), no obvious pattern can be seen for either fit and the distributions of both residuals are Gaussian around zero. Note: The apparent lines visible in the residual for the time domain are an artefact of the resolution of the oscilloscope.

To evaluate which fit is better, it also has to be taken into consideration that in the time domain, the fit requires 5 variables to fit the data set, but in the frequency domain only 3 are needed. The more variables one uses in a fit, the better the resulting function can be adjusted to the data set and therefore, the errors can be minimized.

Considering all of these arguments, it can be said that frequency domain measurements provide a similar accuracy than time domain measurements.

### 3.3.2. Fibre-Loop Cavity

Another type of cavity that has been investigated is a fibre-loop, formed by a strand of fibre where the two ends have been spliced together. The fibre used is a multimode fibre (*FiberTech Optica* AS100/140 IRA), as light travelling in the core and in the cladding experience different losses and a multi-exponential behaviour of the intensity decay is expected. Fibre-loop ring-down spectroscopy had already been used for quantification of different analytes in dilute solutions and small picolitre to nanolitre volumes[16-19]. In the experiments described in this chapter, the focus has been on the comparison of time and frequency domain measurement to further confirm our theoretical model.

#### 3.3.2.1. Experimental Setup

A 25.6 m long strand of multimode fibre was spliced together to form a loop. A commercial fibre coupler (coupling ratio 99:1, *Lightel Technologies*) was used to couple the 810 nm light, produced by a diode laser (*JDSU, SDL-2372, 2W*), into the fibre cavity. The fibre was fixed onto a photomultiplier tube (*Hamamatsu R955*) which was used to detect the scattered light from the loop. A homebuilt laser driver (cf. Chapter 2) allows square wave modulation with rise and fall times of < 10 ns and sine wave modulations of up to 1 MHz, with only very small contributions of higher harmonics (cf. Chapter 2). The laser driver was modulated by using an arbitrary function generator (AFG, *LeCroy* 9100).

A lock-in amplifier (*Stanford Research Systems, SR 844*) was used to determine the phase-shift between the cavity output and the reference given by the AFG. The phase-shift $\phi_0$ introduced by the electronics is acquired prior to fusing the fibre together, to correct the measured phase angle $\phi$, as described.

The time domain measurements were performed by modulating the laser diode in a square wave fashion at a frequency of 1 kHz. An oscilloscope (*Tektronix*, TDS 3032) was used to record the signal and to average 512 traces.

#### 3.3.2.2. Confirmation of Mathematical Model Using a Fibre-Loop Cavity

The fibre-loop cavity was excited for time domain measurements with an 810 nm *cw*-diode laser, which was switched off very quickly, and the intensity decay was recorded. Figure 3.8 shows the decay trace, which has been fitted well by using a tri-exponential decay function (cf. Equation 3.1, *N*=3). The resulting ring-down times are: $\tau_1 = 1.502 \pm 0.007\ \mu s$ (35%), $\tau_2 = 311 \pm 2\ ns$ (47%), and $\tau_3 = 6.7 \pm 0.2\ ns$ (18%). The numbers in brackets give the fractional intensity contribution.

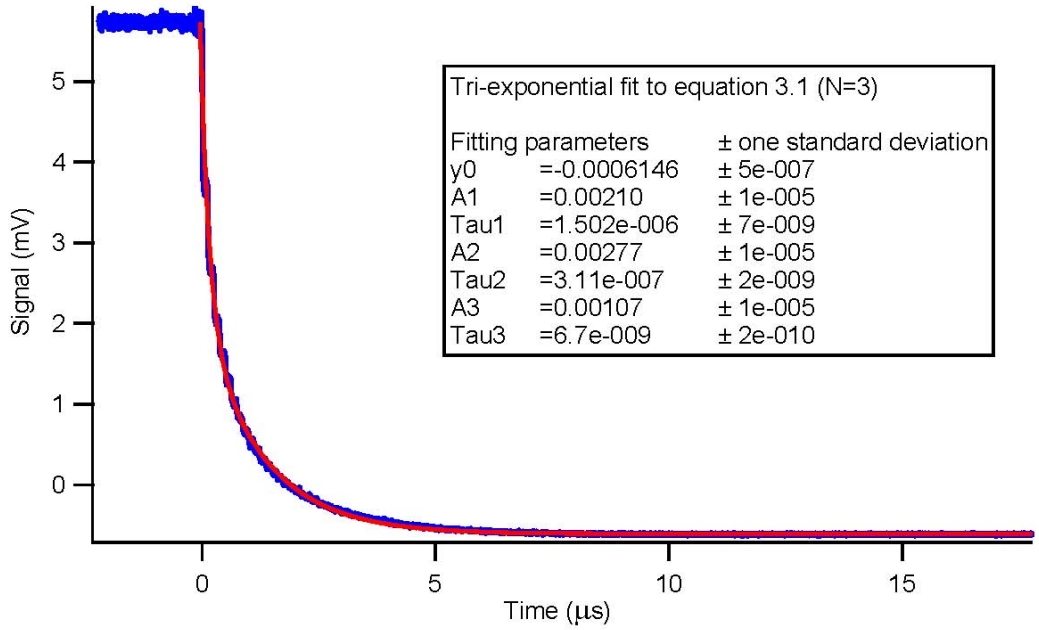


Figure 3.8. Recording of the intensity decay within the fibre-loop cavity after having switched off the light source very quickly. A tri-exponential fit results in ring-down times of $\tau_1 = 1.502 \pm 0.007\,\mu s$, $\tau_2 = 311 \pm 2\,ns$, and $\tau_3 = 6.7 \pm 0.2\,ns$. The fractional intensities are 35%, 47%, and 18%, respectively. A bi-exponential function fits the decay trace equally well but produces slightly shorter ring-down times.

For multimode fibres at least a bi-exponential decay is expected, since the light in the cladding and the core of the fibre experiences different losses and decays at different rates. If some of the light is also guided in the coating of the fibre, a tri-exponential decay is expected. Whether a tri-exponential, bi-exponential, or even a single exponential decay is observed, depends very much on the experimental setup, on the respective optical losses experienced, and on the precision of the detection equipment used. A bi-exponential fit (cf. Figure 3.9) to this decay trace works similarly well, but slightly shorter ring-down times are found: $\tau_1 = 1.296 \pm 0.005\,\mu s$ and $\tau_2 = 189 \pm 1\,ns$. To determine if a bi-exponential or tri-exponential fit is more suitable a more detailed look at the residuals is helpful. When plotting the residuals of the bi-exponential fit, the observed oscillatory pattern might

indicate that there have been too few fitting parameters used. It has been confirmed later by the phase-shift measurement that a bi-exponential function does not provide a satisfactory description of the data. Additionally, when the time domain data is plotted on a log-scale y-axis and again a bi-exponential fit is performed, it becomes obvious, that the longer ring-down time given by the fit is actually too short, since the slope of the fit (middle part) is too steep for the data. Furthermore, this linear part shows that for a long time, only core modes, which are associated with the longest ring-down time, were detected. The short ring-down time is given by the curvature at the beginning of the fit. The plateau at the end denotes converging to a finite value of the fit different from zero. The data had to be slightly adjusted in y-direction by adding a constant to it (cf. different $y_0$ values in the fit parameters), in order to make all values positive, since negative values cannot be plotted on a log-scale. The y-offset of the tri-exponential fit (cf. Figure 3.8) was chosen as the constant.

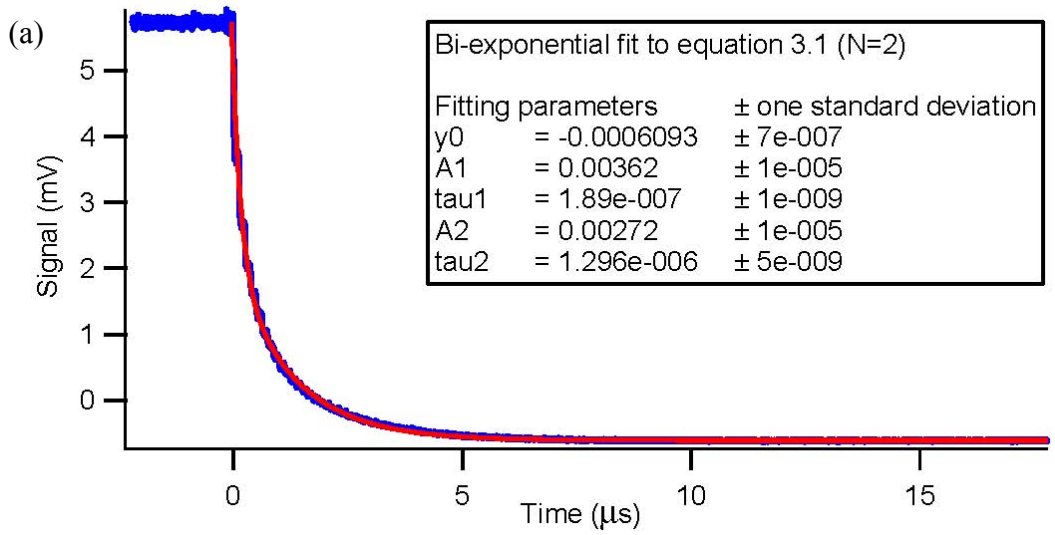

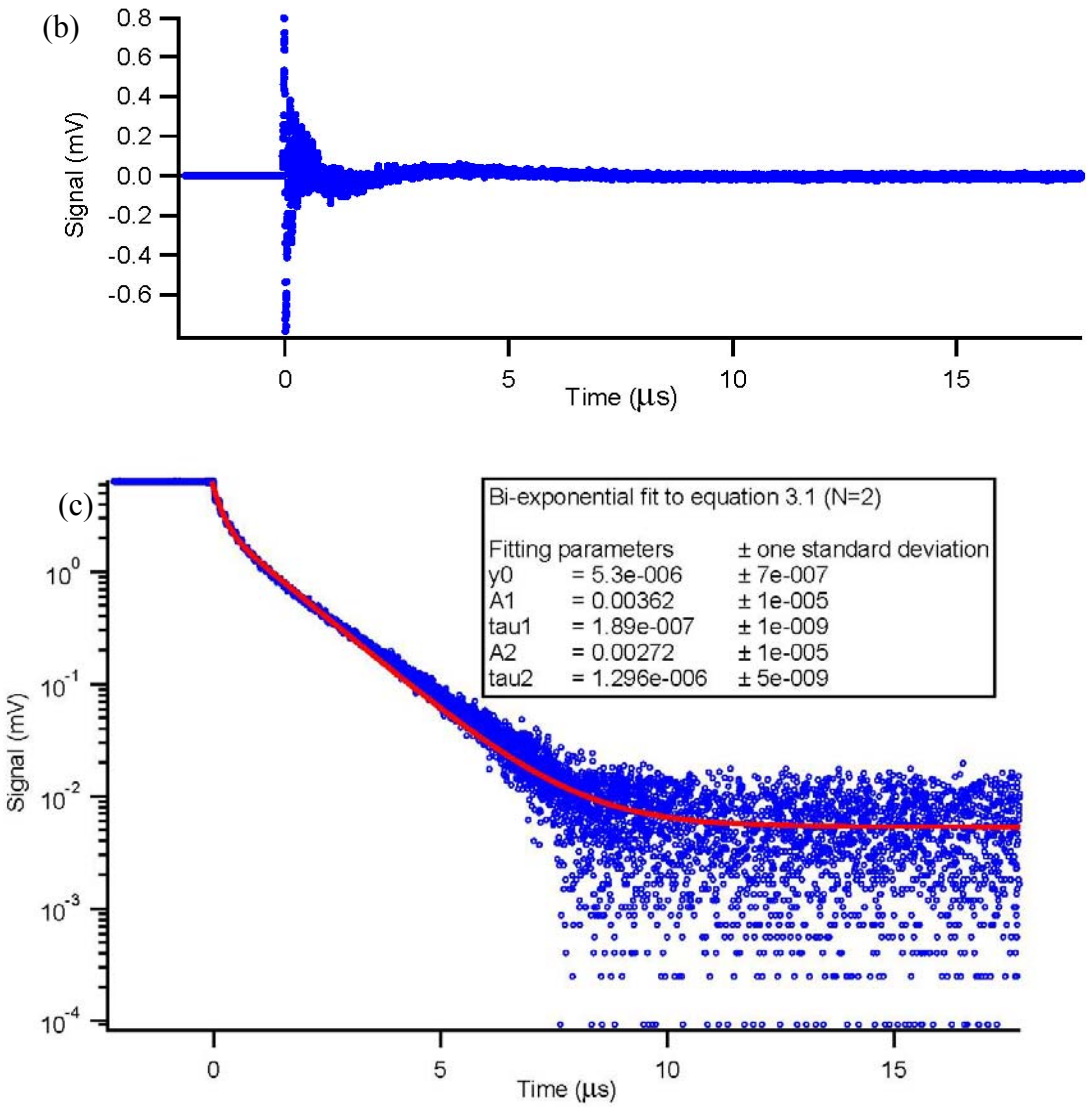


Figure 3.9. (a) Bi-exponential fit to the time domain data results in ring-down times of $\tau_1 = 1.296 \pm 0.005\ \mu s$ and $\tau_2 = 189 \pm 1\ ns$. (b) Residuals of bi-exponential fit. Although the residuals are well centered about the zero line, it seems there is some structure to it. This indicates that there are too few fitting parameters used in the fit. (c) Displays the original trace on a logarithmic y-axis shifted up by $y_0$ of the tri-exponential fit (= -0.00061462), to make all values positive. Fitting a bi-exponential fit to it shows that the long ring-down time, which is represented in the long slope in the middle, does not fit the trace perfectly and suggests that the extracted ring-down time is actually too short (meaning the slope is too steep). This linear region shows in addition that for a long time, only core modes have survived. The fast decay time is represented by the initial curvature of the fit. The plateau at the end arises because the function converges to a finite value different from zero.

Phase-shift data have been collected during excitation the cavity with the same laser, but with a sinusoidal modulation and stepping the frequency from 30 kHz to 1 MHz. Fitting this data to a bi-exponential function (Equation 3.4, *N*=2) produced a poor fit (dashed line in Figure 3.10). A tri-exponential fit (Equation 3.4 in combination with Equation 3.11) resulted in a very good fit to the data and ring-down times of $\tau_1 = 1.57 \pm 0.04\ \mu s\ (\gamma_1 = 29\%)$, $\tau_2 = 320 \pm 9\ ns\ (\gamma_2 = 35\%)$, and $\tau_3 = 17 \pm 2\ ns\ (\gamma_3 = 36\%)$ have been obtained.

A tri-exponential fit to only Equation 3.4, would result in the same ring-down times, but the errors of the amplitudes would be very large, since the system would be over determined (cf. Chapter 3.3.1).

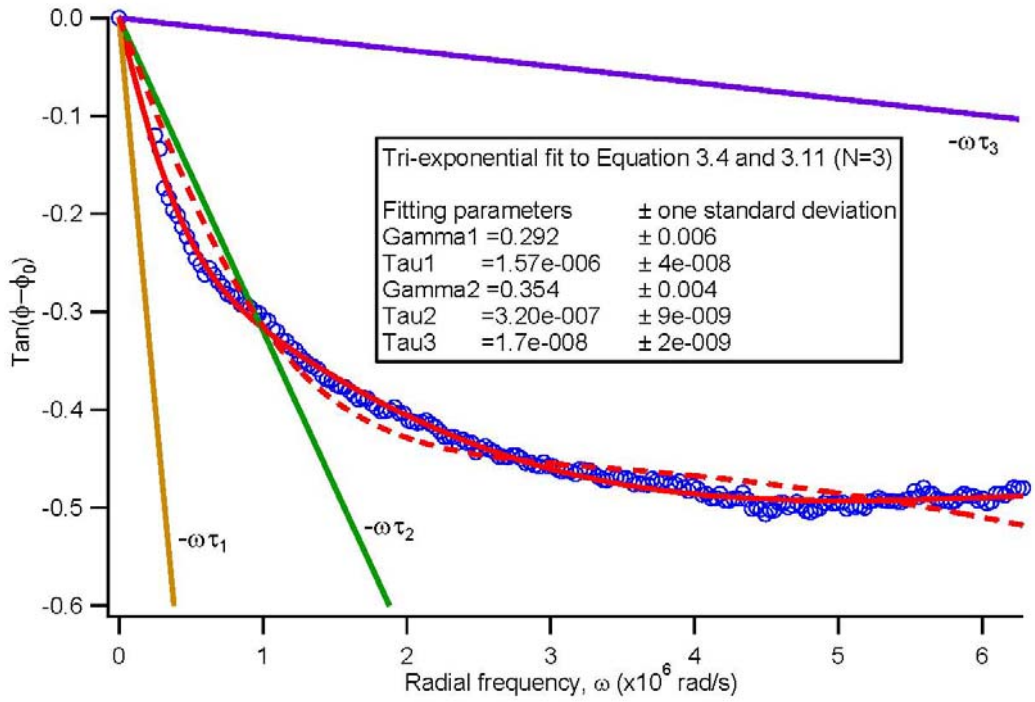


Figure 3.10. Dependence of the tangent of the phase-shift with frequency. The blue open circles indicate the measured data. A tri-exponential fit to Equation 3.4 (N=3) in combination with Equation 3.11 is shown as the red solid line and it fits the data set very well. Resulting ring-down times are: $\tau_1 = 1.57 \pm 0.04\ \mu s$ ($\gamma_1 = 29\%$), $\tau_2 = 320 \pm 9\ ns$ ($\gamma_2 = 35\%$), and $\tau_3 = 17 \pm 2\ ns$ ($\gamma_3 = 36\%$). Fractional intensities are given in brackets. $\gamma_3$ has been calculated from the fact that the sum of all fractional intensities has to add up to one. A bi-exponential fit to the same equations (red dashed line) does not provide a satisfying fit to the data. The three straight lines indicate the expected dependence of the tangent of the phase-shift on the individual ring-down times.

Observations by Tong et al. support the findings and suggest that the two shorter ring-down times are due to light decays in core and cladding of the fibre, respectively.[17] The loss in the core of the fibre could be calculated from its ring-down time and was 8.4% (0.36 dB) per roundtrip and it is mostly due to the insertion loss of the used 2x2 fibre coupler (typical loss of around 5%). The loss in the cladding (second longest ring-down time) contains contributions from the coupler and the higher attenuation of the fibre. The fastest ring-down time is likely associated with a contribution of scattered light.

As already mentioned, the accuracy of the fitting parameters is lower in the phase-shift data than in the time domain data, since there have been many more data points available in the latter (10,000 points) than in the phase-shift measurement (192 points). In comparison, the ring-down times from both measurements are within 4% of each other, although not within the respective fitting error for all determined ring-down times. It becomes apparent that fast decay processes, like the very short ring-down time in this experiment, are difficult to analyze with time domain measurements but can easily be characterized in the frequency domain, by recording phase-shifts at higher modulation frequencies. However, the shortest ring-down time determined from the time domain data is very similar to the response time of the equipment used and can therefore not be reliably measured. Furthermore, the shortest ring-down time contributes about 36% to the overall signal in the phase domain. Finally it is observed that "the intensity ratio of core and cladding modes is found to be about 1:1 in both measurements, which is in accord with the 1:1 ratio of the cross-sectional areas of the fibre core and cladding."[20]

#### 3.3.2.3. Fitting Errors in Cavity Ring-Down Experiments

The presented measurements have demonstrated that phase-shift cavity ring-down measurements provide similar accuracy for CRD measurements as the same experiments performed in the time domain. "Fitting errors of exponential decay processes in the time domain and phase domain have been analyzed extensively in the past."[20] Lerber and Sigrist for instance, developed a new algorithm to increase the accuracy for fitting parameters of

single-exponential ring-down signals and have shown experimental and simulated examples.[21] A detailed comparison of time domain and frequency domain fluorescence decay measurements was performed by Lacowicz et al. They concluded that "phase modulation measurements, when performed over a range of modulation frequencies, will provide time-resolved data that are at least equivalent to those obtained using pulsed excitation"[10].

Comparing the errors from the time domain and the frequency domain data, it has been found that here, the errors in the time domain are lower by a factor of about 5. In the specific case of the current experiment, this is due to the number of points the data can be fitted to.

Judging from the fit residuals of the time and the frequency domain data (Figure 3.11), the time domain data fit using a tri-exponential function seem to perform very well and completely characterize all decay processes, since the residuals follow a normal (Gaussian) distribution. Although the residuals of the fit of the phase-shift data also follow a normal (Gaussian) distribution, there are very obvious oscillations present. It was reasoned earlier in this chapter (Figure 3.9) that a trend or a fluctuation in the residuals indicate to too few fitting parameters. Yet, a fit to four exponentials (Equation 3.4, $N$=4, in combination with Equation 3.11) does not produce a better fit. In fact, the ring-down time values remain the same and the relative amplitudes experience a very large error again, which is indicating an over determination of the system. Furthermore, the residual of a tetra-exponential fit exhibits the same fluctuations as the tri-exponential fit. The origin of the fluctuations remains unknown. It also seems that the normal distribution of the time

domain residuals is much narrower centered around zero than the residuals in the frequency domain. Considering only the middle part of the time domain residuals (from -0.1 mV to 0.1 mV), the error is on the order of 2% of the total signal, whereas the spread of the residuals in the frequency domain is on the order of 3% of the overall signal, thus making them comparable (cf. Figure 3.11).

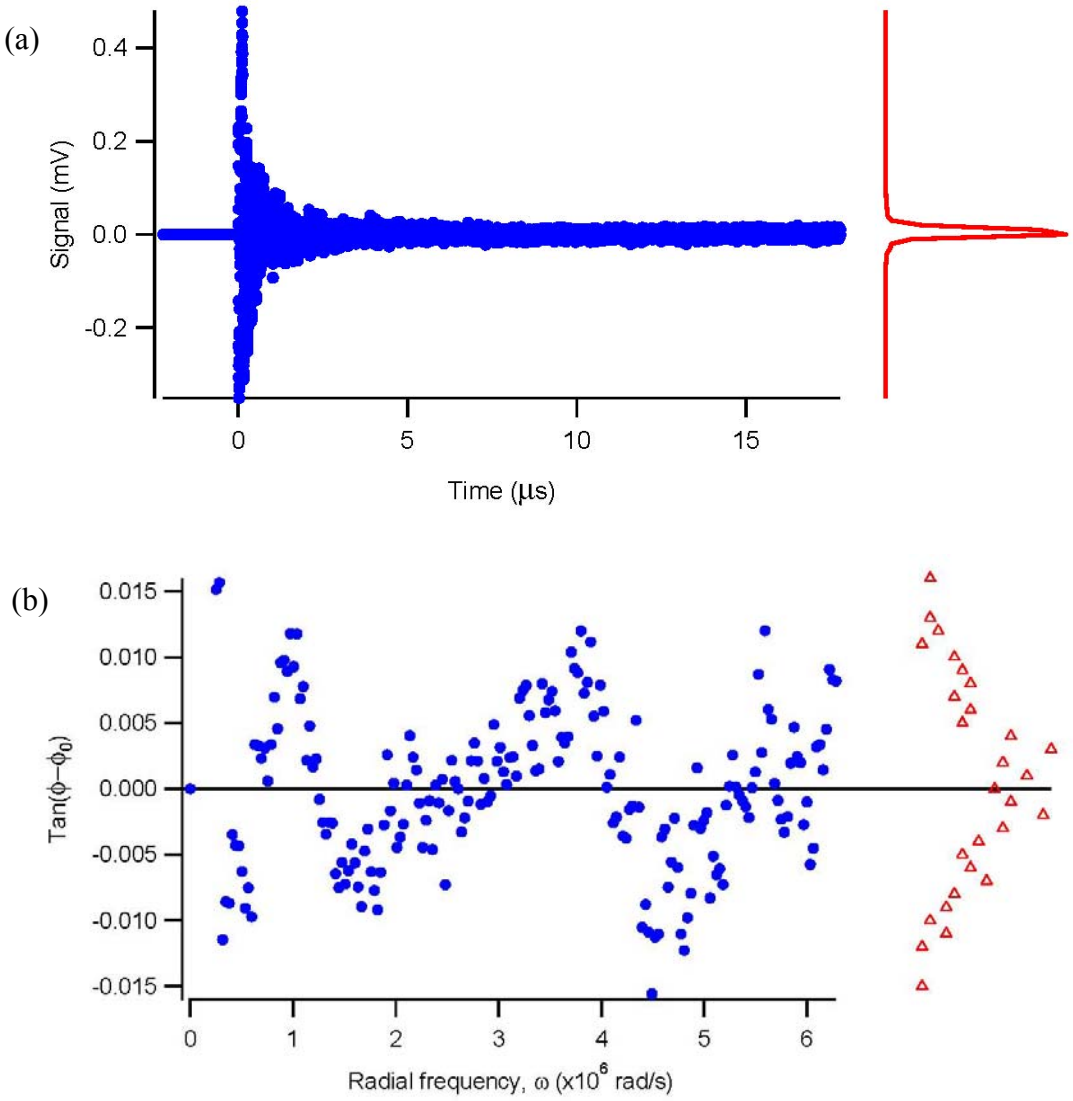


Figure 3.11. Fit residuals in FLRDS measurements in: (a) the time domain and (b) the frequency domain. On the one hand, the residual data from the time domain fit does not show any obvious trend, and the resulting normal (Gaussian) distribution of the residuals is shown on the right of the residual plot (red). On the other hand, the residual data of the frequency domain clearly shows oscillations. An increase in fitting parameters produces the same values as the tri-exponential fit performed here, and the residual shows the same fluctuations. The origin of the fluctuations could not be determined. The residual plot still follows a normal (Gaussian) distribution around zero, though.

Lacowicz et al. also showed that, with a range of modulation frequencies from 1 MHz to 100 MHz, nanosecond fluorescence lifetimes can be determined with an

accuracy of a few picoseconds.[10] Typical fluorescence lifetime measurements involve only the measurement of the phase angle and the modulation depth at a few frequencies, ranging typically from $\omega = 10/\tau$ to $\omega = 1/10\tau$. A fit to Equation 3.4 results in the desired fluorescence lifetimes. Lacowicz et al. further showed that two decay times of $\tau_1 = 1\,ns$ and of $\tau_2 = 2\,ns$ can be distinguished from each other through a fit to phase angles with an only 0.2˚ random error, using only 8 modulation frequencies between 1 MHz and 128 MHz.[10]

## 3.4. Discussion

Equations 3.4 and 3.5 offer a general method to determine ring-down times in cavity ring-down spectroscopy. The mathematical concept can be readily extended to a large number of exponential decay processes. Our approach requires only the measurements of phase angles at a respective number of modulation frequencies in contrast to previous methods, which also required that the laser intensity be measured simultaneously to the phase-shift. "As in previous examples, the determination of the fraction of broadband emission (BBE) to the ring-down times needs to be carried out only once, and all spectra can then be easily corrected for the contributions of the respective decay processes."[20]

The examples shown here can be easily adapted to CRD with mirror cavities. In the following, a comparison of our model with two other studies which also presented models suitable for the description of bi-exponential decay processes, is drawn.

Kasyutich et al.[11, 22] and van Helden et al.[12] used mirror cavities and presented methods to investigate how the combination of phase angle and intensity measurements may be used for the correction to broadband emission from the light source, which is a very common artifact in CRDS. Most diode lasers emit BBE and the BBE contribution to the overall intensity output of a cavity can be greater than 10%. In a very unfavorable case of a quasi-continuous cavity, made with narrowband mirrors and a poor light source, a contribution of up to 50% could be observed (cf. FBG cavity in Reference *Bescherer K., 2009*)[20].

The BBE contributions to the phase angle may originate from two major occurrences: 1. The BBE bypasses the cavity because it falls outside of the reflection spectrum of the cavity mirrors and contributes to the phase-shift. 2. BBE that is largely not absorbed by the sample in the cavity, on account of its broadband characteristics, but is trapped in the cavity. Kasyutich reasoned that the contribution due to trapped BBE is very small, since typically very narrow-band mirrors are used in CRD experiments. In much more broadband cavities, as used in waveguide loop CRD setups, this BBE contribution is expected to be dominant.

Van Helden et al.[12] measured the phase angle corresponding to BBE trapped in the cavity by introducing a strong absorber and hereby reducing the ring-down time corresponding to the sample to a negligible value. That the equations derived by Kasyutich and van Helden are special cases of our model will be shown forthwith.

### 3.4.1. Comparison of Our Theoretical Model with Kasyutich's Expression

The following equation was presented by Kasyutich et al. when they addressed the problem of BBE (called amplified spontaneous emission, ASE) in their work:

$$\tan \varphi_{OUT} = \frac{I_{OA} \sin \varphi_{OA}}{I_{OA} \cos \varphi_{OA} + I_{ASE}} \tag{3.12}$$

Kasyutich determined the intensity and the phase of the ASE contribution to the total output by tilting the rear mirror of their cavity and consequently reducing the finesse of their cavity. The phase angle due to the BBE contribution is set to zero by subtracting the phase of the unaligned cavity. This results in $\phi_1 = \varphi_{ASE} = 0$. The intensity of the ASE was determined independently, which gives $I_1 = I_{ASE}$. The intensity and phase-shift due to the laser light can be set to $\phi_2 = \varphi$ and $I_2 = I$. With these substitutions, Kasyutichs equation transforms into Equation 3.6.

### 3.4.2. Comparison of the Model Used by van Helden with Presented Theory

Van Helden et al. proposed the following expression:

$$\Psi = arctan\left(\frac{A\prime \sin \Delta\phi_A + B\prime \sin(\phi_0 - \phi_B)}{A\prime \cos \Delta\phi_A + B\prime \cos(\phi_0 - \phi_B)}\right) \tag{3.13}$$

Here, Ψ is the overall phase angle, and A' and B' are given as the normalized intensities of the decay of the laser radiation and of the BBE contribution, respectively. The phase-shift due to the empty cavity is given as $\phi_0$, and $\phi_B$ is the phase-shift due to BBE only. $\phi_B$ can be found experimentally by absorbing all the light in the cavity by a strong absorber, as mentioned in Chapter 3.4, and thus reducing the ring-down time due to the sample to practically zero but not affecting the lifetime due to BBE. Analogous to $\Delta\phi_A$, a parameter $\Delta\phi_B$ can be assumed to be $\Delta\phi_B = \phi_0 - \phi_B$, although this parameter is not explicitly defined in the article by Van Helden et al. If substitutions are made, giving $A' = |I_1|$, $B' = |I_2|$, $\Delta\phi_A = \phi_1$, and $\Delta\phi_B = \phi_2$, then, also van Helden's expression is identical to Equation 3.6 presented earlier. Certainly, it is important to mention that the phase angles in both equations are given relative to the input of the cavity, which is set to zero by subtraction of an offset phase angle. This offset phase angle can be obtained from an independent measurement with a low-finesse cavity (for example, by deliberate misalignment) or from a fit of phase-shifts that have been recorded at different optical losses[18, 23].

## 3.5. Conclusion

Fluorescence decay constants had previously been determined through time resolved lifetime measurements and by measuring the shift of the phase of intensity modulated light. These phase-shift measurements are fast and can easily be multiplexed.[24] Similarly, photon lifetimes in optical cavities can be determined. Shown here are two

experimental examples that confirm the theoretical model provided earlier in this thesis. With this model, the amplitude and lifetime of multiple optical loss processes can be reliably determined, using phase-shift measurements at different modulation frequencies. Although one of the experiments presented here was carried out on an optical cavity with a pseudo-continuous spectrum, it can be assumed that the theoretical model is also applicable to systems with resonant cavities, such as mirror-cavities, microtoroids, microsphere resonators, silicon-on-insulator racetrack resonators, and many more that are typically used in CRDS.

The practicality of phase-shift measurements at many modulation frequencies may be debatable for some applications, but applications which utilize low cost light sources and detection systems or which deal with fast decay times can profit from phase-shift CRD measurements. Besides the work group of Dr. Loock at Queen's University, who have applied phase-shift CRDS not only to fibre-loop cavities[25] but also to microsphere resonators[26], other groups have also used this technique for their experiments, for example, on mid-infrared measurements of ethylene[27], on trace-gas measurements in the visible region of the spectrum[28], or on determination of quality factors of micro-cavities[29]. Although this technique can be equally precise as measurements in the time domain, most cavity ring-down experiments are performed in the time-domain. The experiments in Chapter 5 are also measured with a pulsed laser in the time domain, since in the process of building the experimental setup time-domain measurements permit an instant assessment of the optical losses in a ring-down.

## 3.6. References


1. Zalicki, P.; Zare, R. N., Cavity Ring-Down Spectroscopy for Quantitative Absorption-Measurements. *Journal of Chemical Physics* 1995, 102, 2708-2717.

2. Trefiak; Ronald, N. Ringdown spectroscopy in optical waveguides. Master of Science, Queen's University, Kingston, 2007.

3. Engeln, R.; Meijer, G., A Fourier transform cavity ring down spectrometer. *Review of Scientific Instruments* 1996, 67, 2708-2713.

4. Czyzewski, A.; Chudzynski, S.; Ernst, K.; Karasinski, G.; Kilianek, L.; Pietruczuk, A.; Skubiszak, W.; Stacewicz, T.; Stelmaszczyk, K.; Koch, B.; Rairoux, P., Cavity ring-down spectrography. *Optics Communications* 2001, 191, 271-275.

5. Ball, S. M.; Jones, R. L., Broad-band cavity ring-down spectroscopy. *Chemical Reviews* 2003, 103, 5239-5262.

6. Saleh, B. E. A.; Teich, M. C., *Fundamentals of Photonics*. John Wiley & Sons: Hoboken, New Jersey, 2007.

7. Wheeler, M. D.; Newman, S. M.; Orr-Ewing, A. J.; Ashfold, M. N. R., Cavity ring-down spectroscopy. *Journal of the Chemical Society-Faraday Transactions* 1998, 94, 337-351.

8. Engeln, R.; vonHelden, G.; Berden, G.; Meijer, G., Phase shift cavity ring down absorption spectroscopy. *Chemical Physics Letters* 1996, 262, 105-109.

9. Lakowicz, J. R., *Principles of Fluorescence Spectroscopy*. 3rd Edition ed.; Springer, Science and Business Media LLC: New York, NY, 2006.

10. Lakowicz, J. R.; Gratton, E.; Laczko, G.; Cherek, H.; Limkeman, M., Analysis Of Fluorescence Decay Kinetics From Variable-Frequency Phase-Shift And Modulation Data. *Biophysical Journal* 1984, 45, A34-A34.

11. Kasyutich, V. L.; Martin, P. A.; Holdsworth, R. J., Effect of broadband amplified spontaneous emission on absorption measurements in phase-shift off-axis cavity enhanced absorption spectroscopy. *Chemical Physics Letters* 2006, 430, 429-434.

12. van Helden, J. H.; Schram, D. C.; Engeln, R., Phase-shift cavity ring-down spectroscopy to determine absolute line intensities. *Chemical Physics Letters* 2004, 400, 320-325.

13. Nakanishi, T.; Sugiyama, K.; Kitano, M., Demonstration of negative group delays in a simple electronic circuit. *American Journal of Physics* 2002, 70, 1117-1121.

14. Kitano, M.; Nakanishi, T.; Sugiyama, K., Negative group delay and superluminal propagation: An electronic circuit approach. *Ieee Journal of Selected Topics in Quantum Electronics* 2003, 9, 43-51.

15. Nakanishi, T.; Sugiyama, K.; Kitano, M., Simulation of slow light with electronic circuits. *American Journal of Physics* 2005, 73, 323-329.

16. Brown, R. S.; Kozin, I.; Tong, Z.; Oleschuk, R. D.; Loock, H.-P., Fiber-loop ring-down spectroscopy. *Journal of Chemical Physics* 2002, 117, 10444-10447.

17. Tong, Z. G.; Jakubinek, M.; Wright, A.; Gillies, A.; Loock, H.-P., Fiber-loop ring-down spectroscopy: A sensitive absorption technique for small liquid samples. *Review of Scientific Instruments* 2003, 74, 4818-4826.

18. Tong, Z. G.; Wright, A.; McCormick, T.; Li, R. K.; Oleschuk, R. D.; Loock, H.-P., Phase-shift fiber-loop ring-down spectroscopy. *Analytical Chemistry* 2004, 76, 6594-6599.

19. Waechter, H.; Bescherer, K.; Dürr, C.; Oleschuk, R. D.; Loock, H.-P., 405 nm Absorption Detection in Nanoliter Volumes. *Analytical Chemistry* 2009, 81, 9048.

20. Bescherer, K.; Barnes, J. A.; Dias, S.; Gagliardi, G.; Loock, H.-P.; Trefiak, N. R.; Waechter, H.; Yam, S., Measurement of multi-exponential optical decay processes by phase-shift cavity ring-down. *Applied Physics B-Lasers and Optics* 2009, 96, 193-200.

21. von Lerber, T.; Sigrist, M. W., Time constant extraction from noisy cavity ring-down signals. *Chemical Physics Letters* 2002, 353, 131.

22. Kasyutich, V. L.; Martin, P. A., On quantitative measurements in phase-shift off-axis cavity-enhanced absorption spectroscopy. *Chemical Physics Letters* 2007, 446, 206-211.

23. Loock, H.-P., Ring-down absorption spectroscopy for analytical microdevices. *Trac-Trends in Analytical Chemistry* 2006, 25, 655-664.

24. Verveer, P. J.; Squire, A.; Bastiaens, P. I. H., Global analysis of fluorescence lifetime imaging microscopy data. *Biophysical Journal* 2000, 78, 2127-2137.

25. Waechter, H.; Munzke, D.; Jang, A.; Loock, H.-P., Simultaneous and Continuous Multiple Wavelength Absorption Spectroscopy on Nanoliter Volumes Based on Frequency-Division Multiplexing Fiber-Loop Cavity Ring-Down Spectroscopy. *Analytical Chemistry* 2011, 83, 2719-2725.

26. Barnes, J.; Carver, B.; Fraser, J. M.; Gagliardi, G.; Loock, H.-P.; Tian, Z.; Wilson, M. W. B.; Yam, S.; Yastrubshak, O., Loss determination in microsphere resonators by phase-shift cavity ring-down measurements. *Optics Express* 2008, 16, 13158-13167.

27. Grilli, R.; Ciaffoni, L.; Orr-Ewing, A. J., Phase-shift cavity ring-down spectroscopy using mid-IR light from a difference frequency generation PPLN waveguide. *Optics Letters* 2010, 35, 1383-1385.

28. Langridge, J. M.; Ball, S. M.; Shillings, A. J. L.; Jones, R. L., A broadband absorption spectrometer using light emitting diodes for ultrasensitive, in situ trace gas detection. *Review of Scientific Instruments* 2008, 79.

29. Cheema, M. I.; Mehrabani, S.; Hayat, A. A.; Peter, Y. A.; Armani, A. M.; Kirk, A. G., Simultaneous measurement of quality factor and wavelength shift by phase shift microcavity ring down spectroscopy. *Optics Express* 2012, 20, 9090-9098.

# Chapter 4.

# Liquid Core Waveguide Cavity Ring-Down Spectroscopy Using an External Light Source

## 4.1. Introduction

As mentioned in Chapter 1.3, an extension of the sample path gives rise to higher sensitivity in absorption detection. Since the 1980s, so-called liquid core waveguides (LCWs), made from either glass or fluorous polymers, have been implemented in a vast variety of spectroscopic experiments. Recently, other waveguide structures have been designed and used besides LCWs. A liquid core waveguide relies on light guiding based on total internal reflection dictated by Snell's law. Snell's law states that the angle of the refracted beam, $\nu_1$, at a material boundary depends on the angle of incidence, $\nu_2$, and the refractive indices of the materials, $n_1$ and $n_2$ (Equation 4.1).

$$n_1 \sin(\nu_1) = n_2 \sin(\nu_2) \tag{4.1}$$

If $\nu_2$ is greater than a critical angle, $\nu_c$, the beam is totally reflected with an angle, $-\nu_2$. At smaller angles the intensity and polarization of the reflected light is given by Fresnel's equations. The angles are always measured with respect to the normal to the boundary surface (cf. Figure 4.1). Equation 4.1. shows that there can only be a critical angle if $n_1 < n_2$, and that it can be calculated according to Equation 4.2.

$$\nu_c = \arcsin\left(\frac{n_1}{n_2}\right) \tag{4.2}$$

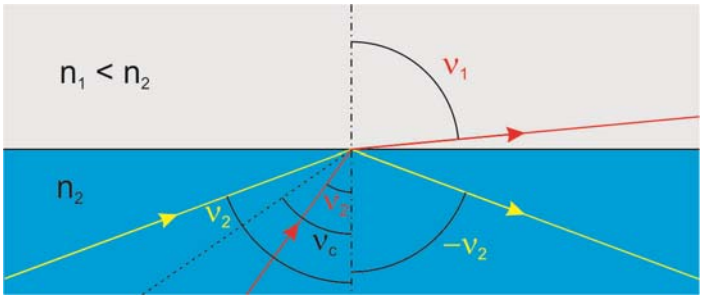


Figure 4.1. Refraction and reflection principle according to Snell's law.

Until end of the 1980s, total internal reflection was only possible for high refractive index liquids, such as dimethylsulfoxide (DMSO), carbon disulfide ($CS_2$), or toluene, but not for water, since there was no material that provided a lower refractive index than that of water. Capillaries and other tubes were coated with a reflective surface, in order to be usable with water, before a breakthrough allowing the construction of water based light guides came with the invention of Teflon AF by *DuPont*.[1]

More recently, hollow core waveguides have been designed, in which the light is confined within the lower refractive index core. These waveguides do not guide light by internal reflection at the core cladding interface, as traditional waveguides do. There are multiple examples for these relatively new kinds of waveguides, such as Bragg waveguides, photonic crystal fibres (PCFs), and anti-resonant reflecting optical waveguides (ARROWs).

Bragg waveguides consist of periodic concentric layers of dielectric coatings of specific thicknesses. A schematic view of these waveguides is presented in Figure 4.2a.

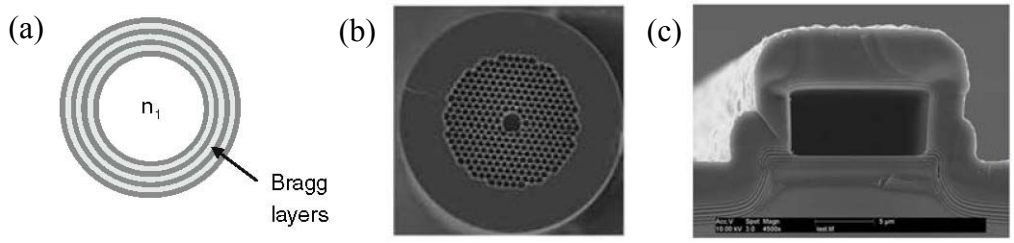


Figure 4.2. Cross sectional views of hollow core waveguides. (a) Bragg waveguide, (b) Photonic Crystal Fibre, (c) ARROW waveguide.[2, 3]

Bragg waveguides are made by rolling a stack of thin layers of dielectrics into a hollow tube and drawing these into optical fibres, similar to drawing glass fibres. Hawkins et al. state that "These Bragg layers can be designed to be reflective for all angles of incidence (omnidirectional guiding) and light can even propagate around bends with very little loss."[3] Light is guided in these waveguides when the wavelength satisfies the Bragg condition. The Bragg condition is usually written for crystal lattice spacing, $d$, with respect to the angle of reflection, $\theta$, and the wavelength of the light, $\lambda$, as can be seen in Equation 4.3. For Bragg waveguides the thicknesses of the dielectric layers is proportional to the lattice spacing in crystals.[a] Such waveguides can be made for a broad center wavelength range from the visible to the mid-infrared spectral range, but each waveguide exhibits only a bandwidth of about 100 nm for each center wavelength.[4]

$$n\lambda = 2d * \sin\theta \qquad (4.3)$$

Photonic Crystal Fibres are akin to Bragg waveguides. More precisely, PCFs are glass fibres with a cross section consisting of a 2D array of holes, or low refractive index

[a] *The Bragg law can also be applied to acousto-optic modulators (cf. Chapter 1) with substituting the lattice spacing, d, with the generated sound wavelength.*

medium (cf. Figure 4.2.b). The periodic array around a solid core, or a center hole, gives rise to light interference in a way that the light intensity overlays constructively in the (hollow) core of the PCF. The cross sectional pattern determines the guiding properties of the PCF and the wavelengths that can be used with the waveguide. These fibres are commonly made from high purity silica tubes, which are assembled into a preform and drawn like a regular glass fibre. Typical diameters of the hollow core in PCFs range from 5 μm to 20 μm, and they can be filled with low refractive index liquids, without causing significant loss of guiding properties. PCFs have been used as long path length optical cells and utilized as, for example, evanescent wave sensors for biomolecules[5], as refractive index sensors to determine sugar content in drinks[6], as Raman spectroscopy cells[7, 8], and as fluorescence sensors[9]. Beyond their applications in optics, PCFs have shown promise as solution channels in capillary electrophoresis[10], but with a bandwidth of about 100 nm in the visible and near-infrared and being mostly single mode, they are hard to incorporate into a broadband optical cavity due to alignment and mode overlap considerations.

Although invented much earlier, in 1986, by Duguay et al.[11], anti-resonant reflective optical waveguides (ARROWs) have only recently been used by researchers as optofluidic sensors.[12-16] These ARROWs are made from channels in different substrates, which are coated with a single layer of dielectric coating, and they rely on interference for light guiding just like PCFs. There are two ways to create such waveguides. First, a coated channel and a coated top plate are bonded together to form the actual hollow structure. Second, thin dielectric coatings for ARROWs can be deposited by thin layer deposition, which has been intensively developed for the production of electronic chips, since it has

the potential of forming layers of a hundred nanometers with a precision of a few percent. For ARROWs, the base dielectrics are deposited first and a sacrificial spacer is added later. This spacer becomes the core of the ARROW after having been dissolved, but beforehand, more dielectrics are coated on top of the spacer to complete the waveguide. An SEM image of the cross section of an ARROW is shown in Figure 4.2.c. Many research groups have utilized this technique and a large variety of experiments with ARROWs have been performed. A review on waveguides, their fabrication and implementations was published by Hawkins et al. in 2007.[2, 3] Although these waveguides are easy to incorporated in chip-based waveguide systems, their geometry and bandwidth (about 50 – 100 nm in the visible and near-infrared) makes them not suitable for our purposes.[12]

In this thesis, the focus was on liquid core waveguides made from glass capillaries. Liquid core waveguides provide the sample volume we aimed for, are easy to use, can be inexpensive and are readily manipulated in the laboratory. Furthermore, the capillaries we used were comparable in size and optical properties with multimode fibres and, consequently, provide more relaxed requirements on alignment than, for example, PCFs which are usually single mode waveguides and have to be interfaced with single mode fibres. When using multimode waveguides, multi-exponential decays of the light intensity have to be considered in the data analysis. Depending on the detection resolution and the losses associated with each of the multiple decays, the detection scheme might simplify to a single exponential decay (cf. Chapter 3).

## 4.2. Single Pass Absorption in Fibre-Coupled LCWs

In CRDS, the cavity system's inherent losses determine the overall performance of the experiment. If these unwanted losses are large, the sample absorption and other desired losses only result in a small change in ring-down time and the setup is no longer useful. The ring-down time can be calculated from Equation 4.4 (which is a different way to display Equation 1.6) and it is obvious that the undesired system-inherent losses should be minimized to optimize the experiment.

$$\tau = \frac{nL}{c_0(-LnT_{setup} - LnT_{sample})} = \frac{nL}{c_0(loss_{undesired} + loss_{desired})} \qquad (4.4)$$

The above equation can be solved for the overall transmission: $T = T_{setup} * T_{sample}$ with $t_{RT} = \frac{nL}{c_0}$

$$T = e^{-\frac{t_{RT}}{\tau}} \qquad (4.5)$$

The overall loss, Z, of a CRDS system, can be calculated from the overall transmission ($Z = 1\text{-}T$) of the system but it can also be determined from the individual losses, $\zeta_i$, of each component, *i*, according to

$$Z = 1 - \prod_i (1 - \zeta_i) \qquad (4.6)$$

It is convenient to express losses not in percentages but in dB, since the dB-losses, $\zeta_i^{dB}$, are additive but the percent-losses, $\zeta_i$, are multiplicative:

$$Z^{dB} = -\sum \zeta_i^{dB} \tag{4.7}$$

with

$$\zeta_i^{dB} = -10\log\left(1-\zeta_i\right) \tag{4.8}$$

In a pulsed CRD experiment, if the losses are much too large, the experiment may even fail completely in the case that it takes the light pulse intensity a shorter period of time to decay below the detection threshold, or below the detection noise level, than it takes the light to do one round trip. Of course, the ring-down time cannot be determined from a fit to only one point. If a square wave-modulated light input is used, an exponential decay trace is visible, but the time constant is a convolution of the signal response function and the exponential decay. In such a high loss experiment, the decay would correspond to either the shut-off process of the light source or the response time (= reciprocal bandwidth) of the detector, whichever is greater. In a phase-shift measurement (cf. Chapter 3), the cavity would respond to a frequency change in a linear fashion, since $\tau$ depends only on the system inherent losses and not on any sample absorption process.

To outline the optimization processes of the incorporation of a liquid core waveguide into a fibre-loop ring-down spectroscopy setup, the various losses associated

with the two experimental building blocks have been studied and shall in the following be characterized in more detail.

As a first step, an appropriate matrix liquid to be used with the LCW has to be found. Then, the dependence of the transmission through an LCW on the refractive index is examined in more detail. Subsequently, geometrical matching of the fibre and the liquid core waveguide is addressed, and the surface quality of the liquid core waveguide ends is examined. Finally, a more detailed investigation of fibre lenses that can be used with higher refractive index liquids surrounding the fibre is performed, and detailed information is given on the construction and use of a simple lensing device to manufacture concave lenses at ferruled fibre ends.

### 4.2.1. Determination of a Suitable Matrix Liquid for the Use with a Liquid Core Waveguide

In order to maximize the sensitivity of a liquid core waveguide-fibre-loop ring-down spectroscopy (LCW-FLRDS) system, the matrix liquid should have high transparency or low absorption loss in the wavelength region of interest. Also, it must have a higher refractive index (RI) than the material of the waveguide tubing, or else the LCW is not guiding. For the experiments described herein, a fused silica capillary with a refractive index of n =1.45[17] was used, so that only matrix liquids with n > 1.45 needed to be considered. There are not many common solvents that satisfy the refractive index

requirements and are also reasonably transparent in the visible spectrum. The following solvents were chosen as potential candidates: bromoform ($CHBr_3$, RI = 1.595), toluene ($C_7H_8$, RI = 1.496), dimethylsulfoxide (DMSO, $C_2H_6SO$, RI = 1.4785), and dimethylsulfoxide-d6 (DMSO-d6, $C_2D_6SO$, RI = 1.476). Although the RI of carbon tetrachloride ($RI(CCl_4)$ = 1.460) is higher than the RI of the capillary, curiously, no light transmission could be detected in the setup described below. Consequently, to increase the refractive index, a 1:1 mixture of DMSO and $CCl_4$ was examined, but the collected data did not result in an obvious trend. The data was discarded and the experiment with carbon tetrachloride was not repeated due to the health hazards associated with the liquid.

To determine the absorption losses of the different liquids, the light intensity as a function of absorption path length was measured with the setup shown in Figure 4.3.

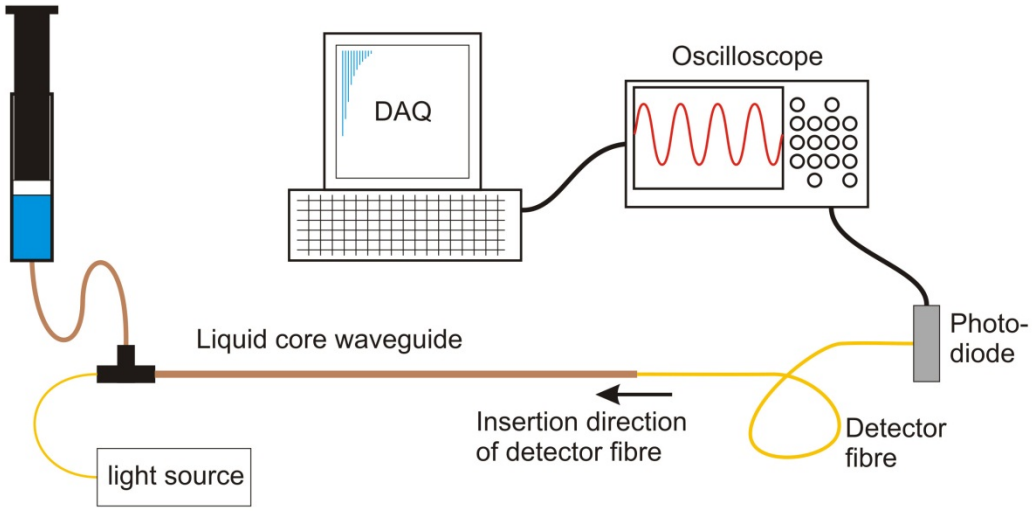


Figure 4.3. Fibre pushing setup to determine the absorption of different solvents in combination with their light guiding properties within a glass capillary. The fibre-coupled light source was coupled to the LCW in a micro-T (*Upchurch*) to the LCW capillary. The LCW capillary had an inner diameter of 250 µm and an outer diameter of 360 µm. The detector fibre had an outer diameter of 125 µm, including the polyimide coating, to easily slide it inside of the LCW without breaking. The solvent was supplied with a glass syringe and a syringe pump at a rate of 10 µL/min and was introduced into the LCW at the micro-T. The detector fibre was then pushed inside the LCW to not create any air or gas bubbles inside the LCW. The light source was modulated sinusoidally, using an arbitrary function generator at 100 kHz, and the peak to peak intensity of the signal was recorded on an oscilloscope.

A fibre-coupled light source was coupled to a long fused silica capillary ($Ø_{ID}$ 250 µm, $Ø_{OD}$ 360 µm) that had been filled with the matrix liquid in question. In addition, a second fibre, with a smaller outer diameter than the inner diameter of the LCW, was connected to a photodiode detector. Then, the loose end of the detector fibre was pushed inside the capillary and subsequently, intensity measurements at fixed distances were taken. The detector fibre was pushed inside instead of pulled out of the capillary, for the purpose of avoiding the creation of bubbles. Two assumptions have been made in this experiment: First, the losses in the detector fibre are negligible and, second, the coupling

from the liquid core waveguide to the detector fibre remains unchanged along the path length.

A different option for performing such measurements is to slide a photo detector along the capillary and detect scattered light from the waveguide. The scatter intensity is proportional to the light intensity inside the waveguide and would produce the same results. There are a few disadvantages to consider with this experimental setup. First, the capillary is usually coated and the scattered light has to travel through the coating to be detected. This reduces the scattered intensity, which considering a well guiding waveguide should be low to begin with, and may not be able to be detected by the photodiode. Additionally, fluctuations of the coating thickness of the capillary will give rise to intensity fluctuations on the detector and are very hard to quantify. If the capillary is uncoated to avoid these effects, the capillary becomes very brittle and might break easily. Second, any scattering center, like micro-bubbles and scratches, will affect the measurement considerably. Third, a measurement with the detector outside of the waveguide will not measure the quality of light confinement to the core, but to the whole capillary. Even a waveguide that exhibits very high guiding properties between cladding and surrounding, but does not have the necessary refractive index difference between the core and the cladding to guide light in the core, will still exhibit a long decay length. Last, moving a photodiode along an extensive path given by the length of the capillary and keeping the alignment between the detector and the capillary with respect to distance and angle consistent is not a trivial task, but will influence the recorded intensity. On the grounds of all these reasons, the setup described in Figure 4.3 was preferred.

The absorption loss due to the pure liquid can be determined from a plot of the intensity measured, *I*, with respect to the path length, *d*. According to Equation 4.9, an exponential fit to the gathered data gives the decay length, δ, which is the inverse of the absorption loss, α.

$$I = I_0 e^{-\alpha d} = I_0 e^{-\frac{d}{\delta}} \qquad (4.9)$$

Strictly speaking, the loss determined in this way is not purely caused by the absorption of the matrix liquid but rather a combination of the light guiding properties of the liquid core waveguide and the absorption of the matrix liquid.

In Figure 4.4, (a) through (d) display the collected data for the selected solvents at 810 nm. An exponential fit included in the figures gives the decay length in cm. The absorption coefficients and the decay lengths are summarized in Table 4.1. Wavelengths of 810 nm, as well as 405 nm for DMSO, were chosen due to the availability of fibre-coupled diode lasers that could be sinusoidally modulated to perform the measurements. It had been expected that toluene-d8 would give a longer decay length than toluene, since DMSO-d6 also had a higher transparency than un-deuterated DMSO, but no conclusive evidence for this isotope effect has been found (cf. Figure 4.5). The large scatter of the data in Figure 4.5 is not understood.

In 2004, Mohammed et al. described distinct light intensity fluctuations within a multimode fibre when it had been excited by the output of a single-mode fibre.[18] These intensity fluctuations gave rise to nodal and focal planes along the propagation direction of

the multimode fibre. Although this effect is found in the publication of Mohammed et al. on a much shorter length scale, it is possible that it extends through a longer multimode waveguide as well. The important difference to our experiments is that Mohammed et al. launched the light into the multimode waveguide from a single mode source. Since this is not the case in our experiment and the effect depends on several parameters, such as core diameters, core and cladding refractive indices, excited modes in both excitation and receiving waveguides, one can dismiss the effect in our system.

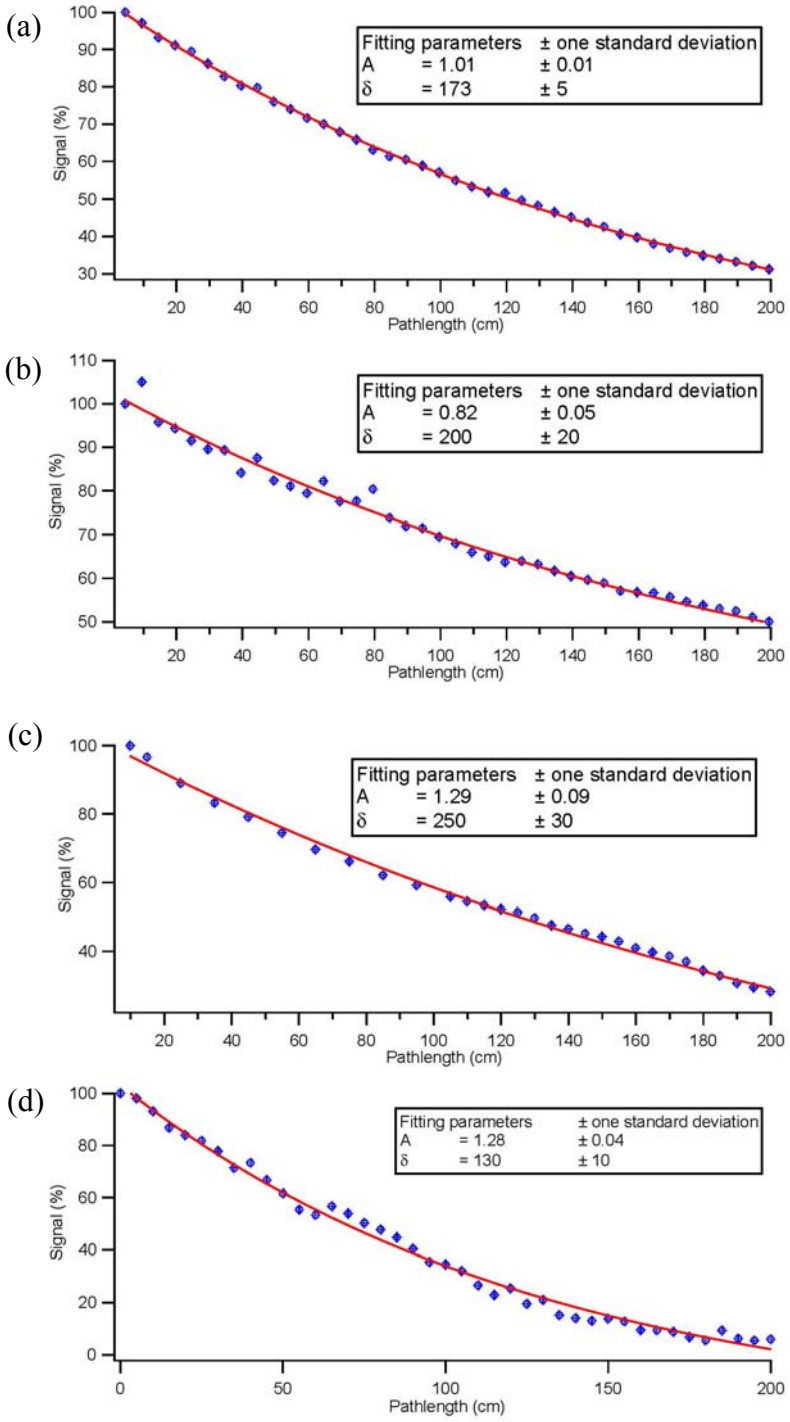


Figure 4.4. LCW absorption measurement at 810 nm of: (a) DMSO (decay length 173 cm; absorption coefficient 5.8 $\times 10^{-3}$ $cm^{-1}$). (b) DMSO-d6 (decay length 200 cm; absorption coefficient 5.0 $\times 10^{-3}$ $cm^{-1}$). (c) Toluene (decay length 250 cm; absorption coefficient 4.0 $\times 10^{-3}$ $cm^{-1}$). (d) Bromoform (decay length 130 cm; absorption coefficient 7.7 $\times 10^{-3}$ $cm^{-1}$). In all the graphs, y-error bars are given as ± 0.001 % which are uncertainties calculated from the uncertainties given by the oscilloscope as standard deviations. The error in

x-direction is ± 0.2 cm. *A* represents the fitted intensity with no liquid core waveguide betweeen the fibre ends.

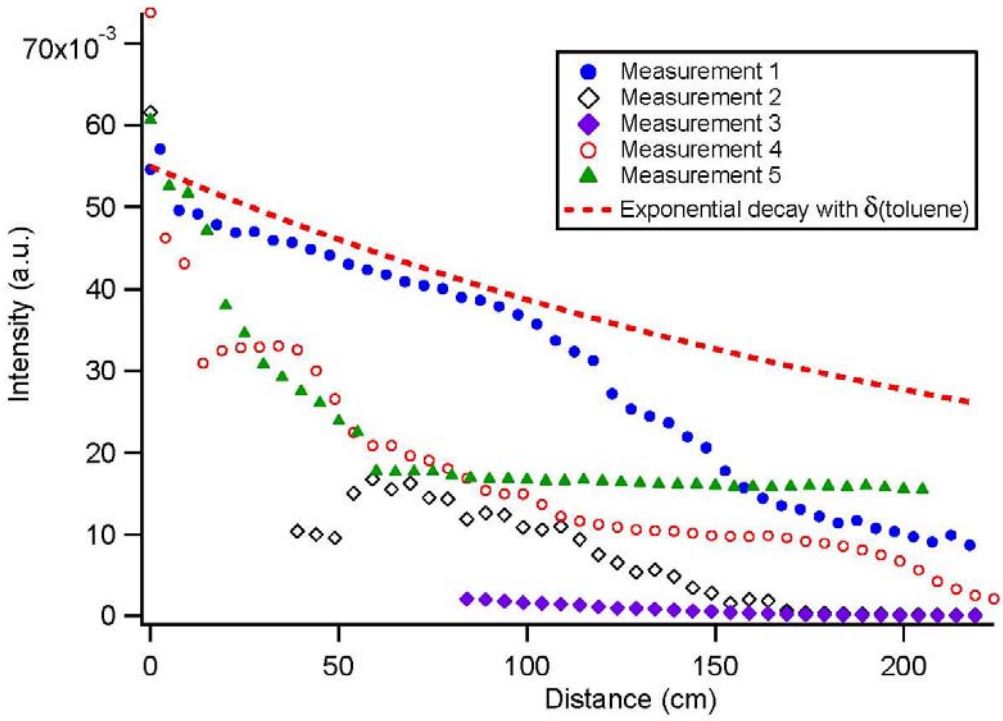


Figure 4.5. Multiple measurements of the decay length of toluene-d8. The randomness of the data suggests that toluene-d8 is unsuitable as a matrix liquid and the previously expected longer decay length with respect to toluene is not evident. The dashed line represents the intensity decay with the decay constant of toluene.

Furthermore, the absorption of DMSO was measured at 405 nm. The respective graph is given in Figure 4.6, with the determined decay length and the absorption coefficient being 38 cm and $2.6 \times 10^{-3}$ $cm^{-1}$, respectively. The wavelength of 405 nm was chosen, due to the availability of a fibre-coupled *cw*-laser which could be intensity modulated. The experiment was undertaken to get qualitative results on the effect of shorter wavelengths on the transmission of the LCW. An appropriately modulated *cw*-light source at the final wavelength used in Chapter 5 (532 nm) was not available.

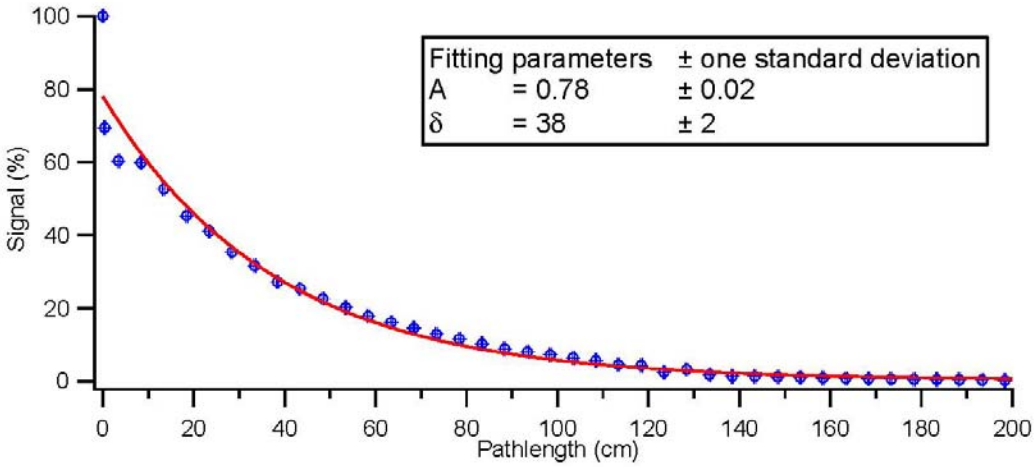


Figure 4.6. Determination of decay length of DMSO in the same setup as in Figure 4.3, but with the use of a 405 nm light source. The decay length is 38 cm, resulting in an absorption coefficient of $2.6 \times 10^{-2}$ $cm^{-1}$. Here, the uncertainty in y-direction is ± 0.01%, which is the readout of the oscilloscope used. The error in x-direction is again ± 0.2 cm

| Solvent | Toluene | CHBr3 | DMSO-d6 | DMSO (810 nm) | DMSO (405 nm) |
|---|---|---|---|---|---|
| decay length (cm) | 250 | 130 | 200 | 173 | 38 |
| Absorption coefficient ($cm^{-1}$) | $4.0 \times 10^{-3}$ | $7.7 \times 10^{-3}$ | $5.0 \times 10^{-3}$ | $5.8 \times 10^{-3}$ | $2.6 \times 10^{-2}$ |

Table 4.1. Summary of decay lengths and absorption coefficients for selected solvents at 810 nm and for DMSO at both 810 nm and 405 nm. The absorption coefficients and decay lengths are not solely dependent on the absorption of the respective solvent, but they also reflect the guiding abilities of the solvent in the glass capillary used.

In the subsequent experiments described here, DMSO was selected as the matrix liquid for its ready availability, ease of handling, and price, although it does not have the longest decay length of the solvents tested. It is apparent that the loss increases strongly if the wavelength is shortened. As DMSO is transparent in the visible it had been expected that DMSO absorbs light at 405 nm and at 810 nm to about the same extent. Generally, absorption spectra of DMSO are only reported below 300 nm, which supports our

assumption.[19] However, it was observed that the DMSO-filled LCW becomes more susceptible to loss of signal due to increased scatter of the light. At shorter wavelengths, a different LCW material might be more appropriate. In order to ascertain this, more studies on increasing transmission in the UV should be performed. For these, toluene might be an appropriate organic solvent.

Of course, the internal structure of the capillary is very hard to control in these experiments. For example, small dust particles or micro-bubbles may introduce scattering centers and skew the intensity measurements performed. Hairline cracks and other damages to the LCW outside of the control of the experimenter can also cause unwanted intensity fluctuations, which explain outliers in the decay traces.

All findings considered, it can be concluded that the above tests are easy and viable option to test waveguide/liquid combinations for the use of LCWs with CRDS and other techniques.

### 4.2.2. Exploration of Benefits Associated with Strongly or Weakly Guided Light in LCWs

Most often, light in an optical fibre is guided in a weakly guiding regime, because the refractive index difference between the core and the cladding is small and, consequently, the critical angle needed for total internal reflection is large. A common fibre has a numerical aperture of 0.22 and a core RI of 1.45, which implies a cladding refractive

index of about 1.433 (cf. Equation 4.11). In our liquid core waveguide the wall material, the cladding of the LCW, has a refractive index of ~1.45 and the matrix liquid used, DMSO, has a refractive index of 1.4785. This RI combination results in a numerical aperture of 0.29. Although this is still considered to be a weak guiding regime of optical waveguides ($n_{core} \approx n_{cladding}$)[20], we wished to explore if a better transmission could be achieved with the same numerical aperture as that of the fibre, and thus a more weakly guiding waveguide.

A simple setup was devised, in which light pulses from a Nd:YAG laser are shone through an LCW and averaged pulse intensities at different refractive indices within the LCW are measured. A schematic of the setup is shown in Figure 4.7.

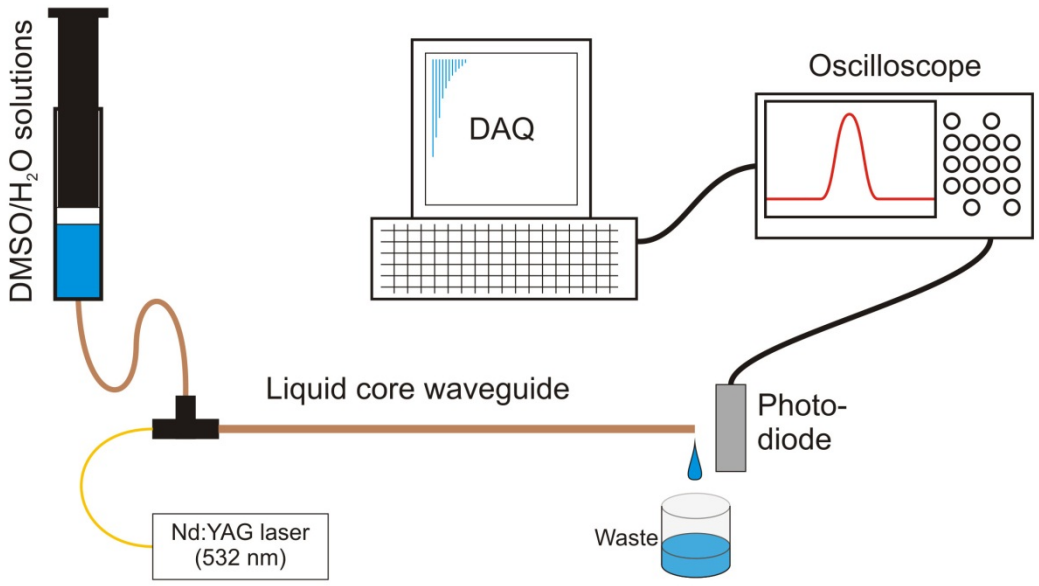


Figure 4.7. Schematic setup for exploring the impact of changes of the refractive index in the liquid core waveguide on the transmission. A 532 nm pulsed Nd:YAG laser was coupled into a 100/140 µm fibre, which was 'butt coupled' to a 100/360 µm LCW in a liquid flow system. The light from the end of the LCW was shone onto a photodiode detector and pulse intensities were recorded on an oscilloscope. The recorded intensities were averaged 512 times on the oscilloscope, before a Gaussian curve was fitted to the pulse shape, in order to determine the peak intensity. Care was taken to record at a point with no flow in the capillary and with a consistent drop on the end of the waveguide. The distance between the end of the waveguide and the photodiode was 10 mm.

In this setup, a 532 nm pulsed Nd:YAG laser was coupled into a 100/140 µm fibre. A 100/360 µm capillary was 'butt coupled' to the fibre end in a homemade aluminium block to inject different liquids into the LCW. Light from the output end of the LCW was shone onto a photodiode detector and pulse intensities were recorded on an oscilloscope. The recorded intensities were averaged 512 times on the oscilloscope and transferred to a computer. Gaussian functions were fitted to the pulse shapes, in order to extract the peak intensity.

Several mixtures of DMSO and water were used to adjust the refractive index of the matrix solution. The refractive index of the mixture was calculated from a volume

weighted average of the RIs of the pure solutions and ranged from pure DMSO (RI = 1.4785) to pure water (RI = 1.33). Figure 4.7 represents the observed intensity change with refractive index of the solvent mixture. Obviously, reducing the RI to extend into the weakly guiding regime of the LCW does not have a beneficial effect on the output intensity and, consequently, on the resulting transmission through the LCW. The explanation for this is that if the values of the refractive indices of core and cladding approach one another, only light with a shallow propagation angle, with respect to the LCW direction, is guided and reaches the detector. Additionally, it is apparent that the light intensity drops after the numerical apertures have been matched ($RI_{core,LCW}$ = 1.4665, red dashed line in Figure 4.8), as not all light emitted from the fibre is guided anymore. Before the matching numerical aperture, the signal fluctuates considerably, but there is a trend to increased transmission with increased core refractive index. At $n_{matrix} < 1.45$, the waveguide no longer guides light and only a weak contribution is observed from light that travels through the wall of the capillary and reaches the detector. However, this had been expected, since the RI of the capillary material is 1.45 and the core has to have a higher refractive index to effect guiding properties.

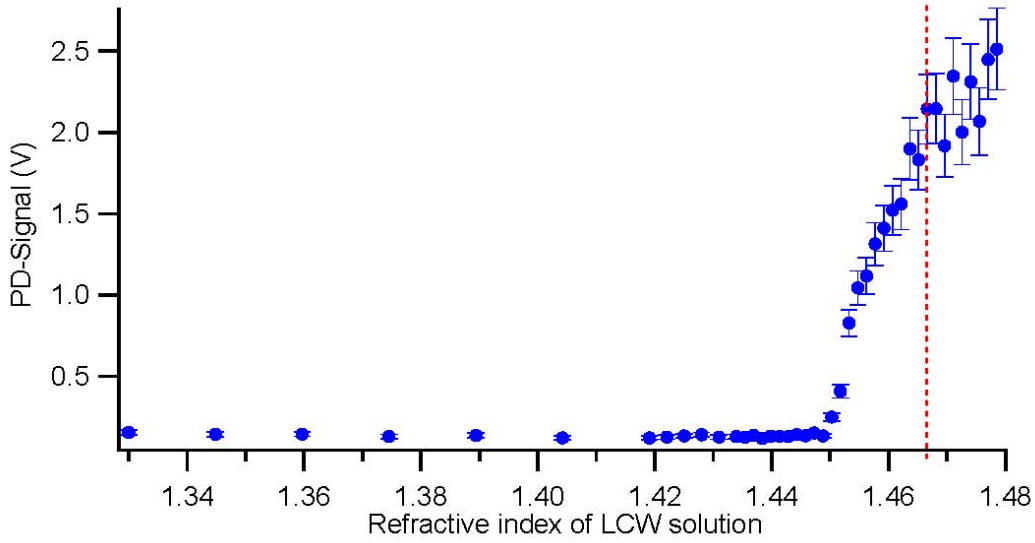


Figure 4.8. Dependency of the intensity transmitted through a 5 cm LCW on the refractive index within the LCW, made from a fused silica capillary. An Nd:YAG laser pulse was coupled into a fibre, which in turn was coupled to the liquid core waveguide, as depicted in Figure 4.7. The LCW was then filled with different DMSO/water mixtures, thereby varying the refractive index from pure DMSO (1.4785) to pure water (1.33), in order to explore the dependency of the guiding properties on the refractive index of the waveguide. The red dashed line represents matching numerical apertures of the light delivering fibre and the LCW.

On the basis of this experiment and its results and on grounds of the ease of its handling, it was decided to use pure DMSO as a matrix liquid, for the purpose of getting the highest intensity transmitted through the waveguide.

### 4.2.3. Geometrical Matching of Liquid and Solid Core Waveguides

For the final desired experimental setup, we needed to couple light from the solid core fibre to the liquid core waveguide and back, while considering transmission losses at both couplings. If the outer diameter of the optical fibre is smaller than the inner diameter

of the liquid core waveguide, two possibilities arise: first, the two waveguides can be 'butt coupled', which means that the first waveguide ends right where the second waveguide begins; second, the two waveguides can be 'inside coupled', meaning that the solid core waveguide reaches into the opening of the liquid core waveguide. If the outer diameter of the fibre is bigger than the LCW's inner diameter, only the 'butt coupled' option remains.

#### 4.2.3.1. 'Inside Coupling' of Fibre and Liquid Core Waveguide

The option to insert the solid core waveguide into the liquid core waveguide is very appealing, as it can be assumed that, given the numerical apertures of the two waveguides are equal, all the light emitted from the smaller fibre is guided within the bigger LCW. To determine the coupling losses, a bidirectional 2x2 fibre coupler (*Lightel Industries*) was used in an FLRDS setup with a fused silica capillary (20 cm) as an LCW, being placed in between the fibre-loop ends. The fibre coupler was made from a multimode fused silica fibre with a 400 µm core and a 440 µm cladding diameter and a splitting ratio of 99/1. The capillary had an inner diameter ($Ø_{ID}$) of 535 µm and an outer diameter ($Ø_{OD}$) of 665 µm. The fibre ends were inserted by about 500 µm into the capillary and were held by a micro-T (*Upchurch*, P-727, *high pressure PEEK tee with 0.5 mm through hole*), ensuring that the capillary could be filled with DMSO. After making sure there were no air bubbles trapped within the liquid core waveguide, which would have greatly interfered with the transmission, a ring-down trace was recorded using a pulsed Nd:YAG laser (*Spectra Physics Quanta Ray INDI-HG*) at a wavelength of 532 nm as light source and a

PMT as detector. The decay of the light pulse is presented in Figure 4.9 and the ring-down time has been determined from an exponential fit to the pulse train. The measured ring-down time was 37 ns.

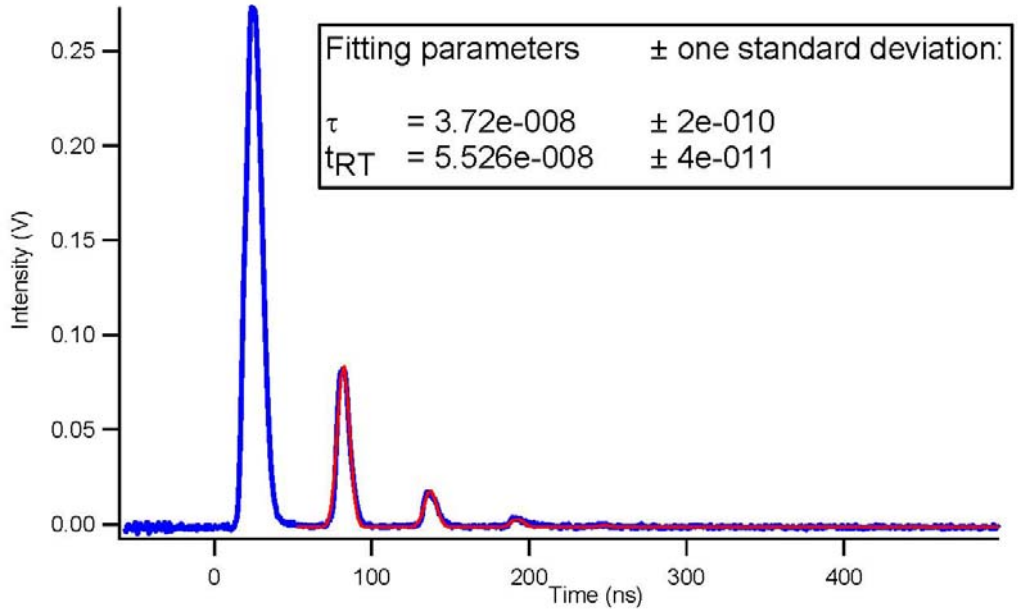


Figure 4.9. Ring-down trace of a glass capillary with an inner diameter of 535 µm and an outer diameter of 665 µm as liquid core waveguide. The fibre ends of the fibre-loop used (core diameter 400 µm, cladding diameter 440 µm) were extending inside the LCW for a few hundreds of micrometers. The first peak was omitted in the fit on the grounds of possible saturation of the PMT, for the laser light had only travelled directly from the laser to the PMT.

From the definition of the ring-down time given in Equations 4.1 and 4.2, the roundtrip losses can be determined to be 77% ($T$ = 0.23, $Z^{dB}$ = 6.4 dB). Having recorded the ring-down time of the same setup without the LCW, but with the fibre ends aligned in a similar fashion, the losses caused by the coupler could be calculated (cf. Figure 4.10) and the coupling losses on account of the LCW could be isolated. The round trip losses in the fibre-loop only, that is without the LCW, could be calculated from the ring-down time for

this setup (122 ns) and results in 36% ($T$ = 0.64, loss = 1.9 dB). These losses include insertion losses of the coupler, losses in the coupler due to the splitting ratio of 99/1, absorption losses of the fibre material, and coupling losses between one end of the fibre and the other. In this setup, a thin film of DMSO was placed between the fibre ends, in order to make as few changes as possible to the setup compared to the setup with the incorporated capillary. The determined differences in round trip losses between setups with and without liquid core waveguides offer a good approximation of the coupling losses between the fibre and the capillary waveguide. The absorption loss caused by the matrix liquid DMSO within the capillary has been assumed to be negligible for a 20 cm liquid core waveguide.

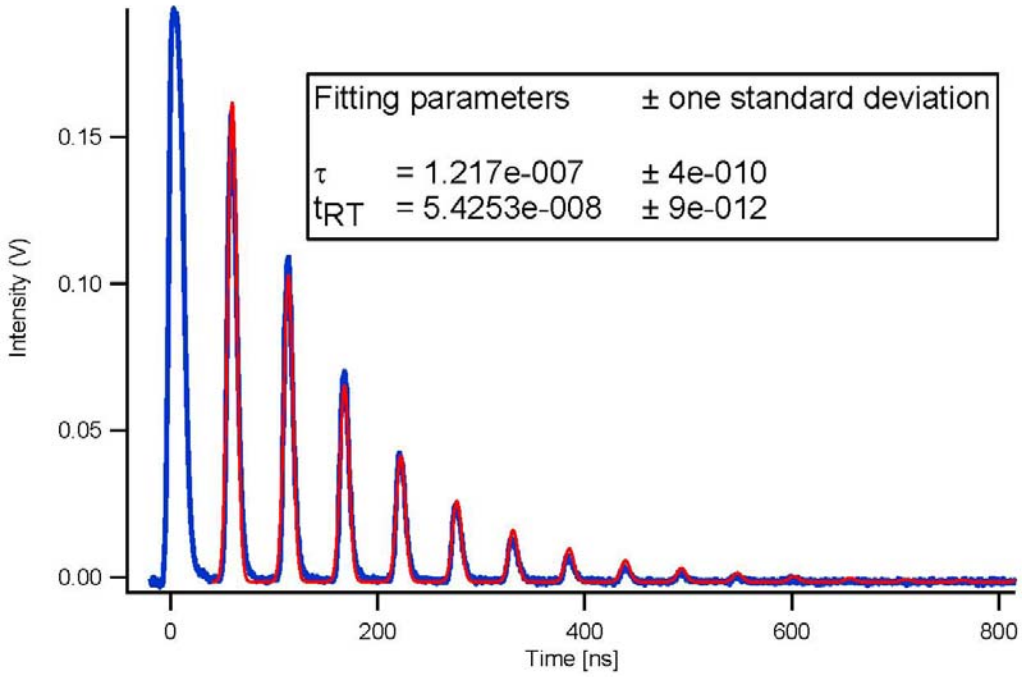


Figure 4.10. Ring-down trace without liquid core waveguide. The fibre ends are aligned in the same way as they were in the setup with the capillaries and they were pushed together as much as possible. From the ring-down trace, the losses generated by the fibre coupler used together with the losses of the alignment of the fibres can be determined to be 36% ( = 1.9 dB).

The calculated coupling losses between LCW and fibre only were 65%, or formally 4.5 dB. It can be assumed, however, that these were induced entirely by the coupling from the larger LCW back into the smaller fibre and not from the coupling from the smaller fibre into the LCW. The core and cladding modes of the fibre are coupled most efficiently with the core modes of the LCW if energy is transferred from the fibre to the LCW. As the light propagates along the liquid core waveguide, the energy of the different core modes of the LCW is mixed and it is also redistributed between cladding modes of the capillary waveguide. The energy in the cladding modes are lost at the end of the waveguide, where the cladding does not overlap with the fibre at all. Additionally, not all

sustained core modes of the LCW find an equivalent in the fibre, which also reduces the efficiency of the energy transfer.

#### 4.2.3.2. 'Butt Coupling' of Fibre to Liquid Core Waveguide

##### 4.2.3.2.1. Core and Cladding Diameters of LCWs Being Smaller than Respective Fibre Dimensions

In all the 'butt coupled' waveguide setups, a small distance between the ends of the waveguides has to be preserved in order to both add and remove liquid from the waveguide. This distance was on the order of a few micrometers and was set manually with the aid of a magnifying glass (magnification 10x). The coupling losses were determined with both core and cladding of the liquid core waveguide having been smaller than the fibre. For this, a capillary with an outer diameter of 360 µm and an inner diameter of 250 µm, was placed between the fibre ends of the fibre-loop (400/440 µm). The ring-down time was determined to be 33 ns (cf. Figure 4.11), which is less than the round trip time. The losses as a consequence of coupling in and out of the LCW were calculated to have been 70% (= 5.3 dB). This was an even higher loss than in the previous case, which was not surprising, since a considerable fraction (about 36%) of the light exiting the fibre core cannot be captured by the LCW and therefore had no opportunity to be guided. The same applies to all the cladding modes within the fibre. This case is very similar to the

previous case in which the LCW is much bigger than the fibre (cf. Chapter 4.2.3.1), but with reversed geometry.

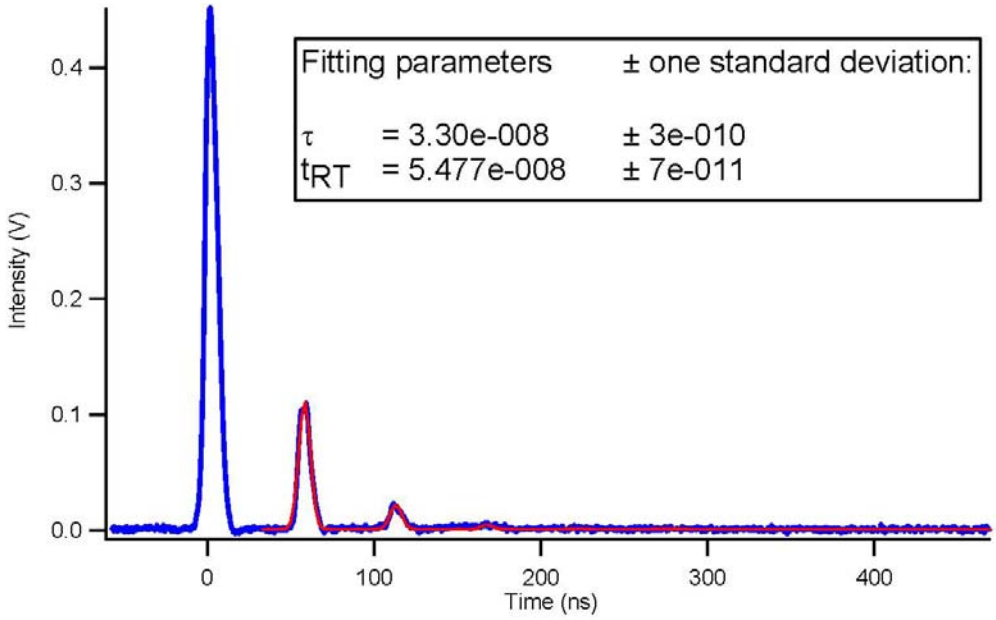


Figure 4.11. Ring-down trace of a glass capillary with an inner diameter of 250 µm and an outer diameter of 360 µm as liquid core waveguide. The fibre ends of the fibre-loop used (core diameter 400 µm, cladding diameter 440 µm) were pushed against the ends of the LCW. The first peak was omitted in the fit, due to possible saturation of the PMT, for the laser light had only travelled directly from the laser to the PMT.

#### 4.2.3.2.2. Matching Cladding Diameters but Mismatched Core Dimensions

As available capillaries are only made in a limited number of sizes and the dimensions of the optical fibre are fixed by the availability of commercial couplers, there is only one example left to explore. Here, the cladding diameter of both waveguides matches and the core of the fibre is larger (400 µm) than the core of the LCW (320 µm). The length of the capillary used as liquid core waveguide was again set to 20 cm for reasons of comparison. A ring-down trace was recorded at 532 nm and is shown in Figure 4.12. The

ring-down time could again be determined from a fit to the pulse train and is 80 ns. After having taken into account the losses owing to the coupler itself (cf. Chapter 4.2.3.1), the losses for the geometrical mismatch of the waveguides result in 22% (= 1.1 dB) for both connections.

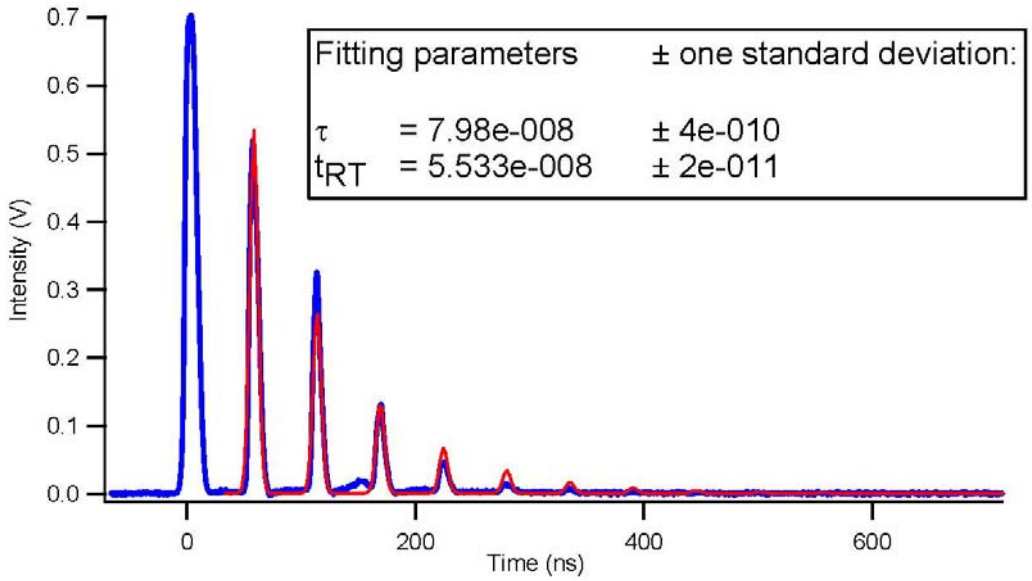


Figure 4.12. Ring-down trace of a glass capillary with an inner diameter of 320 µm and an outer diameter of 440 µm as liquid core waveguide. The fibre ends of the fibre-loop used (core diameter 400 µm, cladding diameter 440 µm) are pushed as much as possible against the ends of the LCW. The first peak was omitted in the fit because of possible saturation of the PMT, for the laser light had only travelled directly from the laser to the PMT.

The coupling losses (1.1 dB) in this case are smaller than in the 'inside coupled' example (4.5 dB) (cf. Chapter 4.2.3.1) and also smaller than in the setup in which both the cladding and core dimensions of the LCW are smaller than that of the fibre (5.3 dB) (cf. Chapter 4.2.3.2.1). This was to be expected, as the closer the geometries become, the more similar is the mode distribution in the individual waveguides. Consequently, the better is the mode overlap and energy transfer.

#### 4.2.3.3. Quantitative Comparison of Matching Dimensions Between Waveguides

From this rather qualitative experiment, it has been concluded that it is crucial to match the geometries of the waveguides as closely as possible to achieve good energy transfer from one to the other waveguide. In the first case, in which the fibre is 'inside coupled' to the liquid core waveguide, it can be assumed that the coupling from fibre to LCW is close to 100% and the transmission from the LCW back to the fibre is very poor. The additional losses in and out of the LCW were calculated to have been at 65% (= 4.5 dB).

The case in which both dimensions, of cladding and core, of the LCW are smaller than the fibre dimensions, is the exact opposite. Here, most of the losses occur from the fibre into the LCW and were calculated to be at 70% (= 5.3 dB), in addition to the losses in the fibre-loop only.

The case with the highest transmission was the arrangement with the matching cladding diameters, which was examined. Although the core diameters were mismatched, the relative difference between the two waveguides was the smallest and consequently resulted in the most favourable combination with losses of 'only' 22% (= 1.1 dB).

Undoubtedly, the amount of energy transferred from one waveguide to the other depends on the mode overlap of the fibre and the LCW. Equation 4.10 gives an estimate of the number of guided modes, $N_m$, in a multimode fibre. The number of modes depend on the core diameter, $D$, the numerical aperture, $NA$, (and consequently, the refractive indices of core and cladding), and the wavelength of the light $(\lambda)$[21].

$$N_m = 0.5\left(\frac{\pi * D * NA}{\lambda}\right)^2 \quad (4.10)$$

The numerical aperture is calculated as

$$NA = \sqrt{n_{core}^2 - n_{cladding}^2} \quad (4.11)$$

The results for our four waveguides, one fibre and three capillaries, are summarized in Table 4.2 below.

| Waveguide | Fibre 400/440 | Capillary 250/360 | Capillary 320/440 | Capillary 535/665 | Fibre 100/140* | Capillary 100/360* |
|---|---|---|---|---|---|---|
| Refractive index (core / matrix liquid) | 1.45 | 1.4785 | 1.4785 | 1.4785 | 1.45 | 1.4785 |
| Refractive index (cladding) | 1.433 | 1.45 | 1.45 | 1.45 | 1.433 | 1.45 |
| Numerical aperture | 0.22 | 0.29 | 0.29 | 0.29 | 0.22 | 0.29 |
| Wavelength (nm) | 532 | 532 | 532 | 532 | 532 | 532 |
| Core diameter (µm) | 400 | 250 | 320 | 535 | 100 | 100 |
| Calculated number of modes | 136,729 | 90,953 | 149,017 | 416,528 | 8,439 | 14,664 |
| Loss for 2 connections (dB) | | 5.3 | 1.1 | 4.5 | | 2.8 |

Table 4.2. Estimation of the number of guided modes in the respective waveguides. Waveguides marked with an asterisk are used and discussed in detail in Chapter 5.

Coupling from a lower number of modes to a higher number of modes is more efficient than in the opposite configuration, due to the high probability of a mode overlap.

If the number of modes is similar between the two waveguides, the probability of good modal field overlap, and therefore efficient coupling, is maximized, as indicated by the data presented above. Additionally, it should be considered if the two waveguides are in direct contact or if there is a gap between them. In case of a gap, not only the mode overlap between the two waveguides, but also the non-guided light distribution, has to be considered, as free space coupling lenses on the waveguide ends change the light distribution and therefore the coupling efficiency.

Although the highest coupling efficiency can be achieved when shining light from a smaller to a larger waveguide in both connectors, it is impossible to form a waveguide loop this way. In the final CRDS experiment (cf. Chapter 5), a different fibre and capillary were used, so that the core geometries matched nominally (100 μm) but the fibre was smaller in cladding diameter than the LCW (140 μm vs. 324 μm). The estimated number of modes for the smaller fibre and smaller LCW used in Chapter 5 are given in Table 4.2, including the calculated loss for using two connections. It can be seen that the loss (2.8 dB) is larger than in the best case presented here (1.1 dB), but it is much smaller than in the other two cases. Although this was surprising, it can be explained by the much smaller geometry of the waveguides in this setup. Since they have a core diameter of 100 μm, a much more accurate alignment is required. Additionally, the cladding diameter is mismatched ($Ø_{OD,fibre} < Ø_{OD,LCW}$), which results in a loss, as the receiving fibre is not capable of capturing all the light travelling through the capillary walls. Although the capillary/fibre combination with similar cladding dimensions produced a smaller loss, it was nonetheless decided to use matching core diameters (cf. Chapter 5), because presumably all the light traveling in the fibre core is transmitted into the core of the LCW

and interacts with the sample. In the case where the cores are mismatched, some of the light travels in the cladding and does not see the sample, which leads to artificially decreased concentrations measured by the setup. The setup with matching cores is extensively discussed in Chapter 5. In conclusion, the experiments presented here confirm that best transmission between two waveguides will be achieved if both the core and the cladding diameters are matched. Unfortunately, this is not possible with off-the-shelf components and the compromise of matching the core for sample interaction and mismatching the cladding is chosen for the final setup.

### 4.2.4. Shape of Liquid Core Waveguide Ends

Coupling from one fibre end to another fibre end across the sample gap is one of the major loss mechanisms in FLRDS and has been previously examined.[22-24] Coupling from a fibre into a liquid core waveguide and back poses a similar problem. Besides geometrical considerations and the choice of the correct matrix liquid (cf. previous chapters), the surface qualities of the receiving and emitting waveguide faces also need to be taken into account.

If the surface of the receiving or emitting capillary end is not parallel to the fibre end facet, losses may occur. Additionally, before transmitting light from one fibre end to another, it is common to polish the fibre ends to optical clarity with various lapping papers (aluminium oxide or diamond coated, 5 μm to 0.3 μm) and polishing compounds. The same procedure cannot readily be applied to liquid core waveguides, since the glass easily

chips off on the inner rim of the capillary. Such chipped edges are scattering light and reduce the light transmission considerably.

Commonly, capillaries, that are manually produced are cleaved with the use of a cleaving stone (*Polymicro*) or with a fibre cleaver (*Fitel S321*) by scoring the glass at one position and subsequently snapping it by bending the capillary. This method produces a very inconsistent surface with varying cleave angles towards the flow direction of the capillary. A more consistent way to cleave a fibre is to pull on the scored fibre to break it apart, instead of bending it. Although this produces more consistent angles, the surface is still uneven, because the breaking line depends on inherent stresses within the capillary wall. Certainly, the advantage of this method is that it produces a sharp edge at the rim of the inner hole.

Precision cleaved capillaries (*Polymicro*) are commercially available, and are capillaries that are machine-cleaved in a high performance mechanical cleaver. In this process, the glass capillary is tensioned along the capillary direction and then scored with a diamond blade. The pretensioning allows a build-up in stress in the fibre that is relieved very quickly when a micro-defect is produced by the diamond blade. This accounts for a very high degree of consistency, as well as for an almost perfectly perpendicular capillary end and for sharp edges. One drawback is that stress cracks in a radial direction occasionally appear. Another disadvantage is that these cleaved capillaries are somewhat expensive (> CA $20 per cleave) and they have to be ordered, which results in a waiting time for the experiment.

Given that we have required capillaries at multiple lengths at short notice to be able to proceed quickly with experiments, an alternative way to produce LCW has been

explored. Despite the fact that polishing capillary ends often produces a chipped rim of the inner hole, as mentioned previously, there are methods that have been tried to overcome this and produce an acceptable surface. The first idea was to fill the hole with a solid that can be dissolved after polishing. It was found that nail polish works quite well to block the hole during the process and helps to produce sharp rims, but it seems that nail polish, although readily soluble in acetone, could not be completely removed and the remains decreased the transmission of the waveguide considerably. Second, attempts were made to block the hole with an inserted wire or other cylindrical and sturdy object. A wire is a perfect help for the polishing, it can be easily inserted, and it has the necessary stability to not break and get stuck in the waveguide. The disadvantage of wires is that they scratch the inner surface of the waveguides and with that, they produce more scatter and lower transmission through the LCW. Third, an alternative to a wire is to fit a smaller capillary or a fibre that has an appropriate outer diameter (coating included) inside the waveguide. By virtue of the coating on the fibre or capillary being softer than the waveguide, this aid does not scratch the inside of the LCW, and it gives enough strength to the inner rim to minimize chipping during the polishing process. Sample pictures of distinct waveguides are given in Figure 4.13.

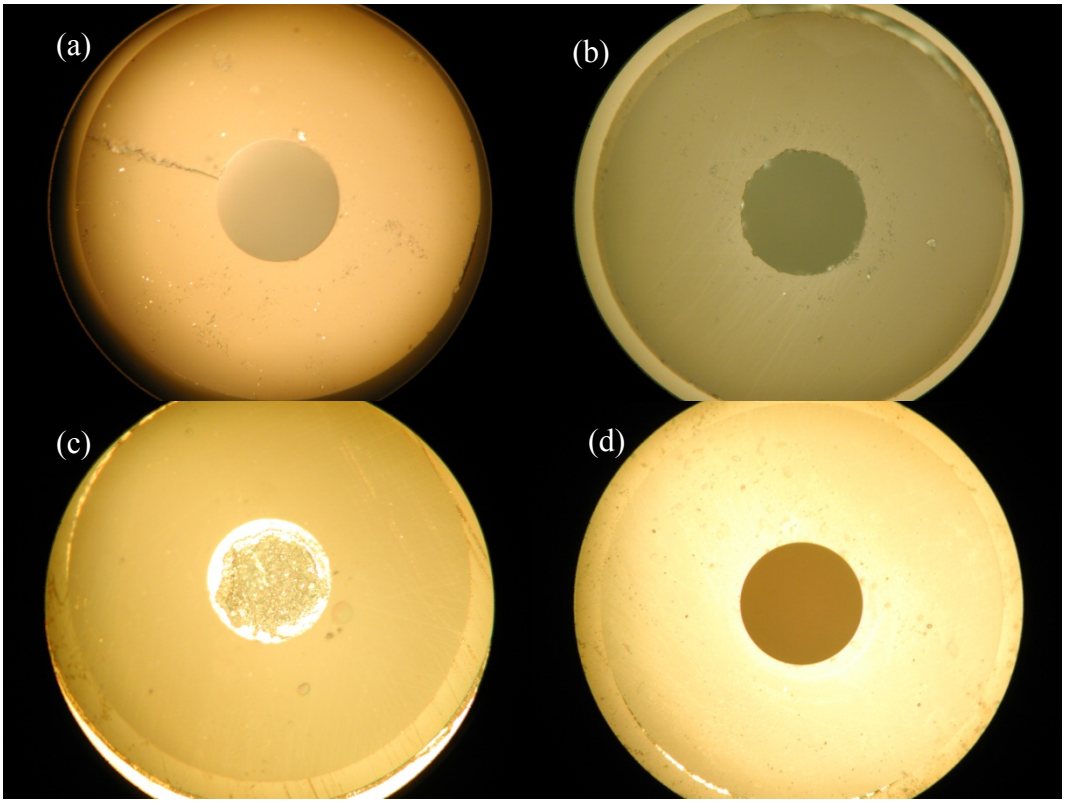


Figure 4.13. Microscope pictures of distinct LCW end faces. (a) Precision cleaved capillary end, purchased from *Polymicro*, with a radial stress crack. (b) Hand polished capillary end, with small chipping of the interior rim. A second capillary stuck into the LCW was used for its production. Polishing without a capillary in the center produces much larger chipping of the 'core'. (c) Polished capillary end filled with nail polish to block the core from debris and to simulate a solid core. (d) After removal of the nail polish, it was evident that the inner rim was completely unchipped. Unfortunately, the nail polish could not be removed completely from inside the LCW, increasing the losses drastically and making the capillary useless.

Summing up, the precision cleaved capillary features the best surface clarity and the sharpest edges, but may be not applicable to all research settings. Its detriment is the long waiting time if these capillaries have to be ordered, or the need for access to a precision cleaver. The precision cleaving process should also produce nice end facets with speciality fibres like PCFs. If a lower cost alternative is needed, manually polished waveguides, with a second capillary or fibre inserted in the core, work for most applications sufficiently well, with slightly higher losses than with the precision cleaved

waveguides. If a completely removable solid, similar to nail polish, can be found, this would be the cheapest and best method to produce waveguides with optically clear and flat ends. This could also be applied to other waveguide materials, like Teflon AF *2400* (RI = 1.29)[1, 25, 26], or different waveguide cross sections, like square waveguides or photonic crystal fibres.

### 4.2.5. Collimating Lenses on Fibre Ends

For coupling efficiently from fibre to LCW and back into the fibre-loop, one also has to consider the quality of the emitting and receiving fibre ends. The simplest treatment is to polish the fibres to optical clarity, as it is commonly done with fibre-fibre connectors. Trefiak et al. showed that lensed fibre ends improve the coupling between fibre ends[22, 27]. Their lenses have been produced by melting the fibre ends in an electrical arc of a fusion splicer. The surface tension draws the glass into a spherical shape. Immersed in a lower refractive index liquid, this shape acts like a common convex lens with the desired focussing effect, which increases the transmission between the fibre ends. Unfortunately, in the research presented in this thesis, the liquid in contact with the fibre during the experiment has a higher refractive index than the fibre. This implies that the lens curvature of the above mentioned modus operandi has to be inverted. In any case, it is not easy to produce such a 'concave' lens.[b] In the following paragraphs, theoretical considerations as

[b] *Note: The produced shape is referred to as a 'concave fibre lens'. In reality, this is only true, if the medium outside of the fibre has a lower refractive index than the fibre. But the medium used in this thesis has a higher refractive*

well as a low cost method of manufacturing concave fibre lenses at the fibre ends, which are embedded into a ceramic ferrule, are presented.

#### 4.2.5.1. Theoretical Model for Simulating Emitted Light Distribution of Lensed Fibres

A Lambertian light source is defined as a light source that emits rays in all directions (within a given solid angle), with the same probability.[28] An example would be a light bulb, a fluorescent tube, or even an LED light if the range of angles is appropriately selected. Taking such a light source and coupling it into a multimode fibre reduces the number of rays to only the rays that are guided within the fibre. This means that all light rays propagating within a fibre exhibit angles that are higher than the critical angle of the fibre. Light emitted from such a fibre at a flat end has an angular distribution that lies within the numerical aperture of the fibre, but with all angles equally 'populated'. In essence, the multimode fibre restricts the angular range of the Lambertian source to the acceptance cone (here, identical to the 'emission cone') of the fibre.

If the fibre end surface is curved, the emitted light cone depends not only on the numerical aperture, $NA$, of the fibre and of the refractive index of the surrounding material, $n_0$, but also on the curvature of the fibre surface, $\sin^{-1}(r/R)$. Here, $R$ designates the radius of the lens curvature, $r_0$ is the fibre core radius, and $r$ is the distance from the fibre axis. All rays that converge at a point $(x, z)$ outside of the optical fibre add up to the intensity at this point, which is expressed in Equation 4.12 and displayed in Figure 4.14.[29]

---

*index, which results in a convex lens made from the liquid used. To avoid confusion and to distinguish ours to previous efforts using convex fibre lenses, the lens described here will nevertheless be referred to as 'concave lens'.*

$$I(x,z)=\sum_{r=-r_0}^{r_0}\begin{cases}1 & \text{if } \beta_1(r)<\alpha(r,x,z)<\beta_2(r)\\ 0 & \text{if } \beta_1(r)>\alpha(r,x,z) \text{ or } \alpha(r,x,z)>\beta_2(r)\end{cases} \tag{4.12}$$

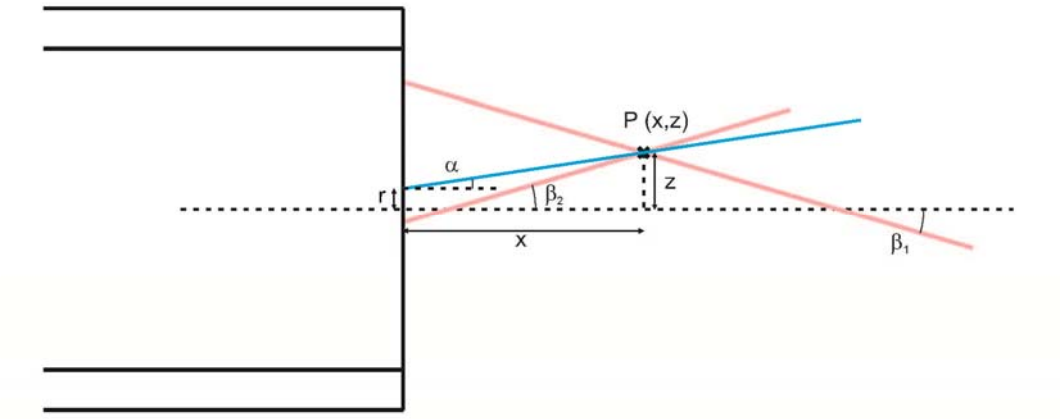


Figure 4.14. Ray representation of the intensity at some point $(x,z)$. The intensity at a point $(x,z)$ is defined by the number of rays converging to this point and emitted from the fibre surface. The propagation angle, $\alpha$, of any given ray to the beam direction, originating from point *r* on the fibre surface, can only be between $\beta_1$ and $\beta_2$, since these angles are the limiting cases, due to the propagation angles within the fibre and the refractive index of the surrounding material.

As mentioned above, the propagation angle of a ray with respect to the beam axis, originating from a point *r* on the fibre surface and passing through point $(x,z)$,

$$\alpha=\arctan\left(\frac{z-r}{x}\right) \tag{4.13}$$

is limited by two 'critical' angles $\beta_1$ and $\beta_2$. These would be simply $\beta_1=-\beta_2=\sin^{-1}(NA/n_0)$ if a flat fibre surface was considered. For a curved surface, the relation is more complicated, and the corresponding ray diagrams are given in Figure 4.15.

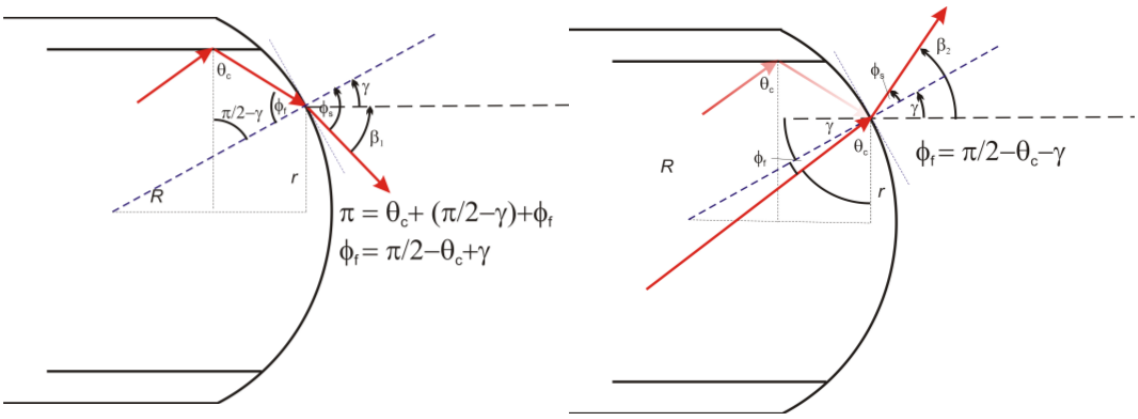


Figure 4.15. Ray diagrams showing the limiting angles, $\beta_1$, (left) and $\beta_2$ (right) as function of the lens radius, $R$, and the critical angle for waveguiding, $\theta_c$. Equations on how these angles are calculated are given next to the respective diagram.

From Figure 4.15 it can readily be verified that for convex lenses:

$$\gamma = \arcsin\left(\frac{r}{R}\right); \quad \theta_c = \arcsin\left(\frac{n_{cl}}{n_{core}}\right); \quad n_0 \sin\phi_s = n_{core} \sin\phi_f \tag{4.14}$$

The critical angle $\beta_1$ is obtained by insertion of

$$\phi_f = \frac{\pi}{2} - \theta_c + \gamma; \quad \beta_1 = \phi_s - \gamma \tag{4.15}$$

Final simplification results in

$$\begin{aligned}\beta_1 &= -\arcsin\left(\frac{r}{R}\right)+\arcsin\left[\frac{n_{core}}{n_0}\cos\left(\arcsin\left(\frac{r}{R}\right)-\arcsin\left(\frac{n_{cl}}{n_{core}}\right)\right)\right] \\ &= -\arcsin\left(\frac{r}{R}\right)+\arcsin\left[\frac{NA\sqrt{R^2-r^2}+r\,n_{clad}}{Rn_0}\right]\end{aligned} \tag{4.16}$$

Similarly, the other limiting angle $\beta_2$ for rays arriving at the interface at an angle of $-\theta_c$ is derived with

$$\phi_f = \frac{\pi}{2}-\theta_c-\gamma\,;\quad \beta_2 = \gamma+\phi_s \tag{4.17}$$

as

$$\beta_2 = \arcsin\left(\frac{r}{R}\right)+\arcsin\left[\frac{NA\sqrt{R^2-r^2}-r\,n_{clad}}{Rn_0}\right] \tag{4.18}$$

For a concave lens, as mentioned earlier, these calculations are simply to be altered by using $R<0$, a negative curvature, and switching $\beta_1$ and $\beta_2$. With these definitions, $\beta_1$ and $\beta_1$ are both positive for positive $R$, and both negative for negative $R$. Furthermore, the signs of angles need to be considered when calculating rays emerging

from a lens with a large curvature, since for small $R$, and high absolute values for $r$ one finds that $\theta_c + \gamma > \frac{\pi}{2}$.

The direct output of Equation 4.12 (cf. Figure 4.16a) for all angles and points on the fibre surface has to undergo three more transformations. First, Equation 4.12 only generates a Fresnel lens output of the intensities and the calculated pixels $(x, z)$ have to be moved along their rows, in order to incorporate the shape of the lensed fibre end. Consequently, all pixels $(x, z)$ are to be moved within each row according to

$$\begin{aligned}
&x \to x - R - \sqrt{R^2 - r^2} && \text{if } R < 0 \text{ and } r < r_{core} \\
&x \to x - R - \sqrt{R^2 - r_{core}^2} && \text{if } R < 0 \text{ and } r > r_{core} \\
&x \to x + \sqrt{R^2 - r^2} - \sqrt{R^2 - r_{core}^2} && \text{if } R > 0 \text{ and } r < r_{core} \\
&x \to x && \text{if } R > 0 \text{ and } r > r_{core}
\end{aligned} \qquad (4.19)$$

Second, the intensity decay has to conserve energy along increasing distance from the fibre surface. Therefore, in the images of Figure 4.16, each column of pixels has been recalibrated to have the same total intensity. This transformation slightly reduces the ripple effect observed at short distances from the fibre end, which results from discretization in the calculation of the angles. The result of this recalibration is exhibited in Figure 4.16.b. This transformation is also used later to calculate the coupling efficiencies between an emitting fibre and an 'ideal' receiving fibre, which has a flat fibre surface, the same dimensions and the same numerical aperture as the emitting fibre.

Third, a transformation is used to generate images that can be directly compared to those observed through the objective of a microscope. Therefore, it is necessary to

generate a cylindrically symmetric three-dimensional (3D) distribution of emission intensities by rotation of the 2D distribution in Figure 4.16.b around the center axis, *I(r,ρ,x)*, followed by an Abel transformation, which is a projection on the detection plane (Figure 4.16 c)[28]

$$\begin{aligned} I(x,z) &= 2\int_{z}^{\infty}\int_{0}^{2\pi} I(r,\rho,x)\frac{r}{\sqrt{r^2-z^2}}\,d\rho\,dr \\ &= 4\pi\int_{z}^{\infty} I(r,x)\frac{r}{\sqrt{r^2-z^2}}\,dr \end{aligned} \tag{4.20}$$

The results of these transformations for the case of a concave lens with $R$ = -75 μm are shown in Figure 4.16.

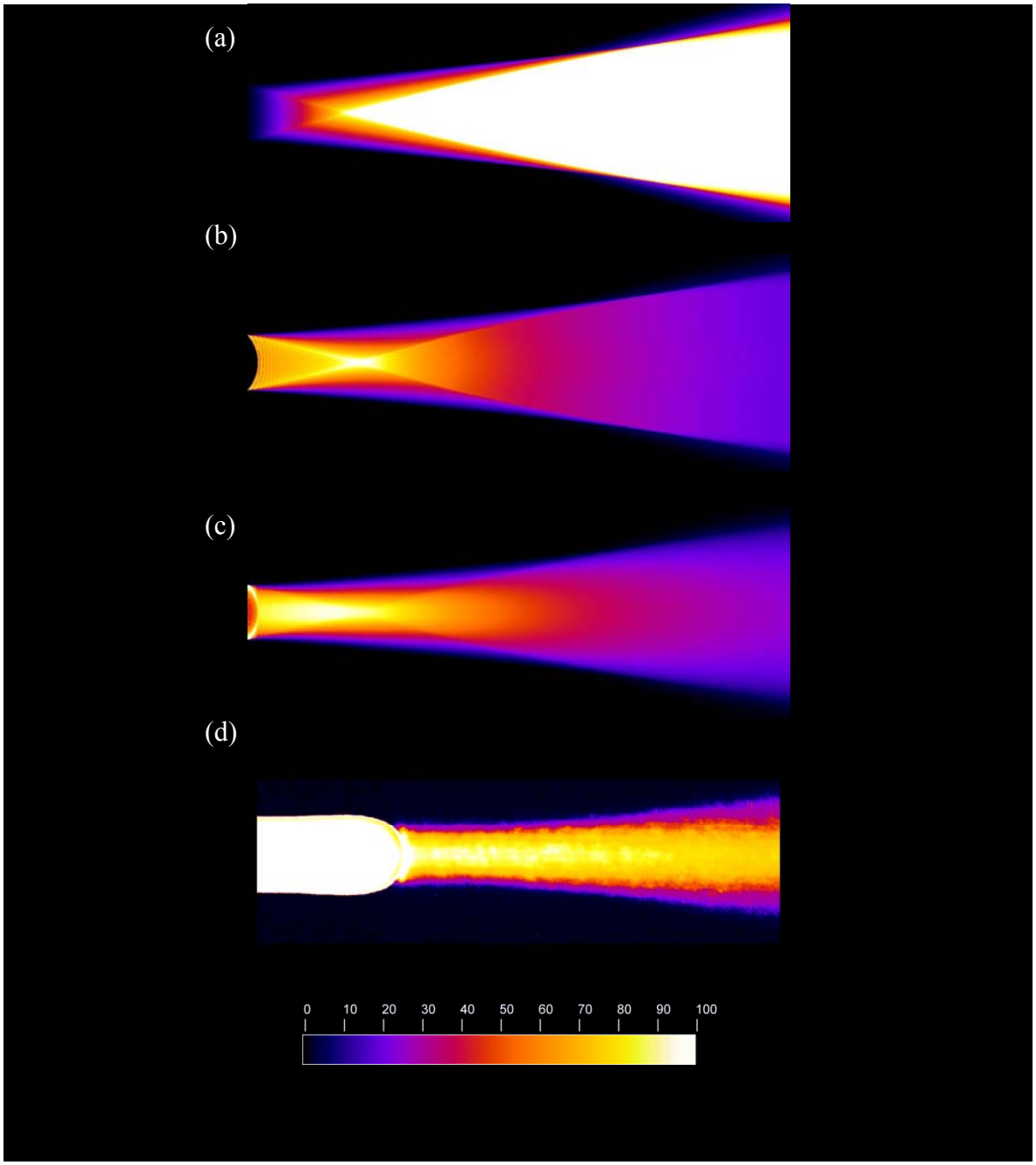


Figure 4.16. Fibre lens emission cones with a fibre lens radius $R$ = 75 µm in water ($n$ = 1.33). In this and all other images, the intensity is colour coded for the purpose of producing a false colour image. The simulation window is 0.4 mm high and 1.0 mm long. The fibre core diameter is 100 µm, $NA$ = 0.22, $n_{clad}$ = 1.433. (a) As calculated from Equation 4.12, (b) after normalization and translation to include the here simulated convex lens, (c) after Abel transform of (b). Ripples at short distance from the fibre lens are a discretization artifact of the simulation. (d) Experimental data on the same scale, recorded using a microscope and adapted from the M.Sc. thesis of Mr. Trefiak[22].

In Figure 4.17, a concave lens emitting into diverse media, ranging from air ($RI = 1.0$) to sapphire ($RI = 1.77$) is displayed. The lens is diverging in air and in ethanol and it is converging in DMSO, and in other media with $n_0 > 1.45$.

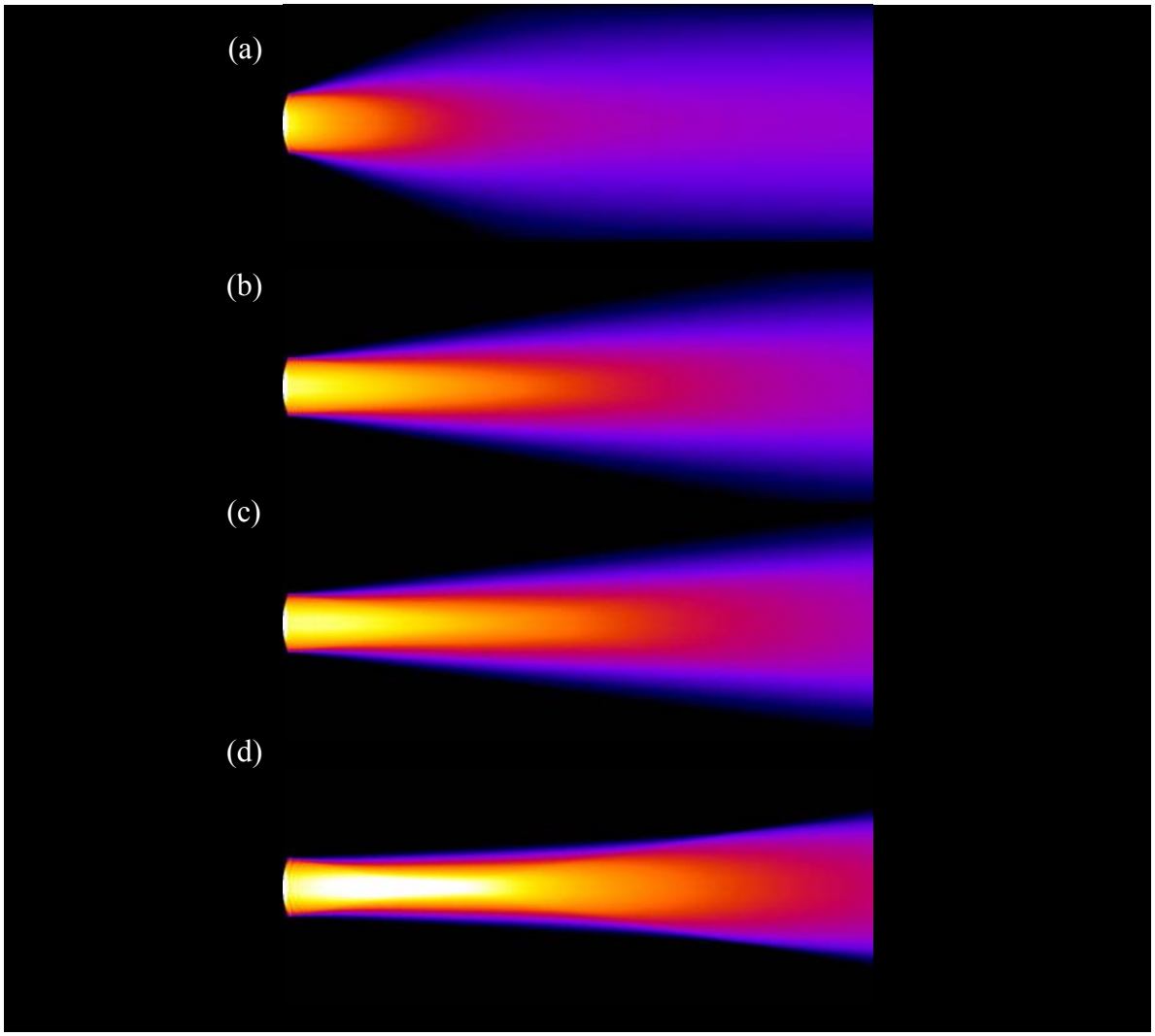


Figure 4.17. Simulated emission from a fibre lens with $NA$ = 0.2, $R$ = -150 µm, $r_0$ = 50 µm, $n_{clad}$ = 1.433. The refractive indices of the media that the light is emitted into are (a) $n_0$ = 1.0 (air), (b) $n_0$ = 1.365 (ethanol), (c) $n_0$ = 1.4785 (DMSO), and (d) $n_0$ = 1.77 (sapphire). The figure shows the Abel transformed image.

As mentioned above, the 2D representation (cf. Figure 4.16.b) is used to calculate the maximal coupling efficiency between one lensed fibre and another flat fibre with

identical numerical aperture and geometry, as a function of distance between the lens and the receiving fibre end. Figure 4.18 shows the coupling efficiency of lenses with radii from $R$ = -60 μm to $R$ = +60 μm (concave and convex lenses, respectively). The media used for these calculations have a refractive index of $n$ = 1.0, 1.33, 1.48 and 1.77, corresponding approximately to air, water, DMSO and sapphire, respectively. For the calculation, it was assumed that there are no other losses except geometric coupling losses and so the considerable effect of scattering and Fresnel reflection at the fibre lens surface were neglected.

Comparison of the coupling efficiencies with earlier experimental data is particularly instructive and also convenient, since the data reported in Figure 4.18 scale linearly with the dimensions of the system. Thus, the coupling efficiency of a 400 μm core diameter waveguide over a 4 mm distance follows the same curve as the 100 μm diameter waveguide over 1 mm, that is presented in these simulations.

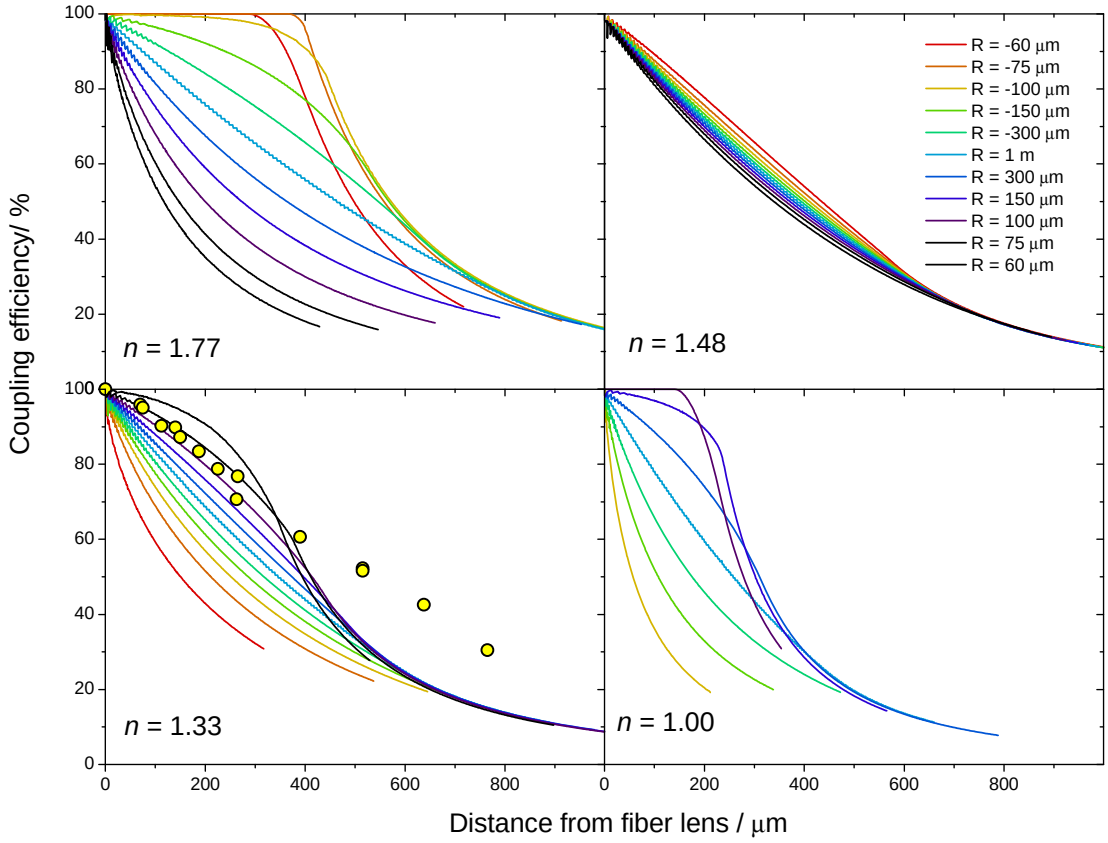


Figure 4.18. Coupling efficiencies of the fibre lens with radii between $R$ = -60 µm and +60 µm, in media with different refractive indices. The fibre core diameter is 100 µm, $NA$ = 0.22, $n_{clad}$ = 1.433. The circles in the bottom left panel have been obtained by re-analysis of the ring-down times recorded from a convex lens with an approximately 75 µm radius emitting into water[24].

### 4.2.5.2. Construction of a Simple Lensing Device

This section describes the construction of a simple device used to manufacture a concave lens at a ferruled fibre end. The device consists of three parts. The first part is used to hold the ferrule in place and connect it to an oscillatory motor. In our experiments an electric toothbrush motor (*Braun Vitality*) was used, as the oscillatory movement is needed

to avoid tangling up the fibre, connecting the ferrule with the coupler used in our system, which would occur if the ferrule was simply rotated. A technical drawing is displayed in Figure 4.19.

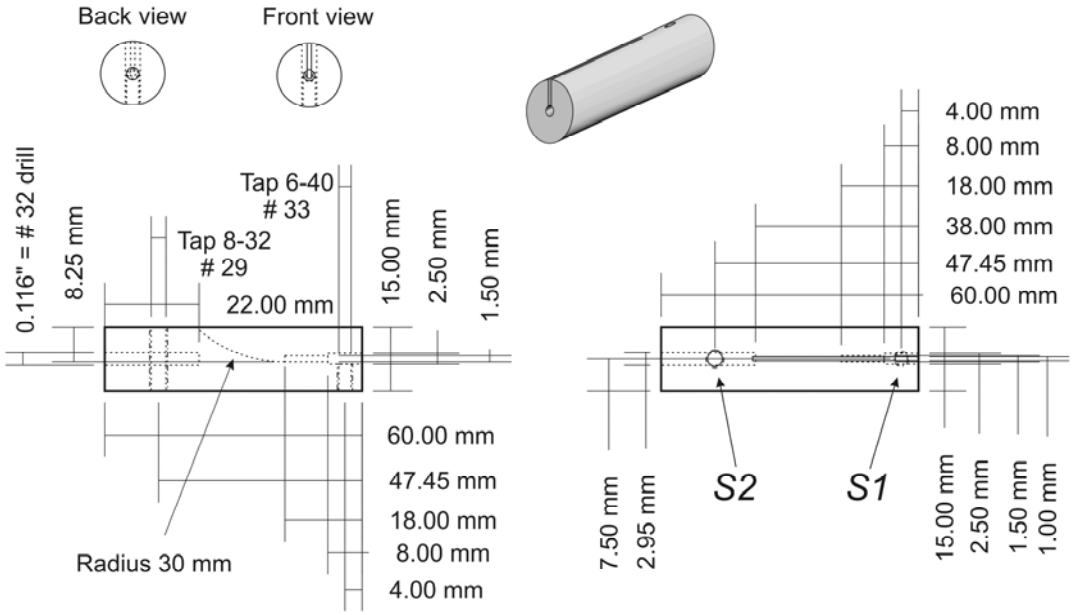


Figure 4.19. Technical drawing of the ferrule holder for the production of concave lenses. The oscillatory motor is connected at the back of the holder but is not included in the drawing. All measurements are given in mm unless otherwise stated. *S1* and *S2* denote the two set screws to hold the fibre ferrule and the motor axis respectively.

The second part aligns the template with the fibre and it also allows the ferrule holder to spin and a lapping paper to be placed between the fibre and the template. Figure 4.20 shows a technical drawing of this second part.

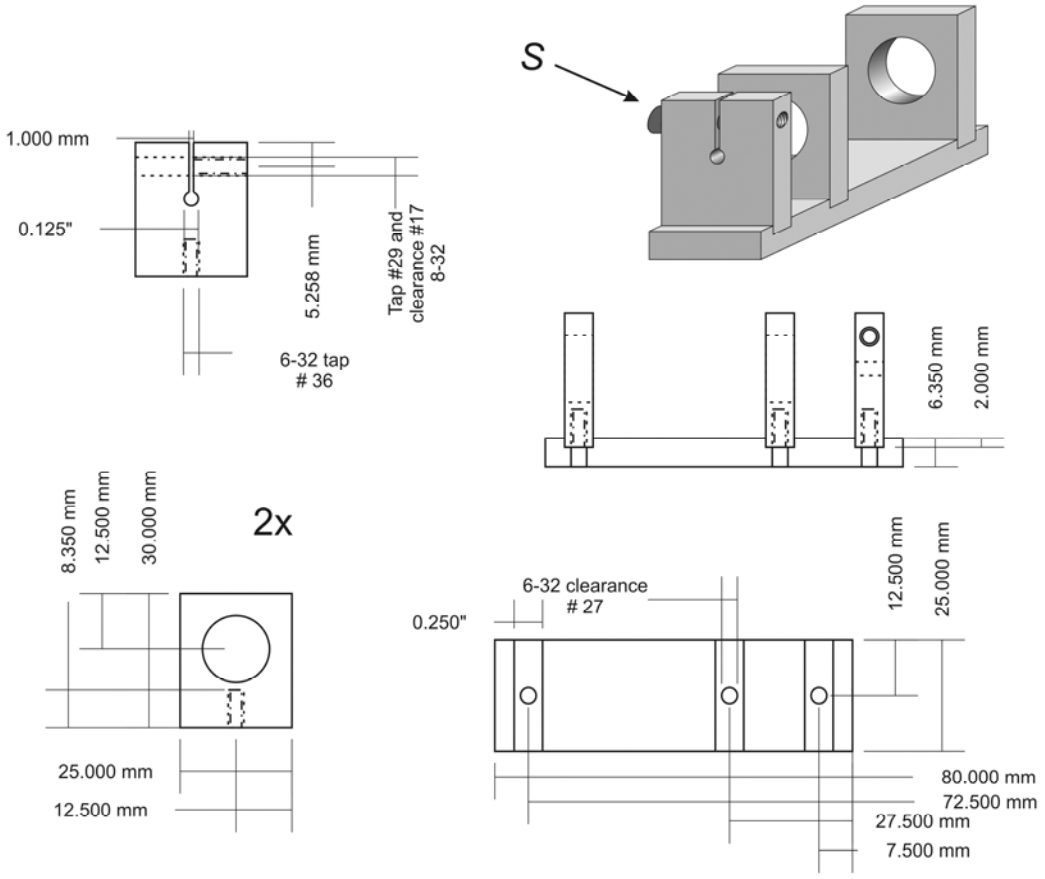


Figure 4.20. Alignment stage for ferrule holder and ruby template. The ferrule holder (part 1) fits through the two bigger holes with a tight fit but enough clearance to spin freely. The two big holes and the small hole in the front, which houses the interchangeable template (part 3), are carefully aligned in X and Y direction. *S* denotes the screw that fixes the template in place.

The third but most important part is a template that sets the radius of curvature of the lens. It was manufactured from a stainless steel fibre ferrule (*Precision Fibre Products - MM-CON2003-SS-1260*) and a microsphere that was glued in place. The original hole in the stainless steel ferrule (Ø 126 µm) was manually opened with different micro-drills for setting the correct depth and diameter for the respective spheres. The ruby sphere had a radius of 150 µm. The radius of curvature of the lens produced with this template was estimated to be very close to the radius of the ruby. Besides the ruby template, two other

templates with sapphires were also manufactured with radii of 175 µm and of 250 µm. The microspheres were commercially available (*Smallparts.com* – but note that these sapphire spheres are no longer available from this supplier). Pictures of these templates are presented in Figure 4.21.

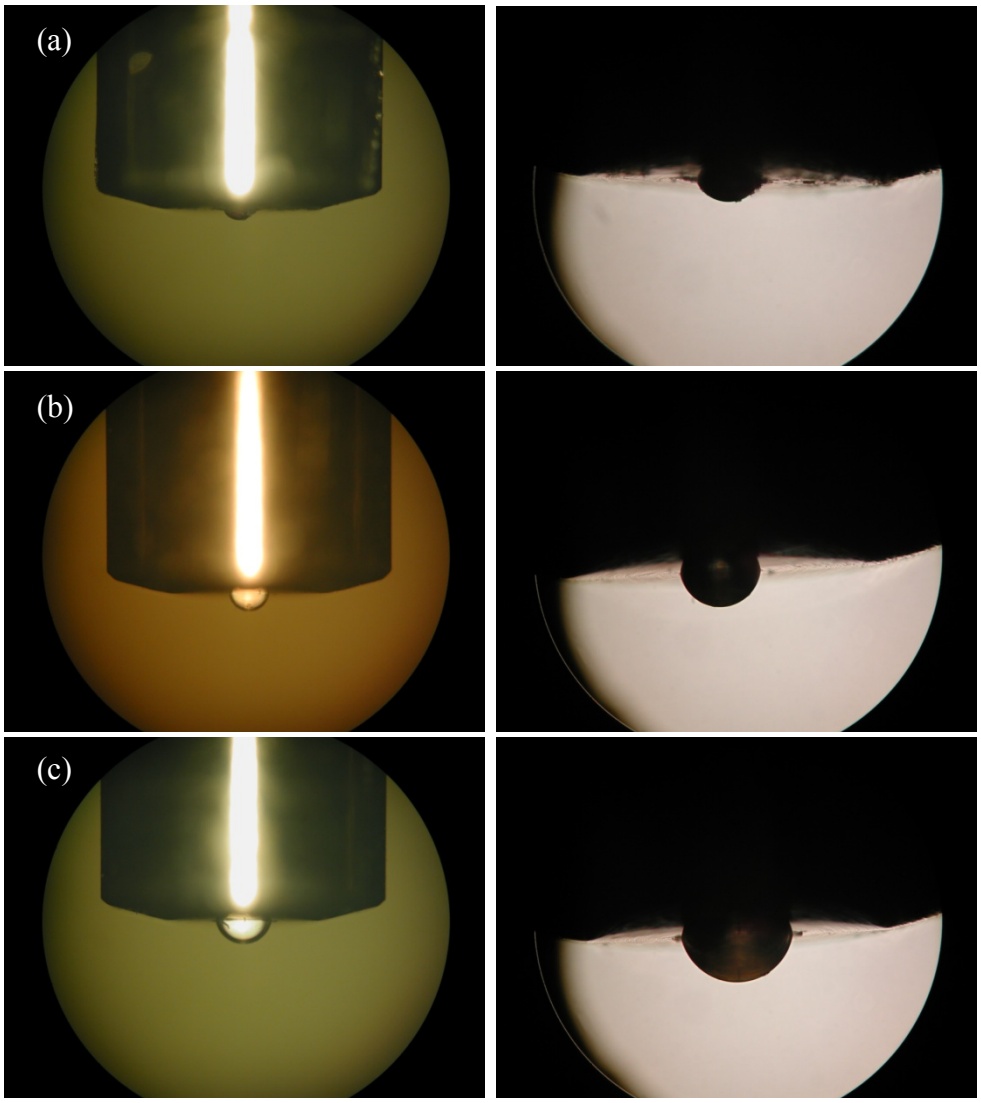


Figure 4.21. Pictures of the templates for concave lens production of a ferruled fibre under a microscope. The left images were recorded at a magnification of 5x with illumination from the top, while the right images were recorded at a magnification of 10x with illumination from the back. (a) Ruby template used with a radius of 150 µm, (b) the smaller sapphire template (R = 175 µm), (c) larger sapphire template with a radius of 250 µm.

#### 4.2.5.3. Description of How to Produce a Concave Lens at the Fibre End

After polishing the fibre ferrule to a flat and optical clear surface (as is also done with SMA and FC/PC fibre connectors), the ferrule is placed into the ferrule holder and fixed with the small set screw (cf. Figure 4.19, *S1*). The fibre that sticks out of the ferrule's rear is directed outwards in the appropriate groove and fixed to the ferrule holder body at the end of the groove with a piece of tape. This prevents the fibre from hitting the sides of the groove while oscillating and thereby being damaged or broken. Subsequently, the ferrule holder is now connected to the oscillatory motor and fixed with the set screw (cf. Figure 4.19, *S2*). The alignment device is fixed in a vise for stability and the appropriate template is set in place and fixed with the screw on top of the device (cf. Figure 4.20, *S*). With that, all preparations are completed and manufacturing of the concave lens can begin.

The ferrule holder (part 1) is inserted through the holes designed for it in the alignment stage (part 2) with one hand and a lapping paper (*aluminium oxide 0.3 µm – Fiber Optic Center Inc.*) is held in between the template and the fibre ferrule with the other hand. After switching on the motor, the ferrule is slowly pressed against the lapping paper, which conforms to the shape of the template. The lapping paper is slowly pulled out, so that the ferrule comes into contact with unused parts of the lapping paper bit by bit. It is necessary to make sure that there is lapping paper between the template and the ferrule at all times, in order to avoid damage to the fibre. No water is needed for this polishing process. The ferrule may be pulled away from the template to reposition the lapping paper if needed. Lapping paper that was used for manual polishing before can be reused in this process, since the rim (width of 1-2 cm) of the lapping paper is usually not used in normal

polishing, but here, the inside of the lapping paper is inaccessible due to the geometries of the alignment stage. After about 1 minute, the motor has to be stopped and the ferrule can be inspected with an eye loupe or, if taken out of the ferrule holder, with a fibre inspection scope (*Thorlabs CL-200*). From a side view, the dip of the fibre ferrule should be clearly visible, but inspecting the fibre with an inspection scope should also reveal no cracks or other imperfections. A reliable way to check for cracks in the fibre is to illuminate the fibre end from the back and simultaneously look at it through the fibre inspection scope without turning the internal light of the scope on.

SEM pictures of a concave fibre lens are shown in Figure 4.22. In the picture, taken with the lowest possible magnification, a small dip in the center of the ferrule is noticeable. Unfortunately, a better picture of the concave shape of the lens is not possible in the SEM picture because of the limited possibilities to tilt of the sample within the instrument.

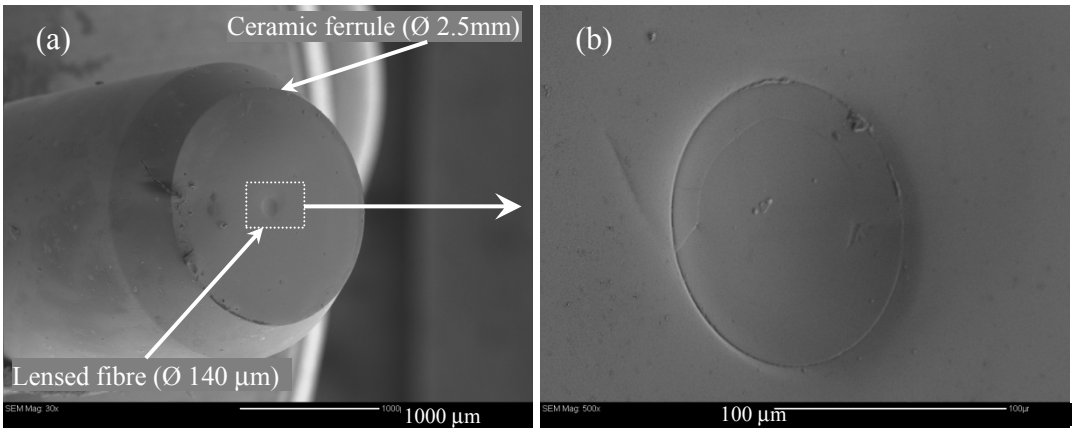


Figure 4.22. SEM pictures of the concave lens at the fibre ferrule. (a) At a magnification of only 30x, the front facet of the ferrule is visible. In the middle, the fibre end appears to be dipped inwards, as it is expected from a concave lens. The ferrule has been tilted by the maximum of 38° for this picture. The concave lens would be more visible at a higher tilt angle, but it is not possible to produce such a picture with the SEM used. (b) At a magnification of 500x, again with the maximum tilt possible, the concave shape of the fibre end is much more evident.

#### 4.2.5.4. Experimental Imaging of Light Distribution Emitted from a Concave Lensed Fibre

In order to examine the validity of our simulation, light from a 532 nm *cw*-laser was diffused using a thin sheet of paper, to emulate a Lambertian source, and was then coupled into a multimode fibre (core diameter 100 µm, cladding diameter 140 µm). This fibre was submersed in a petri dish containing solutions of a fluorescent dye (*Eosin Y*; *BASF*, Germany; used as supplied) in DMSO (*Carl Roth*; used without further purification) or in basic ethanol (96%, *Carl Roth*; used without further purification). The fluorescence emissions from flat and concave fibre ends ($R$ = -150 µm) were imaged using a microscope (Axio Imager.M2m with EC Epiplan-Neofluar 5× objective, *Carl Zeiss MicroImaging*,

Germany). The images were recorded in 8-bit linear gray scale and processed with Image-J software (W. Rasband, *National Institute of Health*, USA).

Figure 4.19 shows microscope images of the respective fibre lens emission for a flat (simulated as $R$ = 1 m) and concave ($R$ = - 150 μm) lens in DMSO (top) and ethanol (bottom). In each panel, the corresponding simulation is on top and the experimental image on the bottom. Furthermore, the emissions of the lensed fibre have been rotated by 180˚ to make long range comparison easier.[c]

[c] *Note: The author thanks Ms. Dorit Munzke, a collaborator with the University of Potsdam, Germany, who performed the above described experiment and produced the experimental pictures of the light output from the lensed fibre.*

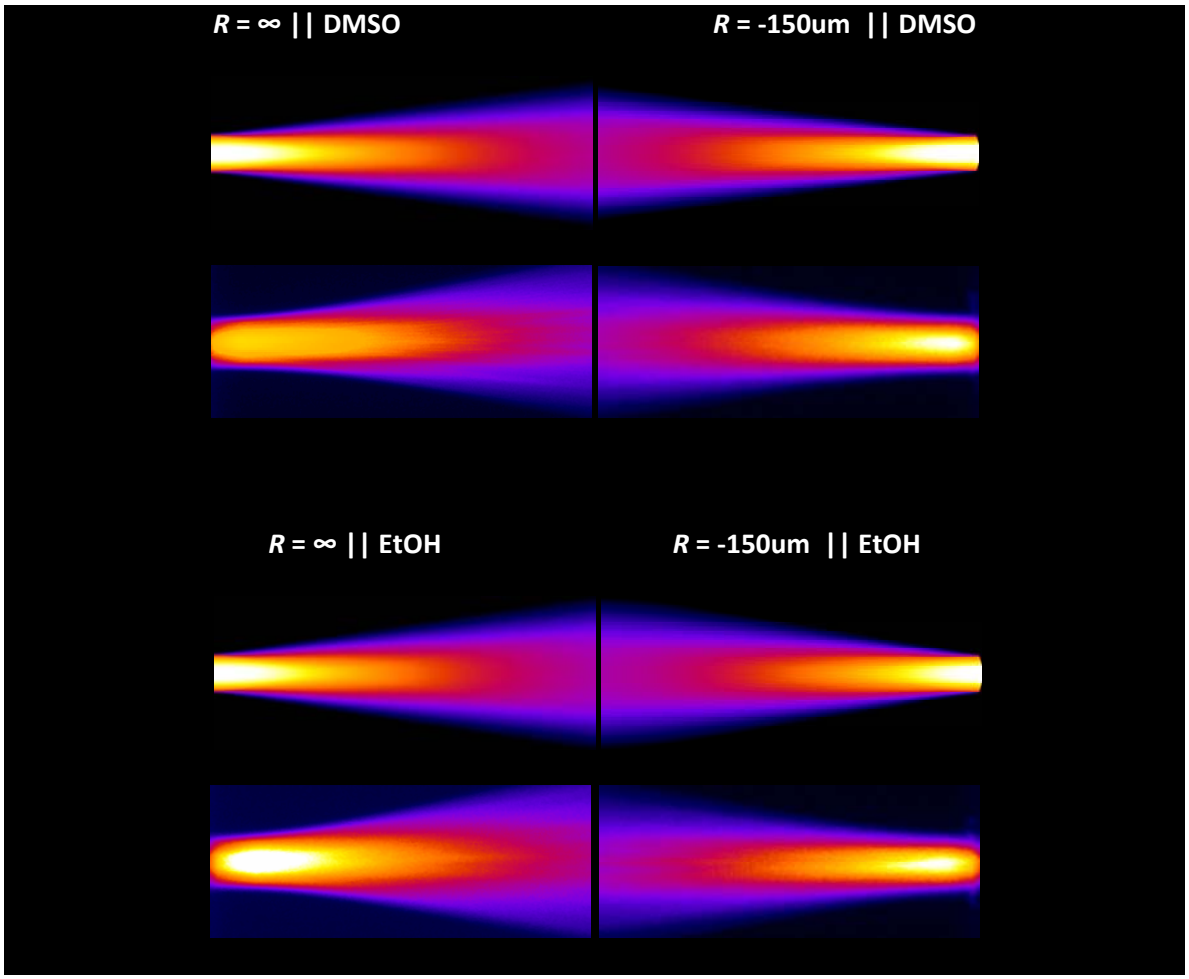


Figure 4.23. Fibre lens emission with a flat fibre end (simulated as $R$ = 1 m) (left side of figure), with $R$ = -150 µm (right side of figure), in pure DMSO (top of the figure) and in pure ethanol (bottom of the figure). The simulation and also experimentally recorded window is 0.4 mm high and 1.0 mm long. The fibre core diameter was 100 µm, $NA$ = 0.22, $n_{clad}$ = 1.433. In each group, the simulation is shown on top and the experimental image on the bottom. Furthermore, the images for the lensed fibre in both media have been rotated by 180˚ to make long range comparison easier.

In general, the experimental data agrees very well with the above calculated images, but, in comparison with the flat fibre end, the focussing effect of the concave fibre lens is very small in both solvents. The divergence of the experimental beam in the case of ethanol imaged with a lensed fibre seems to be less than with the flat end fibre, which is likely an artifact due to failure to normalize the overall intensity in the two experimental

pictures. Concave fibre lenses with a radius of 150 μm were fabricated onto the emitting and receiving fibre-loop ends to increase the transmission into and out of the LCW.

## 4.3. Conclusion

In this chapter, it has been demonstrated how crucial finding the correct matrix solvent is. DMSO has been found suitable for our purposes here, for its refractive index, the transparency in the visible region, the ease of handling, and its low price. Experiments were performed to see whether matching of the numerical aperture of the waveguides is necessary. It has been concluded that the numerical apertures of the fibre and of the LCW should be similar ($NA_{fibre} = 0.22$ and $NA_{LCW} = 0.29$, which is within 30% of each other) but not be matched perfectly, which allowed us to use pure degassed DMSO as a matrix liquid.

However, for an optimized system, the geometries of the LCW and of the fibre should be matched as closely as possible. Furthermore, it has been shown that for non-lensed waveguides, the coupling between the fibre and the LCW depends mainly on the mode overlap and that the combination of matching cladding diameters and unmatched core geometries is to be preferred to non-matching dimensions.

Additionally, the surface quality of the receiving waveguide end has been closely examined. Chipped off glass pieces, especially at the inner rim of the capillary, introduce scattering losses and should be minimized or completely avoided.

Finally, a new method of producing concave fibre lenses has been devised and discussed extensively. Concave fibre lenses collimate light when submersed in high refractive index materials, like DMSO, and are beneficial for CRDS measurements. Although the focussing effect in DMSO is fairly small, a transmission of a few percent more considerably increases the ring-down time in CRDS, thanks to the multi-pass nature of the technique. Data for the effect of lenses on the transmission will be shown and discussed in Chapter 5.

To optimize fibre-loop ring-down setups with incorporated liquid core waveguides, care should be taken on geometrical matching of the waveguides, as well as on matching the numerical apertures. Optically clean surfaces with no scattering centers and concave lenses should be used for coupling from a fibre into an LCW and back, and a suitable combination of LCW material and matrix liquid has to be found for the particular desired application.

## 4.4. References

1. DuPont Fluoroproducts , Teflon AF Amorohous Fluoropolymers H-16577-1. DuPont: Wilmington, DE 19880-0711, USA.

2. Schmidt, H.; Hawkins, A. R., Optofluidic waveguides: I. Concepts and implementations. *Microfluidics and Nanofluidics* 2008, 4, 3-16.

3. Hawkins, A. R.; Schmidt, H., Optofluidic waveguides: II. Fabrication and structures. *Microfluidics and Nanofluidics* 2008, 4, 17-32.

4. Rowland, K. J.; Afshar, V. S.; Stolyarov, A.; Fink, Y.; Monro, T. M., Bragg waveguides with low-index liquid cores. *Optics Express* 2012, 20, 48-62.

5. Jensen, J. B.; Pedersen, L. H.; Hoiby, P. E.; Nielsen, L. B.; Hansen, T. P.; Folkenberg, J. R.; Riishede, J.; Noordegraaf, D.; Nielsen, K.; Carlsen, A.; Bjarklev, A., Photonic crystal fiber based evanescent-wave sensor for detection of biomolecules in aqueous solutions. *Optics Letters* 2004, 29, 1974-1976.

6. Malinin, A. V.; Zanishevskaja, A. A.; Tuchin, V. V.; Skibina, Y. S.; Silokhin, I. Y., Photonic crystal fibers for food quality analysis. In *Biophotonics: Photonic Solutions for Better Health Care Iii*, Popp, J.; Drexler, W.; Tuchin, V. V.; Matthews, D. L., Eds. Spie-Int Soc Optical Engineering: Bellingham, 2012; Vol. 8427.

7. Eftekhari, F.; Irizar, J.; Hulbert, L.; Helmy, A. S., A comparative study of Raman enhancement in capillaries. *Journal of Applied Physics* 2011, 109.

8. Han, Y.; Oo, M. K. K.; Sukhishvili, S.; Du, H., Photonic Crystal Fiber as an Optofluidic Platform for Surface-Enhanced Raman Scattering. In *2nd Workshop on Specialty Optical Fibers and Their Applications Wsof-2*, HernandezCordero, J.; TorresGomez, I.; Mendez, A., Eds. Spie-Int Soc Optical Engineering: Bellingham, 2010; Vol. 7839.

9. Smolka, S.; Barth, M.; Benson, O., Highly efficient fluorescence sensing with hollow core photonic crystal fibers. *Optics Express* 2007, 15, 12783-12791.

10. Sun, Y.; Kwok, Y. C.; Nguyen, N. T., Faster and improved microchip electrophoresis using a capillary bundle. *Electrophoresis* 2007, 28, 4765-4768.

11. Duguay, M. A.; Kokubun, Y.; Koch, T. L.; Pfeiffer, L., Antiresonant Reflecting Optical Wave-Guides in SiO2-Si Multilayer Structures. *Applied Physics Letters* 1986, 49, 13-15.

12. Schmidt, H.; Yin, D. L.; Deamer, D. W.; Barber, J. P.; Hawkins, A. R., Integrated ARROW waveguides for gas/liquid sensing. In *Nanoengineering: Fabrication, Properties, Optics, and Devices*, Dobisz, E. A.; Eldada, L. A., Eds. Spie-Int Soc Optical Engineering: Bellingham, 2004; Vol. 5515, pp 67-80.

13. Yin, D.; Schmidt, H.; Barber, J. P.; Hawkins, A. R., Integrated ARROW waveguides with hollow cores. *Optics Express* 2004, 12, 2710-2715.

14. Yin, D. L.; Deamer, D. W.; Schmidt, H.; Barber, J. P.; Hawkins, A. R., Single-molecule detection sensitivity using planar integrated optics on a chip. *Optics Letters* 2006, 31, 2136-2138.

15. Jenkins, M. H.; Phillips, B. S.; Zhao, Y.; Holmes, M. R.; Schmidt, H.; Hawkins, A. R., Optical characterization of optofluidic waveguides using scattered light imaging. *Optics Communications* 2011, 284, 3980-3982.

16. Measor, P.; Seballos, L.; Yin, D. L.; Zhang, J. Z.; Lunt, E. J.; Hawkins, A. R.; Schmidt, H., On-chip surface-enhanced Raman scattering detection using integrated liquid-core waveguides. *Applied Physics Letters* 2007, 90.

17. Tao, S. Q.; Gong, S. D.; Fanguy, J. C.; Hu, X. M., The application of a light guiding flexible tubular waveguide in evanescent wave absorption optical sensing. *Sensors and Actuators B-Chemical* 2007, 120, 724-731.

18. Mohammed, W. S.; Mehta, A.; Johnson, E. G., Wavelength tunable fiber lens based on multimode interference. *Journal of Lightwave Technology* 2004, 22, 469-477.

19. Hynes, A. J.; Wine, P. H., The atmospheric chemistry of dimethylsulfoxide (DMSO) and mechanism of the OH+DMSO reaction. *Journal of Atmospheric Chemistry* 1996, 24, 23-37.

20. Saleh, B. E. A.; Teich, M. C., *Fundamentals of Photonics*. John Wiley & Sons: Hoboken, New Jersey, 2007.

21. Optical Fiber Tutorial. http://www.fiberoptics4sale.com/Merchant2/optical-fiber.php (accessed 09.10.2012).

22. Trefiak; Ronald, N. Ringdown spectroscopy in optical waveguides. Master of Science, Queen's University, Kingston, 2007.

23. Tong, Z. Fiber-Loop Ring-Down Spectroscopy. Dissertation, Queen's University, 2004.

24. Waechter, H.; Munzke, D.; Jang, A.; Loock, H.-P., Simultaneous and Continuous Multiple Wavelength Absorption Spectroscopy on Nanoliter Volumes Based on Frequency-Division Multiplexing Fiber-Loop Cavity Ring-Down Spectroscopy. *Analytical Chemistry* 2011, 83, 2719-2725.

25. Waterbury, R. D.; Yao, W. S.; Byrne, R. H., Long pathlength absorbance spectroscopy: trace analysis of Fe(II) using a 4.5m liquid core waveguide. *Analytica Chimica Acta* 1997, 357, 99-102.

26. Fujiwara, K.; Kagoshima, T.; Uchida, T.; Miyakawa, T., Fluorometric characteristics of a wave-guide cell with low refractive index. *Spectroscopy Letters* 2003, 36, 551-560.

27. Loock, H.-P., Ring-down absorption spectroscopy for analytical microdevices. *Trac-Trends in Analytical Chemistry* 2006, 25, 655-664.

28. Munzke, D.; Saunders, J.; Omrani, H.; Reich, O.; Loock, H.-P., Modeling of fiber-optic fluorescence probes for strongly absorbing samples. *Applied Optics* 2012, 51, 9.

29. Bescherer, K.; Munzke, D.; Reich, O.; Loock, H.-P., Fabrication and modeling of multimode fiber lenses. *Applied Optics* 2013, 52, B40-B45.

# Chapter 5.

# Use of Liquid Core Waveguides for Determining Nanomolar Concentrations of Model Dyes

## 5.1. Introduction

In the previous chapter we explored different optical schemes to couple light from a multimode fibre optic cable into an LCW and back into the fibre and found (1) that concave fibre lenses may help reduce coupling losses (2) the diameter of the cores of LCW and fibre has to be as similar as possible and (3) that the matrix liquid has to have a refractive index considerably higher than 1.45 for use with silica capillaries. In this chapter we implement the optimized detection scheme and inject model dyes to determine the limit of detection, response time, and repeatability of such measurements.

Two model dyes, *Allura Red AC* and *Congo Red*, were chosen since their absorption profile overlaps well with the laser emission at 532 nm and their solubility is high in DMSO, the preferred LCW matrix liquid. Both dyes have a strong absorption at around 532 nm in DMSO (maximum at: *Allura Red AC*: 516 nm (measured), *Congo Red*[1]: 532 nm). *Allura Red AC* is a common food dye and widely used in energy drinks and candy. It is usually referred to as *FD&C Red No 40*. *Congo Red* was widely used in staining biological samples but the biological industries of some countries have abandoned it, due to its teratogenic nature.[2, 3]

## 5.2. Theory on How to Determine Sample Absorption from Ring-Down Measurements

In Chapter 1 the general aspects of measuring absorbance with CRDS are given. To simplify the comparison between different absorption spectrometers a wavelength-dependent attenuation coefficient, $\alpha^{\lambda}$, is introduced. This is related to the natural logarithm of the transmission in the setup (cf. Chapter 1 Equation 1.6), according to the following equation:

$$-lnT^{\lambda} = \alpha^{\lambda} d = \alpha_e^{\lambda} C d \tag{5.1}$$

The above equation also shows the analogy to Beer-Lambert's law.

For simplicity, the index, $\lambda$, showing a wavelength dependency of the variable, is no longer indicated from here on. The two extinction coefficients of the attenuation in cavity ring-down spectroscopy, $\alpha_e$, and molar extinction coefficient used in Beer-Lambert's law, ε, are related to each other as follows:

$$\alpha_e = \varepsilon * ln10 \tag{5.2}$$

As mentioned previously, in cavity ring-down spectroscopy the decay rate of light within an optical cavity is measured. The ring-down time is related to the transmission of the cavity and the round trip time, as shown in Equation 1.6. By reason of the different refractive indices of our chosen liquid core waveguide and our fibre-loop material, the round trip time of Equation 1.4 has to be expressed as:

$$t_{RT} = \frac{n_{fibre}L_{fibre}+n_{LCW}L_{LCW}}{c_0} \quad (5.3)$$

The transmission of the cavity, $T_{cavity}$, is dependent on all the losses which the light encounters in the cavity. These losses can be divided in constant losses, for example, fibre attenuation losses, losses at splices and gaps, and losses in couplers, and sample specific losses that may change with concentration, which can be quantified by Beer-Lambert's law (cf. Chapter 1 Equation 1.1). To extract only sample specific losses, the ring-down time with sample, $\tau$, and without sample, $\tau_0$, can be related to each other and the sample concentration can be calculated. For this, the absorption of the sample can be determined by multiplying the difference of the inverse ring-down times with the round trip time according to Equation 5.4. Here, the absorption , $A_e$, is expressed with respect to base-*e*:

$$\left(\frac{1}{\tau}-\frac{1}{\tau_0}\right)t_{RT} = A_e = \alpha_e Cd = \varepsilon Cd * \ln 10 \quad (5.4)$$

A common method to reduce the limit of detection is elongating the path length for the interaction between sample and light. The method of our choice for this is to use a liquid core waveguide coupled into a fibre-loop cavity, as merely increasing the gap width of the fibre-loop would introduce too many system-inherent losses.

## 5.3. Experimental Measurement of Model Dye Absorptions

### 5.3.1. *Allura Red AC* Dye

The second harmonic (532 nm) of a Nd:YAG laser (*Spectra Physics Quanta Ray GCR-11*) was coupled into a UV-grade multimode fibre, with a 200 μm core and a 220 μm cladding (*Polymicro FDP200220240*), employing a lens ($f$ = 20 cm). The UV-fibre was then connected to the FC/PC connector of the input end of a 99/1 2x1 multimode (core 100 μm, cladding 140 μm) fibre coupler (*Lightel Technologies* – with fibre from *FiberTech Optica AS100/140IRA*; NA = 0.22), with the use of an SMA/FC adapter. The two remaining ends (99% transmission) are at first connected to each other with the help of two zirconia ferrules for *xy*-alignment, forming a loop with the length of 14.4 m. A PMT was placed at a slight bend of the loop fibre to detect the scattered light proportional to the light travelling in the cavity. A schematic of the setup is shown in Figure 5.1.a. The resulting ring-down trace is shown in Figure 5.1.b.

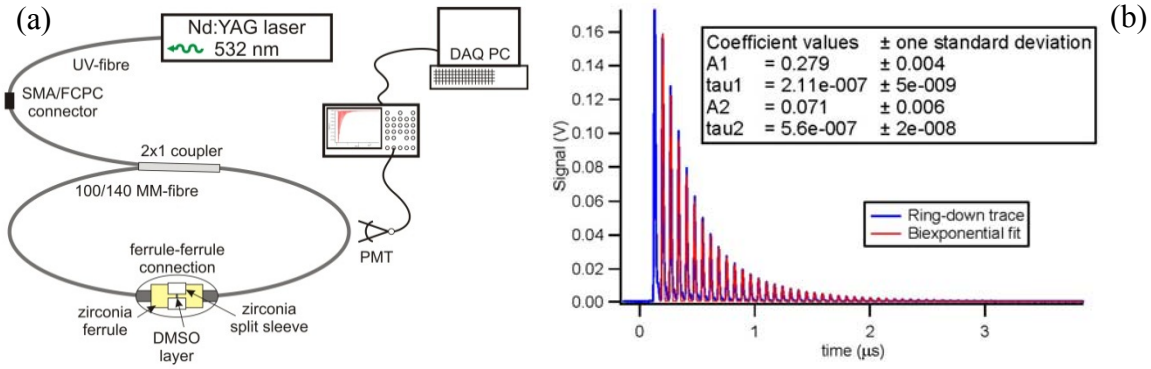


Figure 5.1. Setup used to determine coupling losses in the 14.4 m long fibre-loop setup. (a) Schematic of setup without LCW. A PMT was placed at a slight bend of the loop fibre to detect the scattered light proportional to the light travelling in the cavity. (b) Ring-down trace for fibre-loop only. From the core ring-down time, $\tau_2$, the round trip losses have been calculated to be 11.6% (0.54 dB).

On the fibre ends, which were connected to form a loop, concave lenses were fabricated with the help of lapping papers, an oscillatory ferrule holder, and a ruby template (cf. Chapter 4.2.5). In order to use the lenses to focus or collimate the light a liquid with a $n_{LCW} > n_{fibre}$ was placed in between them (dimethylsulfoxide (DMSO, *Fischer Chemical,* refractive index (RI) 1.4785)). Judging from the bare fibre-loop ring-down trace (Figure 5.1.b), the roundtrip losses are 11.6% (= 0.54 dB) and are due to the coupler (nominal loss 1% = 0.04 dB), the attenuation of the fibre ($a_{fibre}$ = 14 dB/km = 0.003%/cm), one ferrule-ferrule connection (estimated as 5% = 0.22 dB), and insertion losses. Next, a 5 cm long fused silica capillary (*Polymicro TSP100375* $Ø_{ID}$ 100 µm, $Ø_{OD}$ 363 µm, RI = 1.45) was positioned in between the two fibre ends by the help of zirconia ferrules on either side for alignment (cf. schematic setup in Figure 5.2.a). The previously manufactured collimating lenses were kept at the fibre ends to increase the transmission between LCW and fibre (cf. Chapter 4.2.5).

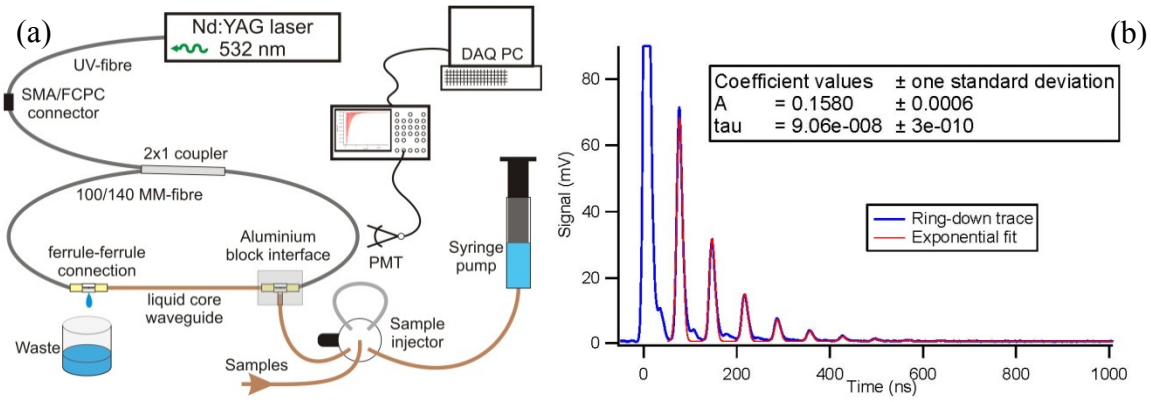


Figure 5.2. LCW-FLRDS setup used to determine model dye absorptions. (a) Schematic setup with LCW. The first connection of fibre and LCW was placed into a homemade aluminium block interface to be able to pump the sample solutions through the system, whereas the second connection was placed over a waste beaker. Sample solutions were prepared beforehand by dissolving and diluting the powdered dye in DMSO. The flow speed was set at the syringe pump to 10 µL/min. (b) Ring-down trace for LCW-fibre-loop. It is evident that the ring-down time has decreased with respect to the bare fibre-loop (Figure 5.1.b) and the losses have increased to 53.9% (= 3.4 dB). The shoulder that is evident in the first couple of peaks of the ring-down trace is an artifact of either the laser or the electronics and has been detected even without the loop cavity present. The first peak has been omitted because of a possible saturation of the detector.

The capillary's actual $Ø_{ID}$ was 101 µm (manufacturer's data), which was very close to the core diameter of the loop fibre (100 µm), but the outer diameter of the capillary differed greatly from the cladding diameter of the used fibre (360 µm vs. 140 µm). The capillary was filled with DMSO. Introducing the LCW filled with pure DMSO decreased the ring-down time from 563 ns to 90 ns (Figure 5.2.b). Samples of *Allura Red AC* (*Sigma Aldrich*, 80% dye content), dissolved in degassed DMSO (used without further purification), were injected into the LCW with a sample injector (*Upchurch Rheodyne 7725*) and a homemade injection block (aluminium block interface, cf. Appendix 1), that housed one of the ferrule-ferrule connections between fibre and capillary. The interaction volume has been calculated from the volume of the LCW, resulting in 400 nL for a 5 cm long capillary. Samples were injected into the LCW as plugs of 20 µL with a flow rate of

10 µL/min, and ring-down traces were recorded on an oscilloscope (*Tektronix DPO3054*) and averaged 16 times. The averaged traces were transferred to a homemade *Visual Basic* (VB) program via USB. An *Igor Pro* function (*WaveMetrics Igor Pro 6.1*) embedded in the VB code fitted the traces on the fly and all fitting parameters have been recorded.

### 5.3.2. *Congo Red* Dye

For the *Congo Red* dye measurements, the same setup as for *Allura Red AC* was used with minor modifications. The light source was changed to an Nd:YAG laser manufactured by Continuum (*Continuum Powerlite Precision 8030*), due to availability in the laboratory, but the coupling scheme stayed the same as in the *Allura Red AC* experiment. Instead of a 5 cm long LCW, a 10.1 cm long fused silica capillary (*Polymicro TSP100375*) was placed in between the two fibre ends. The capillary's actual $Ø_{ID}$ was 99 µm (manufacturer's data). The slight difference in capillary $Ø_{ID}$ decreased the ring-down time after filling with DMSO slightly more than in the previous setup, to 63.5 ns. Samples of *Congo Red* (*The British Drug Houses LTD*), dissolved in degassed DMSO (used without further purification), were injected into the LCW in the same way as described above. The detection volume has been calculated from the volume of the LCW, resulting in 777 nL. Samples were injected into the LCW as plugs of 20 µL or 50 µL with a flow rate of 1 µL/min and averaging of 256 waveforms on the oscilloscope. Data were collected using the same procedure as in the *Allura Red AC* experiment.

## 5.4. Results

### 5.4.1. Measurement of *Allura Red AC* Samples in a 5 cm Liquid Core Waveguide

20 µL injection volumes of sample concentrations of *Allura Red AC* in DMSO, ranging from 1 nM to 1000 nM, were injected and the ring-down time has been recorded. A time scan of the ring-down time of these injections has been recorded and shown in Figure 5.3.

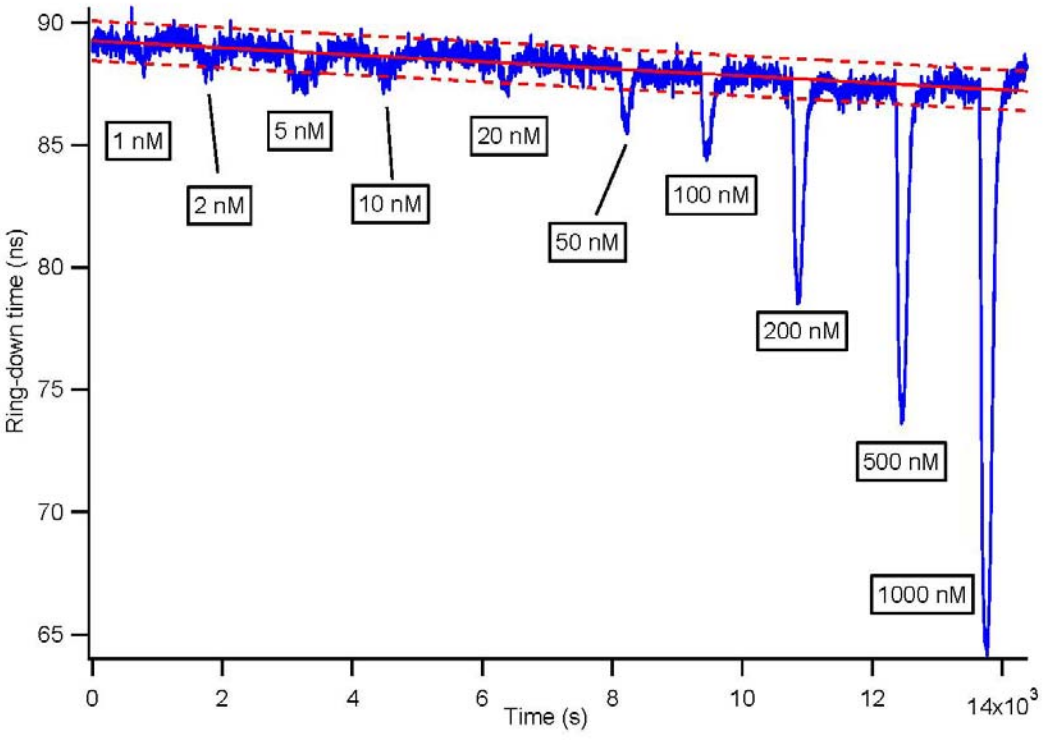


Figure 5.3. Time-dependent recording of the ring-down time for different sample injections, ranging from 1 nM to 1000 nM *Allura Red AC* in DMSO. The red solid line shows the baseline of the system with a slope of -500 ps/h. The red dashed lines represent the ±3σ-baseline level with σ = 0.27 ns.

The ring-down time for the baseline was extracted by averaging 100 baseline points, while the system was only filled with DMSO. The baseline noise could be obtained

by calculating the standard deviation of the baseline and is ±0.27 ns. This baseline standard deviation can be compared with the standard error of the curve fitting procedure. The latter error (typically $\delta\tau$ = 0.3 ns, cf. Figure 5.2.b) is indicative of how well the ring-down transient can be fitted with an exponential decay function, whereas the baseline noise is a measure of how precisely consecutive ring-down times can be measured. These two values do not necessarily have to be the same.[4] In a limiting case, when all other errors are negligible, these errors are identical. "For example, if the loss in the cavity varies with time due to, for example, mechanical perturbations, the baseline noise can be quite large, despite the fact that each of the transients is given by a near perfect exponential function."[5] In the present case, we found that the baseline error is limited by the error of fitting the ring-down trace. This is likely to be a result of the small number of round trips and the fact that cladding mode contributions in the fibre and LCW, which lead to a bi-exponential decay function, are excluded from the fit. This also shows that the setup is remarkably stable. For all the concentrations, Gaussian curves have been fitted to the individual peaks of this trace and the ring-down times have been calculated from the Gaussian peak height. According to Equation 5.4, a plot of the difference between the inverse ring-down times multiplied by the round trip time against concentration yields a straight line, according to Beer-Lambert's law, and is shown in Figure 5.4. The error of the Gaussian peak height has been propagated to obtain the error of the absorption shown as y-error bars. The x-error bars are propagated errors of the dilution series performed to achieve the individual concentrations, having started from neat powder and pure DMSO.

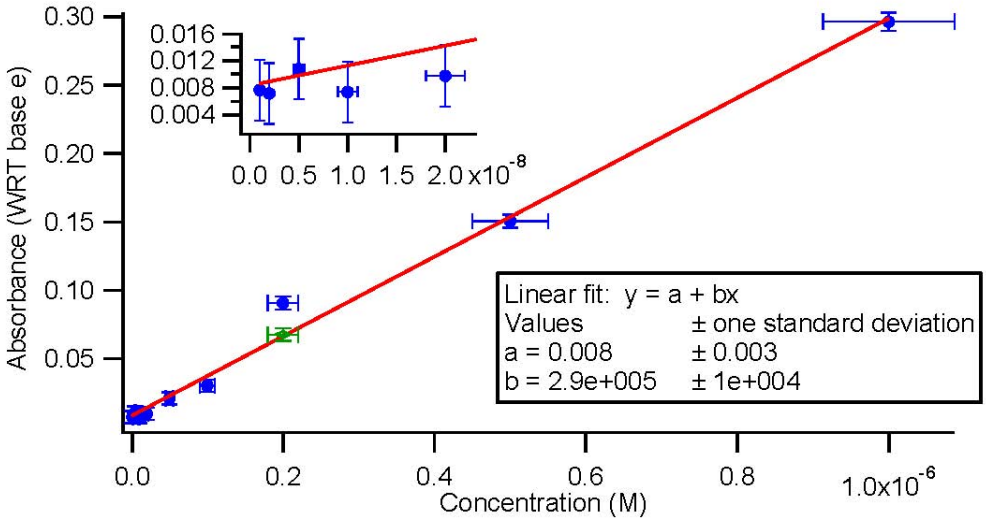


Figure 5.4. Calibration graph of *Allura Red AC*. The absorption has been calculated according to Equation 5.4. The slope of a linear fit (red) gives the attenuation coefficient (based on the natural logarithm) of *Allura Red AC*. The inset shows a zoom into the lower concentrations. The horizontal error bars have been calculated from the errors of the balance (± 0.0001 g), of the pipettors (5% v/v – according to manufacturer's data), and of the volumetric flasks (0.2% v/v) used to make the solutions. Although it seems that the error decreases with decreasing concentration, which is true for the absolute error of the concentration, the relative error of the concentration increases. The vertical error bars have been derived from the fit error of the peak height of Gaussian fits to the individual injection peaks. The green data point is the corrected value of the solution for 200 nM, as calculated from the precision experiment in the following.

One may think that the limit of detection (LOD) can be calculated from this calibration plot as is sometimes done in analytical methodology. By determining the confidence interval of the calibration line[4] and extrapolating it to the concentration of the blank (neat DMSO), one can calculate the respective uncertainty of the signal (here, the absorption term $\left(\frac{1}{\tau}-\frac{1}{\tau_0}\right)t_{RT}$ ). This 'signal uncertainty' corresponds to an LOD of about 60 nM for *Allura Red AC* in DMSO (using the corrected value for 200 nM in the calibration curve). Considering the original time-dependent trace of the ring-down time, the peak for 50 nM, which is lower than the LOD calculated from the calibration curve,

can be clearly distinguished from the baseline, which suggests that the actual LOD is much lower. By calculating the LOD from the calibration curve, one assumes that the sensitivity of the technique is constant. This assumption is not valid in cavity ring-down spectroscopy. In Figure 5.3, it is obvious that the limit of detection at a 3σ signal-to-noise level is 5 nM and the sensitivity of the absorption measurement increases as the concentration is reduced. Improving the instrumental setup, and thus increasing the precision and reducing the baseline noise, would lead to a further improvement of the LOD.

To show the precision of the ring-down signal, a concentration of 200 nM of *Allura Red AC* was injected 10 times into the setup. A real-time measurement of the ring-down time is shown in Figure 5.5.a. The amplitude of a Gaussian function fitted to each injection peak gives the ring-down time difference to the baseline. When the ring-down time change for each injection is plotted, the calculated average ring-down time decrease for this concentration is 7.09 ± 0.13 ns (Figure 5.5.b).

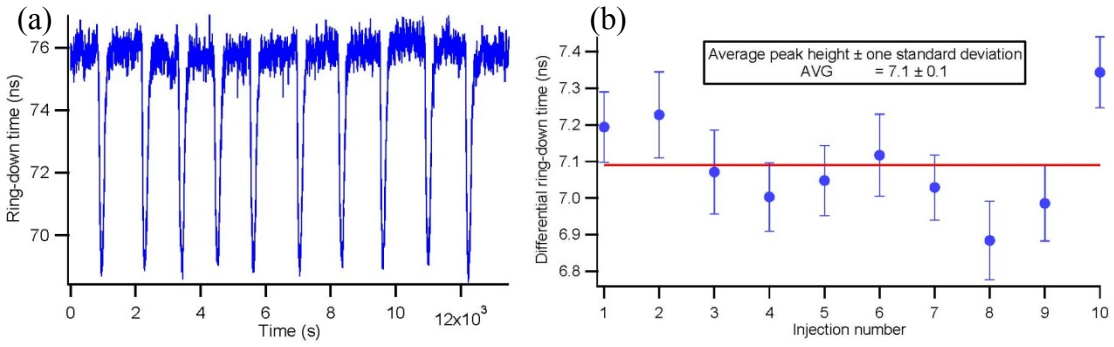


Figure 5.5. Precision experiment using *Allura Red AC*. (a) Time-dependent recording of ring-down time for 10 injections of 100 nM *Allura Red AC*. (b) Differential peak heights in ns resulting in an average of 7.09 ± 0.13 ns.

The precision experiment also shows that the previously measured point for 200 nM *Allura Red AC* in the concentration measurement was outside the confidence interval. A decrease of the ring-down time by 7.09 ns, as opposed to the previously obtained value of 9.25 ns (cf. Figure 5.3), places the measurement point at 200 nM much closer to the calibration curve (green data point in Figure 5.4).

From Figure 5.4, a molecular extinction coefficient with respect to base-*e* can be extracted for *Allura Red AC*, giving $\alpha_e = 5.8 \times 10^4$ $M^{-1}cm^{-1}$. In accordance with Equation 5.2, this results in a molecular extinction coefficient of $\varepsilon = 2.5 \times 10^4$ $M^{-1}cm^{-1}$. For confirmation purposes, the absorption coefficient was determined to be $\varepsilon = 3.0 \times 10^4$ $M^{-1}cm^{-1}$ using a standard UV-Vis spectrometer (*Ocean Optics USB4000*), with the use of a quartz glass cuvette and at a higher concentration range of 10 µM to 50 µM. Since the molar extinction coefficient should not change with concentration, it is assumed that some of the light is bypassing the sample in the wall of the LCW, and is hereby artificially lowering the $\varepsilon Cd$ term. Similar effects have been reported previously by other authors.[6,7] Since this effect is characteristic of the setup, it can be included in the calibration and an appropriate factor should be introduced in the extinction coefficient.

A measurement to prove the reproducibility could not be performed because an obstruction in the 5 cm liquid core waveguide rendered the LCW useless.

### 5.4.2. Measurement of *Congo Red* Samples in a 10 cm Liquid Core Waveguide

20 mL injection volumes of *Congo Red* in DMSO, ranging from 1 nM to 1000 nM, were injected into the setup as described above (cf. Chapter 5.3.2) and the ring-down time has been recorded. The change of the ring-down time caused by these injections is shown in Figure 5.6.

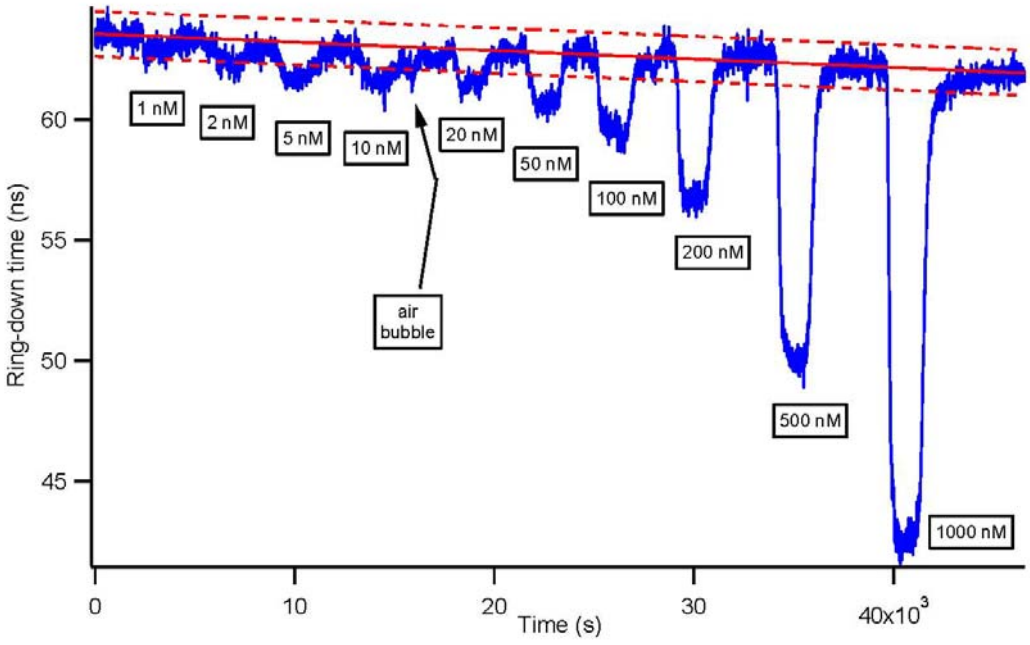


Figure 5.6. Recording of ring-down time change in time for different sample injections of *Congo Red* in DMSO. Concentrations range from 1 nM to 1000 nM. The red solid line shows the baseline of the system with a slope of -130 ps/h. The two dashed lines represent the ±3σ-limit of the baseline noise with σ = 0.31 ns.

The standard deviation of the ring-down time of pure DMSO over 100 measured points is $\sigma = \pm 0.31$ ns.

The ring-down times of the baseline and the concentrations can be extracted by averaging the baseline and the peak plateaus again over 100 points. A calibration graph of

the absorbance, calculated from the difference of the inverse ring-down times multiplied by the round trip time (cf. Equation 5.4), of *Congo Red* in DMSO is shown in Figure 5.7.

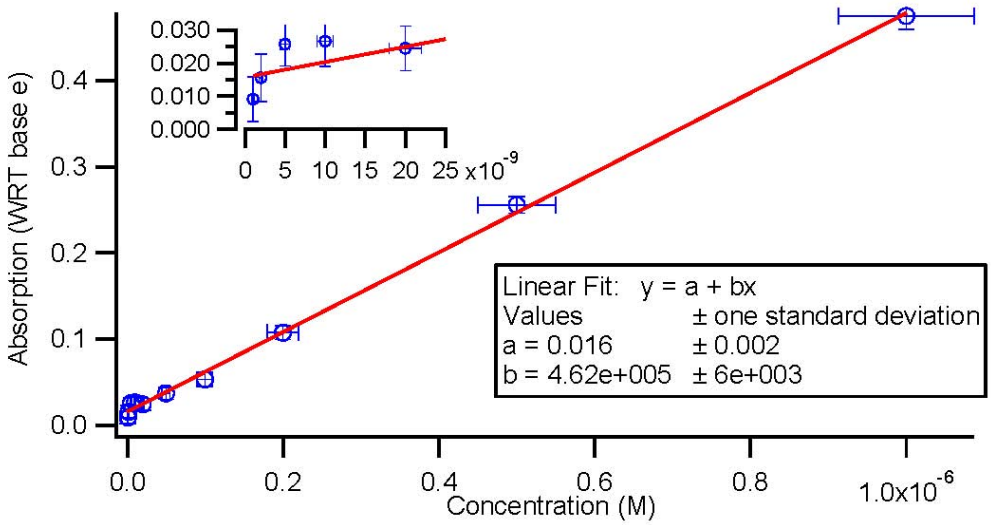


Figure 5.7. Calibration curve of *Congo Red* in DMSO at 532 nm. The inset shows an expansion of the lowest concentrations (1 nM to 20 nM). The slope of a linear fit (red) gives the attenuation coefficient (based on the natural logarithm) of *Congo Red* within the 10 cm LCW. The horizontal error bars have been calculated from the errors of the balance (± 0.0001 g), of the pipettors (5% v/v – according to manufacturer's data), and of the volumetric flasks (0.2% v/v) used to make the solutions. Although it seems that the error decreases with decreasing concentration, which is true for the absolute error of the concentration, the relative error of the concentration increases. The vertical error bars have been derived from the standard deviation of the plateau average (average over 100 points) of the individual injections.

From this calibration plot, an LOD may be calculated, with the use of the same statistical models[4] as applied to the measured *Allura Red AC* sample dye, and results in LOD = 90 nM of *Congo Red* in DMSO, while the actual limit of detection can be derived from Figure 5.6 and is 5 nM as well. The noise in both the baseline and the injection plateaus illustrates that there is room for improvement for this technique. At the detection limit of 5 nM one calculates $2.3 \times 10^{9}$ *Congo Red* molecules to be present in the liquid core waveguide with an attenuation of $3.6 \times 10^{-4}$ $cm^{-1}$.

A linear fit to this data gives the attenuation coefficient to base-*e*, $\alpha_e = 46248\ M^{-1}cm^{-1}$. This can be converted into the usual given molar extinction coefficient by division by the factor ln(10), which yields $\varepsilon = 20000\ M^{-1}cm^{-1}$. For comparison, UV-Vis spectra of five (much higher) concentrations were measured in a regular spectrometer (*Ocean Optics USB4000*) with the use of a 1 cm quartz glass cuvette. The spectra show two excitation maxima at 344 nm and 532 nm in DMSO[1], while a linear regression of a plot of absorption at 532 nm against concentration yields a straight line, with a molar extinction coefficient of $31000\ M^{-1}cm^{-1}$ (cf. Figure 5.8).

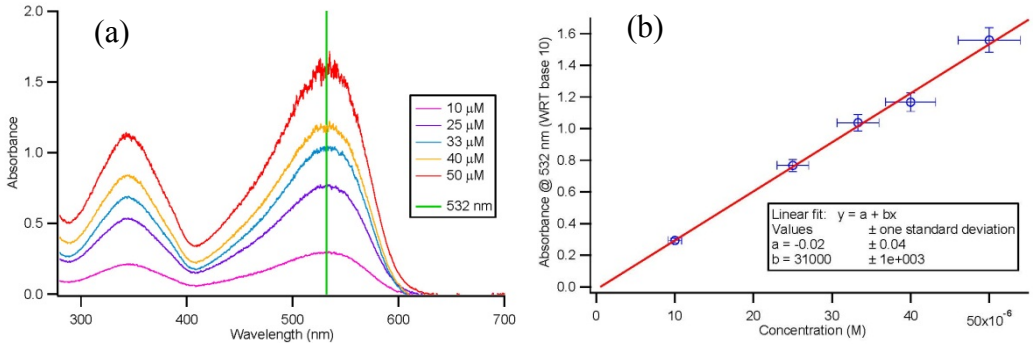


Figure 5.8. UV-Vis spectra of *Congo Red*. (a) Absorbance spectra of *Congo Red* in DMSO, measured with an *OceanOptics USB4000* spectrometer and a 1 cm glass cuvette. The green line represents the laser light used in the LCW-CRDS system. The two absorption maxima at 344 nm and 532 nm are evident. (b) Calibration graph for a wavelength of 532 nm. Y-error bars are plotted as 5% of the absorbance signal. X-error bars are propagated errors for the dilution made from a 100 µM stock solution. The red line is a linear fit that results in a molar extinction coefficient $\varepsilon = 31000\ M^{-1}cm^{-1}$.

According to Beer-Lambert's law (Chapter 1 Equation 1.1), the extinction coefficient ε is independent from the concentration range used. As before, the core diameter of the LCW is mismatched to the core diameter of the fibre – here it is slightly smaller whereas before it was slightly larger. More importantly, the light emitted from the

fibre end diverges slightly, despite its manufactured lens. Taking this into account, some light can bypass the sample in the cladding of the LCW without interacting with the analyte as already discussed for the previous dye (cf. Chapter 5.4.1).

To determine the precision of the ring-down signal, a concentration of 100 nM was injected 11 times into the setup. A long 50 µL sample plug was injected to be able to see the plateauing of the absorption more clearly. The ring-down time change during the injections were recorded (Figure 5.9) and the average of the signal spread has been calculated to be 3.7 ± 0.3 ns.

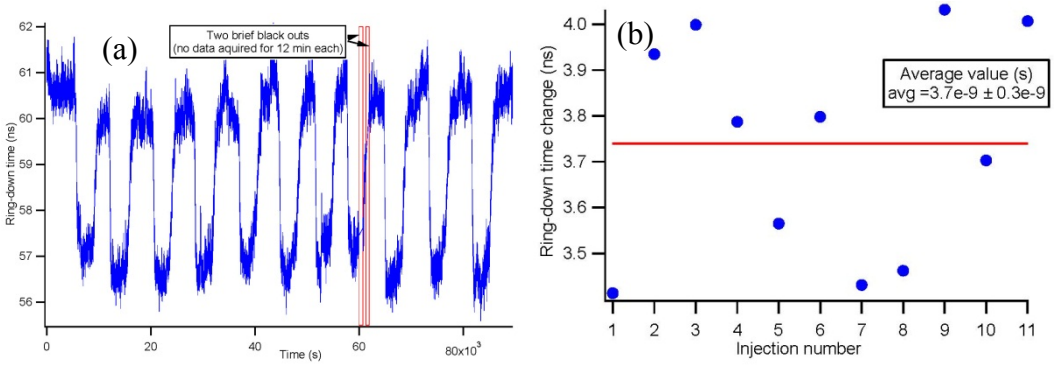


Figure 5.9. Precision measurement of *Congo Red* in DMSO. (a) Time-dependent recording of the ring-down time of 11 injections of 100 nM *Congo Red*. Two brief electrical power outages (red rectangles) occurred during the scan but did not affect the measurements. However, no data were recorded within 12 minutes after each blackout, as the computer had to restart. (b) Plot of the ring-down time change of the 11 injections and their average (3.7 ns).

Generally, the reproducibility of a measurement is also of concern in the evaluation of analytical techniques. To further assess the precision of the concentration measurements, three different concentrations (20 nM, 50 nM, and 100 nM) of *Congo Red*

in DMSO were measured in a random order. A plot of the ring-down time change with time is shown in Figure 5.10.

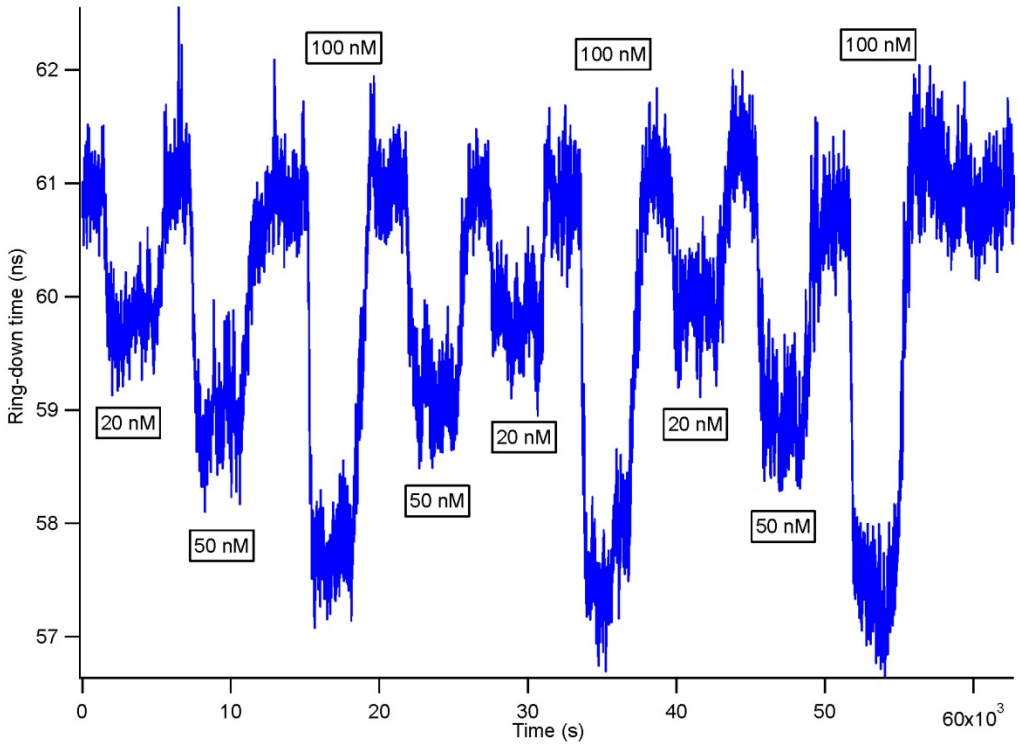


Figure 5.10. Ring-down time change of three different concentrations of *Congo Red* that were randomly injected. It is observable that the individual concentrations have not been affected by a lower or higher concentration injected right before.

## 5.5. Discussion

The combination of the two absorption methods of measurement, long path length absorption with the use of LCW and of CRDS, has provided the expected improvement, but also exposed the disadvantages of the two techniques. This is most obvious with the alignment between fibre and LCW being crucial. Our alignment was not optimal and

resulted in the 20% reduction of the attenuation that we found when using the 5 cm LCW, and 33% when using the 10 cm LCW.

To optimize the combined technique, one has to consider the dependence of the optical loss, $t_{RT}/\tau$, on its different factors. Equation 5.5, is the reciprocal of Equation 1.6 (cf. Chapter 1). It illustrates the dependence of the optical loss on several loss terms: the transmission loss through splices and couplers within the optical fibre, which includes the transmission loss between the fibre and the LCW ($-\ln T_{splice}$), the attenuation loss in the fibre material ($\alpha L$), and the transmission loss through the sample gap. In our case, the last term is given by the transmission loss through the matrix liquid (here DMSO, i.e. $-\ln T_{gap} = -\ln T_{DMSO}$), and by the sample absorption ($\varepsilon C d$),

$$\frac{t_{RT}}{\tau} = -\ln T_{splice} + \alpha L - \ln T_{DMSO} + \varepsilon C d \qquad (5.5)$$

Equation 5.5 can be rewritten by substituting the transmission of the matrix liquid $T_{DMSO}$ with the respective exponential decay function exp(-$d$/$\delta$), which depends on the length of the LCW, $d$, and the decay length of DMSO, $\delta$.

$$\frac{t_{RT}}{\tau} = -\ln T_{splice} + \alpha L + \frac{d}{\delta} + \varepsilon C d \qquad (5.6)$$

To increase the sensitivity of the concentration measurement, the first three optical loss terms have to be minimized. Assuming an ideal case of $T_{splice} = 1$ and $\alpha = 0$, the optical loss only depends on the attenuation in the LCW, due to scattering and absorption of the matrix liquid, as well as the sample absorption within the LCW. The sensitivity, which is the derivative of (Equation 5.5) with respect to the concentration, is simply given by $S = \varepsilon d$. While one would therefore suppose that the LCW should be as long as possible for maximal sensitivity, there is a limit to the length of the LCW that is practically useful, since $d/\delta$ also scales linearly with the length of the liquid core waveguide, $d$. Clearly, it is advantageous to increase the decay length of the matrix liquid, which would make the dependence of the optical loss on the sample absorption dominant, but with a given solvent/capillary combination this parameter cannot readily be reduced. A final consideration is the non-linear dependence of the measurement accuracy on the optical loss. For a very large loss the ring-down times are small, but the measurement accuracy (about 0.3 ns) is the same as it would be for long ring-down times (low loss). Thus, it is beneficial to select the length of the LCW in a way that the $d/\delta$ loss term does not introduce too high background loss. As a rule of thumb, the length $d$ should be chosen such that the optical loss $t_{RT}/\tau > 1$.

Ideally, the technique should have not only a high sensitivity, but also a low limit of detection. Whether a change in concentration can be detected depends on the ability to detect small changes in the optical loss. In our system, the change due to sample absorption within the system at the limit of detection is $\varepsilon Cd = 31000 LM^{-1}cm^{-1} \times 5 * 10^{-9}\,\mathrm{M} \times 10 cm = 0.0016$. Here, the optical loss due to

scattering and absorption of the matrix liquid is 37-times higher ($\frac{d}{\delta} = \frac{10}{173} = 0.0578$) than the sample loss, which shows how sensitive CRDS is.

Interestingly, the round trip time also depends on the length of the liquid core waveguide (cf. Equation 5.3). If one assumes that the whole loop is made from the LCW ($L$=0), and substituting $t_{RT} = nd/c_0$, Equation 5.6 simplifies to

$$\frac{1}{\tau} = \frac{\left(-\ln T_{splice}\right)c_0}{nd} + \frac{c_0}{n\delta} + \frac{\varepsilon C c_0}{n} \tag{5.7}$$

where the only dependence of the optical loss on the length of the LCW cavity, $d$, lies in the term representing the loss of light coupling into and out of the cavity and fusing the LCW ends together, $-\ln T_{splice}$. The optical loss introduced by the sample is independent from the cavity length. In this case, to keep the optical loss small, a long cavity would be beneficial.

The improvement that the combination of the techniques brings about compared to the individual methods becomes evident when a side by side comparison is performed as in Table 5.1. In this table, not only the stated limits of detection from our previous work and work of others are listed, but also the calculated (or estimated) volume in the detection cell is given. Of particular interest is the product of this interaction volume with the minimal detectable attenuation, $\sigma_{\min} = V_{\det} \times \varepsilon \times C_{LOD}$, being a property that is equivalent to the minimal required absorption cross section. Using the cross section, $\sigma_{min}$, instead of the

more commonly used minimal detectable attenuation, $\alpha_{\min} = \varepsilon \times C_{LOD}$, as the guiding design parameter is useful when the size of the detection volume is important and the number of detected molecules is more relevant than the number density or the concentration. For example, when comparing the use of a 1m long liquid-filled cavity ($V_{\text{det}}$ = 1 L) with that of a 1 m long liquid core waveguide ($V_{\text{det}}$ = 1 μL), one may find that the minimal detectable absorption, $\alpha_{\min} = \varepsilon \times C_{LOD}$, is similar in both cases, giving $C_{\text{LOD}}$ in the nanomolar regime for strong absorbers. By contrast, the minimal detectable change in absorption cross section, $\sigma_{\min} = V_{\text{det}} \times \varepsilon \times C_{LOD}$, is a million times lower for the liquid core waveguide, meaning that the number of molecules in the detection volume is lower by that factor. Consequently, using the minimal detectable change in absorption cross section as a metric, one would propose that, in this case, the LCW is the superior technology.

Table 5.1, lists parameters found in a number of previously reported absorption systems that were designed for micro-analysis. Aside from the concentration at the limit of detection, $C_{LOD}$, the minimal detectable attenuation, $\alpha_{min}$, and the minimal detectable change in absorption cross section, $\sigma_{min}$, is listed. According to the table, the concentration at the limit of detection spans over 7 orders of magnitude, whereas $\alpha_{min}$ ranges only from about $10^{-5}$ $cm^{-1}$ to 0.1 $cm^{-1}$. Interestingly, $\sigma_{min}$ is calculated to be in a much smaller range, from about 10 to 4000 $\mu m^2$, where the highest values are associated with systems in which only a small fraction of the light is interacting with the sample in the detection volume. The table also reveals, somewhat surprisingly, that a well-designed single pass LCW system can outperform cavity enhanced methods if either the round trip losses are very high or the detection volume is large.

Using $\alpha_{min}$, or $\sigma_{min}$ for comparison, the present system competes fairly well or even favourably with other systems, which indicates that a combination of cavity ring-down detection and liquid core waveguide materials provides advantages over other methods, especially when the sample volume is restricted. This advantage is, to some extent, offset by the increased complexity of the setup and the stringent requirement to maintain low cavity round trip losses.

| Dye solution | Method | λ (nm) | Interaction length, *L* | ε ($M^{-1}cm^{-1}$) | $V_{det}$ | $C_{LOD}$ (nM) | $\varepsilon \times C_{LOD}$ ($cm^{-1}$) [d] | $\sigma_{min}$ ($\mu m^2$) | Ref |
|---|---|---|---|---|---|---|---|---|---|
| *Allura Red AC* in DMSO | LCW FLRDS | 532 | 50 mm | 29600 | 400 nL | 5 | $3.41 \times 10^{-4}$ | 13.6 | this thesis |
| *Congo Red* in DMSO | LCW FLRDS | 532 | 101 mm | 31000 | 777 nL | 5 | $3.57 \times 10^{-4}$ | 27.7 | this thesis |
| Malachit green in Ethylene glycol | liquid jet - CRD | 628 | 23.2 µm | 99750 | 41 nL [e] | 71 | 0.0162 | 66.4 | 8 |
| Brilliant Blue-R in water | normal incidence cuvette - CRD | 630 | 2 mm | 106000 | 800 µL | 1 | $5.1 \times 10^{-5}$ | 4100 | 9 |
| Quinalizarin in MeOH 5%, acetic acid/water 80:20 | Brewster angle flow cell - CRD | 470 | 300 µm | 9000 | 10 µL [f] | 30 [g] | $6.22 \times 10^{-4}$ | 622 | 10 |
| Crystal violet in EtOH | Liquid filled cavity-CRD | 532 | 2 mm | 54500 | 12 µL [h] | 3.7 [i] | $3.14 \times 10^{-4}$ | 376 | 11 |
| Bacteriochlorophyll *a* in $d_6$-acetone | Liquid filled cavity-CRD | 783 | 1.75 mm | 44000 [j] | 10 µL | 0.2 | $1.6 \times 10^{-5}$ | 16 | 12 |
| Tartrazine in aqueous phosphate buffer pH = 7.2 | Fibre gap FLRDS | 405 | 800 µm | 22660 | 100 nL | 900 | 0.02 | 200 | 13 |
| Tartrazine in aqueous phosphate buffer pH = 7.2 | Fibre gap FLRDS | 405 | 190 µm | 22660 | 6 nL | 5000 | 0.261 | 157 | 14 |
| Rhodamine 6G in water | Fibre gap FLRDS | 532 | 180 µm | 53000 [k] | 19 nL | 930 | 0.11 | 209 | 15 |
| K $MnO_4$ in water | Fibre gap FLRDS | 532 | 466 µm | 4800 | 132 nL | 214 | $2.4 \times 10^{-3}$ | 31.2 | 16 |
| $CoCl_2$ $6H_2O$ in water | PCF | 510 | 50 cm | ~ 6 [l] | 94 nL | 25 mM | 0.34 | 1410 | 7 |
| Fe(II)-ferrozine complex in water | LCW | 562 | 4.47 m | 27600 | 300 µL | 0.2 | $1.3 \times 10^{-5}$ | 165 | 17 |
| Double stranded DNA in water | LCW | 260/280 | 15 mm | 0.02 mL $\mu g^{-1}$ $cm^{-1}$ | 250 nL | 0.1µg $mL^{-1}$ | $4.6 \times 10^{-3}$ | 50 | 18 |
| Bromothymol blue in 1 mM NaOH (aq) | LCW | 613 | 20 mm | 40059 | 1000 nL | 22 | $2 \times 10^{-3}$ | 88 | 6 |

Table 5.1. Comparison of different long path length absorption techniques, CRDS experiments and the here described setup.

[d] *For some entries, the minimal detectable absorption (base-e) was calculated from $C_{LOD} \times \varepsilon \times ln(10)$.*

[e] *Calculated from the beam diameter in the cavity $(1.5mm)^2/4 \times \pi \times 0.0232$ mm.*

[f] *Only approximately 500 nL of the 10 mL cell volume interacted with the light.*

[g] *Given as $2.5 \times 10^{-8}$ g/mL.*

[h] *Approximately 4 µL of the 12 µL cell volume interacted with the light.*

[i] *Calculated from 2.5 nM at the $2\sigma$ level.*

[j] *Was observed to be a little less than the literature value of about 60,000 $M^{-1}$ $cm^{-1}$, probably due to degradation or contamination.*

[k] *Not given but calculated from the base-e absorption coefficient of 122,000 $M^{-1}cm^{-1}$.*

[l] *Not given but estimated from Fig. 4 in Ref 7. Sun, Y.; Yu, X.; Nguyen, N. T.; Shum, P.; Kwok, Y. C., Long path-length axial absorption detection in photonic crystal fiber. Analytical Chemistry 2008, 80, 4220-4224.*

The baselines in Figures 5.3 and 5.6 exhibit slopes of -500 ps/h and -130 ps/h. Although the reason for the slow reduction of the ring-down time over the course of the experiment remains unknown, one has to consider that during the entire experiment hydraulic pressure is exerted by the syringe pump on the couplings between fibre and LCW. "It is conceivable that material fatigue may be the cause for the slow decrease of cavity finesse."[5] Dye deposition from the multiple injections might also be a cause for lowering the transmission through the LCW. We found that the baseline slope was found even when no sample but pure DMSO was injected.

## 5.6. Conclusion

A new experimental setup that incorporates liquid core waveguides into fibre-loop ring-down spectroscopy has been presented. Two model dyes, *Allura Red AC* and *Congo Red*, were used to evaluate the performance of the experimental setup. The objective of decreasing the limit of detection to the nanomolar range without exceeding the detection volume of 1 μL was met. The *Congo Red* experiment utilizes a detection volume of 777 nL, whereas the *Allura Red AC* setup achieves a detection volume of 400 nL. Both of these volumes are compatible with modern analytical methods, such as micro-HPLC and others. The limit of detection has been determined to be 5 nM for both dyes.

## 5.7. References


1. Pigorsch, E.; Elhaddaoui, A.; Turrell, S., Spectroscopic Study of pH and Solvent Effects on the Structure of Congo Red and its Binding Mechanism to Amyloid-Like Proteins. *Spectroc. Acta Pt. A-Molec. Biomolec. Spectr.* 1994, 50, 2145-2152.

2. Material Safety Data Sheet - Congo Red. http://fscimage.fishersci.com/msds/60200.htm (accessed 17.10.2012).

3. Sounding out Congo Red. http://www.sciencecodex.com/sounding_out_congo_red (accessed 17.10.2012).

4. Loock, H.-P.; Wentzell, P. D., Detection limits of chemical sensors: Applications and misapplications. *Sensors and Actuators B: Chemical* 2012, 173, 157-163.

5. Bescherer, K.; Barnes, J. A.; Loock, H.-P., Absorption Measurement in Liquid Core Waveguides Using Cavity Ring-Down Spectroscopy. *Analytical Chemistry* Accepted March 2013.

6. Mishra, S. K.; Dasgupta, P. K., Capillary scale light emitting diode based multi-reflection absorbance detector. *Analytica Chimica Acta* 2007, 605, 166-174.

7. Sun, Y.; Yu, X.; Nguyen, N. T.; Shum, P.; Kwok, Y. C., Long path-length axial absorption detection in photonic crystal fiber. *Analytical Chemistry* 2008, 80, 4220-4224.

8. Alexander, A. J., Flowing liquid-sheet jet for cavity ring-down absorption measurements. *Analytical Chemistry* 2006, 78, 5597-5600.

9. Islam, M.; Seetohul, L. N.; Ali, Z., Liquid-phase broadband cavity-enhanced absorption spectroscopy measurements in a 2 mm cuvette. *Applied Spectroscopy* 2007, 61, 649-658.

10. Snyder, K. L.; Zare, R. N., Cavity ring-down spectroscopy as a detector for liquid chromatography. *Analytical Chemistry* 2003, 75, 3086-3091.

11. Bahnev, B.; van der Sneppen, L.; Wiskerke, A. E.; Ariese, F.; Gooijer, C.; Ubachs, W., Miniaturized cavity ring-down detection in a liquid flow cell. *Analytical Chemistry* 2005, 77, 1188-1191.

12. McGarvey, T.; Conjusteau, A.; Mabuchi, H., Finesse and sensitivity gain in cavity-enhanced absorption spectroscopy of biomolecules in solution. *Opt. Express* 2006, 14, 10441-10451.

13. Waechter, H.; Munzke, D.; Jang, A.; Loock, H.-P., Simultaneous and Continuous Multiple Wavelength Absorption Spectroscopy on Nanoliter Volumes Based on Frequency-Division Multiplexing Fiber-Loop Cavity Ring-Down Spectroscopy. *Analytical Chemistry* 2011, 83, 2719-2725.

14. Waechter, H.; Bescherer, K.; Dürr, C.; Oleschuk, R. D.; Loock, H.-P., 405 nm Absorption Detection in Nanoliter Volumes. *Analytical Chemistry* 2009, 81, 9048.

15. Rushworth, C. M.; James, D.; Lee, J. W. L.; Vallance, C., Top Notch Design for Fiber-Loop Cavity Ring-Down Spectroscopy. *Analytical Chemistry* 2011, 83, 8492-8500.

16. James, D.; Oag, B.; Rushworth, C. M.; Lee, J. W. L.; Davies, J.; Cabral, J. T.; Vallance, C., High-sensitivity online detection for microfluidics via cavity ringdown spectroscopy. *Rsc Advances* 2012, 2, 5376-5384.

17. Waterbury, R. D.; Yao, W. S.; Byrne, R. H., Long pathlength absorbance spectroscopy: trace analysis of Fe(II) using a 4.5m liquid core waveguide. *Analytica Chimica Acta* 1997, 357, 99-102.

18. Pan, J. Z.; Yao, B.; Fang, Q., Hand-held Photometer Based on Liquid-Core Waveguide Absorption Detection for Nanoliter-scale Samples. *Analytical Chemistry* 2010, 82, 3394-3398.

# Chapter 6.

# Conclusion

Modern analytical techniques require high sensitivity, but also strive for low sample consumption. In the research described in this thesis, an approach has been made to decrease the limit of detection for samples of hundreds of nanolitres up to microlitres, with the use of CRDS and liquid core waveguides. A compromise between the smallest sample volume and a low limit of detection has been made, keeping in mind the requirements for online detection in modern analytical industry, such as a sample volume below 1 μL and being able to combine the detection scheme with flow systems.

First, a theoretical model has been described that shows that phase-shift detection in the frequency domain is as capable of determining multiple ring-down times as time domain measurements, with a similar precision (cf. Chapter 3). Second, this has further been confirmed using an electric circuit, which acts as a ring-down cavity with, in this case, two time constants that are set by the electric components. The set ring-down times were 10 μs and 90 μs, and the phase-shift measurement produced 12.50 ± 0.08 μs and 94 ± 5 μs. A control experiment in the time domain confirmed these values with ring-down times of 12.6 ± 0.1 μs and 90.8 ± 0.3 μs, respectively. As has been explained, the ring-down times set by the electronic components are calculated on the basis of their nominal value, but their actual value can differ by up to 10% of their nominal value depending on the uncertainty of the used components. Third, a multimode fibre-loop cavity was examined and the theoretical model was confirmed because of the good agreement of the

time constants resulting from both frequency domain and time domain measurements. Additionally, it was discovered that a fit of the time domain data to a bi-exponential function works equally well and produces slightly lower ring-down times. Nevertheless, a closer look at the residuals revealed that there was one additional process unaccounted for. Fitting a tri-exponential function to the data set gave ring-down times of 1.501 ± 0.007 μs, 311 ± 2 ns, and 6.7 ± 0.2 ns for the time domain measurement, and decay constants of 1.57 ± 0.04 μs, 320 ± 9 ns, and 17 ± 2 ns for the frequency domain measurement. Although not all of these values agree with each other within errors, it has to be considered that the short ring-down time in the time domain is actually shorter than the pulse width of the light source and thus cannot be taken as a reliable value. Moreover, the shortest ring-down time is only represented by the first few points in the decay trace and the accuracy of fitting this parameter is decreased. A similar argument is made for the longest ring-down time in the frequency domain, which is represented by the first part of the recorded frequency domain curve as well. In general, the fit accuracy is higher in the time domain than in the phase-shift measurement, since the fit is based on 10 000 versus 192 points. In conclusion, it can be stated that frequency domain measurements are superior over time domain measurements in accurately determining fast ring-down times, although the frequency has to be scanned over multiple decades. This increases the measurement time in phase-shift measurements, but time domain measurements have comparable durations since they require averaging of waveforms.

Fourth, the presented theoretical model has been compared to proposed models from Kasyutich et al. and van Helden et al. and it has been shown that their models are special cases of our more general model.

For the measurements described in Chapter 3, our laser diode driver had to be reengineered because the shut-off time of the laser diode was not fast enough. The driver was successfully reengineered and a shut-off time reduction from 145 ns to about 6 ns was achieved (cf. Chapter 2). Although the working principle of the reengineered driver is very similar to a commercial laser diode driver sold by *Thorlabs*, our model is capable of handling much higher currents for high power laser diodes.

In order to incorporate a glass capillary as an LCW into a fibre-loop ring-down setup, different preliminary experiments were performed (cf. Chapter 4). Foremost, a suitable matrix liquid had to be found and it has been discovered that the liquids that are most suitable as core medium are DMSO and toluene, on account of their low absorption in the visible spectrum. After considering their ease of handling, price, and toxicity, DMSO was chosen as core liquid for all further experiments.

Furthermore, it was investigated if lowering the refractive index of the core liquid, which produced more weakly guided light, would prove beneficial to the transmission through the LCW. This was done by mixing DMSO with water in different ratios and measuring the total intensity at the LCW output. It was found that with less strongly guided light, the output intensity dropped steadily until no light whatsoever was guided in the core at RI = 1.45. It was decided, taking also simplicity into account, that degassed pure DMSO was to be used without further purification. Degassing of the solution was performed avoid bubbles formation in the setup due to spontaneous degassing while in use.

In addition, the consequences of a geometrical mismatch between the fibre and the LCW on the transmission at the fibre/LCW interfaces was investigated. For the limited

availability of capillary diameters, only certain cases of the relation of core and cladding diameters of both waveguides could be investigated and compared. The connection causing the greatest loss that was examined, contributed an additional 70% (= 5.3 dB) to the system, given that both LCW dimensions were smaller than the core diameter of the fibre. The least loss observed resulted from a matching cladding diameter but mismatching core diameter ($Ø_{ID,fibre} > Ø_{ID,LCW}$). This was not surprising to find, since similar geometries result in comparable cross sections and mode structures of the two waveguides, and it was decided that it would be even more beneficial for the transmission to match the core diameters with different cladding diameters ($Ø_{OD,fibre} < Ø_{OD,LCW}$) in the final setup (cf. Chapter 5). However, the setup used in Chapter 5 ultimately resulted in higher losses than the arrangement with matching claddings. Although this was initially unexpected (reasons for this result are discussed in Chapter 4), it was concluded that it is crucial to match cores to achieve the highest overlap of the light and the sample to maximize the sensitivity to a change in concentration of the sample, although the transmission of the LCW is decreased in this case with respect to the best case discussed in Chapter 4. A brief comparison of the number of guided modes in the core of the different waveguides confirmed the overall trend.

For fibre optic connections, it is common practice to polish the connectors to increase the light transmission at the connection. A closer look was taken at the surface quality of the LCW that has been achievable in the laboratory. It was confirmed that surface damages to the capillary face are disadvantageous, as has already been known to be the case for fibre-fibre connections. Furthermore, it was found that the inner rim of the LCW should be as sharp as possible to not scatter light. It was found that precision cleaved

glass capillaries demonstrated the best surface quality and the best rim shape. To save money and time we also used manually polished capillaries, which have a second capillary or fibre inserted for the polishing process to keep debris out and strengthen the inner surface. These capillaries have worked almost as well and could be fabricated more quickly and cheaply compared to than the precision cleaved glass capillaries.

Simultaneously, a procedure was developed to produce convex liquid lenses at the LCW-fibre interface, since it has been reported previously that lenses be advantageous to minimize loss in fibre-fibre transmissions. The liquid lens was produced by creating a hemispherical indentation in the glass surface of the fibre. Intensity output distributions and coupling efficiencies of fibre lenses with different radii of curvature have been modeled and results on theory and experiment are given in Chapter 4.2.5.

Finally, a FLRDS setup was built and 5 cm long, or 10 cm long, glass capillary waveguides were inserted one at a time as a sample gap. This setup was then subjected to two model dyes, namely *Congo Red* and *Allura Red AC*, and absorption measurements at 532 nm were performed. The measured detection limit for both dyes, dissolved in DMSO, was 5 nM and a dynamic range of about 3 orders of magnitude was successfully analysed. From the absorption measurements, the molar extinction coefficient was determined, and it was found that the coefficient was actually lower than the absorption coefficient determined by regular UV-Vis absorption spectroscopy. It was concluded that some light had bypassed the sample solution in the glass capillary wall and had thereby lowered the contribution of the Beer-Lambert Absorption term $\varepsilon Cd$ to the optical loss. This effect has also been described in the literature previously.[1, 2]

Precision and repeatability measurements have also been performed to fully characterize the system. The new LCW-FLRDS setup was then compared to other direct absorption techniques and liquid CRDS experiments. Although our setup does not use the smallest possible volume, the detection volume has still been comparably small (<1 μL) and, therefore, the setup can be easily incorporated in, or adapted to, separation techniques, such as high performance liquid chromatography. After all, the limit of detection is very low, although not quite the lowest so far achieved for liquid CRDS. Moreover, as can be seen in Table 5.1, the longest detection path used in CRDS is provided by our setup. This entails also the lowest absorption cross section, being achieved because the light interacts to nearly 100% with the injected sample in the liquid core waveguide.

Summing up, the new method of incorporating LCWs into FLRDS experiments has successfully achieved the initially set goal of providing small detection volumes (< 1 μL). This satisfies the volume requirements of modern analytical techniques, and, additionally, also provides a low detection limit in the nanomolar range.

## 6.1. References

1. Mishra, S. K.; Dasgupta, P. K., Capillary scale light emitting diode based multi-reflection absorbance detector. *Analytica Chimica Acta* 2007, 605, 166-174.

2. Sun, Y.; Yu, X.; Nguyen, N. T.; Shum, P.; Kwok, Y. C., Long path-length axial absorption detection in photonic crystal fiber. *Analytical Chemistry* 2008, 80, 4220-4224.

# Chapter 7.

# Future Work

## 7.1. Using Teflon AF as Waveguide Material

As in every new analytical method, there is room for improvement in the experimental setup. One disadvantage of the LCW-CRD experiment is that the matrix liquid is DMSO, which was chosen to achieve light guiding properties within the LCW. Yet, in most industrial processes aqueous solutions are common. Since the refractive index of water is only about 1.33 water cannot guide light through glass capillaries. As discussed in Chapter 1, many liquid core waveguide experiments are performed using waveguides that are either made from Teflon AF coated capillaries or made entirely from Teflon AF to provide light guiding also with aqueous solutions. Since Teflon AF has a lower refractive index than water (1.29 vs. 1.33), LCW-FLRDS experiments utilizing Teflon AF as LCW material would be applicable to all kinds of solvents, which would make the technique much more universal, and this method could be readily incorporated in pharmaceutical, or other industrial, processes for online measurements. Therefore, it would be worthwhile to engage in further experiments and research to integrate Teflon AF waveguides in FLRDS experiments.

## 7.2. Creating the Probe Light within the Waveguide Cavity

As discussed in Chapter 4, the system-inherent losses should be kept as low as possible, in order to enhance the absorption effect of the sample of interest. Although not too much of a concern in mirror-based CRD systems, it is very challenging to introduce light into waveguide-based ring-down experiments. One elegant way to do this would be to create the probe light within the cavity itself, for example, by means of fluorescence. If the waveguide was coated with a fluorescing layer or a fluorophore would be contained in the matrix liquid, photo excitation from the outside would create probe light inside the cavity and a small part of the light would be guided within the waveguide. The amount of guided light can be estimated by calculating the volume fraction of the light that is guided in the waveguide. This light occupies two spherical cones, one for each guided direction, with point angles equal to twice the maximum propagation angle inside the waveguide assuming an isotropic fluorescence light emission from a point source. The propagation angle, $\alpha$, within the waveguide is $\alpha = \frac{\pi}{2} - \theta_c$ with $\theta_c$ being the critical angle given by the refractive indices of the core, $n_{core}$, and cladding, $n_{cladding}$, materials. An isotropic light distribution fills a sphere around a point source with light. The volume of this sphere[3], $V_{ISO}$, is given by Equation 7.1.

$$V_{ISO} = \frac{4}{3}\pi R^3 \tag{7.1}$$

$$V_{SC} = \frac{2}{3}\pi R^2 h \tag{7.2}$$

The volume of a spherical cone[4], $V_{SC}$, is given in Equation 7.2. A spherical cone is a sum of a cone[5] with a point angle, $\alpha$, and a slanted side length of, $R$, and a spherical cap[6] with the height, $h$, of a sphere with radius, $R$. The height if the spherical cone, $h$, is defined by the height of the spherical cap. The relation of the height, $h$, to the point angle, $\alpha$, of the cone and the radius, $R$, of the sphere is given in Equation 7.3.

$$h = R * (1 - \cos\alpha) \tag{7.3}$$

Combining Equation 7.2 and 7.3 gives

$$V_{SC} = \frac{2}{3}\pi R^3 (1 - \cos\alpha) \tag{7.4}$$

The amount of guided light within the waveguide is then the ratio of the volume of two spherical cones to the volume of the sphere of total fluorescently emitted light from an isometric point source and is given by Equation 7.5.

$$I_{guided} = \frac{2V_{SC}}{V_{ISO}} = \frac{2\frac{2}{3}\pi R^3 (1 - \cos\alpha)}{\frac{4}{3}\pi R^3} = 1 - \cos\alpha \tag{7.5}$$

As mentioned earlier, the propagation angle, $\alpha$, is defined by the refractive indices of the core and cladding material and $\cos\alpha$ can be expressed as follows.

$$\cos\alpha = \cos\left(\frac{\pi}{2} - \theta_c\right) = \sin\theta_c = \frac{n_{cladding}}{n_{core}} \qquad (7.6)$$

Assuming a liquid core waveguide made from a fused silica capillary (RI = 1.45) as cladding and DMSO (RI = 1.4785) as core liquid as presented in this thesis, the guided light with such a waveguide produced by fluorescence can be calculated to be 1.9% of the total light created assuming an isometric distribution. Although this is a very small fraction, fluorescence excitation would still provide a promising approach to input light into the optical cavity, since it does not introduce losses due to couplers.

## 7.3. Extending the Sample Path to the Whole Loop Cavity Length

Of course, when striving for even lower detection limits, it is easy to imagine what would happen if the sample path length could be increased even further. The maximum path length imaginable in a waveguide cavity ring-down setup would be realised if the whole cavity was made from the sample cell, that is if the entire waveguide loop was produced from the sample capillary. This idea raises the question of how to introduce both the sample and the light into the cavity. Light introduction could be done by the means of fluorescence (cf. 7.2) or by adapting the notch coupling scheme examined by Rushworth et al.[7] The top notch coupling technique could potentially also be combined with a simultaneous liquid introduction into the cavity.

Making the whole cavity from the sample loop opens up to the possibility of incorporating such optical waveguide cavities and absorption techniques in lab-on-a-chip

devices. Our research group has already considered this possibility and a glass chip has been designed. Loop structures of different depths and widths have been etched into a glass substrate and covered with another glass plate, providing access holes to introduce liquid into the different waveguides. The resulting glass chip layout is presented in Figure 7.1.

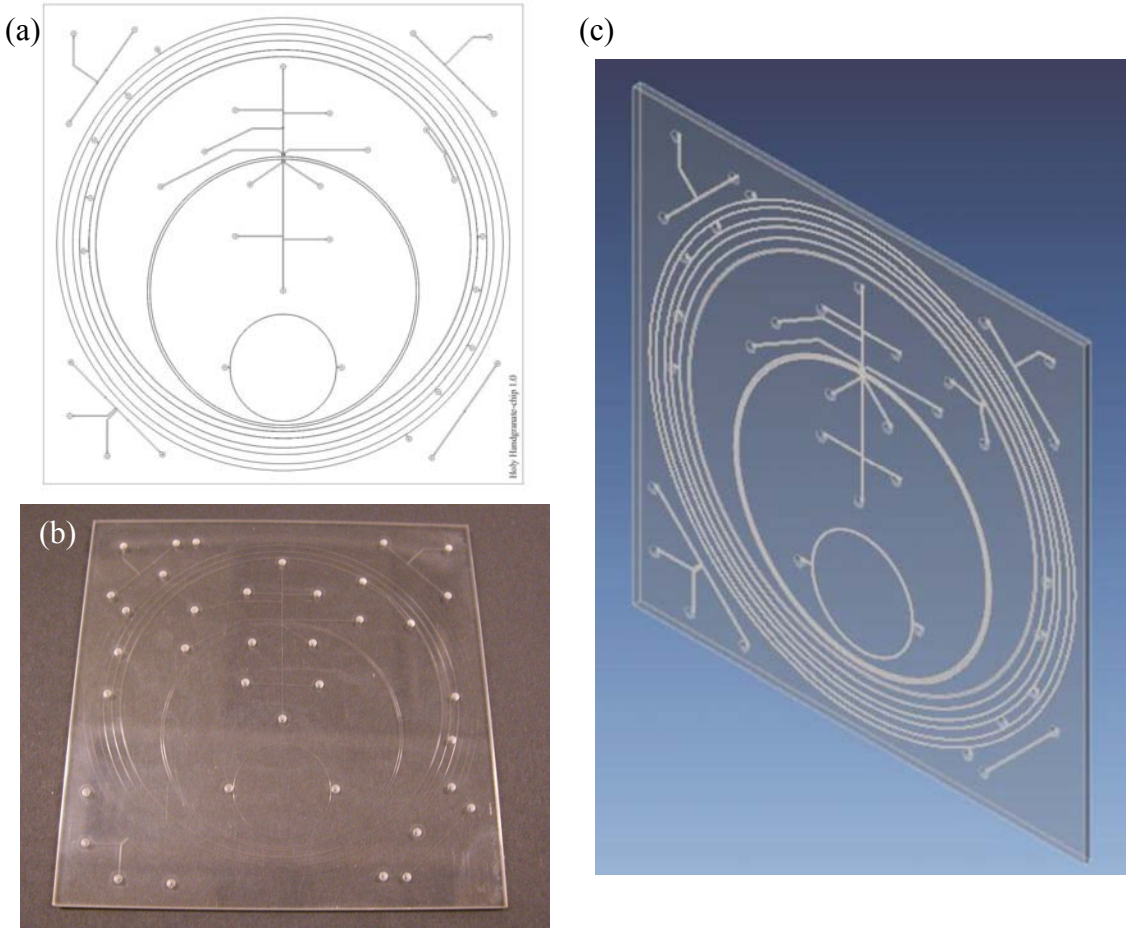


Figure 7.1. The glass chip with different liquid core waveguide loops. (a) A schematic diagram of the design of the chip. Channel depths are either 5 µm (three biggest ring channels) or 40 µm. Waveguide widths range from 20 µm to 300 µm, and loop diameters range from 2 cm to 8.5 cm. There are two different loops designed on this chip: 1. Loops with opposing liquid inlet and outlet and 2. waveguides for which the liquid inlet and outlet are close to each other and are separated only by a thin wall. The latter option opens the possibility for the loop waveguides to be intersected with a microfluidic channel in the spot where the liquid inlet and outlet are separated from each other. The microfluidic channel can, for example, be used for

microfluidic separation, and the LCW cavity ring-down spectroscopy setup can be used as a UV-Vis spectroscopy detector. (b) A picture of the glass chip. (c) A 3D drawing of the glass chip.

## 7.4. Exploiting the Broadband Nature of Liquid Core Waveguides

Fibre-loop ring-down spectroscopy can be used at multiple wavelengths at the same time, thanks to the broadband nature of the waveguides. This was explored by Waechter et al. by using either two lasers and two different dyes and later by using two UV-LEDs and measuring DNA purity.[8] Multiwavelength measurements can be adapted to liquid core waveguide cavity ring-down experiments as well, as LCWs also permit broadband transmission from UV wavelengths to near infra-red wavelengths depending on the liquid used.

Then, two measurement principles could be exploited: the wavelength discrimination could either be performed before the cavity or after the cavity. First, measurements, for which the wavelength discrimination is done before the cavity, can either be performed with sequential injection of light pulses at different wavelengths and observation of the ring-down trace in the time domain, one wavelength at a time, or by modulating different wavelengths at slightly different modulation frequencies for frequency domain measurements and filtering the overall signal at the cavity output with the use of multiple lock-in amplifiers to record each phase-shift separately. The latter has been demonstrated for two wavelengths by Waechter et al.[8]

Second, if the wavelength discrimination is performed after the cavity by means of a dispersion element, such as a prism or an optical grating, a white light source, such as

a supercontinuum light source, could be used. The light source would have to be intensity modulated and the phase-shift of the intensity modulated output at each wavelength could then be related to the absorption within the cavity. Analogous to an intensity-modulated light source one could couple a very short but transform-limited laser pulse, such as a femto-second pulse, to the cavity and observe the ring-down events at each wavelength separately with a detector array, such as a charge coupled device (CCD). Alternatively to a very short single pulse, a frequency comb could be used as an input light source as well.[9]

Ultimately, the first step to multi-wavelength detection in liquid core waveguide ring-down setups would be to characterize the behaviour of LCWs and their requirements at shorter wavelengths, such as UV or near UV wavelengths.

In conclusion, liquid core waveguide cavity ring-down spectroscopy has the potential of becoming a very versatile absorption technique, that can be used to record absorption spectra with a very high sensitivity for a wide range of wavelengths and having the capability of being incorporated in industrial separation techniques as an online detector or in microfluidic devices to analyze small sample volumes.

## 7.5. References

1. Wolfram Research, I. Wolfram MathWolrd - Sphere. http://mathworld.wolfram.com/Sphere.html (accessed 9.11.2012).

2. Wolfram Research, I. Wolfram MathWorld - Spherical Cone. http://mathworld.wolfram.com/SphericalCone.html (accessed 9.11.2012).

3. Wolfram Research, I. Wolfram MathWorld - Cone. http://mathworld.wolfram.com/Cone.html (accessed 09.11.2012).

4. Wolfram Research, I. Wolfram MathWorld - Spherical Cap. http://mathworld.wolfram.com/SphericalCap.html (accessed 9.11.2012).

5. Rushworth, C. M.; James, D.; Lee, J. W. L.; Vallance, C., Top Notch Design for Fiber-Loop Cavity Ring-Down Spectroscopy. *Analytical Chemistry* 2011, 83, 8492-8500.

6. Waechter, H.; Munzke, D.; Jang, A.; Loock, H.-P., Simultaneous and Continuous Multiple Wavelength Absorption Spectroscopy on Nanoliter Volumes Based on Frequency-Division Multiplexing Fiber-Loop Cavity Ring-Down Spectroscopy. *Analytical Chemistry* 2011, 83, 2719-2725.

7. Gagliardi, G.; Avino, S.; Fabian, M.; Salza, M.; Ferraro, P.; De Natale, P., Optical-frequency-comb based interrogation of fiber resonators. In *21st International Conference on Optical Fiber Sensors*, Bock, W. J.; Albert, J.; Bao, X., Eds. Spie-Int Soc Optical Engineering: Bellingham, 2011; Vol. 7753.

# Appendix: Devices Built for CRDS Setups and CRDS Research in Our Laboratory

## Appendix 1. Aluminium Block Interface

Aluminium block interfaces are used to provide a liquid tight seal around ferrule-ferrule connections of fibres and LCWs.

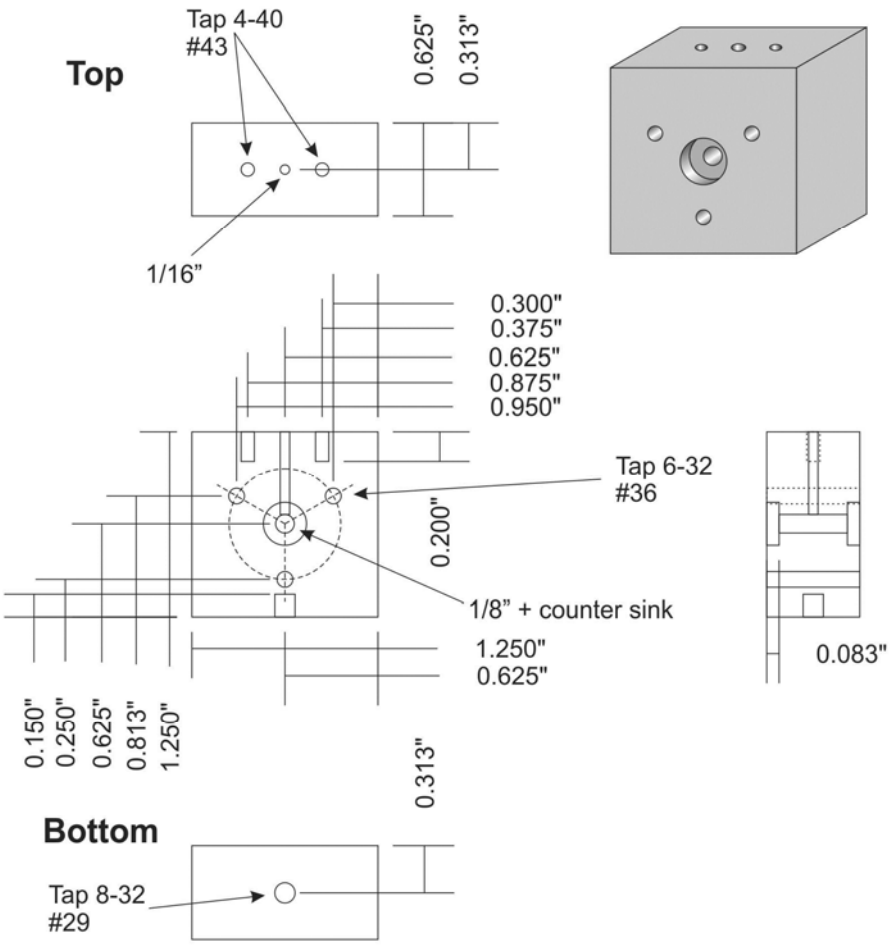


Figure A.1. Aluminium block interface. It allows liquid introduction into the LCW and seals the ferrule-ferrule connection between the fibre and the LCW.

Appendix 2. Ferrule Positioning Collet (Design)

The ferrule positioning collet is used for moving a ferrule within an aluminium block interface axially with respect to the other ferrule. The resolution is 0.635 mm per full turn of the adjustment screw. The ferrule slides through the collet from the back. The collet grips the ferrule, once it is inserted into the aluminium block interface, and turning the adjustment ring moves the collet, which is clamped into the collet holder.

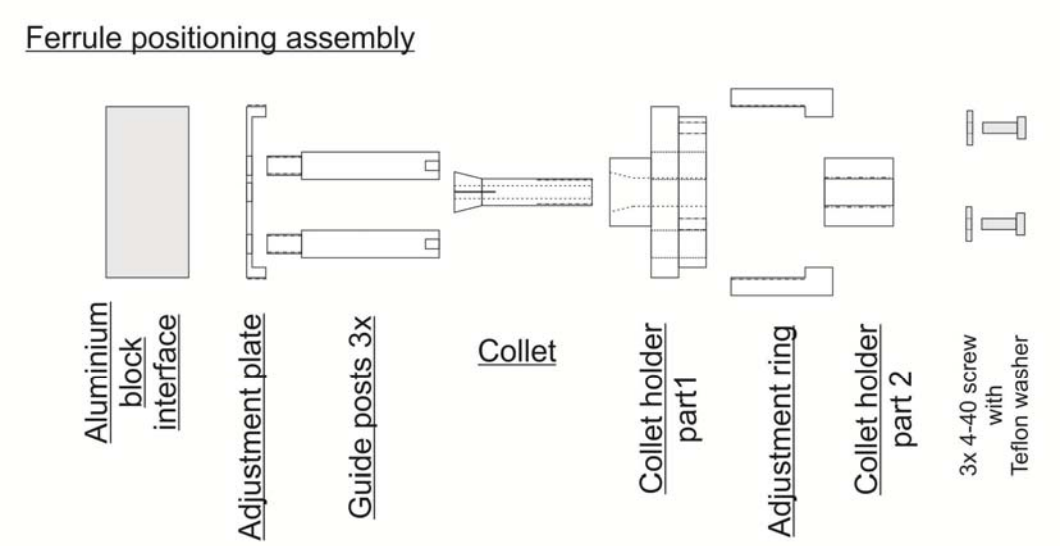


Figure A.2.1. Explosive view of the ferrule positioning assembly. The individual parts are shown in the following figures.

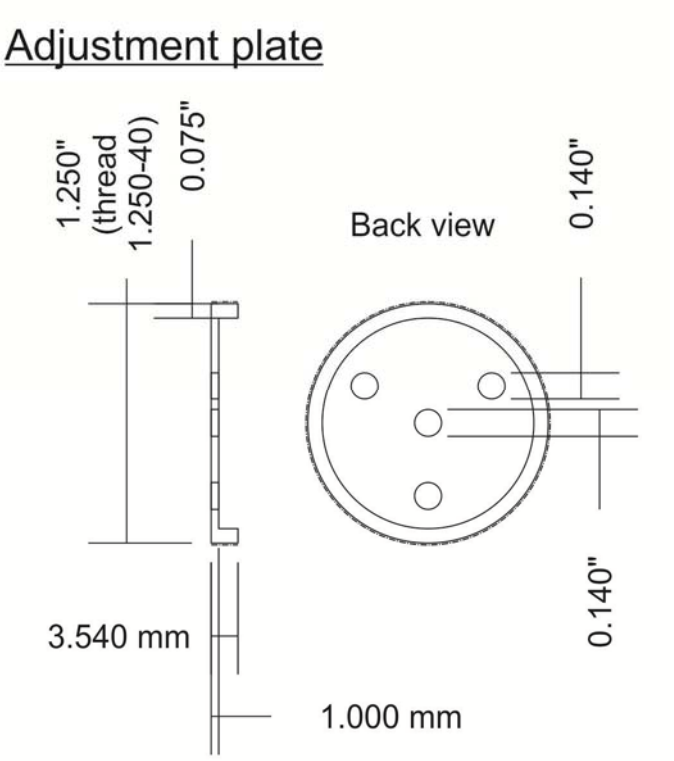


Figure A.2.2. Adjustment plate of the ferrule positioning assembly. It serves two purposes. On the one hand, it provides the thread that the adjustment ring (Figure 8.7) threads on. On the other hand, it is screwed onto the aluminium block interface with the use of the guiding posts (Figure 8.4), and therefore exerting pressure on the O-ring that seals the ferrule.

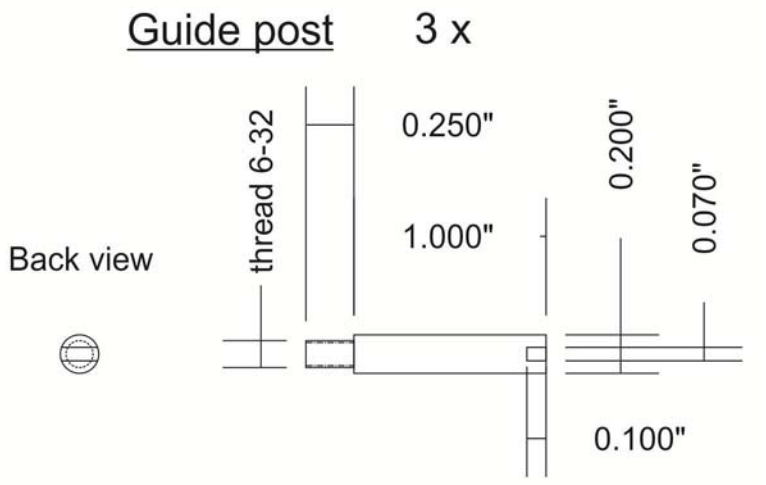


Figure A.2.3. Guide posts. The collet holder slides on the guide posts back and forth.

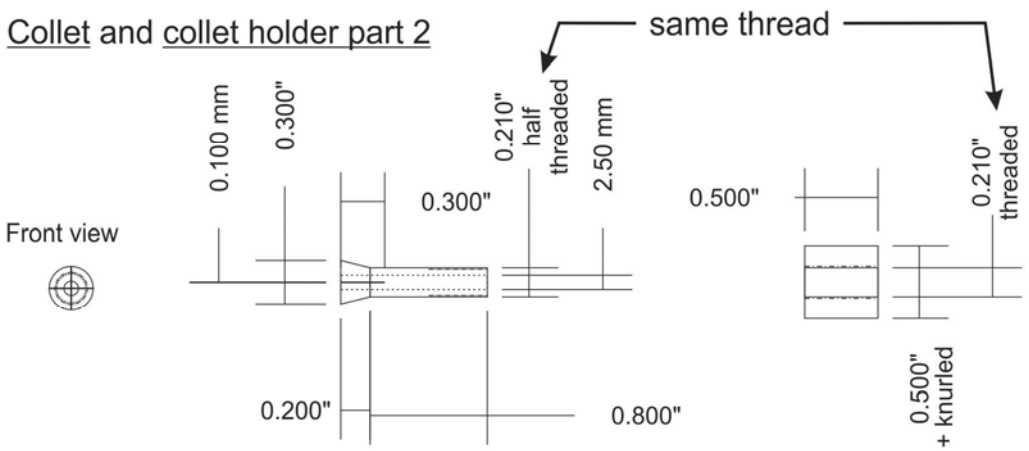


Figure A.2.4. Collet and part 2 of collet holder. The collet slips over the ferrule from the back. By tightening the collet holder part 2, the collet is pulled into the collet holder, which tightens the collet onto the ferrule.

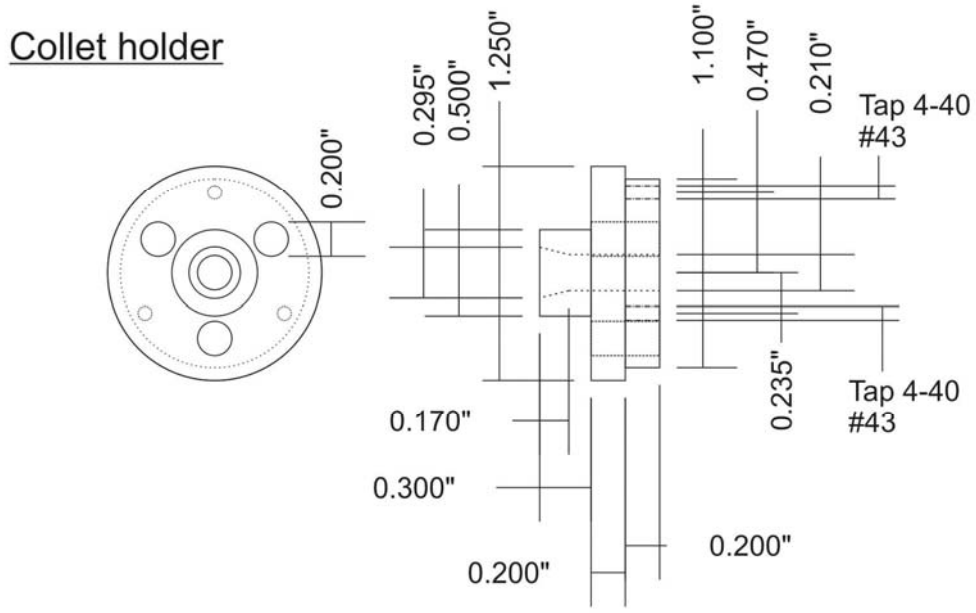


Figure A.2.5. Collet holder. This part slides back and forth on the guide posts and holds the collet. Tightening the collet is done by tightening the collet holder part 2 and with that pulling the collet into the collet holder. The cones of the collet and of the collet holder then press against each other and clamp the collet tightly around the ferrule. The collet holder is held in place within the adjustment ring by the front rim on the collet holder and by three screws with Teflon washers (not shown here, cf. Figure 8.2) in the back.

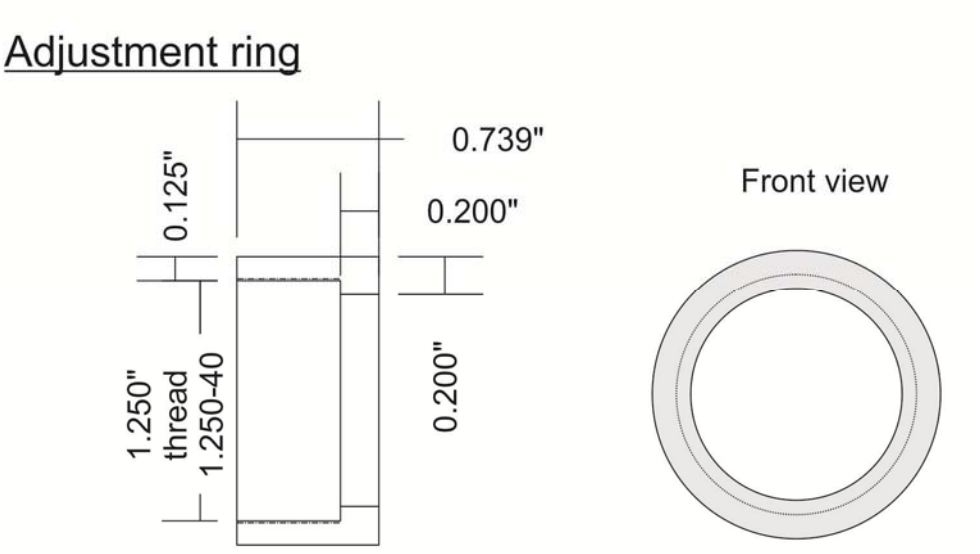


Figure A.2.6. Ferrule positioning assembly adjustment ring. The adjustment ring threads over the adjustment plate and it moves the collet holder in and out when being turned. The collet holder is fixed to the adjustment ring by a rim on the collet holder itself and by three screws with Teflon washers in the back (cf. Figure 8.2).

Appendix 3. Ferrule Holder for Gluing LCWs

A simple aluminium stage has been created to hold ferrules and waveguides in place while being glued together. Since the stage is made from metal, it can be put into an oven for curing epoxy glues. The pedestals for the ferrules can be adjusted freely to any spacing.

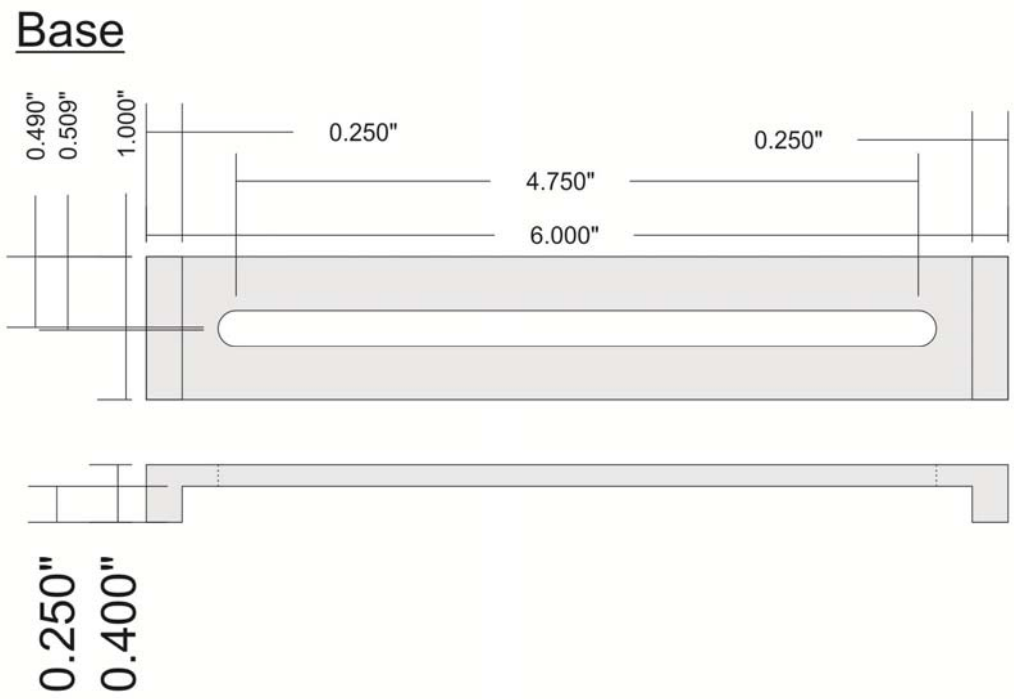


Figure A.3.1. Ferrule gluing stage base. A simple stage for gluing ceramic ferrules to LCWs and fibres has been devised for the purpose of curing the glue in the oven at 150˚ C.

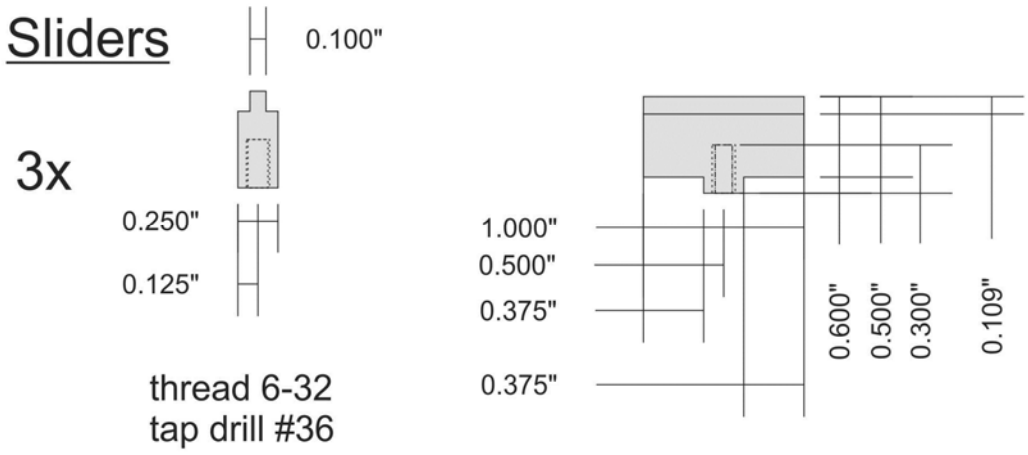


Figure A.3.2. Ferrule gluing stage sliders. Three sliders were manufactured to be screwed onto the base, to provide the appropriate support for the ferrules, and to be adjustable.

Appendix 4. Interfaces Made by Micro-Milling

With the use of a micro-drill press and end micro-mills (ball end or square end), many grooved interface plates have been manufactured in various plastics, aluminium, and glass. The travel distance for the linear stage was 25.4 mm and a rotary stage provided the possibility to change the angle (1˚ resolution) and create two, or more, intersecting grooves.

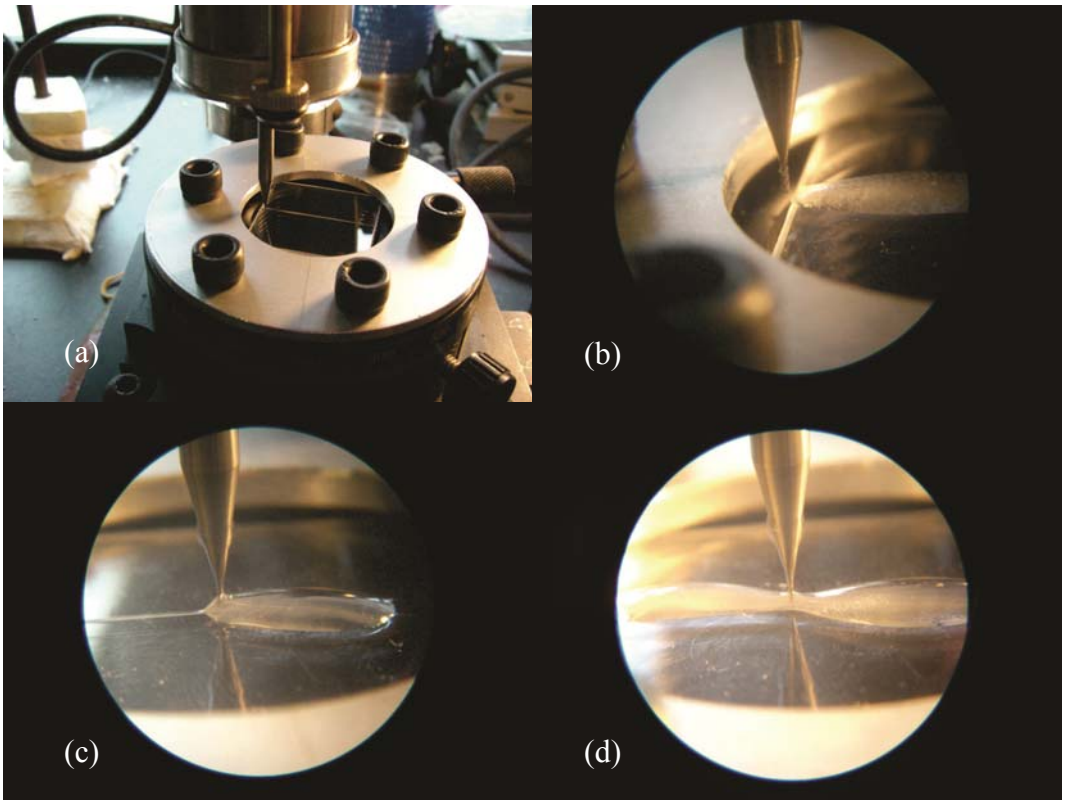

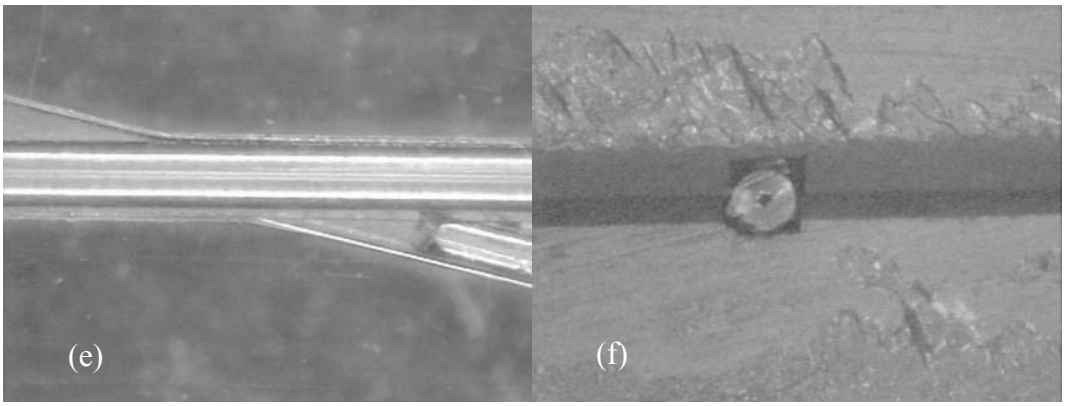


Figure A.4. Micro-milled interfaces. With the use of a micro-drill press, a linear, and a rotational stage, multiple fibre interfaces have been produced mostly from plastic but also from glass plates. The plastic, or glass, plates were affixed onto a rotational stage, which in turn was screwed onto a linear stage. This stage assembly was then placed under a micro-drill press (cf. 8.4.a), but instead of a drill bit, a micro-milling bit (*Drill Technology*) was used. The material could be moved back and forth (x-direction) with the linear stage, and rotated with the rotational stage, for producing angled channels. The depth was set at the drill press. Pictures (b) through (d) show views at different stages of the milling process. The rotation speed was held at approximately 1500 rpm for plastics, and was increased to 6000 rpm for glass. The translation speed was approximately 0.6 mm per minute, which was controlled manually at the linear positioning stage. Depths of approximately 0.012 mm were milled at one pass. Glycerin was used as a cooling and cutting fluid. Figure (e) shows two channels for an FLRDS interface at an angle of about 10˚. A capillary and a fibre were inserted to show the final alignment. A head-on picture of a square cut channel with an inserted capillary is shown in (f). One half of the final channel was cut into the top and the other half into the bottom plate. Besides square channels, also round channels were produced with a ball end micro-mill.

Appendix 5. Fibre Scope Attachments (Design)

A fibre scope attachment has been designed, in order to be able to look at the end face of a bare fibre held in a commercially available fibre holder.

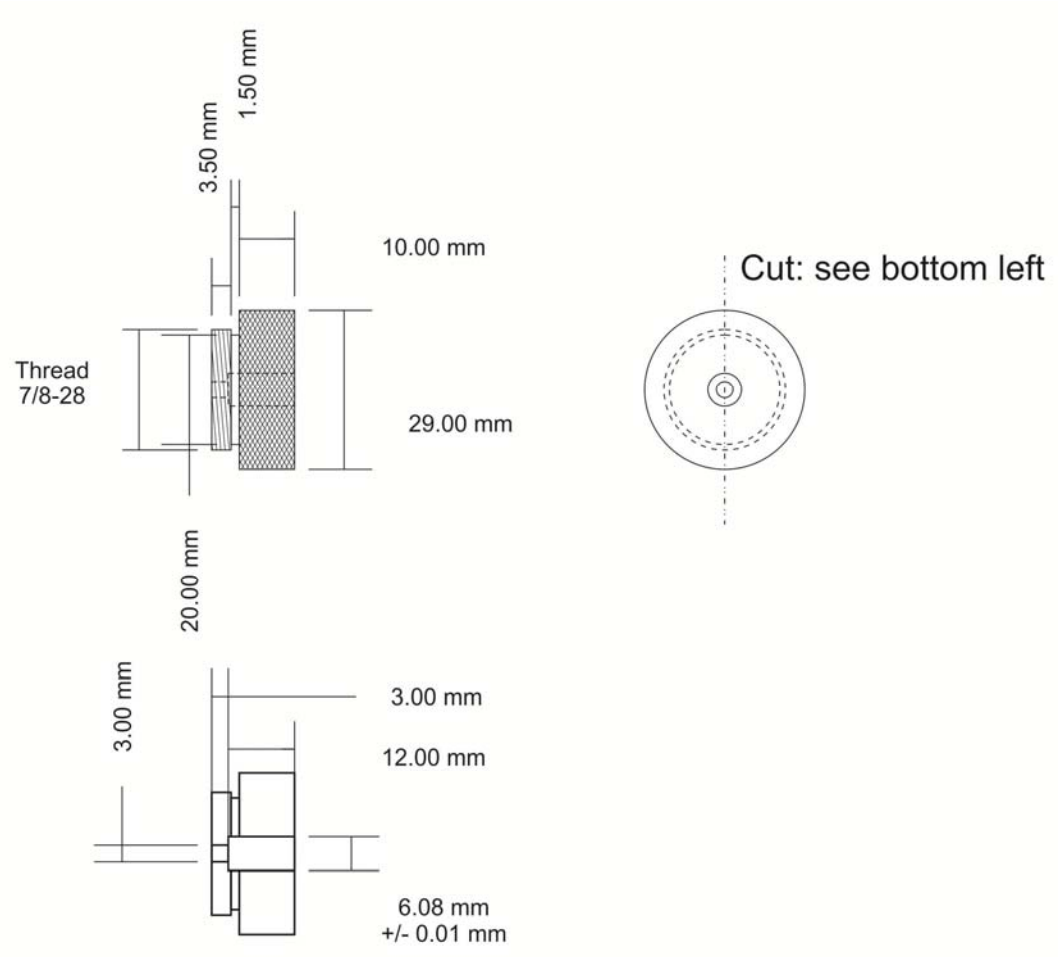


Figure A.5. A fibre inspection scope attachment for bare fibres. The attachment allows for the inspection of optical fibres, held in a bare fibre holder, with the use of the fibre inspection scope *CL-200* from *Thorlabs*.

Appendix 6. Fibre Stripper Micrometer Screw Attachment

A micrometer screw has been attached to a wire stripper for being able to adjust the opening of the wire stripper that is used to strip optical fibres without scratching or destroying them.

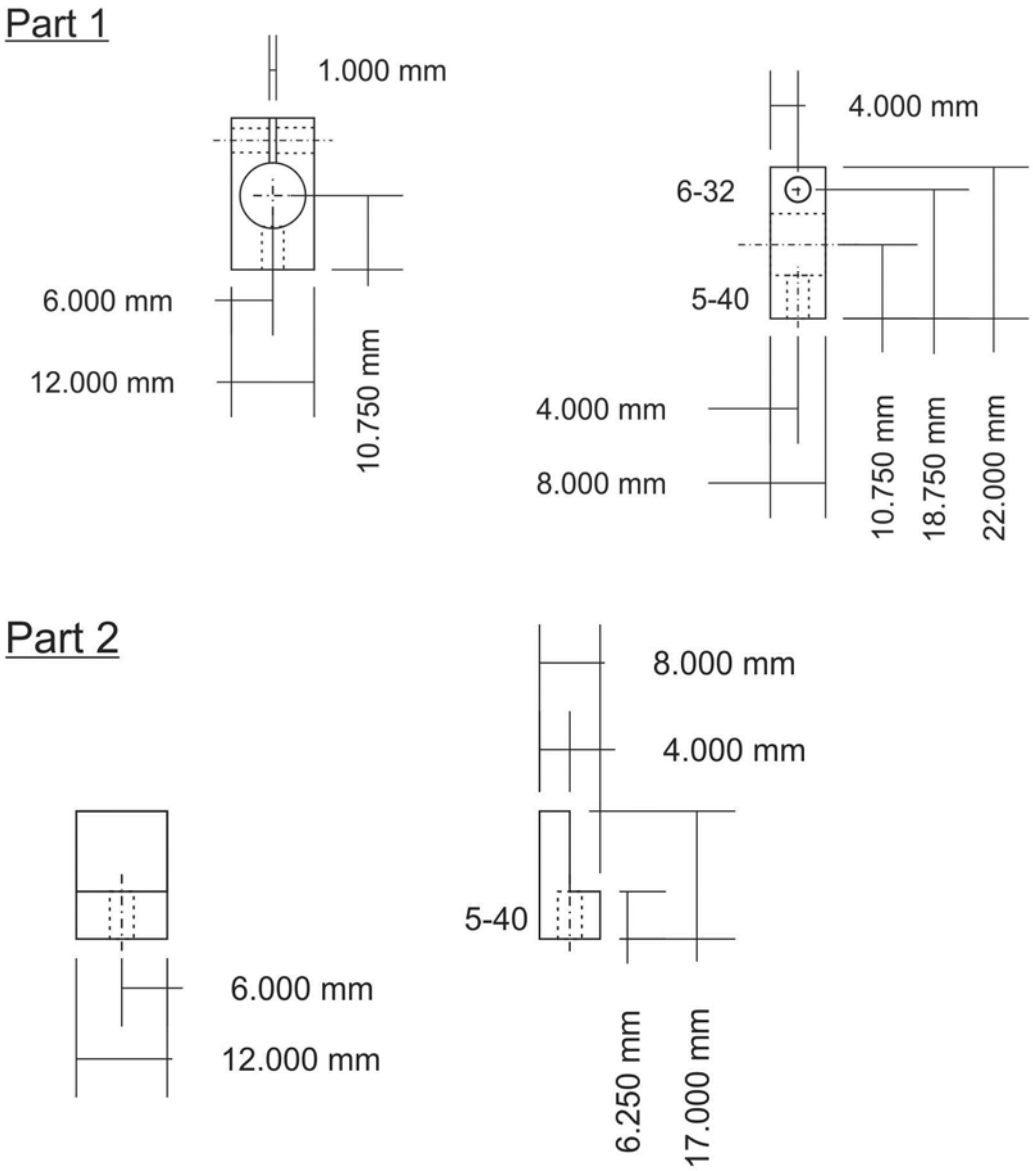


Figure A.6. Micrometer screw attachment for a wire stripper. A micrometer screw has been attached, with the above shown braces, to a wire stripper.

## Appendix 7. LED Holder for Multiple LEDs as Light Source (Design)

Since LEDs are cheap, available at many different wavelengths, and have recently become much brighter, they have become more interesting as light sources for spectroscopy. A holder for seven LEDs has been designed, in which six LEDs are arranged around a center LED. The outer LEDs are tilted, in order to focus the light output. Five holders have been produced with the use of a CNC mill. Three LED holders have been used with seven LEDs each, at 470 nm, 505 nm, and 532 nm, to build high intensity light sources. The LEDs can be sinusoidally modulated up to 20 MHz. Furthermore, the LEDs can be placed in front of a tapered light tube, focussing the emitted beam that can then be coupled into an optical fibre.

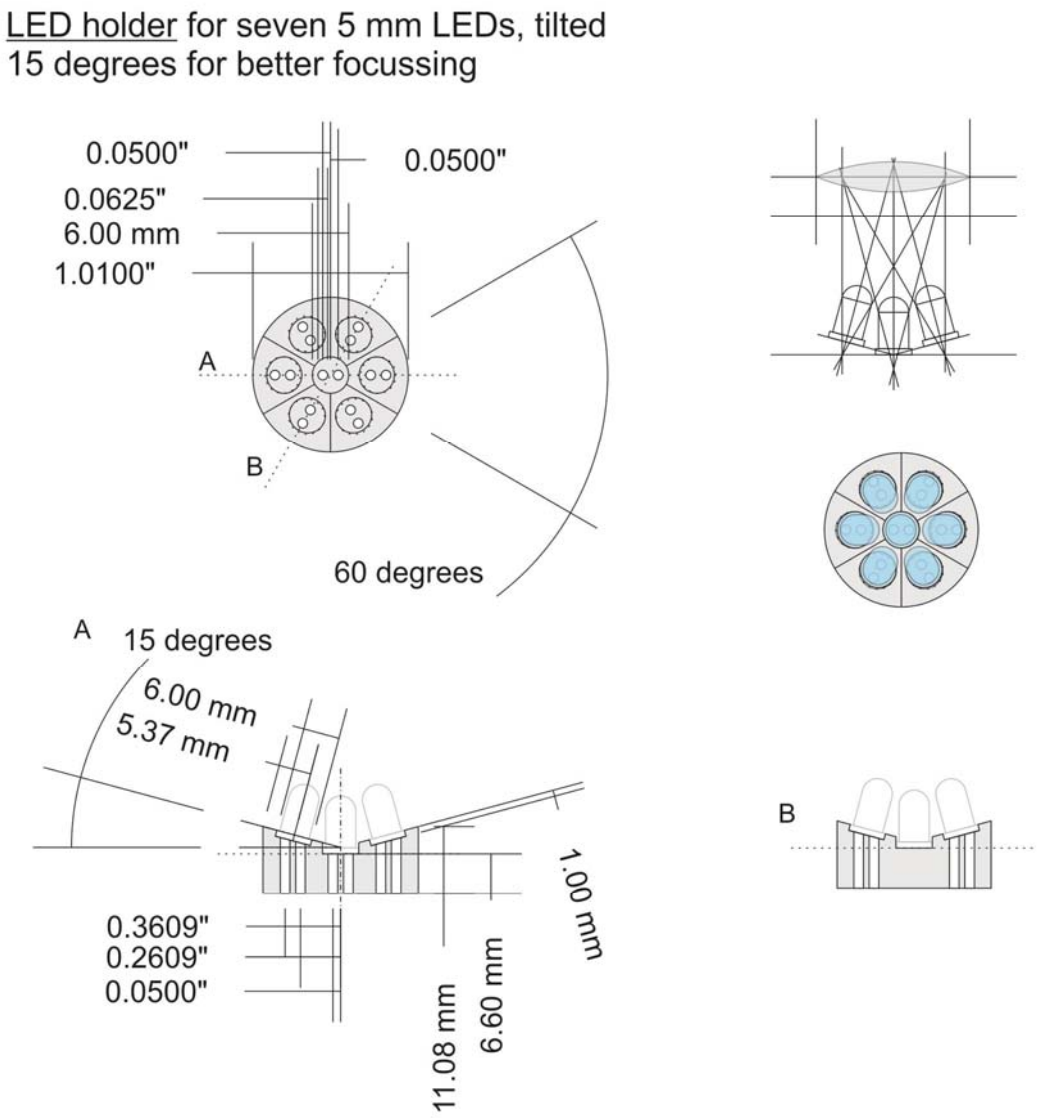


Figure A.7. A holder for seven 5 mm LEDs. The outer LEDs are tilted by 15° towards the inner LED, slightly focussing the light. In this light source, LEDs of either one or multiple colours can be placed. If focussed through different optics, the output can be coupled into an optical fibre. The LEDs can be addressed one by one or all at once, and typically, LEDs can be modulated up to multiple MHz frequencies. Light sources at 532 nm, 505 nm, and 478 nm have been manufactured.

Appendix 8. LED Illumination Ring for Camera Microscope

The camera microscope used in our laboratory was lacking a proper light source. Consequently, a plastic LED attachment ring has been designed and manufactured, featuring sixteen bright white LEDs. The LEDs have been tilted to focus their output about 3 cm away from the microscope lens, at the focal point of the microscope. The LEDs have been connected in parallel and powered by a single external power supply. A current setting resistor has been incorporated in the circuit.

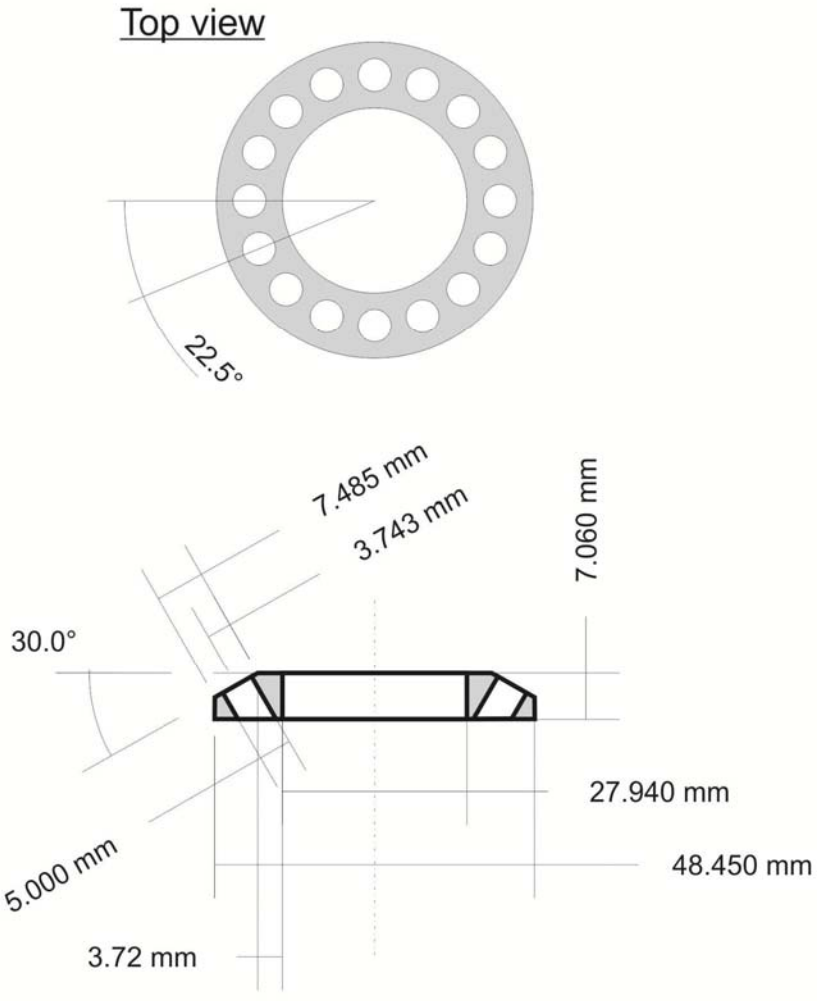


Figure A.8. LED light ring. A light ring for a telescopic microscope camera has been designed, featuring sixteen bright white LEDs.

Appendix 9. PMT Socket Holders

PMTs have been fixed in black metallic boxes and for the attachment of the PMT sockets, sheet metal parts have been manufactured.

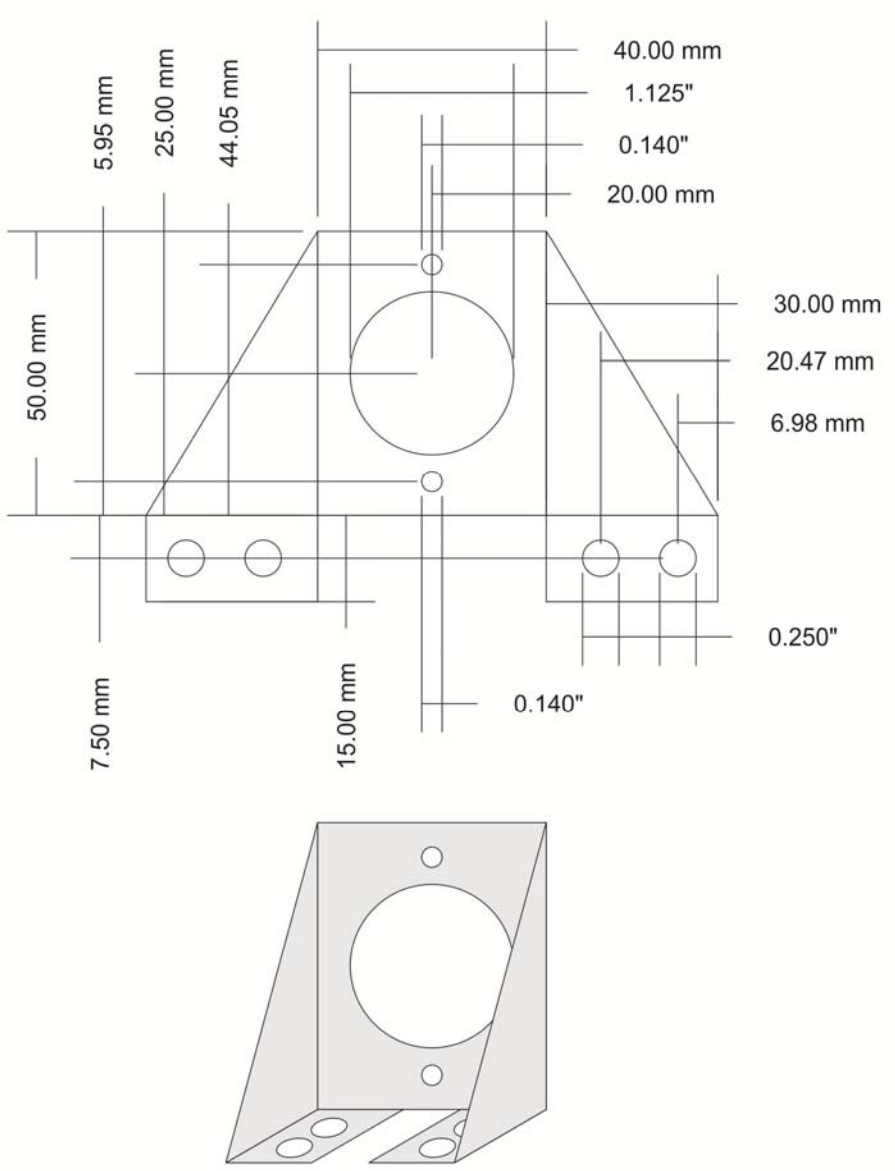


Figure A.9. Photomultiplier tube socket holder. Three new PMTs have been purchased, and each of them has been fixed into a metal detector box by the means of a PMT socket. The sheet metal holder for the PMT sockets is shown above.